Structural and Biochemical Characterization of the Lid-Loop of Acyl Protein Thioesterase

Dissertation zur Erlangung des
akademischen Grades
Doktor der Naturwissenschaften
(Dr. rer. nat)

vorgelegt der
Fakultät Chemie und Chemische Biologie
der **Technischen Universität Dortmund**

durchgeführt am
Max-Planck-Institut für molekulare Physiologie,
Dortmund

von

Arthur Thomas Porfetye, M. Sc.

Dortmund, September 2016

Die vorliegende Arbeit wurde im der Zeit von Oktober 2011 bis September 2016 am Max-Planck-Institut für molekulare Physiologie in Dortmund unter der Anleitung von Dr. Ingrid Vetter durchgeführt.

Erster Gutachter
Prof. Dr. Daniel Rauh
Technische Universität Dortmund

Zweiter Gutachter
Prof. Dr. Andrea Musacchio
Max-Planck-Institut für molekulare Physiologie

CONTENTS

1 SUMMARY 1

2 ZUSAMMENFASSUNG 3

3 INTRODUCTION 5

3.1 TARGETED CHEMOTHERAPEUTICS IN CANCER THERAPY 5

3.2 GTP-BINDING PROTEINS 5

3.3 RAS, PROTOTYPIC MEMBER OF THE RAS SUPERFAMILY 7

3.3.1 POST-TRANSLATIONAL ACYLATION OF RAS PROVIDES MEMBRANE AFFINITY 8

3.4 ACYL PROTEIN THIOESTERASE BELONGS TO THE FAMILY OF A,B-HYDROLASES 9

3.4.1 STRUCTURAL FEATURES OF APT ISOFORMS 11

3.4.2 BORON-BASED INHIBITORS OF ACYL PROTEIN THIOESTERASE 15

3.4.3 B-LACTONE CONTAINING PALMOSTATIN B AND PALMOSTATIN M 15

3.4.4 CERULENIN SHARES SOME FEATURES WITH PALMOSTATIN M 16

3.4.5 2-BROMOPALMITATE AS PRODUCT MIMIC AND INHIBITOR OF APT 17

4 GOAL OF THIS STUDY 18

5 RESULTS 19

5.1 CRYSTAL STRUCTURES OF APT IN COMPLEX WITH INHIBITORS 19

5.1.1 CRYSTAL STRUCTURE OF YEAST APT SERVES AS MODEL FOR STRUCTURAL INVESTIGATION OF INHIBITORS OF HUMAN APT1 19

5.1.2 CRYSTAL STRUCTURE OF THE YEAST APT – PALMOSTATIN B COMPLEX 25

5.1.3 CRYSTAL STRUCTURE OF THE YEAST APT - PALMOSTATIN M COMPLEX 32

5.1.4 CRYSTAL STRUCTURE OF HUMAN APT1 IN COMPLEX WITH CERULENIN 38

5.1.5 CRYSTAL STRUCTURE OF HUMAN APT1 IN COMPLEX WITH 2-BROMOPALMITATE 43

5.1.6 SUMMARY OF APT – INHIBITOR COMPLEXES 49

5.1.7 BINDING OF 2BP TO HUMAN APT INVESTIGATED BY STOPPED FLOW 49

5.1.8 DISSOCIATION OF THE HUMAN APT1 – 2BP COMPLEX INVESTIGATED BY STOPPED FLOW 52

5.2 ANALYSIS OF THE LID-LOOP FORMING THE HYDROPHOBIC BINDING TUNNEL 53

5.2.1 DESIGN OF DIFFERENT LID-LOOP MUTANTS 54

5.2.2 CRYSTAL STRUCTURES AND BIOCHEMICAL ACTIVITY OF HUMAN APT1 L171A AND L171V MUTANTS 55

5.2.3 CRYSTAL STRUCTURE OF HUMAN APT1 L58A MUTANT 58

5.2.4 CRYSTAL STRUCTURE AND BIOCHEMICAL ACTIVITY OF HUMAN APT1 L73A MUTANT 61

5.2.5 CRYSTAL STRUCTURE OF HUMAN APT1 L73A IN COMPLEX WITH 2BP 66
5.2.6 CRYSTAL STRUCTURE AND BIOCHEMICAL ACTIVITY OF HUMAN APT1 LP INSERTION MUTANT 71
5.2.7 BIOCHEMICAL ACTIVITY OF LID-LOOP TRUNCATION MUTANTS ΔL73S74 AND ΔS74P75 OF HUMAN APT1 75
5.2.8 CRYSTAL STRUCTURE OF HUMAN APT1 ΔL73S74 76
5.2.9 CRYSTAL STRUCTURE OF HUMAN APT1 ΔL73S74 IN COMPLEX WITH 2BP 80
5.2.10 CRYSTAL STRUCTURE OF HUMAN APT1 ΔS74P75 86
5.2.11 HUMAN APT1 ΔI71-D76 LID-TRUNCATION MUTANT SHOWS LOWEST ACTIVITY 89
5.2.12 CRYSTALLIZATION OF HUMAN APT1 ΔI71-D76 90
5.2.13 HYPOTHETICAL NON-PRODUCTIVE BINDING MODE OF PPTS ENABLED BY THE NON-WILD TYPE TUNNEL ENTRANCE 90
5.2.14 BINDING OF 2BP IS DEPENDENT ON THE LID-LOOP OF HUMAN APT1 92
5.2.15 DISSOCIATION OF HUMAN APT1 LID-LOOP – 2BP COMPLEXES 93
5.2.16 SUMMARY OF THE LID-LOOP MUTANTS OF HUMAN APT1 95
5.3 SHALLOW GROOVE AS POTENTIAL SECONDARY BINDING SITE 96
5.3.1 OBSTACLES FOR CRYSTALLOGRAPHIC INVESTIGATION OF THE SHALLOW GROOVE AS SECONDARY BINDING SITE 97
5.3.2 CRYSTAL STRUCTURE OF HUMAN APT1 M60S APO AND IN COMPLEX WITH 2BP 98
5.3.3 CRYSTAL STRUCTURE OF HUMAN APT1 ΔM60 APO FORM AND IN COMPLEX WITH 2BP 101
5.3.4 CRYSTAL STRUCTURE OF HUMAN APT1 ΔM60+M202A 104
5.3.5 INHIBITION OF HUMAN APT1 BY A HEXADECYLATED PEPTIDE 107
5.4 ANALYSIS OF THE DIMER INTERFACE OF LID-LOOP MUTANTS AND POINT MUTATIONS 109
5.4.1 ANALYSIS OF THE INTERFACE FORMED BETWEEN THE LID-LOOP AND THE CORE OF APT IN HUMAN APT1 WILD TYPE AND LID-LOOP MUTANTS 112
5.4.2 COMPARING THE LID-LOOP OF HUMAN APT AND LIPASES 113

6 DISCUSSION 116

6.1 *S. CEREVISIAE* APT SERVES A MODEL FOR STRUCTURAL INVESTIGATION OF INHIBITOR COMPLEXES 116
6.1.1 CERULENIN BINDING TO HUMAN APT1 PROVIDES INSIGHT INTO EPOXIDES AS NUCLEOPHILIC TRAP 117
6.1.2 2-BROMOPALMITATE SERVES AS A PRODUCT MIMIC TO INVESTIGATE THE BINDING TO APT 118
6.2 ANALYSIS OF THE LID-LOOP 119
6.2.1 THE SIDE CHAIN OF L73 IS ESSENTIAL FOR A PRE-FORMED TUNNEL 120
6.2.2 THE EXTENDED LID-LOOP BLOCKS THE BINDING TUNNEL 121

6.2.3 SHORTENED LID-LOOPS STILL PRE-FORM A SHORT HYDROPHOBIC TUNNEL BUT FAIL TO EFFICIENTLY COORDINATE THE SUBSTRATE 122
6.2.4 THE WILD TYPE LID-LOOP STABILIZES LIGAND BINDING 123
6.2.5 CALCULATION OF THE BINDING STRENGTH OF THE LID-LOOP TO THE CORE PROTEIN 124
6.2.6 PEPTIDE BINDING TO HUMAN APT1 125
6.3 COMPARISON OF LIPASES, ESTERASES AND APT 126

7 MATERIAL AND METHODS 128

7.1 CHEMICALS 128
7.1.1 KITS 128
7.1.2 ENZYMES 128
7.1.3 PROTEIN AND NUCLEIC ACID STANDARDS 128
7.1.4 BUFFERS 128
7.1.5 BACTERIAL STRAINS 129
7.1.6 MEDIA AND ANTIBIOTICS 129
7.1.7 MACHINES 129
7.2 CLONING, PROTEIN EXPRESSION AND PURIFICATION 130
7.2.1 PREPARATION OF CHEMICALLY COMPETENT *E. COLI* 130
7.2.2 TRANSFORMATION OF CHEMICALLY COMPETENT *E. COLI* 130
7.2.3 ISOLATION OF PLASMID DNA 131
7.2.4 SEPARATION OF DNA USING AGAROSE GEL ELECTROPHORESIS 131
7.2.5 POLYMERASE CHAIN REACTION 131
7.2.6 DNA SEQUENCING 131
7.2.7 MOLECULAR CLONING OF GENES AND GENE FRAGMENTS 131
7.2.8 EXPRESSION AND PURIFICATION OF PROTEINS 132
7.2.9 SDS PAGE 132
7.2.10 COOMASSIE STAINING OF PROTEIN GELS 132
7.2.11 SIZE EXCLUSION CHROMATOGRAPHY 133
7.2.12 DETERMINATION OF PROTEIN CONCENTRATIONS 133
7.2.13 MASS SPECTROMETRY 133
7.3 PROTEIN CRYSTALLOGENESIS 133
7.3.1 SUMMARIZED THEORY OF CRYSTALLOGENESIS 133
7.3.2 CRYSTALLIZATION SCREENING 134
7.3.3 CRYSTALLIZATION REFINEMENT IN HANGING DROPS 134
7.3.4 CRYSTAL PREPARATION FOR X-RAY DIFFRACTION EXPERIMENTS 134
7.4 X-RAY CRYSTALLOGRAPHY 135

7.4.1 SUMMARIZED THEORETICAL BACKGROUND 135
7.4.2 X-RAY DIFFRACTION DATA COLLECTION 136
7.4.3 DATA REDUCTION, PHASING AND STRUCTURE BUILDING 137
7.4.4 STRUCTURE VALIDATION 137
7.4.5 GENERATION OF LIGAND MODEL RESTRAINTS 137
7.4.6 ILLUSTRATION OF CRYSTAL STRUCTURES AND ANNOTATING IMAGES 137
7.5 BIOCHEMICAL ACTIVITY ASSAY 137
7.5.1 PPTS ENZYME KINETICS 138
7.5.2 INHIBITOR IC_{50} DETERMINED IN ENZYMATIC ACTIVITY ASSAY USING OPTS AS SUBSTRATE 138
7.5.3 ANALYSIS OF THE ACTIVITY ASSAY DATA 138
7.6 STOPPED FLOW 138
7.6.1 STOPPED FLOW BINDING RATE CONSTANT 139
7.6.2 STOPPED FLOW DISSOCIATION RATE CONSTANT 139
7.6.3 DOPC VESICLES 140
7.6.4 PEPTIDE SYNTHESIS AND MODIFICATION 140
7.7 CALCULATION OF THE FREE SOLVATION ENERGY USING PISA 140

8 REFERENCES 141

9 ACKNOWLEDGEMENTS 146

10 OTHER PUBLICATIONS OF THIS AUTHOR 147

11 EIDESSTATTLICHE VERSICHERUNG (AFFIDAVIT) 148

12 APPENDIX 149

1 Summary

Cancer formation depends on the acquisition of multiple attributes via mutations of the genome to obtain replicative advantages of the tumor cells. Ras is a well-characterized small GTP-binding protein involved in signaling cascades regulating cell growth and proliferation. 25% of all human tumors contain a mutated form of Ras, making it an interesting target for cancer research. Ras activity is controlled via the bound G-nucleotide and the subcellular localization at the plasma membrane, achieved by posttranslational lipidation of the C-terminus of all four human isoforms of Ras. Correct subcellular compartmentalization of Ras is achieved by a cycle of constant de-palmitoylation catalyzed by Acyl Protein Thioesterase (APT), and re-palmitoylation at the golgi coupled to vesicular transport to the plasma membrane. Inhibition of APT disturbs this cycle, leading to entropy-driven random distribution of Ras over all cellular membranes resulting in a decreased local concentration at the plasma membrane and subsequently a reduced signaling activity of Ras.

The suspected binding site of palmitoylated protein is a solvent-accessible hydrophobic tunnel where one wall is pre-formed by a “lid-loop”, a unique structural motif not described in the literature for other proteins so far. Different chemical classes of APT inhibitors have been described in the literature, but no structural data of APT-inhibitor complexes were available before. This thesis contains the first complex structures of *S. cerevisiae* APT with palmostatin B and palmostatin M and confirmed the hydrophobic tunnel as binding site of the aliphatic moiety. The β-lactone core of palmostatin inhibitors is covalently bound via a reversible ester to the active site serine. The activated epoxide of Cerulenin can also act as nucleophilic trap for the active site as seen in the structure of the covalent complex with human APT1. 2-Bromopalmitate (2BP) is a product mimetic of high similarity, and confirmed (as competitive inhibitor) binding inside the tunnel also for non-covalently attached aliphatic fatty acids.

The influence of the tunnel-forming lid-loop on substrate binding and catalytic activity of APT has not been described in the literature. APT belongs – like lipases and cutinases/esterases - to the family of α,β-hydrolases. The active site of lipases is covered by a flexible lid that is interfacially activated upon membrane attachment, while the active site of cutinases and esterases is open and accessible due to the lack of any covering loop. In this thesis, different lid-loop mutants of APT were crystallized and tested on biochemical activity. The proper formation of the wild type tunnel entrance was shown to be crucial for defined ligand binding and efficient catalysis as the tunnel entrance defines the insertion depth of the palmitate moiety, thus positioning the (thio-)ester at the active site serine. Mutations altering the shape of the tunnel entrance or increasing the flexibility of the lid-loop show less defined binding of 2BP (as seen in the crystal structures of the complexes with 2BP) that can serve as basis for a hypothetical unproductive binding mode of the test substrate PPTS. The lid-loop mutants having an altered tunnel entrance show a significantly reduced biochemical activity of about 25% compared to the wild type. A mutant lacking the complete lid-loop

shows only 3% biochemical activity. Stopped Flow measurements corroborate that the tunnel formed by the lid-loop plays an essential role in defined binding of the palmitate moiety inside the hydrophobic tunnel. Lid-loop mutants also show a faster dissociation rate of the 2BP complex than the wild type of human APT1.

Human APT1 forms a typical weak dimer in crystals (and potentially in solution), which blocks the potential secondary binding site for palmitoylated peptides and/or acyl chains. Attempts to free this binding site for structural investigation of a complex of human APT1 and a hexadecylated peptide were not fruitful so far. However, peptide binding could be shown indirectly via inhibition of biochemical activity of APT.

APT crystallizes always with the lid-loop in the tunnel-forming conformation except for one structure of *O. punctata* APT that contains two of four monomers with an opened lid-loop. The potential of an opening lid-loop of APT (similar to the lid of lipases) was analyzed by comparing the available prediction of membrane insertion of different proteins, that predict APT to be weakly associated to membranes, a binding that is enhanced by the N-terminal palmitoylation of APT. Binding of the lid-loop to the APT core protein is stronger than the membrane insertion of APT, but membrane binding strength could change if the lid-loop were in an open conformation. Thus, no reliable prediction on this hypothesis is possible at the moment.

Combining activity assay data with the crystal structures, I conclude that for efficient substrate turnover the stability and shape of the entrance of the binding tunnel are of crucial importance. In contrast to lipases (where the lid regulates activity), the function of the lid-loop of APT is to form a stable tunnel to coordinate the substrate at the active site and thus stabilizing the transition state of catalysis. We therefore postulate that APTs are an individual structural and functional class between lipases and cutinases/esterases within the family of α,β-hydrolases.

2 Zusammenfassung

Die Entstehung von Krebs ist abhängig vom Erwerben mehrerer vorteilhafter Fähigkeiten durch Mutationen des Erbguts. In 25% aller humanen Tumoren liegt eine Mutation von Ras vor, weshalb es ein interessantes Ziel in der Krebsforschung darstellt. Ras ist ein gut charakterisiertes kleines GTP-bindendes Protein, welches in verschiedenen Signalkaskaden zur Regulation von Zellwachstum und -teilung involviert ist. Die Aktivität von Ras wird durch das gebundene G-Nukleotide sowie die subzelluläre Lokalisation an der Plasmamembran durch post-translationale Lipidierung der C-termini aller vier humanen Isoformen von Ras reguliert. Die korrekte subzelluläre Kompartmentalisierung wird durch einen konstanten Zyklus aus De-palmitoylierung durch Acyl Protein Thioesterase (APT) und Re-palmitoylierung am Golgi verbunden mit vesikulärem Transport zur Cytoplasmamembran gewährleistet. Inhibition von APT unterbricht diesen Zyklus und führt zu einen Entropie-getriebenen Verteilung von Ras über die gesamten Intrazellulären Membranen, was in einer verringerten lokalen Konzentration und damit verbunden geringeren Signalweiterleitung resultiert. APT-Inhibitoren verschiedener chemischer Klassen sind in der Literatur beschrieben, allerdings waren keine strukturellen Daten von APT - Inhibitor Komplexen verfügbar.

Die vermutete Bindestelle von palmitoylierten Proteinen ist ein dem Lösungsmittel zugänglicher hydrophober Tunnel neben der katalytischen Triade, dessen Außenwand durch einen *„lid-loop“* geformt wird, ein einzigartiges und in der Literatur noch nicht beschriebenes Strukturmotiv. Die Kristallstrukturenstrukturen von *S. cerevisiae* APT im Komplex mit Palmostatin B und Palmostatin M wurden in dieser Dissertation gelöst und bestätigen den hydrophoben Tunnel als Bindungsstelle der Fettsäure. Neben dem β-Lactone der Palmostatin Inhibitoren, welches kovalent durch einen reversible Ester an das katalytische Serin gebunden wird, zeigte die Struktur des Komplex mit Cerulenin das Potential von aktivierten Epoxiden als Falle für das nucleophile Serin. 2-Bromopalmitat (2BP) ist ein Produkt Analoga von hoher struktureller Ähnlichkeit, welches die Bindung im Tunnel von (kompetitiven) nicht kovalent gebundenen aliphatischen Fettsäuren nachweist.

Der tunnelformende *lid-loop* wurde noch nicht detailliert auf seinen Einfluss bei Substratbindung und katalytischer Aktivität in der Literatur beschrieben. APT gehört – wie auch Lipasen und Cutinasen/Esterasen – zur Familie der α,β-Hydrolasen. Während das aktive Zentrum von Lipasen durch einen „Deckel“ (engl. *lid*) abgeschirmt ist, welcher sich bei Membranenassoziation öffnet, ist das aktive Zentrum von Cutinasen und Esterasen frei zugänglich. In dieser Dissertation wurden verschiedene *lid-loop* Mutanten von humanen APT1 kristallisiert und auf biochemische Aktivität getestet. Ein korrekt gebildeter Tunneleingang ist essentiell für die Koordination von Liganden und effiziente katalytische Aktivität. Mutationen, welche die Form des Tunneleingangs oder die Flexibilität des *lid-loop* signifikant verändern zeigen eine verringerte Koordination von 2BP in den jeweiligen Komplex-Kristallstrukturen. Diese Strukturen erlauben auch einen hypothetischen nicht-produktiven Bindungsmodus des Testsubstrats PPTS. Mutanten mit verändertem Tunneleingang

haben eine reduzierte biochemische Aktivität von ca. 25% verglichen mit dem human APT1 Wildtyp, eine Restaktivität von lediglich 3% wurde bei einer Mutante ohne *lid-loop* gemessen. *Stopped Flow* Messungen bestätigen die Rolle des durch den *lid-loop* geformten Tunneleingang bei der Binding von 2BP im hydrophoben Bindungstunnel. Die Dissoziation von 2BP aus einem APT-Komplex ist durch Mutation des *lid-loop* erhöht.

Humanes APT1 bildet in Kristallen (und wahrscheinlich in Lösung) ein typisches schwaches Dimer, welches die potentielle sekundäre Bindungstelle für das Substratprotein und/oder weitere Fettsäureresten blockiert. Strukturelle Untersuchungen von humanem APT1 - Peptid Komplexen waren bis jetzt nicht erfolgreich, jedoch konnte die Bindung eines hexadecylierten Peptid indirekt durch die Inhibition der biochemischen Aktivität von APT nachgewiesen werden.

Fast alle Kristallstrukturen von APT zeigen den *lid-loop* in den Tunnel-formenden Konformation, einzig eine Struktur von *O. punctata* APT enthält zwei von vier Monomeren mit geöffnetem *lid-loop*. Die Möglichkeit eines sich öffnenden *lid-loop* von APT (ähnlich zu dem *lid* von Lipasen) wurde analysiert durch Vergleich der Voraussage über Proteininsertion in Membrane sowie der theoretischen Bindungsstärke des *lid-loop* zu APT selbst. Die berechnete Interaktion des *lid-loop* mit dem Kern von APT ist stärker als die vorhergesagte Membraninsertion von APT, allerdings ändert sich die Insertion in eine Membran durch ein hypothetisches Öffnen des *lid-loop*, weshalb keine verlässliche Vorrausage getroffen werden kann.

Die Daten der biochemischen Assay und Kristallstrukturen zeigen, dass der *lid-loop* durch die Bildung eines stabilen Tunnels mit definiertem Eingang eine für effiziente biochemische Aktivität essentielle strukturgebende Funktion hat, statt wie im Fall von Lipasen den Zugang zum katalytischen Zentrum zu regeln. Daher kann postuliert werden, dass APTs eine eigenständige strukturelle und funktionale Klasse – zwischen Lipasen und Cutinasen/Esterasen – innerhalb der α,β-Hydrolasen bildet.

3 Introduction

3.1 Targeted chemotherapeutics in cancer therapy

Modern cancer therapy relies on a combination of the three pillars of surgery, radiation therapy and chemotherapy. Conventional chemotherapy administering cytotoxic drugs has severe side effects due to the lack of selectivity. Knowledge about the cancer-causing and promoting malfunction of individual proteins can be used to specifically address these mutant versions of the protein, thereby focusing the destructive potential on the cancer cells. This approach is referred to as 'targeted cancer therapy' [1].

The design of selective small molecular compounds targeting requires a detailed knowledge about structural and biochemical properties of the mutated protein as well as its role in the cellular signaling network. Due to the high abundance of mutations in the *ras*-gene and their strong effect in human cancer, the small GTP-binding protein Ras is one prominent target for cancer therapy. Extensive research in the past decades yielded considerable knowledge about Ras, but failed to produce an inhibitor. The following chapter provides a rough overview on the family of GTP-binding proteins, and a more detailed description of Ras is given in Chapter 3.3, followed by the introduction of APT in Chapter 3.4, which might provide an approach to indirectly target Ras activity in cancer.

3.2 GTP-binding proteins

Energy can be gained of all four nucleoside triphosphates (NTPs) by hydrolysis of the γ-phosphate, but unlike adenosine triphosphate (ATP) that is the cell's currency in energy metabolism and a source of phosphate for protein phosphorylation[2], guanosine triphosphate (GTP) is mostly used as regulating co-factor of protein involved in signal transduction cascades. GTP-binding proteins (following referred to as G-proteins) can be found in all three kingdoms of life and contain a set of motifs responsible for GTP-specificity and binding. These motifs are highly conserved through all G-proteins, indicating a common ancestor. Guanine binding and specificity is set by G1-G5 motif, phosphate and metal binding by PM1-3 and the specificity by G1'-G3' motif. G1/PM1 motif is the P-loop GxxxxGKS/T, G2/PM2 is a Threonine in the switch I loop, G3/PM3 is a DxxG motif and G4/G2' N/TKxD is largely responsible for the GTP specificity. A weakly conserved SAK is considered G5/G3', but not present in all G-proteins. The conserved N-terminal 166 amino acids of Ras are considered the minimal G-binding fold[3], illustrated in Figure 1.

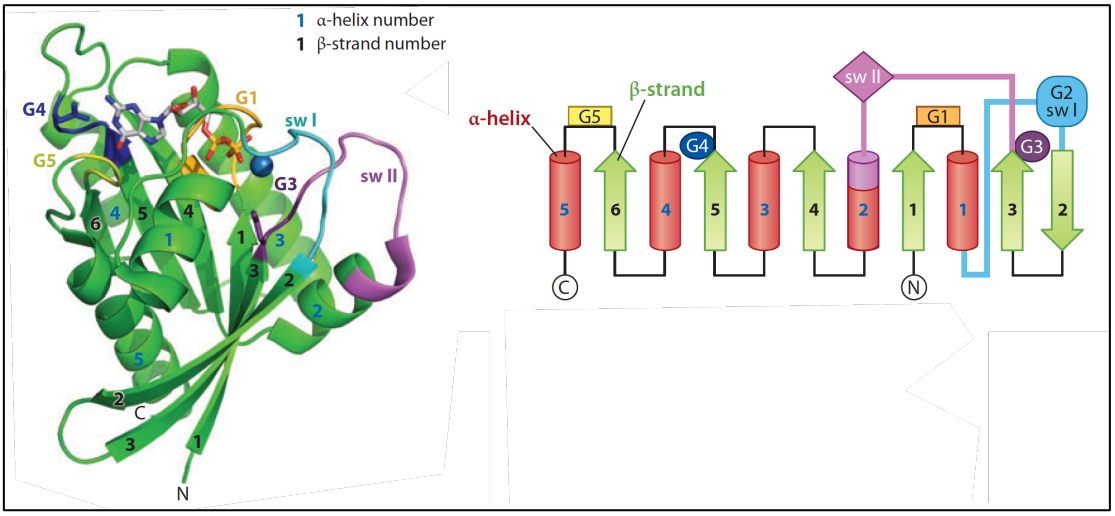

Figure 1: Minimal G-protein fold presented exemplarily on Ras (green) bound to GppNHp (yellow) and Mg^{2+} (blue sphere) (PDB ID 5p21), also shown as 2D topology (right). Switch 1 and switch 2 are coordinated by the γ-phosphate of GppNHp in the active state. G1-5 motifs provide selectivity for guanine nucleotides. Figure taken from [3] and modified using Gimp[4].

G-proteins function as a molecular switch. The active conformation is in the GTP-bound state, with the γ-phosphate bound by main-chain hydrogen bonds between G2 motif Threonine in the α1-β2 loop (switch I) and G3 Glycine located in the β3- α2 loop (switch II). In this conformation the G-protein can interact with downstream effectors leading to cell proliferation[5]. Both switch I and II undergo a structural change upon GTP γ-phosphate hydrolysis, termed the 'loaded-spring' mechanism that is conserved through all G-proteins[5,6]. Interaction of the γ-phosphate with the main chain amides instead of side chains might enable a stronger coordination and higher flexibility of the switch II due to the glycine, and additionally tolerates sequence variation for effector specificity[3].

The intrinsic GTPase activity is usually rather slow in the range of 10^{-4}-10^{-5} s^{-1}, resulting in sustained signal transduction via binding of the GTP-form to downstream effectors until a GTPase-Activating Protein (GAP) binds to the active small G-protein, thus enhances the intrinsic GTPase activity to 1-10 s^{-1}, leading to GTP-hydrolysis and deactivation[3,7,8]. Some multimeric G-proteins trigger GTPase activity by dimerization. GDP release and GTP reloading is facilitated by Guanine Exchange Factors (GEFs) and the higher cellular concentration of GTP[9-11].

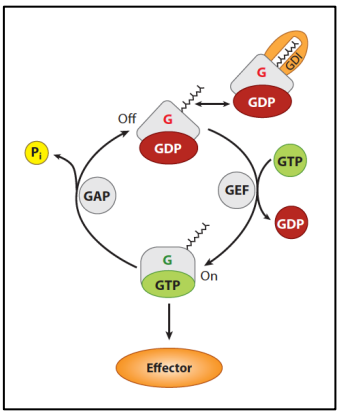

Figure 2: Nucleotide-regulated cycle of G-protein activity. Ras belongs to the monomeric small G-proteins, which are activated by GEF-mediated GDP-GTP exchange. Hydrolysis of GTP is enhanced by complex-formation with a GAP. Image taken from [3].

The superclass of G-proteins can be divided into two large subclasses. The first SIMIBI (signal recognition, MinD, BioD) class contains signal recognition particle (SRP) GTPases, ATPases involved in protein localization and chromosome partitioning and a group of proteins with metabolic activity related to phosphate transfer. The latter subclass of G proteins, TRAFAC (designated after translation factors), contains those and proteins involved in signal transduction (for example the Ras-like superfamily), cell mobility and intracellular transport[3,12].

The following chapter will describe the Ras protein, the prototypic member of the Ras superfamily. Mutations of Ras enhance cell growth and tumor formation in about 25% of all human cancer[13,14], making Ras an attractive target for cancer therapy.

3.3 Ras, prototypic member of the Ras superfamily

The Ras superfamily is a family of small GTP-binding proteins named after the prototypic member discovered in Rat sarcoma virus and contains about 150 proteins in humans, all being 20-25kDa of molecular weight as mostly consisting of the GTP-binding domain. Small G-proteins are monomeric in solution[15,16]. Also belonging to the Ras-subfamiliy are Rho (Ras homolog) involved in the control of the cytoskeleton[17], Ran (Ras involved in nuclear transport)[18], Rab (Ras-like protein in brain) and Arf/Sar1 (ADP ribosylation factor)[19].

The three human *RAS* genes encode the four proteins H-Ras, N-Ras and the two splice variants K-Ras4A and K-Ras4B. H-Ras and K-Ras were discovered in the 1960s by Harvey[20] and Kirsten[21] as the oncogene responsible for leukemia in sarcoma virus infected rats. N-Ras was identified in human neuroblastoma cells in 1982[22,23]. All Ras proteins contain the highly conserved minimal G-binding fold (amino acids 5-166)[15,24,25] with a hypervariable C-terminal region. The G-binding fold contains switch I and switch II which change their conformation depending on the nucleotide bound[3,6] as described in chapter 3.2 before. The most common oncogenic mutation in Ras proteins at G12 blocks the interaction with its GAP that is necessary to deactivate the molecular switch by hydrolysis of bound GTP to GDP, thereby leaving Ras constitutively in its active state, which leads to uncontrolled cell growth[7]. This can be explained by analysis of the Ras•GDP•AlF_3•RasGAP complex (PDB ID 1wq1, [26]) and RhoA•GDP•AlF_3•GAP complex (PDB ID 1tx4, [27]) structures, that show how the so-called “arginine finger” is inserted next to G12/G13 into Ras (G14/A15 in RhoA) next to the γ-phosphate, highlighting that any mutation to a residue with larger side chain would lead to a steric clash preventing acceleration of GTP hydrolysis. Fast GTPase activity without Arg-finger has been reported for Ran, were the Ran-intrinsic nucleophilic glutamine is correctly positioned for GTP hydrolysis upon formation of the ternary Ran•GppNHp•RanBP1•GAP complex (PDB ID: 1k5d/1k5g, [28]).

The high percentage of human tumors containing mutations in one or more *ras*-genes indicates their strong oncogenic potential and significant role in tumorgenesis and cancer development[13]. To investigate their importance in fetal development and on overall survivability *ras*-deficient mice have been bred. N-Ras deficient mice have been found to be vital without any observed development defect, and adults of both sexes are fertile[29]. H-Ras deficient mice are vital, fertile, and show no

defects in neuronal development[30]. Crossbreeding of H-Ras and N-Ras deficient mice led to H-/N-Ras double null mutants, which are also vital and show normal development[30]. However, K-Ras deficient mice die from liver defects and signs of anemia during embryonic development[31], showing that only K-Ras is essential for mice development. Despite the unaltered phenotype of a H-/N-Ras deficient mouse, tumors can be dependent e.g. on mutated H-Ras, as shown in mouse models[32].

3.3.1 Post-translational acylation of Ras provides membrane affinity

The hypervariable C-terminal region varies in sequence and lipid modification between the four human isoforms of Ras. All Ras proteins are post-translationally farnesylated and mono- (H-Ras, K-Ras4A) or dually palmitoylated (N-Ras) at the hypervariable C-terminal region; only the splicing variant K-Ras4B is not palmitoylated, but instead contains a poly-lysine stretch next to the farnesylated cysteine to enhance membrane association[33-35].

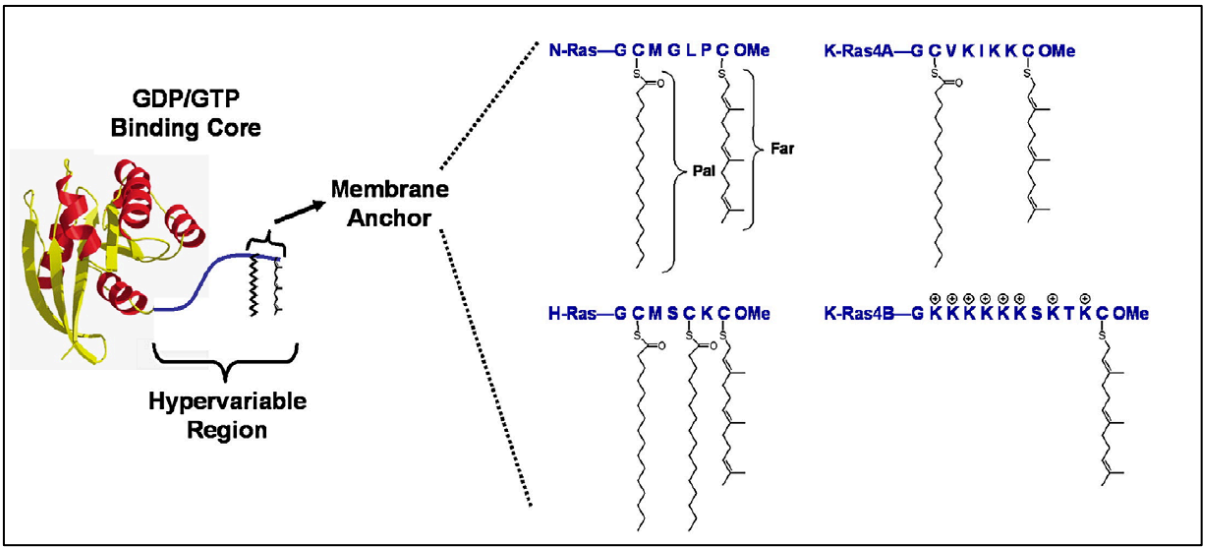

Figure 3: Human Ras-isoforms and their post-translational modifications. All four human Ras isoforms share a highly conserved GTP-binding core, but vary in sequence and lipid modification at the C-terminal hypervariable region. All Ras isoforms are farnesylated. Figure taken from[36].

Ras farnesylation by farnesyl-protein transferases[37] and palmitoylation by DHHC9/GCP16 [38,39] happens at the golgi complex. Following the post-translational modification, Ras is shuttled through vesicular transport towards the membrane[40] where it acts as a molecular switch in signal transduction cascades regulating cell growth and proliferation. Entropy-driven diffusion of membrane associated Ras would lead to a random distribution of Ras trapped at all endo-membranes, resulting in a decreased local concentration at the plasma membrane and a decreased signaling activity[41]. To circumvent this, the palmitoylated isoforms of Ras are proposed to be constantly de-palmitoylated by Acyl Protein Thioesterase (APT)[42], thereby detaching it from the membrane and enabling faster diffusion to the golgi, where Ras is re-palmitoylated and cycled back to the plasma membrane[41,43]. This constant cycle of de- and re-palmitoylation maintains a high local concentration of Ras at the plasma membrane necessary for correct signal transduction, and also presents a soft spot for modulating activity of indelible active mutated Ras and reverting cancerous phenotypes[44-46].

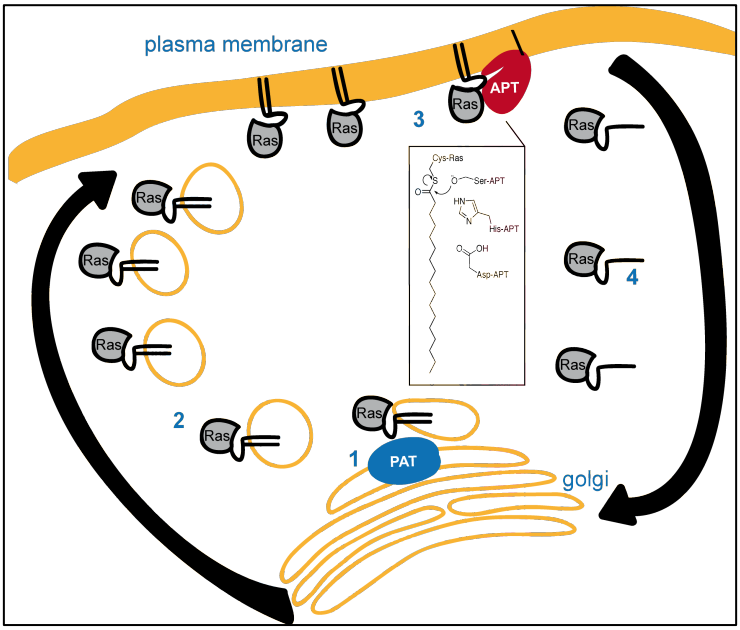

Figure 4: Palmitoylation cycle of Ras. Post-translational lipidation at the golgi includes a irreversible farnesyl thioether, and (depending on the Ras protein) up to two palmitoyl thioester groups (1). Ras is then transported via vesicular transport (2) towards the plasma membrane, where it acts as molecular switch regulated by the bound nucleotide. Membrane release and de-palmitoylation by APT (3) leads to trafficking of Ras towards the golgi, where re-palmitoylation initiates the restart of the cycle. Image created using Adobe Illustrator.

While farnesylation is an irreversible lipid modification at cysteine residues via a thioether bond, palmitoylation via a thioester is reversible. Ras signaling activity is not only depending on the nucleotide bound to it, but also on its correct subcellular localization. Therefore, one approach to decrease Ras signaling activity caused by constitutively active mutants included farnesyl-protein transferase inhibitors to interfere with Ras maturation, but it has been shown that in cells treated with the farnesyl-protein transferase inhibitor tipifarnib Ras localization is rescued by geranyl-geranylation[47].

Ras extraction from the plasma membrane is not understood in detail. In its farnesylated/palmitoylated state, simple off-diffusion is unlikely due to the high membrane affinity of palmitoylated proteins[48,49]. There is no protein or mechanism for an active Ras extraction known so far, but it could be possible that APT itself is not only responsible for depalmitoylation but also membrane extraction of the palmitate membrane anchor of its substrates.

3.4 Acyl protein thioesterase belongs to the family of α,β-hydrolases

Acyl protein thioesterase (APT) belongs to the family of α,β-hydrolases. The α,β-hydrolase family is defined via its fold, that contains a three-layered (a/b/a) core with a central sheet of 8 β-sheets (of which β-sheet 2 is anti-parallel) in an order of 12435678, connected and surrounded by 6 α-helices (see Figure 5) [50,51]. Insertions and extensions of the α-helices form a variety of structural features of different sub-classes. The conserved catalytic triad consisting of a nucleophilic serine, basic histidine, and acidic aspartate; the reaction mechanism is described further below in Figure 7.

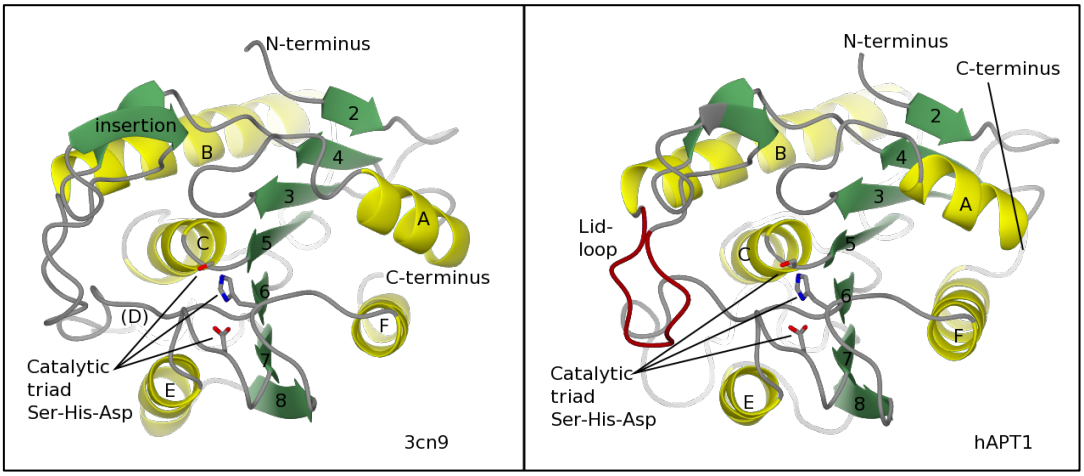

Figure 5: Left: Overview of a carboxyl esterase from *Pseudomonas aeruginosa* (PDB ID: 3cn9) as an example of the minimal fold of a α,β-hydrolase protein. The canonical fold contains a central sheet formed by 8 β-sheets shown in green, with β-sheet 2 being anti-parallel. The connecting α-helices are presented in yellow and labeled A-F from N- to C-terminus. Right: Structure of human APT1 contains a lid-loop (shown in red) formed by an extension of helix B. This lid-loop forms the hydrophobic binding tunnel next to the active site.

The class of α,β-hydrolases contains 41 protein superfamilies according to the SCOP data base, among which are proteases, lipases, esterases, peroxidases, epoxide hydrolases and dehalogenases[51,52]. These classes are neither conserved in sequence nor function, but share the before mentioned conserved α,β-hydrolase fold, indicating a common ancestor[53].

The active site of esterases is located on the surface close to a small binding pocket suitable to bind and be readily accessible for the specific substrate without rearrangements of the protein. Esterases hydrolyze a variety of short-chained (thio-) esters, but are unable to bind longer aliphatic chains[54].

Lipases contain an additional loop that completely covers the active site and its surrounding hydrophobic patch. This loop opens upon binding to membranes and vesicles, thus revealing the active site to the substrate, typically long-chained mono-/di-/triglycerol esters[55]. Lipases contain a hydrophobic binding tunnel next to the active site that accommodates the long aliphatic chain of its substrate and stabilizes it during hydrolysis (compare PDB ID: 4lhe, [55,56]).

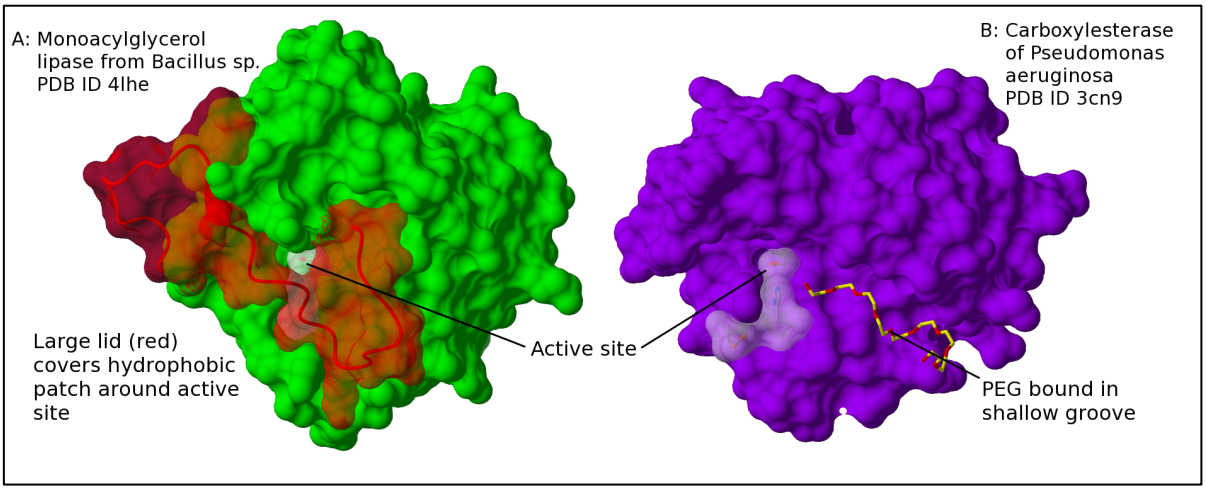

Figure 6: Comparison of a monoglyceride lipase of *Bacillus* sp.[56] and carboxylesterase of *Pseudomonas aeruginosa*[57]. A: The large lid (red) of the lipase (green) completely covers the active site and surrounding hydrophobic patch. B: The active site of the esterase is accessible and not covered by a lid. A PEG molecule is bound in this structure in a shallow groove.

The reaction mechanism of a/β-hydrolases is depicted in Figure 7 in detail, showing the catalytic triad of APT consisting of serine, histidine and aspartate. The hydroxyl moiety of the active site serine is thought to be deprotonated by the histidine-aspartate diad, which acts as proton sink. The thus activated serine oxyanion (Figure 7, red) performs a nucleophilic S_N2 attack on the thioester of e.g. palmitoylated Ras, forming a tetrahedral intermediate (Figure 7, yellow), which charged oxyanion is stabilized by hydrogen bonds via the backbone amides that form the oxyanion hole. In the following, the oxyester at the active site serine is formed with the thiol of the cysteine of Ras as leaving group, leaving the palmitoylated active site serine of APT (Figure 7, purple) as reaction intermediate. The deacylation of APT is performed in a similar mechanism, using a water molecule (Figure 7, blue) as nucleophile. This hydrolytic water is deprotonated by the histidine-aspartate dyad similar to the prior described formation of the reactive serine oxyanion, and subsequently attacks the serine palmitate ester. The oxyanion of the tetrahedral reaction intermediate is stabilized by the oxyanion hole, and the serine of APT poses the leaving group when palmitate is re-formed.

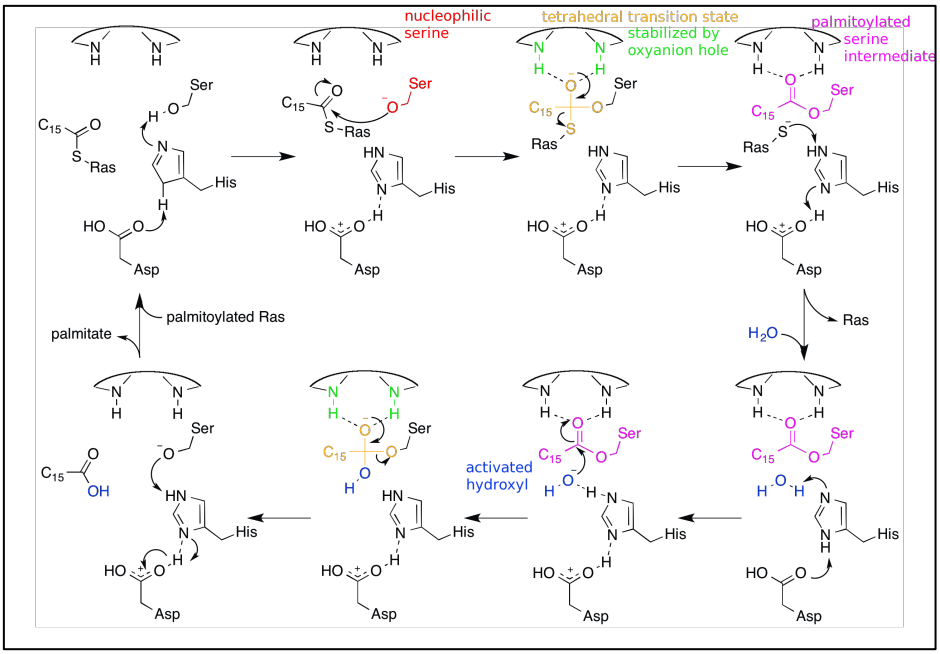

Figure 7: Schematic reaction mechanism of APT with palmitoylated Ras as exemplary substrate. Histidine and aspartate of the catalytic triad act as electron sink and deprotonate the active site serine; the nucleophilic serine oxyanion (red) performs a S_N2 attack on the palmitate thioester of e.g. Ras. The tetrahedral intermediate (yellow) is stabilized by the oxyanion hole (green), formed by backbone amides. The palmitate ester of the active site serine of APT is formed with Ras as leaving group. Regeneration of APT occurs in a similar mechanism, involving a water molecule (blue) as nucleophile that is activated in a same mechanism. APT is the leaving group of the tetrahedral intermediate upon formation of palmitate. Reaction scheme created using ChemBioDraw.

3.4.1 Structural features of APT isoforms

Acyl protein thioesterase (APT) contains the canonical α,β-hydrolase fold as well as the obligatory catalytic triad consisting of S114, H203 and D169. The positively charged oxyanion hole is formed by the backbone amides of L25 and F115 next to the active site serine. [58]. There are two known human isoforms sharing 66% sequence identity, which had been initially identified as lysophospholipases, hence named LYPLA1/2[59,60], but it was shown to be responsible for the majority of the cytosolic protein de-acylation activity[42]. A related protein, lysophospholipase-like 1

(LYPLAL1, also referred to as APT1L), sharing about 33% sequence identity with APT1, had been discovered in genome-wide association studies to influence body fat distribution and waist-hip-ratio[61]. Structural characterization of the protein revealed significant differences in the topology of the substrate binding site resulting in the specificity for shorter esters as substrates despite the sequence homology (PDB ID 3uov)[62]. Notably, LYPLAL1 is unable to hydrolyze esters with long chains.

APT1 and APT2 are rather promiscuous with regard to their substrates, among which are e.g. H/N-Ras[41,42,45], α-subunit of trimeric G-proteins (Gα)[42], endothelial nitric-oxide synthase (eNOS)[63], RGS4[42] or SNAP-23[64]. However, some specificity has been reported, as GAP43 is depalmitoylated only by APT2[65], and Caveolin, a small transmembrane protein palmitoylated at the cytoplasmatic C-terminal end, is not depalmitoylated by APT1[63]. Deacylation of the secreted hunger peptide octanoyl-ghrelin and lysophosphocholine present in the serum by APT was suggested[66,67], opening the question if APT is secreted or leaked out of the cell into the serum.

Further investigation are required to elucidate if both or only one of human APT1 and APT2 are involved in Ras cycle regulation, and a more detailed understanding of substrate and inhibitor binding is required to for further inhibitor development[68].

APT1 contains a hydrophobic substrate-binding tunnel next to the catalytic serine formed by a flexible extension of helix B that was proposed to bind the palmitoyl moiety during hydrolysis. Initially it was not clear if this tunnel binds the palmitate moiety, as in monomer B of the published crystal structure (PDB ID 1fj2, [58]) the tunnel is obstructed by L73 and F176. However, in all structures solved in our group, the binding tunnel is pre-formed and solvent accessible[69]. The dimer packing of the published structure of human APT1 (PDB ID 1fj2) pushes L73 inwards, thus closing the tunnel. Human APT1 crystallizes as a conserved dimer (or multiples of this dimer), and the published structure of human APT1 (PDB ID 1fj2) forms a rotated version of the dimer compared to the structures solved in our group, most likely due to the larger cloning artifact of construct of the published structure[69]. The structures of human APT1 and APT2 were crystallized by Marco Bürger[69] and are shown below in Figure 8.

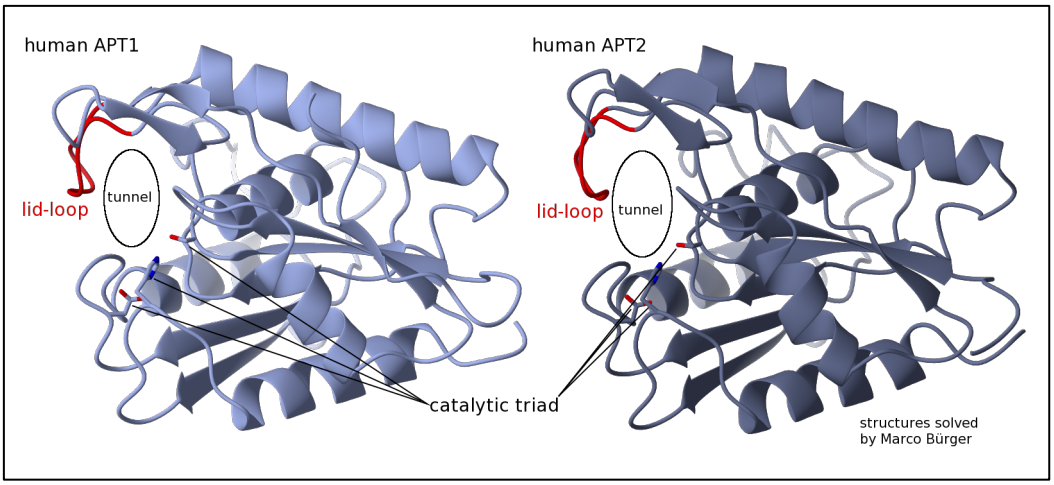

Figure 8: Human APT1 (left) and APT2 (right) presented as ribbon. Both structures were solved by Marco Bürger[69]. The tunnel (highlighted by the circle) is pre-formed by the lid-loop (red) next to the active site serine of the catalytic triad.

In LYPLAL1, this tunnel is permanently obstructed by a conserved arginine, thereby rendering the protein unable to bind and cleave long-chained esters like palmitoylated proteins or lysophospholipids as initially assumed, and limits the range to shorter substrates, (PDB ID 3uov, [62]) comparable to the structurally related carboxylesterase from *Pseudomonas aeruginosa* (PDB ID 3cn9, [57]). Palmitoyl protein thioesterase 1/2 (PPT1/2), although closely related by sequence, is located in lysosomes and does not regulate spatial distribution of palmitoylated proteins[70]. As described further below, PPT1 lacks the hydrophobic tunnel, and binds palmitate in a surface exposed groove. To our knowledge (communications with Ingrid Vetter), revealed that a pre-formed and solvent-accessible hydrophobic tunnel like in APT is a unique feature of APT that has not been reported for other proteins so far, and it also has not been explicitly mentioned as such (due to the closed tunnel) by the authors of the original article[58].

The shape of the binding tunnel varies slightly between human APT1 and APT2, as shown in Figure 9. In the absence of ligands, some flexible side chains like F176 and R144 in human APT1 can move into the tunnel and narrow its exit.

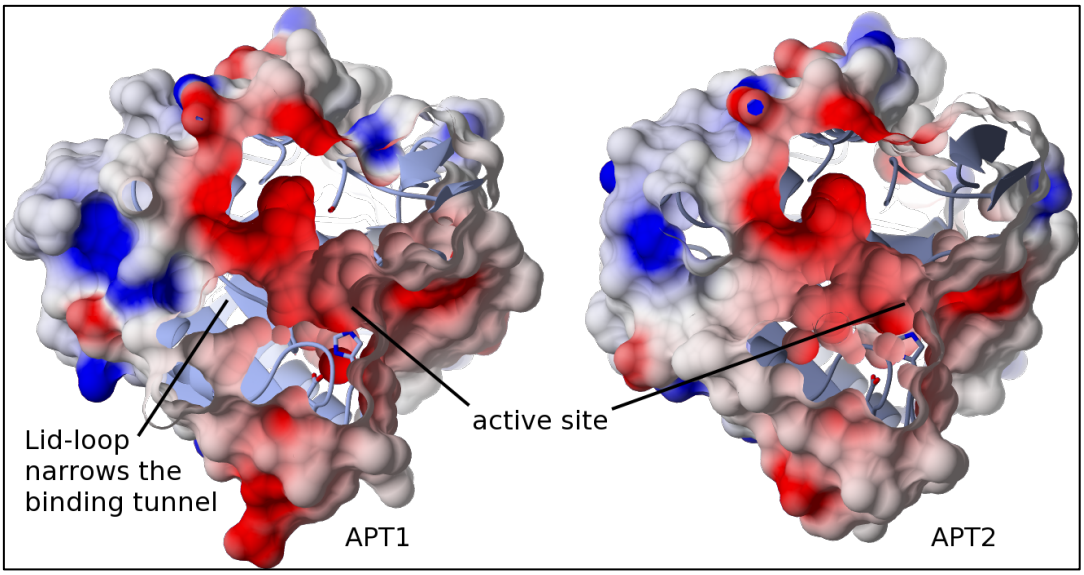

Figure 9: Comparison of the shape of the hydrophobic binding tunnel of human APT1 and APT2. Both structures were solved by Marco Bürger and presented in[69]. The surface around the active site and tunnel entrance is conserved, but the shape of the binding tunnel slightly differs. The tunnel exit can be narrowed by flexible side chains in the absence of a ligand bound to the tunnel.

The residues forming the hydrophobic tunnel are highly conserved between APT1 and APT2, the only significant difference is R144 located at the exit of the tunnel in APT1, which corresponds to H142 in APT2[69]. Furthermore, two residues in the hinge region at the start and end of the lid-loop are altered, namely I70+I71 / L70+M71 of human APT1 / APT2, and S77+Q78 / A77+P78 in human APT1 / APT2, which could affect the flexibility of the lid-loop. For further details, refer to[69].

Human APT contains three tryptophan residues. One tryptophan residue (W140/W142 in human APT1/2) is located inside the hydrophobic binding tunnel, forming parts of its inner wall. The second tryptophan (W32 in human APT1/2) is located at a solvent exposed shallow groove next to the active site that is expected to bind the substrate protein. The third tryptophan (W67) is part of the hydrophobic core of the protein, excluded from the solvent. The position of the three tryptophans in the structure is shown in Figure 10.

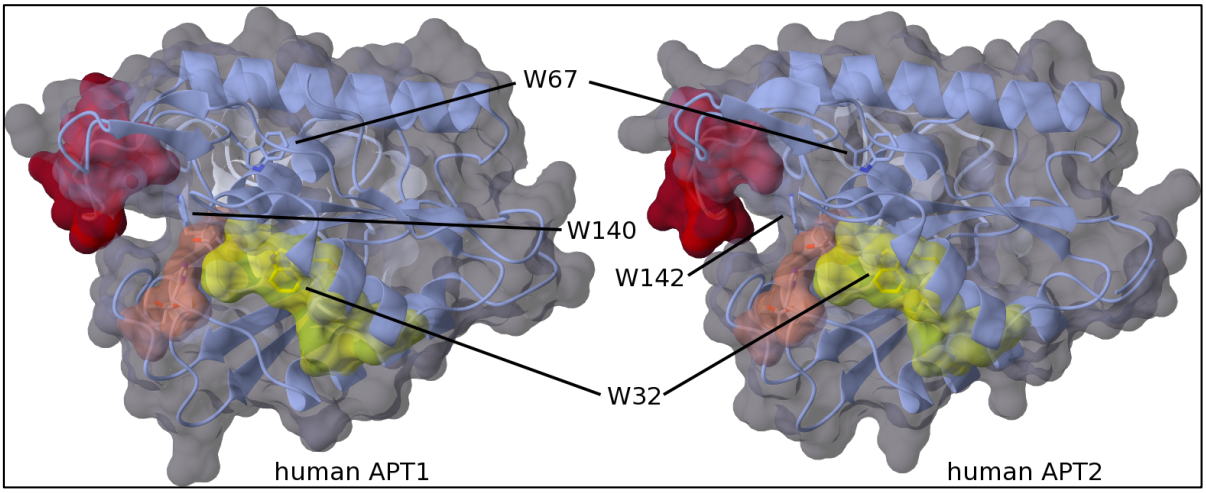

Figure 10: Highlighting the structural features of human APT1 and APT2. Both isoform contain three tryptophan residues. W140 form the inner wall of the hydrophobic tunnel formed by the flexible lid-loop (red). W32 is located in the shallow groove (yellow) predicted to bind the substrate protein. W67 is buried in the hydrophobic core of the protein and not accessible to solvent. The active site is highlighted in coral.

Human APT1 forms a dimer in crystals (shown below in Figure 11), and analytical ultra-centrifugation (AUC) has shown that this dimer is also formed in solution, with a K_D of 2.8 µM, while human APT2 and *Saccharomyces cerevisiae* APT do not dimerize in solution, as confirmed by AUC[69]. The dimer of human APT1 is formed via the hydrophobic patch next to the active site and is observed in three different crystal forms, being rotated by about 2˚ within crystals of different space groups and unit cells[69]. It is unknown if the dimerization has a biological role as regulator of activity, e.g. at high local concentrations at the membrane in cells.

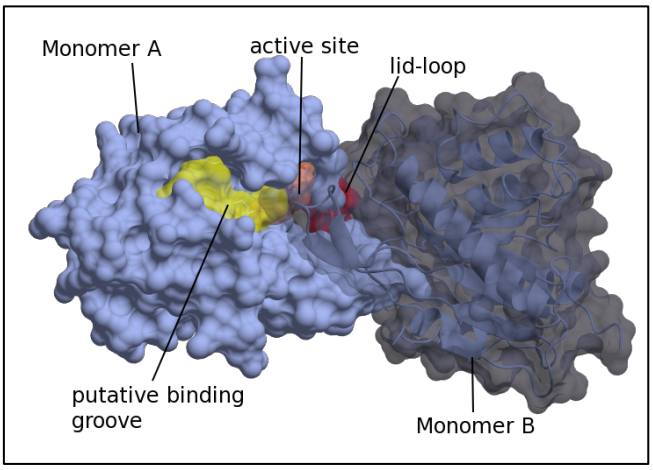

Figure 11: Dimer of human APT1[69]. In both monomers, the lid-loop (red) and catalytic triad (orange) are buried in the dimer interface. Parts of the putative binding groove (yellow) close to the active site are also covered by the second monomer of the dimer, presented with transparent surface (grey) on top.

The closest human relative to APT/LYPLA family are PPT1/2[71]. Both protein acyl thioesterases are responsible for the de-palmitoylation activity *in vivo*, but are spatially separated: PPTs are part of the lysosomal degradation machinery[70], while APTs are present in the cytosol[42]. Both APT and PPT cleave long chain thioesters from proteins, but PPT1 binds the palmitoyl moiety on a conspicuous surface groove (PDB ID: 1eh5, [72]) while APTs contains a pre-formed hydrophobic binding tunnel next to the active site. A comparison of the structures shows significant differences in the insertions at B and D α-helices, connecting β-sheets 4 to 5, and 6 to 7, respectively. These

insertions form the binding site for palmitate moiety of substrate proteins. In APT1, insertion B contains the lid-loop forming the outer wall of the substrate binding tunnel and is longer than the B α-helix in PPT1, while the insertion at the D α-helix of PPT1 is vastly extended and forms the surface exposed palmitate-binding groove (see Figure 12).

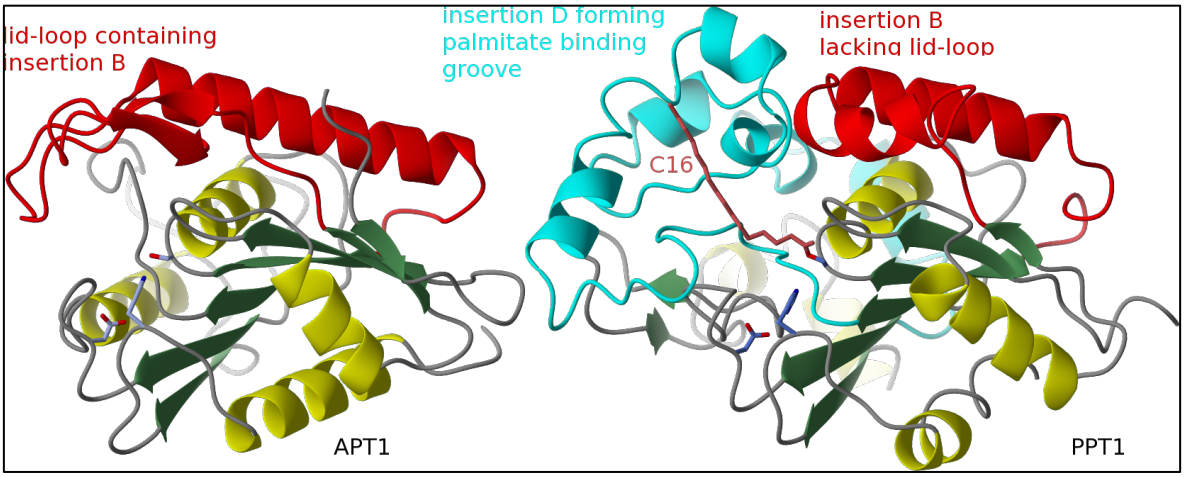

Figure 12: Structural comparison of APT1 and PPT1. Insertion B (red) of APT1 (left, PDB ID 1fj2, [58]) contains the flexible lid-loop that forms the hydrophobic tunnel next to the active site (blue sticks). In PPT1 (right, PDB ID 1eh5, [72]), insertion B is shorter and palmitate (red) is bound by the extended insertion D (cyan).

3.4.2 Boron-based inhibitors of acyl protein thioesterase

The identification of APT as a regulator of Ras subcellular localization[41,42] started the search for an inhibitor to modulate Ras activity. Clinical inhibitors of other serine hydrolases utilized a boronic acid moiety as nucleophilic trap for the active site serine[73]. Therefore, commercially available boronic acids have been tested for APT inhibition, and some have been found to have sub-µM potency[46]. Due to the covalent binding at the active site serine, boronic and borinic acids have slow off-rates and show long-lasting inhibition of APTs. One borinic acid has been shown to inhibit APT potently enough to reduce N-Ras dependent ERK-phosphorylation and partially revert the phenotype of MDCK-F3 cells[46]. The boron-based inhibitors lack isoform-specificity but showed no cell toxicity, indicating that they do not target essential proteins[46]. Complex structures of boronic acids with yeast APT have been solved in the course of my master thesis[74], proving the feasibility of obtaining inhibitor complexes of yeast APT.

3.4.3 β-lactone containing palmostatin B and palmostatin M

A second chemical class of potent inhibitor of APTs had been identified from a synthesized compound collection based on a central β-lactone that was inspired by lipstatin and tetrahydrolipstatin (also known as orlistat, Figure 13), the natural substrate and a commercial inhibitor of gastric lipase[44,75,76]. The first generation contained an aliphatic tail intended to mimic the acyl chain of natural substrates and replaced the thioester of the natural substrate by a central β-lactone core that acts as nucleophilic trap for the active serine[77]. An aromatic head group was connected to the β-lactone core via a short linker, and of the four different enantiomers palmostatin B (see Figure 13) proved to be the most potent. Further optimization replaced the bulky head group with a flexible sulfonyl-propylene-dimethylamino group (Figure 13). This head group mimics

lysophospholipid, a substrate of APT identified earlier[78]. The central β-lactone core and aliphatic tail were kept unchanged compared to palmostatin B[77]. However, structural proof of this binding mechanism is not available so far.

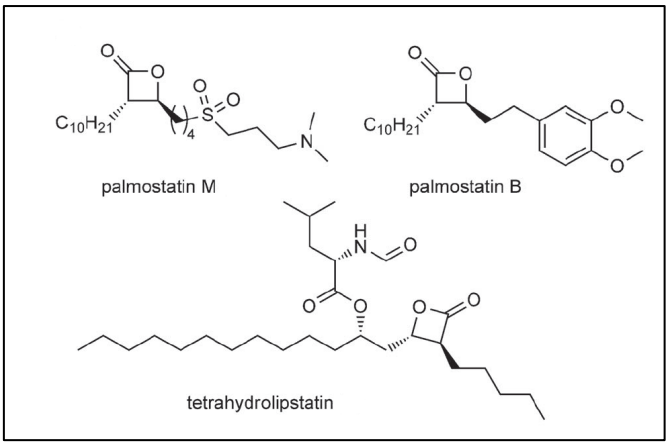

Figure 13: Palmostatin M and palmostatin B, sharing a common β-lactone core inspired by tetrahydrolipstatin (also known as orlistat). Figure taken from[46].

3.4.4 Cerulenin shares some features with palmostatin M

Cerulenin is a antifungal small molecule produced by *Cephalosporium caerulens*. Cerulenin inhibits the multienzyme complex Fatty Acid Synthase (FAS) and interferes with malonyl-CoA binding and metabolism[79,80]. FAS is upregulated in many precursors of invasive types of cancer[81]. It has been suggested that Cerulenin affects protein acylation[82], and it shares some structural and functional similarities with palmostatin M as shown in Figure 14.

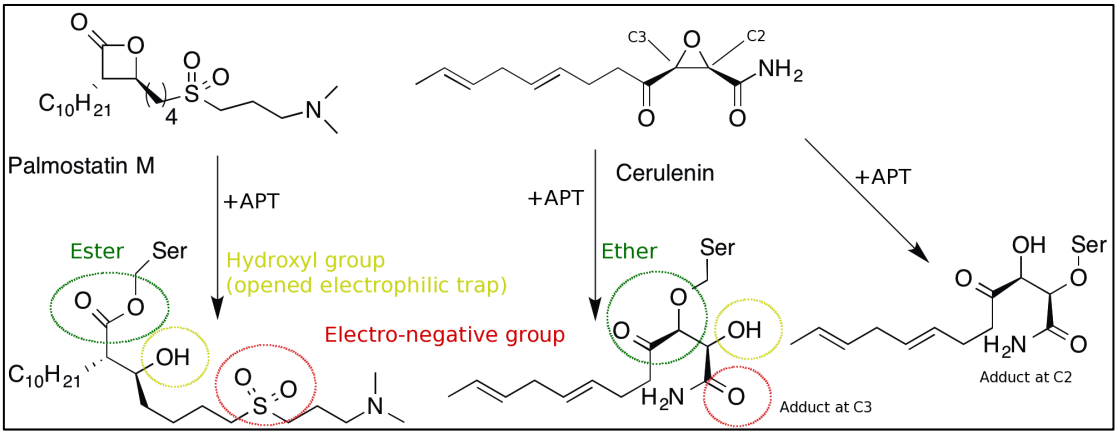

Figure 14: Comparison of Cerulenin and palmostatin M and proposed structure of the covalent complex with the active site serine of APT. The chemical groups expected to address the same functional groups of the protein are highlighted in the same colours. Image created using ChemBioDraw13 and modified using Gimp[4].

Both the electrophilic β-lactone of palmostatin M and the epoxide of Cerulenin can act as a trap for the nucleophilic serine of the active site, leading to a covalent adduct, which is an irreversible ether in case of Cerulenin. The β-keto-function next to the opened expoide could bind the protein similar to the opened β-lactone of palmostatin M, although there is one additional carbon atom in case of the Cerulenin adduct formed upon attack at C3. The unsaturated tail of Cerulenin both at C7 and C10 in *trans*-configuration, which is restrained in flexibility compared to the saturated tail of palmostatin M, but might be able to bind inside the hydrophobic tunnel of APT. For this reasons,

Cerulenin was also studied as a covalent inhibitor of APT in this thesis. Different studies showed covalent binding of Cerulenin at both C2[83,84] and C3[85] of the epoxide.

3.4.5 2-Bromopalmitate as product mimic and inhibitor of APT

2-Bromopalmitate (2BP) is the α-brominated palmitic acid (shown in Figure 15), and commonly used to inhibit Protein Acyl Transferases (PAT) during *in vivo* experiments[86]. Its striking similarity with the product of de-palmitoylation reactions has led to investigations that showed its inhibitory effect on APT activity[87]. The kinetic data obtained indicated an un-competitive mode of action on APT using palmitoyl-CoA as substrate[87]. This data and conclusion is surprising, since due to the remarkable similarity with the product it is unclear why 2BP should not address the same binding site as the palmitate moiety of a palmitoylated protein.

Besides in crystallographic studies, 2BP was used in the course of this thesis for biochemical and biophysical experiments. A important advantage of this compound is the better solubility in aqueous solutions compared to palmitate.

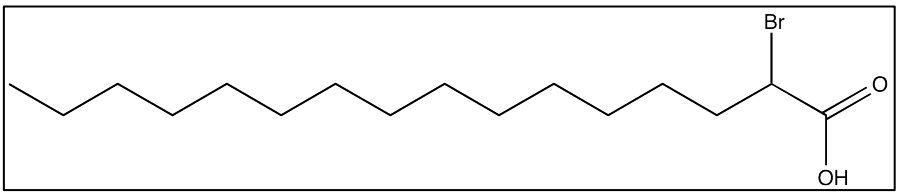

Figure 15: Structure of 2-Bromopalmitate (2BP). The bromine-substituted carbon in α-position to the carboxylic acid is chiral, and 2BP is supplied by Sigma Aldrich as racemic mixture. Figure created using ChemBioDraw 13.

4 Goal of this study

Ras is a small GTP-binding protein that plays an important role in signal cascades controlling cell growth and proliferation, and tumor-growth promoting mutants of Ras can be found in 25% of all human tumors. Ras activity is regulated by the bound G-nucleotide and the sub-cellular localization at the plasma membrane. Membrane localization is achieved by post-translational lipidation of the C-terminus, and properly maintained by a constant cycle of de-palmitoylation by acyl protein thioesterase (APT) and re-palmitoylation at the Golgi coupled to vesicular transport to the membrane. Direct approaches to inhibit Ras activity in cancer were not successful so far. Inhibition of APT disrupts this cycle and reduces the local Ras concentration and thus the Ras activity in cancer.

APT inhibitors of different chemical classes have been described in the literature, but structural data is missing. Therefore, different APT – inhibitor complexes will be structurally investigated by x-ray crystallography to identify their exact binding mode to provide a starting point for further rational drug design. APT contains a pre-formed hydrophobic tunnel next to the active site which outer wall is formed by a lid-loop. It is unknown if the lid-loop is involved in substrate binding, and if the shape and stability of the lid-loop is related to biochemical activity. To address these questions, mutants of human APT1 containing an altered lid-loop will be structurally characterized on the formation of the hydrophobic tunnel and compared to the effect on biochemical activity. The shallow groove is a potential secondary binding site for the natural substrates, palmitoylated proteins and/or further acyl chains, but has not been verified yet, thus co-crystallization with lipid-modified peptides will be pursued.

5 Results

5.1 Crystal structures of APT in complex with inhibitors

5.1.1 Crystal structure of yeast APT serves as model for structural investigation of inhibitors of human APT1

Different structures of human APT1 obtained by Marco Bürger in the course of his doctoral thesis revealed an active site blocked by crystal contacts[69]. Efforts to obtain structural data of any inhibitor in complex with either human APT1 or APT2 have failed so far[88]. To overcome this problem the homolog in yeast (sharing 36% sequence identity to human APT1) had been subjected to screening for crystallization conditions, resulting in well-diffracting crystals. The first structure of yeast APT was solved by Marco Bürger and refined in the course of my master thesis[74]. A second structure that crystallized under optimized conditions in a different space group and diffracted to higher resolution is presented here and is used for further comparisons.

The best diffracting apo crystal of yeast APT was obtained in hanging drops from optimized conditions initially set up to obtain a complex structure with the inhibitor palmostatin B via co-crystallization (Figure 16). The crystal structure was solved as described in Chapter 7.4 of Material and Methods. The crystallographic statistics are shown in Table 1. First, the high-resolution structure is analyzed in this chapter, followed by a comparison with the previously presented structures of yeast APT[69,74] and human APT1[69].

Figure 16: Crystals of yeast APT apo. The best-diffracting crystal of yeast APT grew in 30% PEG4000, 0.1 M Li_2SO_4 and 0.1 M Tris pH 8.5. The condition also contained 5 µM palmostatin B. Crystals grew within 14 days in hanging drops. Image taken using an Olympus DP21 camera attached to an Olympus CX-60 microscope.

Table 1: Crystallographic statistics of the yeast APT apo structure. Values for the highest shell are given in parentheses. Values for Ramachandran plot are given for favoured, allowed and outlier.

	yeast APT apo	yeast APT apo[74]		yeast APT apo	yeast APT apo[74]
Data collection			Refinement		
Space group	$P2_1\ 2_1\ 2_1$	$P4_2\ 2_1\ 2$	Resolution (Å)	45.61-1.44 (1.48-1.44)	19.98-2.20 (2.26-2.20)
Cell dimensions			Number of Reflexes	396851 (9484)	50658 (3407)
a, b, c (Å)	44.70, 45.94, 91.22	145.86, 145.86, 96.84	Rwork	17.13 (29.7)	20.9 (25.7)
α, β, γ (°)	90, 90, 90	90.0, 90.0, 90.0	Rfree	20.66 (29.7)	26.7 (30.1)
Resolution (Å)	45.61-1.44 (1.48-1.44)	48.62-2.2 (2.26-2.2)	Number of Atoms		
Monomers / au	1	4	Protein	1822	7037
Wave length (Å)	0.97857	0.977	Ligand/Ions	6	4
CC $^1/_2$	100 (55.6)	(no value)	Water	167	165
I / σ(I)	24.6 (1.59)	11.56 (3.23)	B-factor (Å2)		
Completeness (%)	96.3 (71.7)	99.72 (99.97)	Protein	22.4	62.4
Redundancy	11.85 (5.24)	3.80 (4.00)	Ligand	34.5	83.0
			Water	33.2	54.1
			RMSD		
			Bond length (Å)	0.0239	0.022
			Bond angle (°)	2.40	2.142
			Ramachandran (%)	97.88 / 2.12 / 0	95.83 / 3.84 / 0.33
			Clashscore	3	14.04
			Rotamer outlier (%)	3.06	13.77
			Molprobity score	1.77	2.81

The asymmetric unit of the high-resolution crystal structure contains one molecule of yeast APT with an active site accessible to the solvent. Yeast APT does not form a dimer in solution as observed in human APT1[69]. The lid-loop is part of a crystal contact to one neighboring molecule. The Figure 17 illustrates the crystal contact that leaves the active site accessible. The active site contains a glycerol molecule soaked into to the crystal by the cryo solution. Although the crystallization condition contains 5 µM palmostatin B, which is expected to bind at the active site, palmostatin B is washed out of the active site due to insufficient concentration in the cryo solution.

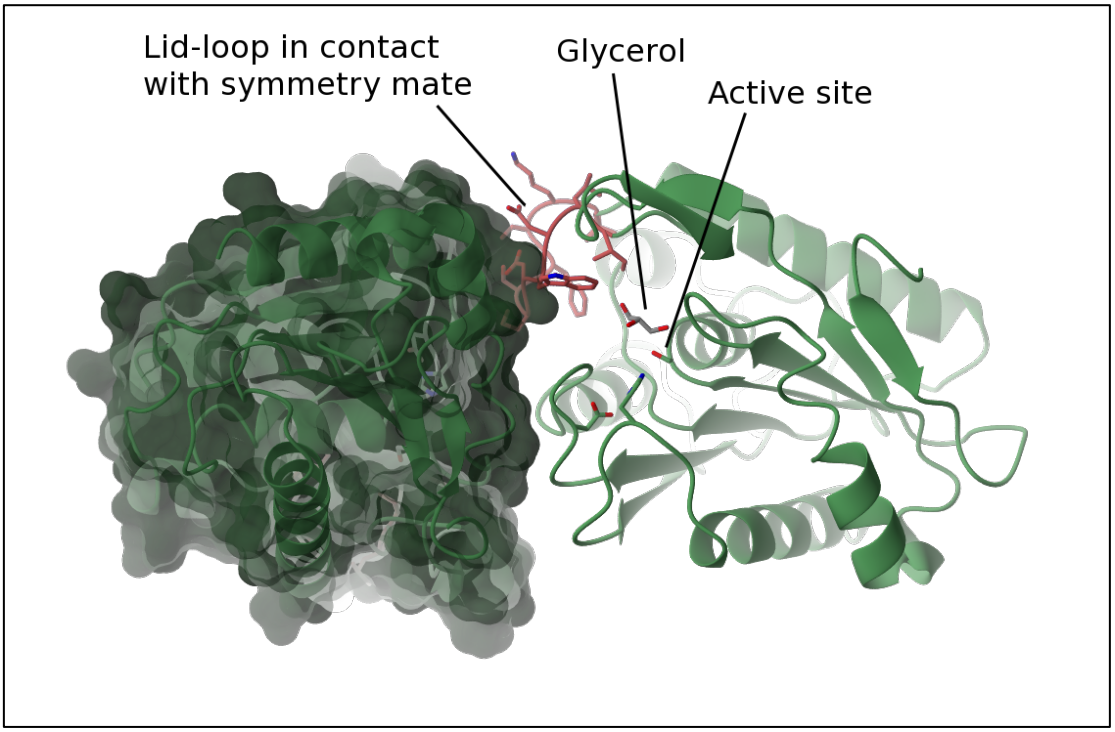

Figure 17: Accessible active site of yeast APT. The lid-loop (cartoon in red) is involved in a crystal contact with a neighbor molecule (left, dark green).

The hydrophobic tunnel, that accommodates the substrate palmitoyl moiety, is pre-formed by the lid-loop. In yeast APT, the surface of the hydrophobic tunnel is formed by the side chains of I74, W77, P79 and F81 located in the lid-loop, and F72, F145, V175, V176, and L180 of the core protein. The orientation of these side chains is shown in the Figure 18.

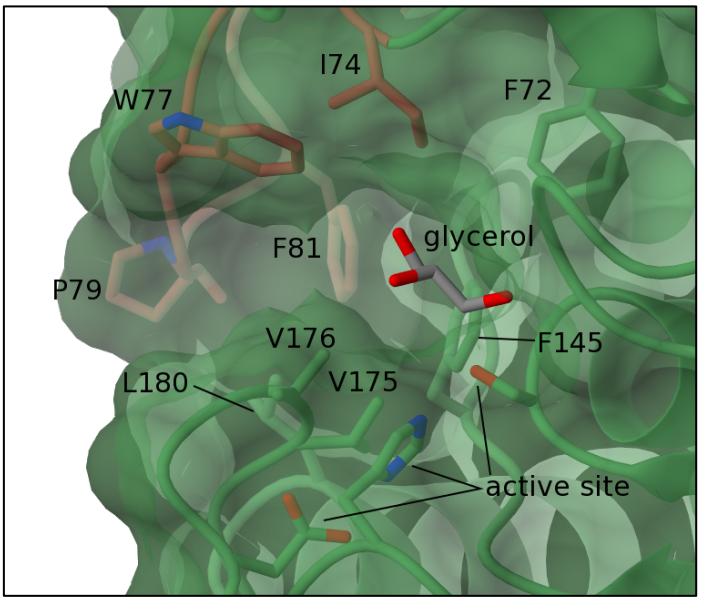

Figure 18: The hydrophobic tunnel of yeast APT with relevant residues labeled and shown as sticks. Amino acids of the lid-loop are colored red. The glycerol molecule bound at the active site is shown as grey sticks.

The different environments in the crystal of the two datasets allow a comparison of the flexibility of parts of the protein. The structure solved in $P4_2\,2_1\,2$ contains four monomers (A-D) per asymmetric unit with different contacts to the neighbor molecules: in monomer B, D78 and S80 are close to K101 of the neighboring molecule, and P79 of the tip is located close to M172. In monomer C a salt bridge between E76 and D78 is formed with K101 of a symmetry molecule, and P79 at the tip of the

lid-loop is packed to P133 and W134 of a symmetry molecule. The most prominent changes are found on the side chain of W77, with rotation of up to 180˚ even though no direct contact of this residue could be observed, indicating that the different conformations of the indole side chain are potentially energetically comparable. The electron density is not as well defined as for the other side chains of the lid-loop. The lid-loop is quite similar in the four monomers with an rmsd of 0.50 to 0.92 Å for 10 Cα atoms. The largest movement of the lid-loop of about 1 Å is observed at the tip, measured at the Cα of P79 between monomer C, where the lid-loop is involved in crystal contacts, and monomer D, where the lid-loop is located at a solvent channel and not influenced by crystal contacts.

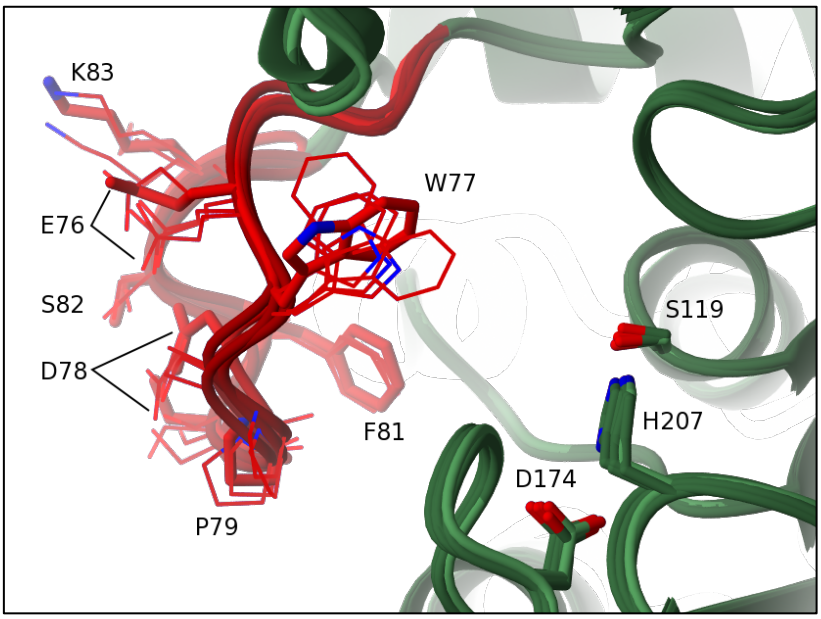

Figure 19: Comparison between both structures of yeast APT. The high-resolution structure solved in space group $P2_1\ 2_1\ 2_1$ is shown in green with a red lid-loop, the side chains are highlighted as sticks. The four monomers of the structure are superimposed on the high-resolution structure and colored dark green, with a dark red lid-loop and side chains as stick model. Most prominently, the orientation of the indole of W77 varies.

Taken together, the conformation of the lid-loop of yeast APT in this crystal is only slightly influenced by the crystal packing.

In the following part, the high-resolution structure of yeast APT is compared with human APT1. The overall structure of yeast APT is similar to human APT1, with an rmsd of 1.38 Å over 211 Cα atoms. Upon close inspection of the active site of yeast APT, the hydrophobic binding tunnel displays an unusual shape. While human APT1, and in fact all other APT structures solved by our group[69], have a straight hydrophobic tunnel with the exit on the opposite site of the protein, the tunnel of yeast APT turns by nearly 90˚ and exits on the side of the protein. This is caused by a different amino acid sequence of the lid-loop, which is shown below in Figure 20.

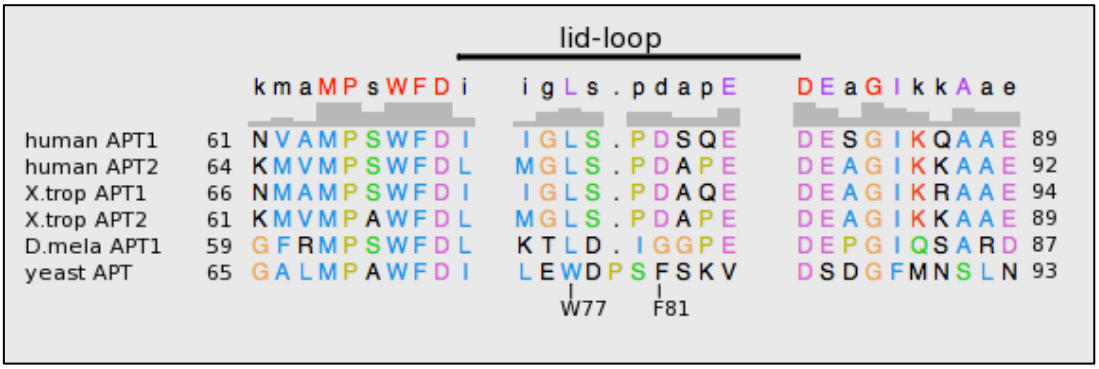

Figure 20: Structural alignment of the lid-loop sequence of APTs from different organisms. Alignment is based on the structures solved by Marco Bürger[69]. The lid-loop of yeast APT has an insertion of one amino acid, leading to repositioning of the conserved proline (not in *D. melanogaster*). The following negatively charged residues aspartate and glutamate (76 and 79 in human APT1) are replaced by an aliphatic phenylalanine and a valine residue in yeast APT. Structure based sequence alignment created using Chimera[89].

The structure-based sequence alignment of the lid-loop shows an insertion in the sequence of yeast APT, thus displacing the almost completely conserved P74 (numbering according to human APT1) further to the tip of the lid-loop. The sequence following the proline (SFSKV) is not conserved in yeast and lacks the negatively charged D76 and E79 (Figure 20). Instead, in yeast APT these positions are occupied by larger aliphatic residues, of which F81 blocks the tunnel approximately at the middle of the tunnel (Figure 21). The conserved L73, located at the entrance of the tunnel next to the active site, is replaced by a larger W77 of the yeast APT lid-loop.

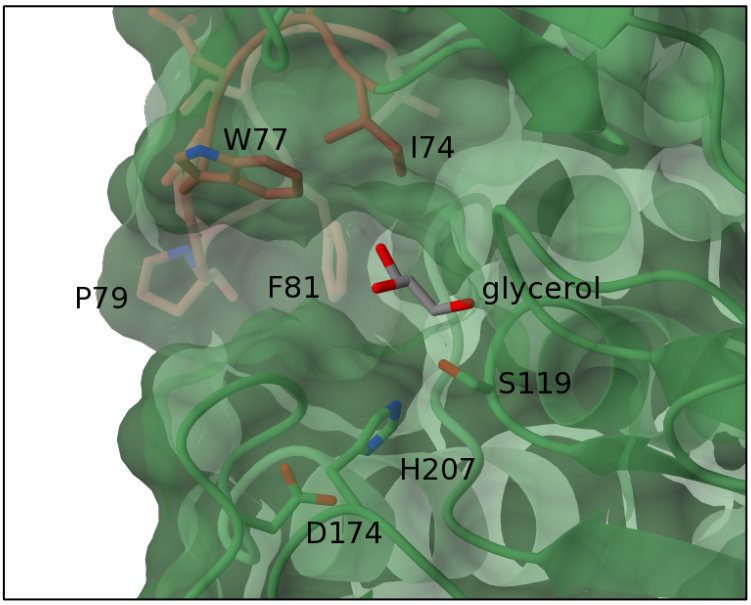

Figure 21: Detailed view on the active site and tunnel of yeast APT. The catalytic triad consists of S119, H207 and D174. A glycerol molecule binds next to the active serine. F81 blocks the straight tunnel leading away from the active site, thus redirecting the tunnel to exit in front of P79. The side chain of W77 is tilted upwards, so that the tunnel is not formed completely, resulting in a deep hydrophobic groove.

In this crystal structure, the conformation of W77 at the tunnel entrance results in formation of a groove instead of a tunnel, as it is found in our structures of APTs from other organisms. The indole side chain is in 3.7Å distance to the side chains of I74 and A62, i.e. the range of van-der-Waals contacts. The shorter side chain of A62 (corresponding to L58 of human APT1) leaves space for the indole ring of W77 to move towards A62, while simultaneously the short V175 on the lower part cannot reach to W77, resulting in a gap between W77 and V175. In human APT1 however, the

corresponding amino acids are three leucines, L58 directs L73 downwards where it is in closer range to L171, thus forming the round entrance of the linear hydrophobic tunnel. The role of these three leucines of human APT1 is further investigated in Chapter 5.2.2, 5.2.3 and 5.2.4.

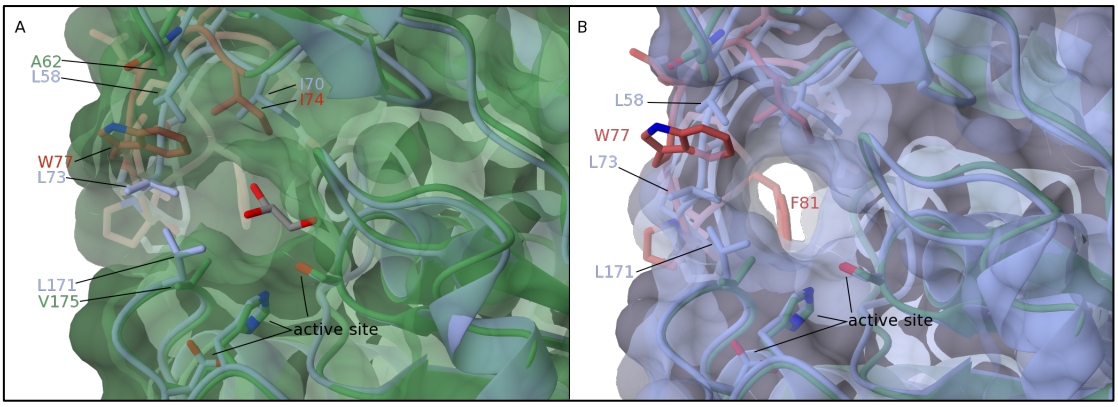

Figure 22: Comparison of the lid-loops of yeast APT (shown in green with the lid-loop highlighted in red) and human APT1 (blue). A: The indole side chain of yeast APT W77 is rotated towards A62 and I74, resulting in a gap between W77 and V175. B: In human APT1, L58, L73 and L171 form a round entrance of the straight binding tunnel, whereas in yeast the tunnel is blocked by F81. The glycerol molecule at the active site of the yeast APT structure is not shown for clarity.

A shallow groove next to the active site could be a binding site for the peptide of palmitoylated proteins, or for a second palmitoyl-moiety or for the farnesyl modification. The residues forming the groove are conserved in close proximity to the active site, but then diverge with increasing distance, as illustrated for yeast APT in Figure 23.

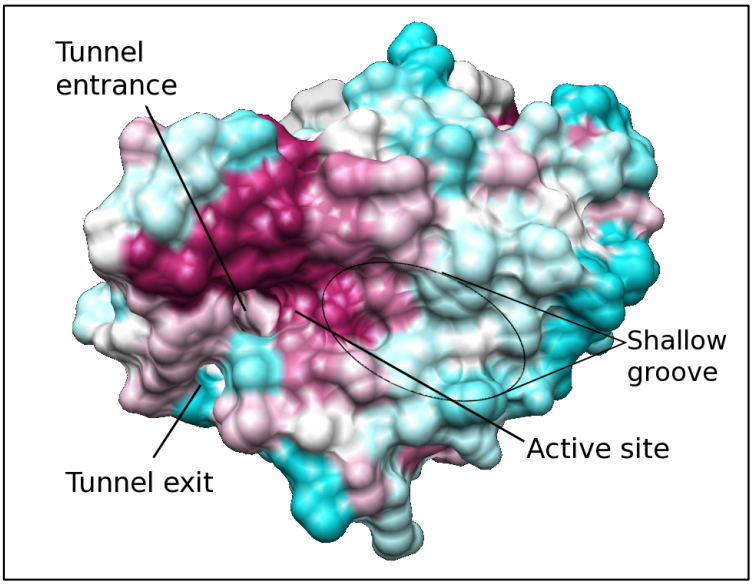

Figure 23: Conservation of the shallow groove next to the active site of yeast APT. Conserved residues are colored in magenta, less conservation is shown as a gradient from white to cyan. The conservation is based comparisons of the structures of human APT1/2, *X. tropicalis* APT1/2, *D. melanogaster* APT1 and yeast APT solved by Marco Bürger[69] and reveals highly conserved regions at the active site and at the tunnel entrance. The shallow groove is a secondary binding site for e.g. peptide of a palmitoylated protein. The conservation is high in close proximity to the active site, but becomes more variable with increasing distance from the active site. Image created using Chimera[89] and annotated using Gimp[4].

A more detailed comparison between human APT1 and model yeast APT is shown in Figure 24. As mentioned above, the residues close to the active site are conserved, namely F118 and W30 (yeast APT numbering). T209 and L214 in yeast APT correspond to S205 and M210 in human APT, keeping the electrostatic properties of the side chains comparable. Interestingly, the position of the

bulky F32 residue in yeast is occupied by A35 in human APT. Y36 of yeast APT corresponds to I39 in human APT, with the polar hydroxyl group of Y36 pointing to the charged end of the groove, which is formed by E215 and R40 in yeast APT. In human APT, E215 of yeast APT corresponds to A210 that lacks a polar side chain, which is compensated by the side chain of Q207 next to it. The R40-containing helix of yeast APT is shortened in human APT1 by one turn, leaving the space of R40 to be occupied by K214 in human APT1. The hydroxyl group of T209/S205 is not completely conserved, but can be found in several APTs.

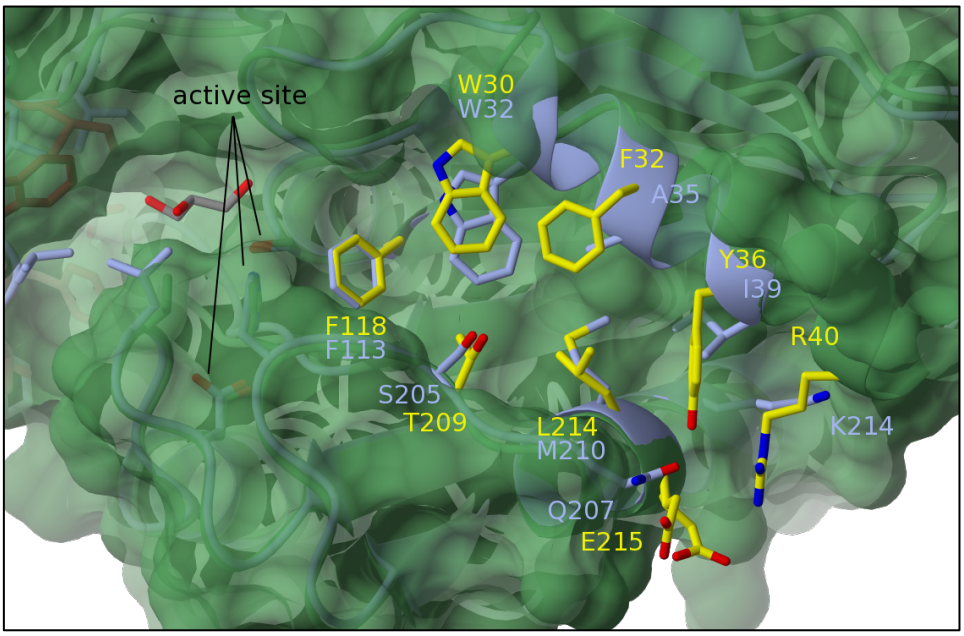

Figure 24: Detailed comparison between yeast APT and human APT1. Yeast APT is represented in green, with the side chains forming the shallow groove highlighted in yellow. Human APT is colored in blue, with the corresponding side chains highlighted as sticks. Close to the active site, the groove is conserved and hydrophobic, with increasing distance the surface becomes more polar.

Despite the minor structural differences between yeast APT and human APT1, yeast APT is useful as a model to structurally investigate inhibitor binding: First, the crystal packing of yeast APT leaves the active site solvent-accessible in contrast to the previously solved structures of human APT1. This allows soaking of ligands into the crystals. Second, the aliphatic tail of inhibitors is flexible enough to bind inside the bent hydrophobic tunnel of yeast APT. Third, although the binding groove is only partially conserved among APTs, small molecule ligands could address the conserved residues close to the active serine.

5.1.2 Crystal structure of the yeast APT – palmostatin B complex

Palmostatins are non-isoform-specific APT inhibitors that have been characterized and investigated in previous publications[44,45,90]. As described in Chapter 3.4.3, Palmostatins are based on a β-lactone core acting as a nucleophilic trap coupled to an aliphatic tail to mimic the palmitoyl moiety of posttranslationally modified proteins, plus different head groups. Inhibition of biochemical activity of yeast APT by palmostatins with a sub-µM IC_{50} has been shown before[74]. The significantly higher IC_{50} of palmostatin B and yeast APT compared to human APT1 and APT2 (800 nM compared to 5.4 nM and 19 nM, respectively) indicates that some stabilizing interaction is not possible in yeast APT.

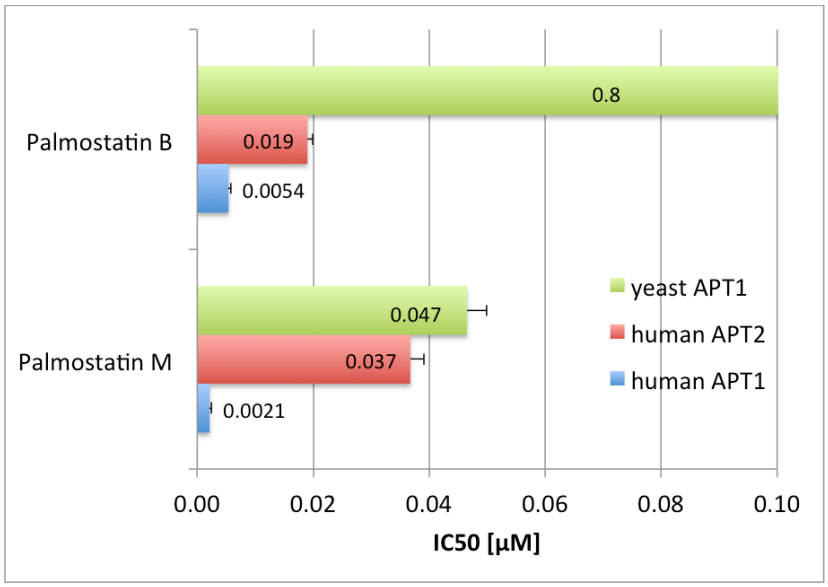

Figure 25: Inhibitory effect of palmostatin B and palmostatin M on yeast APT, human APT1 and APT2. IC_{50} values were determined as described in [74] using XLfit. Palmostatin B is significantly less potent on yeast APT compared to both human isoforms. Graph created using Microsoft Excel.

Palmostatin B was co-crystallized with yeast APT under optimized conditions similar similar to the crystallization condition of the apo structure of yeast APT. Macro-seeding of complex crystals to drops containing fresh protein-inhibitor complex in solution considerably increased the diffraction quality of crystals. The harvested crystals were transferred to drops on cover slips containing dried-out palmostatin B (DMSO of stock solution was evaporated). The cryo solution contained reservoir solution plus 10% glycerol and additional fresh 2.5mM palmostatin B, in which the crystal was soaked only for less than a minute. Fresh palmostatin B is essential in the cryo solution, as the covalent complex has a short half-life due to hydrolysis of the ester.

Data collection and structure solution via molecular replacement using the yeast APT apo structure is described in Chapter 7.4. The crystals of space group $P2_1\ 2_1\ 2_1$ diffracted to 1.7Å at the synchrotron.

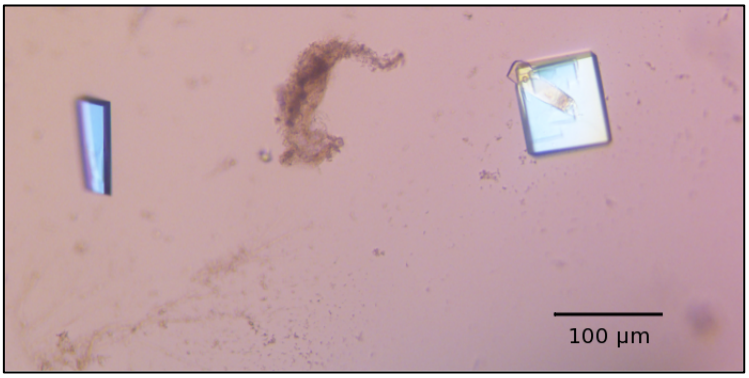

Figure 26: Crystals of yeast APT in complex with palmostatin B. The right crystal grew around a macro-seeded crystal, still visible in yellow. The left crystal appeared after 3 hours and grew slowly for 7 days when it was isolated and used for data collection. The condition #89 from Classics screen contains 30% PEG 4000, 0.1 M Li_2SO_4, and 0.1 M Tris pH 8.0 - 8.5. Crystals were grown in hanging drops on glass slides in 24-well plates and photographed using an Olympus DP21 attached to an Olympus CX-60 microscope with polarization filter. Scale bar inserted using Gimp[4].

Table 2: Crystallographic statistics of yAPT - palmostatin B complex. Values for the highest shell are given in parentheses. Values for Ramachandran plot are given for favoured, allowed and outlier.

	yAPT – Palmostatin B		
Data collection	17 Jun 2012	Refinement	
Space group	$P2_12_12_1$	Resolution (Å)	45.1-1.7 (1.74-1.7)
Cell dimensions		Number of Reflexes	80522 (6234)
a, b, c (Å)	44.34 45.26 90.21	Rwork	18.8 (36.5)
α, β, γ (°)	90.00 90.00 90.00	Rfree	23.2 (32.3)
Resolution (Å)	45.1-1.7 (1.74-1.7)	Number of Atoms	
Monomers / au	1	Protein	1756
Wave length (Å)	0.9785	Ligand/Ions	27
CC $^1/_2$	99.7 (61.5)	Water	132
I / σ(I)	9.1 (1.6)	B-factor (Å2)	
Completeness (%)	89.2 (93.8)	Protein	25.8 ± 10.1
Redundancy	2.3 (2.3)	Ligand	47.5 ± 16.7
		Water	38.6 ± 12.2
		RMSD	
		Bond length (Å)	0.019
		Bond angle (°)	1.88
		Ramachandran (%)	97.37 / 2.63 / 0.0
		Clashscore	9.92
		Rotamer outlier (%)	3.73
		Molprobity score	2.08

Interestingly, the asymmetric unit of yeast APT in complex with palmostatin B contains only one monomer. The crystal packing is identical to the apo yeast APT structure in the same space group $P2_1\,2_1\,2_1$ and comparable unit cell dimensions, obtained under similar conditions that was used for macro-seeding to obtain the inhibitor complex. In human APT1, the crystals always contained a dimer that buried the hydrophobic patch around the entrance of the binding tunnel, close to the active site. In contrast, yeast APT structures do not show similar contacts in the crystals. Instead, the active site is accessible, and the lid-loop is part of crystal contacts, as shown in Figure 27. This corresponds to a relatively low B-factor, the Cα atoms of the lid-loop have an average B-factor of 29.88 $Å^2$, which is not significantly increased compared to the protein main chain overall B-factor of 23.50 $Å^2$. The buried interface of human APT1 dimers ranges from 1659 to 2415 $Å^2$ ([69], PDB ID 1fj2) whereas the largest buried surface in yeast APT is 605 $Å^2$.

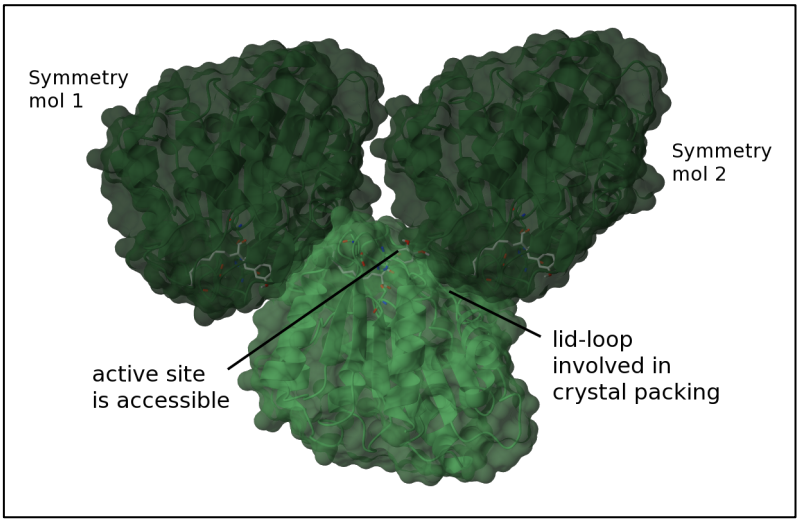

Figure 27: Crystal contacts of the yeast APT - palmostatin B complex. No extended interfaces are formed in the crystal, similar to the structure of yeast APT apo that crystallized in the identical space group with similar unit cell parameters. The active site remains accessible, and the lid-loop is involved in crystal contacts.

A comparison of the palmostatin B complex and the high-resolution structure of the apo form of yeast APT described in Chapter 5.1.1 reveals a nearly identical structure with an rmsd of 0.25Å over 226 amino acids. Yeast APT apo and the complex with palmostatin B crystallized in the same space group $P2_1\,2_1\,2_1$ and a similar unit cell. Binding of palmostatin B causes only marginal differences in the lid-loop and overall structure (Figure 28).

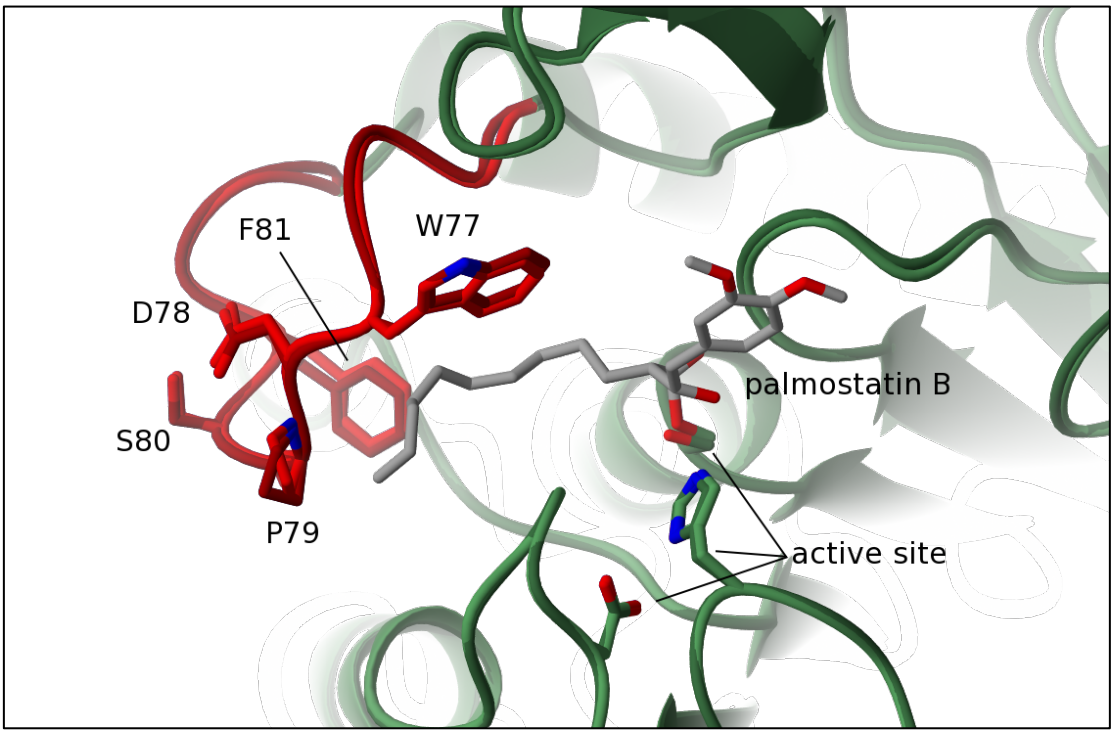

Figure 28: Comparison of the yeast APT the apo structure (dark green) and in complex with palmostatin B (green). The lid-loop of the complex (red) is not changed in its conformation compared to the apo structure (dark red), with the side chains being oriented identical in both structures.

Since both the palmostatin B complex and the high-resolution structure of the apo form of yeast APT crystallized in a very similar unit cell and same space group, the complex was compared to the older structure of the apo form of yeast APT crystallized in $P4_2\,2_1\,2$[69,74]. This apo form of yeast APT containing four monomers per asymmetric unit, was used for comparison to investigate the

influence of crystal contacts. Due to the different environment of the four monomers, monomers A and D possess lid-loops exposed to a solvent channel, unaffected by crystal contacts. In contrast, the individual lid-loops of monomers B and C are both part of different crystal contacts.

The four monomers each have an overall rmsd between 0.44 to 0.54 Å over 224 to 225 amino acids. The local rmsd of the lid-loops only are increased to 0.75 to 0.98 Å, indicating a larger flexibility of the loop than the rest of the core protein, but no significant change upon binding of palmostatin B.

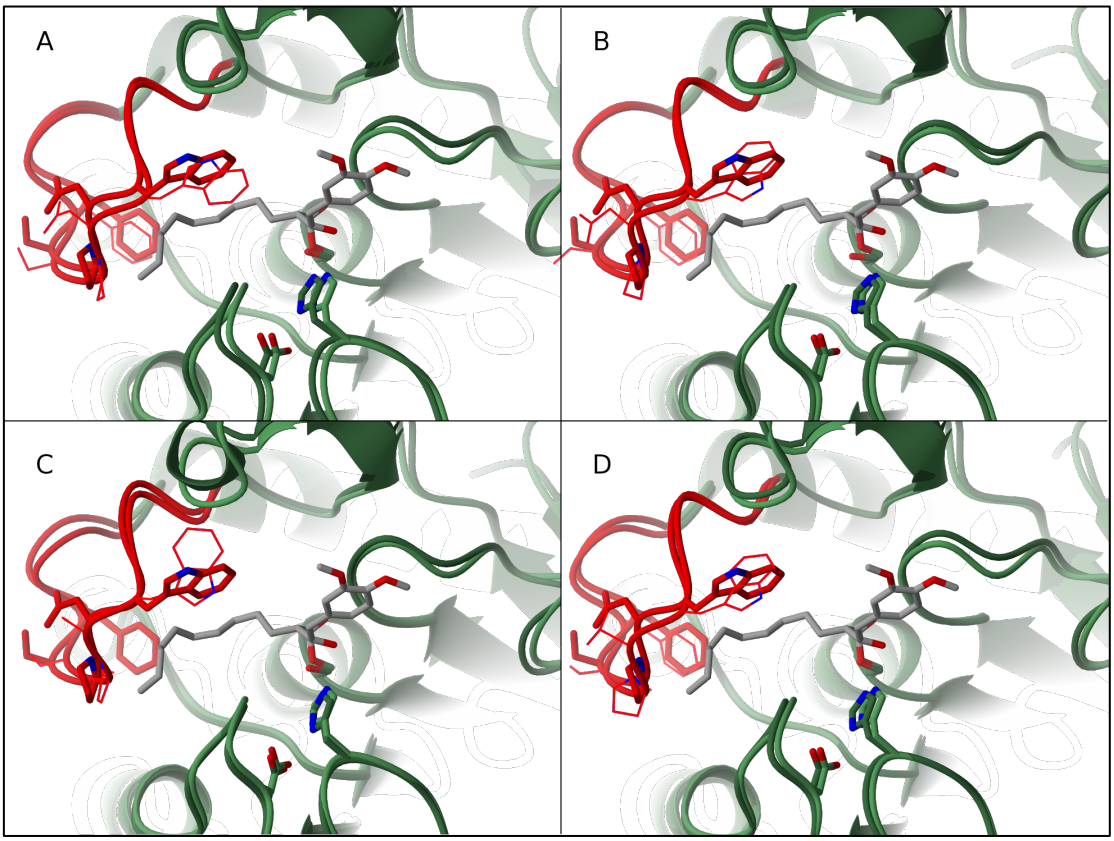

Figure 29: Comparison of the four monomers of the previous structure of yeast APT in apo form refined to 2.2 Å [master thesis] with yeast APT in complex with palmostatin B. The conformation of the lid-loop (dark red) slightly varies insignificantly between the four monomer (A-D) of the asymmetric unit of yeast APT apo (dark green) and the palmostatin B complex (green/lid-loop in red). The different rotamers of W77 observed in the apo structure of yeast APT are the most prominent changes, but also indicate certain flexibility at this position.

Well-defined electron density was visible for the aliphatic tail, as well as for the β-lactone moiety of palmostatin B (Figure 30). The β-lactone core of palmostatin B acted as a nucleophilic trap as designed,[44] and was found to be covalently bound to the active site serine. The aliphatic decanoic tail is located inside the hydrophobic tunnel next to the active site. However, the aromatic head group lacks a well-resolved electron density despite the high resolution of the diffraction data, indicating a weak, statistically disordered binding of the head group corresponds to multiple conformations.

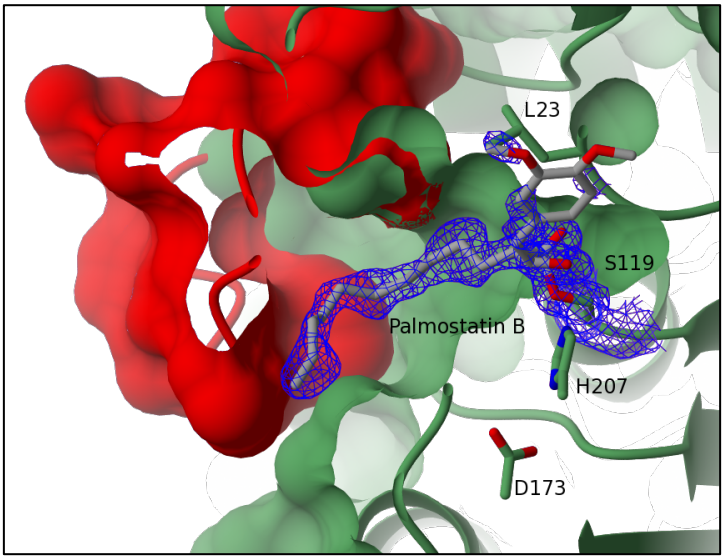

Figure 30: Yeast APT in complex with Palmostatin B. Palmostatin B (grey sticks) is bound covalently via an ester bond resulting from the nucleophilic attack of S119 on the β-lactone core of Palmostatin B. The well resolved electron density shows the opened β-lactone covalently attached to S119. The hydrophobic tail occupies the hydrophobic binding tunnel formed by the flexible lid-loop (shown in red). The head group is probably mostly oriented close to L23 at the tunnel entrance, but the lack of well-defined electron density indicates multiple binding modes. Electron density shown as blue mesh scaled to 1 δ.

The active site serine itself is covalently linked to the hydrolyzed β-lactone core, forming an ester bond (Figure 31). The oxyanion hole formed by the backbone amides of L23 and Q120 stabilizes the transition state of the tetrahedral intermediate of the attacked β-lactone (in case of the a palmitoylated protein, the palmitoylate thioester), and forms H-bonds with the ester of the resulting stable covalent complex. The newly formed hydroxyl group of the opened β-lactone forms a hydrogen bond with Nε of H207 of the catalytic triad. G24 and D63 are in close vicinity to the methylethers of the head group that is placed in accordance to the geometric restrains due to the weak electron density. A 2D representation of the interaction of palmostatin B with yAPT generated with LigPlot+[91] is shown in Figure 31.

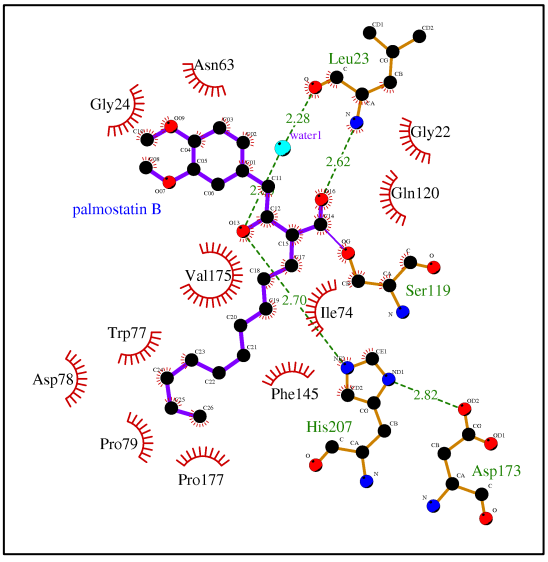

Figure 31: 2D representation of the interactions of palmostatin B with yeast APT. The aliphatic tail is bound in the hydrophobic tunnel. The active site serine opened the β-lactone; the resulting ester is stabilized by the backbone amide of L23 and Q120 that forms the oxyanion hole. The head group is positioned according to geometric restraints due to the lack of clean electron density; therefore the interactions shown here is representative of one of multiple possible orientations of the head group. Figure generated with LigPlot+[91].

Two positions of water molecules at the active site in the palmostatin B complex with the apo form of yeast APT are compared in Figure 32. Water molecule 1 is coordinated by the side chain of D25 and the carbonyl oxygen of L23, and present in both crystals. In the apo form, a second water molecule is coordinated by Nε2 of H207 and the first water molecule; this second water molecule is activated through de-protonation by H207 and regenerates APT by attacking the palmitoyl-serine ester reaction intermediate (see Figure 7 for detailed information). Strikingly, the exact position of this water molecule is occupied by the hydroxyl group of the opened β-lactone in the palmostatin B complex, as illustrated in Figure 32. This impedes hydrolysis of the covalent complex, and enables the observation of the covalently bound palmostatin B by x-ray crystallography.

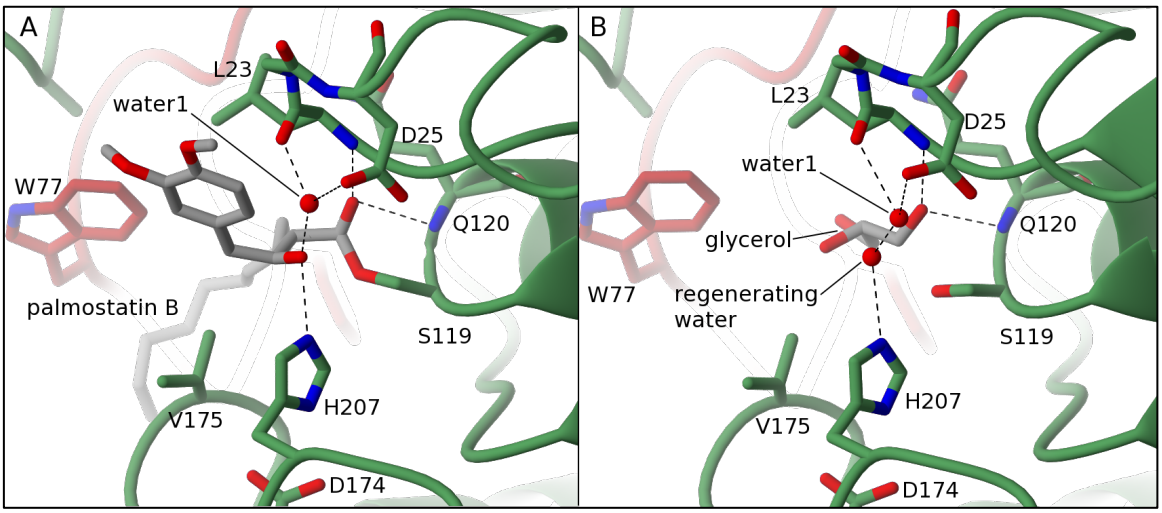

Figure 32: Comparison between water coordination next to the active site serine in the palmostatin B complex (A) and apo form (B) of yeast APT. Palmostatin B forms hydrogen bonds via the ester to the oxyanion hole backbone amides of L23 and Q120, similar to the glycerol molecule found in the apo form. The apo form contains two water molecules, the first being coordinated by the carbonyl oxygen of L23 and the carboxylic acid side chain of D25, and the enzyme regenerating water that is coordinated by the first water and activated by H207. In the palmostatin B complex, the first water is also present but moved by 0.7Å, but the exact position of the regenerating water is occupied by the hydroxyl resulting from the opened β-lactone of palmostatin B, thereby slowing down hydrolysis of the palmitoyl-serine ester.

The interaction of palmostatin B with APT can be divided in the three parts of the ligand: the β-lactone core is bound by the active site and coordinated by the oxyanion hole, the aliphatic tail is located inside the hydrophobic tunnel, and the head interacts with amino acids close to the active site. The individual amino acids are shown above in Figure 31. Amino acids interacting with the β-lactone core and the head group are conserved between yeast and human APT (Figure 33).

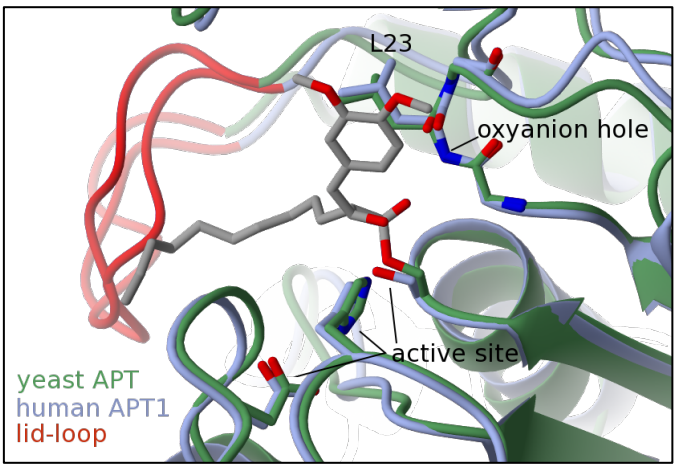

Figure 33: Superimposition of human APT1 apo and the yeast APT - palmostatin B complex. The amino acids interacting with the head and core of palmostatin B are conserved and shown as sticks. The lid-loop forming the hydrophobic tunnel is not conserved and the tunnel differs in shape, but the aliphatic tail of palmostatin B is flexible enough to fit into either a bent or linear tunnel.

In summary, conditions could be found for successful soaking of yeast APT crystals with the covalent inhibitor palmostatin B. Clear electron density for the inhibitor revealed a binding in the hydrophobic tunnel and covalent attachment to the active site serine. The head group apparently does not interact with the protein. Therefore, an inhibitor with a larger head group was investigated as described in the following.

5.1.3 Crystal structure of the yeast APT - palmostatin M complex

Palmostatin M was designed as the next generation of β-lactone based inhibitors (see Figure 13). The search for a common motif in shape and charge of two of APTs natural substrates; lysophospholipids and palmitoylated H-Ras C-terminus, resulted in the long and flexible head group of palmostatin M that should address the same hydrogen bond network as the natural substrates (see Chapter 3.4.3). Indeed, the modified head group increased affinity for human APT and *in vivo* potency in cells[77].

Crystallization screens were set up as described in Material and Methods. Several PEG-containing conditions resulted in well-diffracting crystals, but many structures solved from these crystals lacked evidence of binding of palmostatin M, or had very low occupancy of the inhibitor. Refinement of the condition that already resulted in well-diffraction crystals of apo yeast APT and the yeast APT palmostatin B complex worked also for the complex of yeast APT and palmostatin M. Crystals were grown in drops (containing 0.2 M $LiSO_4$, 0.1 M Tris-HCl pH 8.0 and 32% PEG 4000) placed on palmostatin M dried on glass plates (1 µl of 10mM stock, DMSO of stock solution was left to evaporate). The best-diffracting crystal was isolated in a thin liquid film directly from the drop without transfer to a cryo solution. Diffraction data was collected and the structure was solved via Molecular Replacement and refined to a resolution of 2.4 Å as described in Material and Methods. The crystallographic statistics is summarized in Table 3. Interestingly, the crystals of the yeast APT - palmostatin M complex now belong to space group $P4_2 2_1 2$ containing four monomers per asymmetric unit, in contrast to the palmostatin B complex that belongs to space group $P2_1 2_1 2_1$ and one monomer per asymmetric unit obtained under similar crystallization conditions, but similar

space groups and unit cell to one of the apo form of yeast APT (compare Table 3 to Chapter 5.1.1, Table 1).

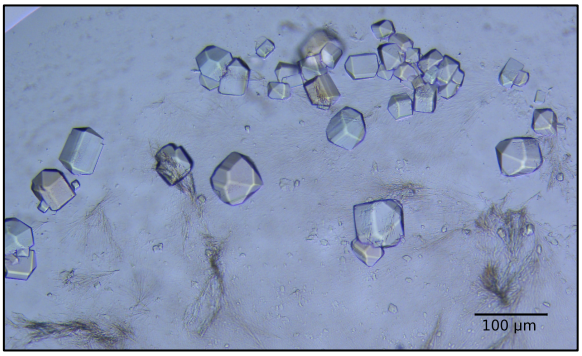

Figure 34: Crystallization drop of yeast APT in complex with palmostatin M. The drop (containing yeast APT (1.2 mM) mixed at 1:1 ratio with reservoir solution containing 0.2 M Li_2SO_4, 0.1 M Tris-HCl pH 8.0, and 32% PEG 4000) was placed on palmostatin M dried on a glass cover slip. Clean, single crystals were isolated for x-ray diffraction data collection in a thin liquid film directly from the drop without cryo solution. Crystals photographed using an Olympus DP21 camera attached to an Olympus CX-60 microscope with polarization filter. Scale bar inserted using Gimp[4].

Table 3: Crystallographic statistics of the complex of yeast APT and palmostatin M. Values for the highest shell are given in parentheses. Values for Ramachandran plot are given for favoured, allowed and outlier.

	yAPT – palmostatin M		
Data collection	26 Oct 2012	Refinement	
Space group	P 4_2 2_1 2	Resolution (Å)	48.38-2.4
Cell dimensions		Number of Reflexes	356262 (25851)
a, b, c (Å)	145.6, 145.6, 96.8	Rwork	17.7 (25.7)
α, β, γ (°)	90.0, 90.0, 90.0	Rfree	24.6 (35.5)
Resolution (Å)	48.38-2.4 (2.46-2.40)	Number of Atoms	
Monomers / au	4	Protein	7036
Wave length (Å)	0.9786	Ligand/Ions	146
CC $^1/_2$	99.8 (83.4)	Water	441
I / σ(I)	13.6 (2.3)	B-factor (Å2)	
Completeness (%)	100 (99.9)	Protein	53.1 ± 16.5
Redundancy	8.6 (8.6)	Ligands	79.0 ± 26.0
		Solvent	50.5± 8.3
		RMSD	
		Bond length (Å)	0.014
		Bond angle (°)	1.58
		Ramachandran (%)	96.48 / 3.52 / 0
		Clashscore	2.54
		Rotamer outlier	2.67
		Molprobity score	1.59

The crystal indexed in $P4_2 2_1 2$ contained four monomers per asymmetric unit, with similar packing to the yeast APT apo structure crystallizing in the same space group. Similarly to this apo crystal form, all monomers have an active site accessible by solvent channels, and two of four monomers

(C+D) have the lid-loop located at a solvent channel not influenced by crystal contacts, while the lid-loop of monomer A and B is part of different crystal contacts as shown in Figure 35. The different environment might have influence on the conformation of the head group of palmostatin M, as shown later in detail in this chapter.

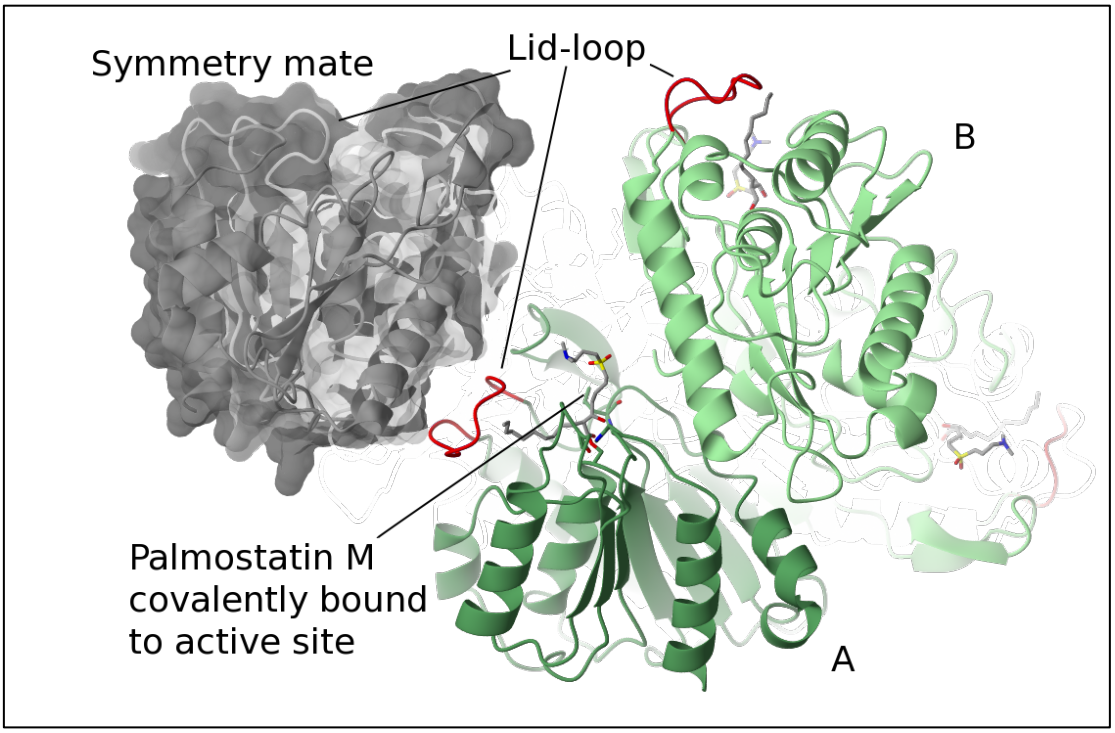

Figure 35: Exemplary view of the crystal packing of yeast APT - palmostatin M complex. All four monomers have the active sites accessible through solvent channels of the protein. The lid-loop of monomers A(dark green)/B(light green) is part of crystal contacts to symmetry mates (grey) and thus could reduce its flexibility, shown here for monomer A.

The structure was refined to a resolution of 2.4 Å and contained positive difference electron density ranging from the active site serine both upwards to the protein surface and down into the hydrophobic tunnel, which could be unambiguously fitted to Palmostatin M. Similar to palmostatin B, the β-lactone core is covalently bound as an ester to the nucleophilic hydroxyl of the active site serine. The aliphatic tail binds inside the hydrophobic tunnel. The distinctive flexible head group of palmostatin M is bound to the protein surface in close proximity of the active site. Its orientation varies between the four monomers of the asymmetric unit. Three of the four monomers (A-C) contain palmostatin M in a conformation with the head group located in front of W77 of the lid-loop, although in monomer C the electron density is quite weak. However, the electron density of palmostatin M bound in monomer D is the best defined for the whole inhibitor, including the head group. Here, the head group forms a charged interaction with the backbone amide oxygen of L23 instead. The sulfonyl group is coordinated by the amide of N63 in all four monomers, but whilst in three monomers (Figure 36, grey) the flexible amine is located in front of the side chain indole of W77, the head group of the fourth palmostatin M (turquoise) in chain D electrostatically interacts with the oxygen of the backbone amide of L23. However, the electron density is weaker for the head group than for the covalently bound core and aliphatic tail, demonstrating the flexibility of the

head group and statistically disordered binding. A superimposition of the four monomers with a focus on palmostatin M is shown in Figure 36.

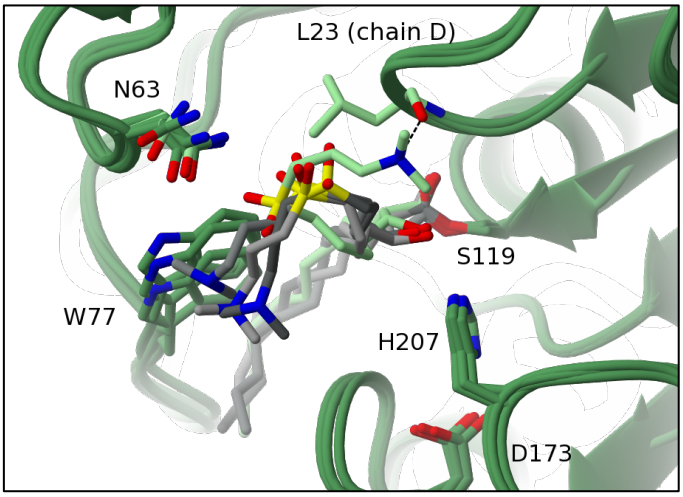

Figure 36: Superimposition of all four chains of yeast APT - palmostatin M complex. The opened β-lactone core and aliphatic tail are identically bound in the four monomers. The head group of three molecules (grey) shows relatively weak electron density in front of W77, whereas the tertiary amide of the head group of the fourth molecule (turquoise, monomer D) shows a well defined density and seems to form a charged interaction with the backbone carbonyl oxygen of L23.

As shown in Figure 36, monomer D contains palmostatin M bound with its head group in front of L23. In this monomer, the electron density is the best defined, suggesting that this orientation of the head group is more stable. A reason for the different binding modes is the crystal packing. In monomer A, the space in front of L23 is blocked by the N-terminal end of monomer C, as shown in Figure 37A. This prevents the binding of the palmostatin M head group at the amide backbone of L23, as it would clash with the neighbor's N-terminus. The space in front of L23 in monomer B is limited by Q39 of monomer C to a narrow gap only allowing to accommodate three water molecules (Figure 37B), blocking the amide oxygen of L23 by crystal contacts as binding site of the head group of palmostatin M. The active site and lid-loop of monomer C are positioned next to a solvent channel, resulting in enough space for palmostatin M to bind in front of L23, and the electron density indicates a mix of both conformations of the head group bound next to L23 and W77.

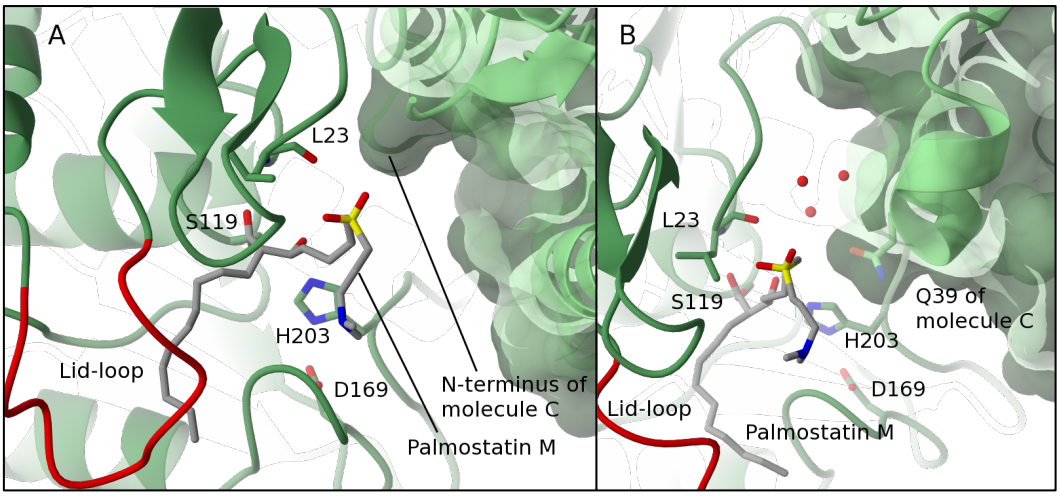

Figure 37: A: L23 of monomer A is blocked by the N-terminus of monomer C, thus preventing binding of the palmostatin M head group at this position. B: Narrow gap between L23 of monomer B and Q39 of monomer C. The head group of palmostatin M is bound at the indole ring of W77.

An analysis of the interactions of yeast APT with palmostatin M is shown for both conformations of the head group, taking chain A as example for the head group bound in front of W77, and chain D containing palmostatin M in the second conformation of the head group where the tertiary amide of the head group forms a charged interaction with the carbonyl of L23. The analysis of the interaction was carried out using LigPlot+[91] and is shown in Figure 38.

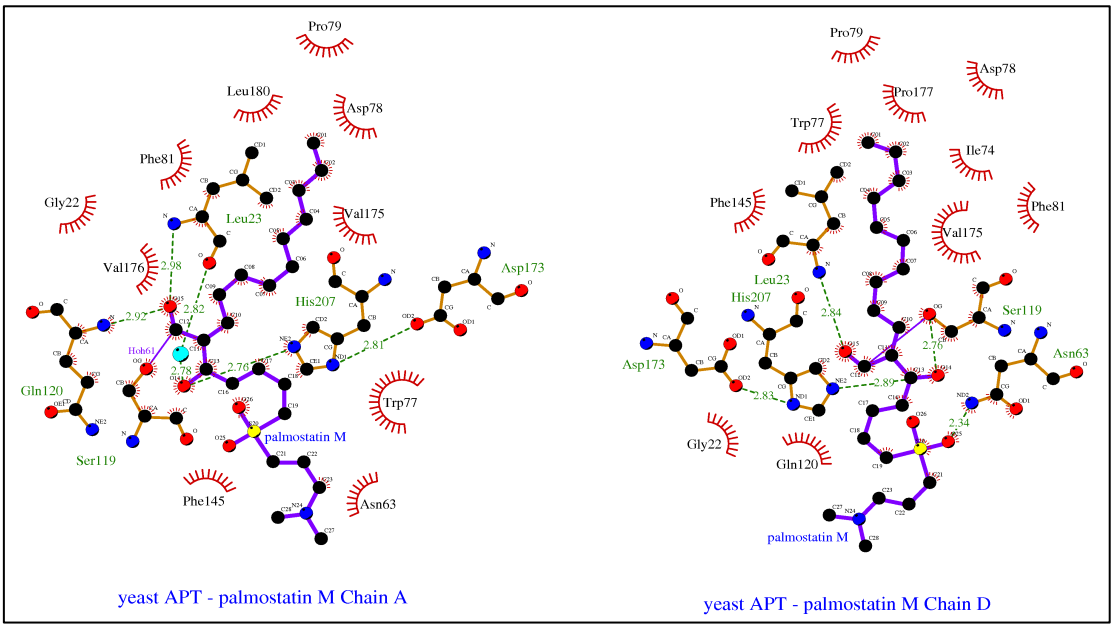

Figure 38: Analysis of the binding mode of palmostatin M to yeast APT. In all four monomers, palmostatin M is covalently bound by S119 via the opened β-lactone with aliphatic tail inside the tunnel. The sulfonyl moiety of the flexible head group is coordinated by N63 in all four monomers. Three of the four monomers (A,B,C) have evidence to bind palmostatin M in the mode as observed in chain A (left), with the head group folding onto the lid-loops W77. Monomer D (right) contains palmostatin M with the head group in a different orientation bound close to L23. Structure analyzed using LigPlot+[91].

The comparison with the apo structure of yeast APT crystallized in the same space group and very similar unit cell shows the induced fit of palmostatin M binding on the lid-loop. Both monomers (A and B) whose lid-loop is involved in crystal contacts show only minor outwards movement of the lid-loop by less than one Ångstrom compared to the apo structure (measured at the Cα of P79) caused by palmostatin M binding inside the tunnel (see Figure 39A). A stronger influence by Palmostatin M binding is observed on the lid-loop of monomer C and D. In these monomers of the complex structure, the Cα of P79 is moved by nearly 2 Å compared to the apo structure (see Figure 39B). The lid-loop of the latter monomers C and D is located next to a solvent channel and forms no contacts to neighbor molecules. Other parts of yeast APT like the L23 or the A62 containing loops are not affected in their conformation by binding of palmostatin M. The minor movements of the lid-loop upon ligand binding corroborate the rigidly pre-formed binding tunnel. This is illustrated in the following Figure 39.

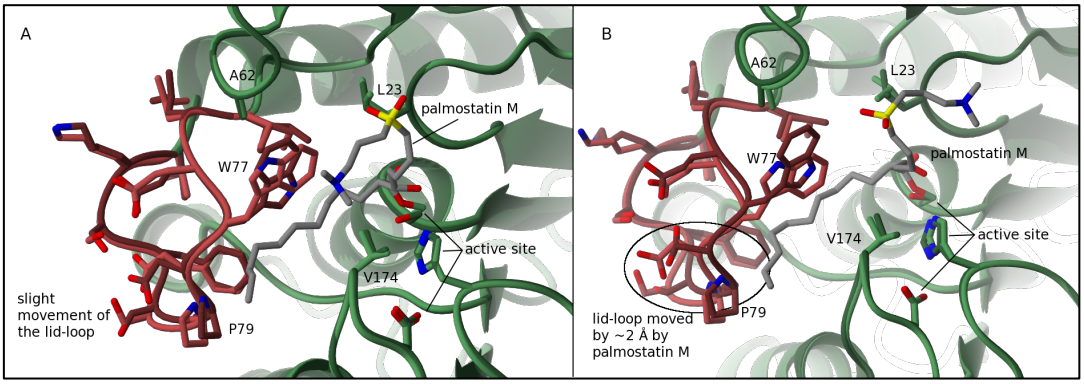

Figure 39: Comparison of the effect of palmostatin M on the lid-loop. Panel A shown a monomer of yeast APT (green, lid-loop in red) in complex with palmostatin M (grey) superimposed with yeast APT apo. The lid-loops of both structures are part of crystal contacts, which might lead to a slightly biased conformation. The monomer superimposed in panel B has the lid-loop located next to a solvent channel, enabling induced fit movements of the tip in the case of the palmostatin M complex.

A superimposition of a monomer of yeast APT - palmostatin M complex and apo form of human APT1 has an rmsd of 1.27Å over 209 Cα and is shown in Figure 40. The active site residues, L23, and N63 are conserved between yeast and human. The amino acids of the lid-loop, and thus the surface at this side of the tunnel entrance is not conserved. It remains unclear if the head group of palmostatin M would prefer the same or a different orientation in human APT1. As noted above, it is probably impossible to get the structure of human APT1 in complex with palmostatin M since the active sites are not accessible in all available crystal forms, at least of the wild type (see also Chapter 5.3).

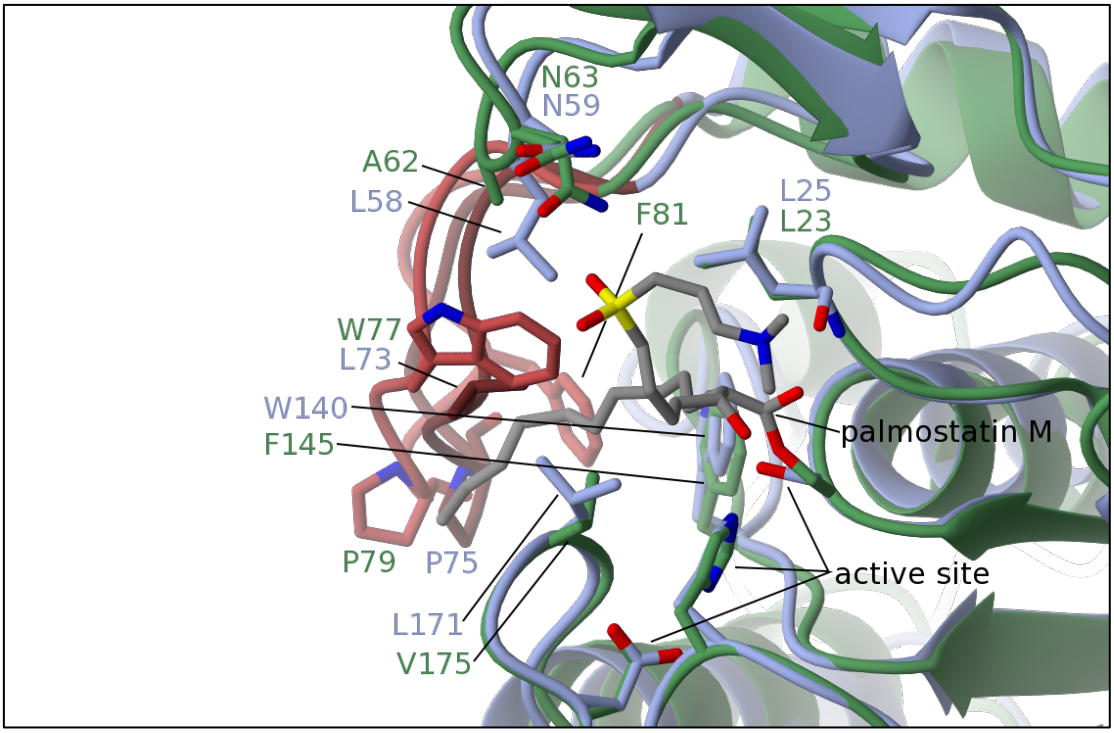

Figure 40: Superimposition of yeast APT (green) in complex with palmostatin M (grey) and human APT1 (blue). The lid-loop of yeast and human APT is colored in red and dark red, respectively. Interesting amino acids interacting with palmostatin M are highlighted as sticks, the residue numbers are shown in the respective color. The L23 and N63 residues, interacting with the head group of palmostatin M in yeast APT, are conserved, in contrast to the residues of the lid-loop.

As the head group of palmostatin M was designed to target the same binding site as lysophosphocholine (see Introduction Chapter 3.4.3), it can only be speculated that this structure

represents the likely binding mode of a lysophosphocholine molecule. However, due to the lack of structures available of a lysophosphocholine in complex with APT, the confirmation of the binding mode is not possible at this time.

In summary, both inhibitors B and M of the palmostatin class bind covalently at the active site serine via the β-lactone core and the aliphatic tail is tightly coordinated inside the hydrophobic tunnel. Merely the head group differs and provides the likely reason for improved affinity and *in vivo* activity of palmostatin M, as it is longer and more flexible to provide additional interaction with the protein. Interestingly, the head group of palmostatin M seems to interact with the conserved part of the surface.

5.1.4 Crystal structure of human APT1 in complex with Cerulenin

Cerulenin was discovered as antifungal antibiotic that inhibits fatty acid metabolism by covalently binding to FAS[79] (see Chapter 3.4.4) that is upregulated in many invasive cancers[81]. It has been also suggested that Cerulenin inhibits protein acylation[82]. Palmostatin M and Cerulenin share some structural features (see Figure 14), a hydrophobic tail next to an electrophile, and potential for a comparable hydrogen network coordination of their respective head groups. Consequently, we wondered whether Cerulenin could also serve as an inhibitor of APT where the activated epoxide would serve as nucleophilic trap for the catalytic serine of APT. High resolution crystal structures of beta-ketoacyl-ACP synthase II (FabF) in non-covalent and covalent complex with Cerulenin had been reported recently (PDB ID 4ls7 / 4ls8, [85]). In this case, Cerulenin is attached to the active site cystein where the covalent bond is formed to the carbon C3 of the inhibitor, in contrast to the previously proposed C2 carbon (Figure 14).

An attack on the epoxide by the nucleophilic serine of APT results in an irreversible ether, and depending on affinity, reactivity and incubation time, equilibrium could be completely shifted to the covalent complex prior to crystallization. This provides an advantage for crystallographic approaches since crystal growth is usually slower (hours to weeks) than the the hydrolysis of reversible complexes like in the case of palmostatin B and M. Human APT1 wild type (1.3 mM) and Cerulenin (up to 9-fold molar excess) were mixed in gelfiltration buffer (see Chapter 7.2.11) and incubated at 20˚C for 400 min. Complex formation was monitored via ESI-MS as described in Chapter 7.2.13. An equimolar human APT1 - Cerulenin adduct could be observed nearly instantly (data not shown). After 400 min incubation of human APT1 wild type with a 6-fold molar excess of Cerulenin (8.4 mM), a maximum binding of three Cerulenin molecules per human APT1 protein is observed (Figure 41), but also showed that a significant fraction of unmodified protein remains in the sample. Using a simple 1,2-hexadecylpoxide lacking any electron-drawing groups next to the epoxide does not result in significant modification of APT (data not shown).

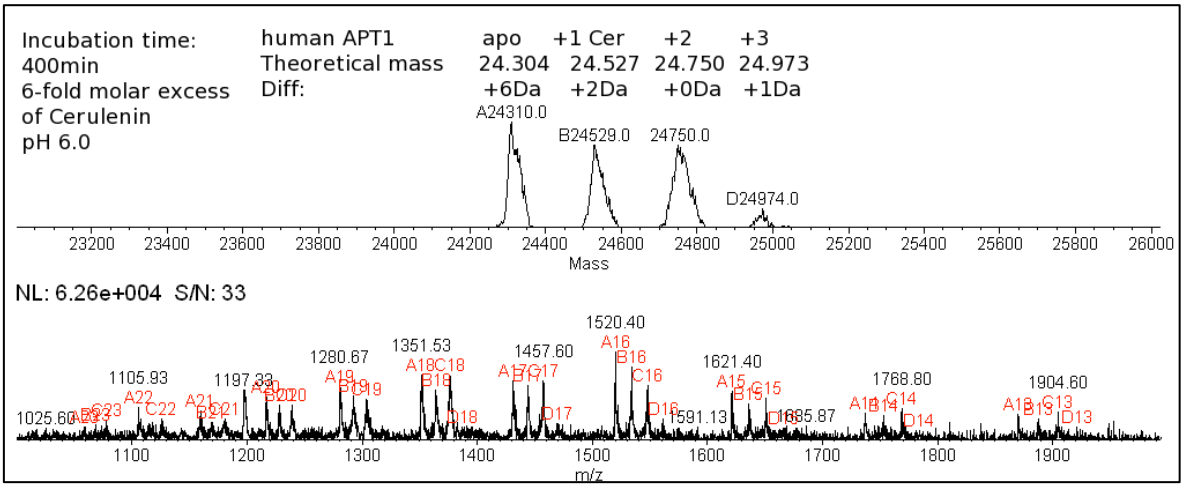

Figure 41: Formation of the covalent human APT1 – Cerulenin complex monitored via ESI LC-MS. After 400 min incubation of 1.3 mM human APT1 wild type with 8.4 mM Cerulenin at 20˚C, the apo form of human APT1 (peak A, m=24,310.0 Da) and the single (m=24,529.0 Da), dual (m=24,750.0 Da) and triple (m=24,974.0 Da) adduct with Cerulenin are observed (peaks B, C, D). LC-MS data analyzed using Xcalibur (ThermoFisher) and MagTran[92] and the figure prepared using Gimp[4].

Encouraged by the expected stable ether bond adduct at the active site serine, Cerulenin was co-crystallized with human APT1. Three different molar ratios (1:3, 1:6, 1:9; 1.3 mM of human APT1 to 3.9 mM, 7.8 mM and 11.7 mM Cerulenin, respectively) of the human APT1 - Cerulenin complex were subjected to screening yielding reasonably diffracting crystals, which were isolated directly from the screening plate. Diffraction data to a resolution of 2.5 Å was collected at SLS in Villigen, CH and the structure was solved via MR using the apo form of human APT1 wild type as template. The statistics of the structure are summed up in Table 4.

Figure 42: Crystallization drop of human APT1 in complex with Cerulenin. The drop contained human APT1 (1.4 mM) and Cerulenin (4.5 mM). Screening condition G1 / #73 of Core1 screen containing 20% PEG 3350 and 0.18 M tri-ammonium citrate. Crystals grew within one week and were isolated directly from the screening plate. Image taken by Formulatrix Imager.

Table 4: Crystallographic statistics of the refinement of the human APT1-Cerulenin complex. Values for the highest shell are given in parentheses. Values for Ramachandran plot are given for favoured, allowed and outlier.

	human APT1 - Cerulenin		
Data collection	16Apr 2014	Refinement	
Space group	P 4_2 2_1 2	Resolution (Å)	45.6-2.5 (2.57-2.5)
Cell dimensions		Number of Reflexes	990309 (38294)
a, b, c (Å)	91.15 91.15 255.53	Rwork	20.7 (33.6)
α, β, γ (°)	90.00 90.00 90.00	Rfree	24.0 (41.3)
Resolution (Å)	45.6-2.5 (2.57-2.5)	Number of Atoms	
Monomers / au	4	Protein	6756
Wave length (Å)	0.91887	Ligand/Ions	112
CC $^1/_2$	100 (64.2)	Waters	67
I / σ(I)	21.2 (1.65)	B-factor (Å2)	
Completeness (%)	100 (100)	Protein	64.7 ± 18.3
		Ligand	88.7 ± 20.3
		Waters	61.1 ± 15.0
		RMSD	
		Bond length (Å)	0.0154
		Bond angle (°)	1.82
		Ramachandran (%)	96.19 / 3.59 / 0.22
		Clashscore	8.39
		Rotamer outlier	3.24
		Molprobity score	2.10

As expected, human APT1 is covalently modified with Cerulenin at the active site, and the aliphatic tail is bound in the substrate binding tunnel. The crystal structure of human APT1 in complex with Cerulenin contains four monomers per asymmetric unit. The four monomers are arranged in such a way that the largest interface is not related to the dimer observed for the apo form of human APT1 (Figure 43A). Closer inspection of the residues located in the new interface reveals a strong difference electron density at the thiols of C168 and C206, which are exposed on the surface, indicating a covalent modification by Cerulenin. The binding of Cerulenin would clash with monomer B of the apo form dimer. In addition, Cerulenin contains a long hydrophobic tail, and thus forms a new hydrophobic patch, which supports the formation of this interface. The modification of the surface exposed cysteines was observed in all crystals obtained from different human APT1 – Cerulenin ratios, varying from 3:1, 6:1 and up to 9:1, all resulting in crystals of comparable diffraction and electron density quality. The comparison of the new interface of the Cerulenin complex to the human APT1 apo dimer is depicted in Figure 43B.

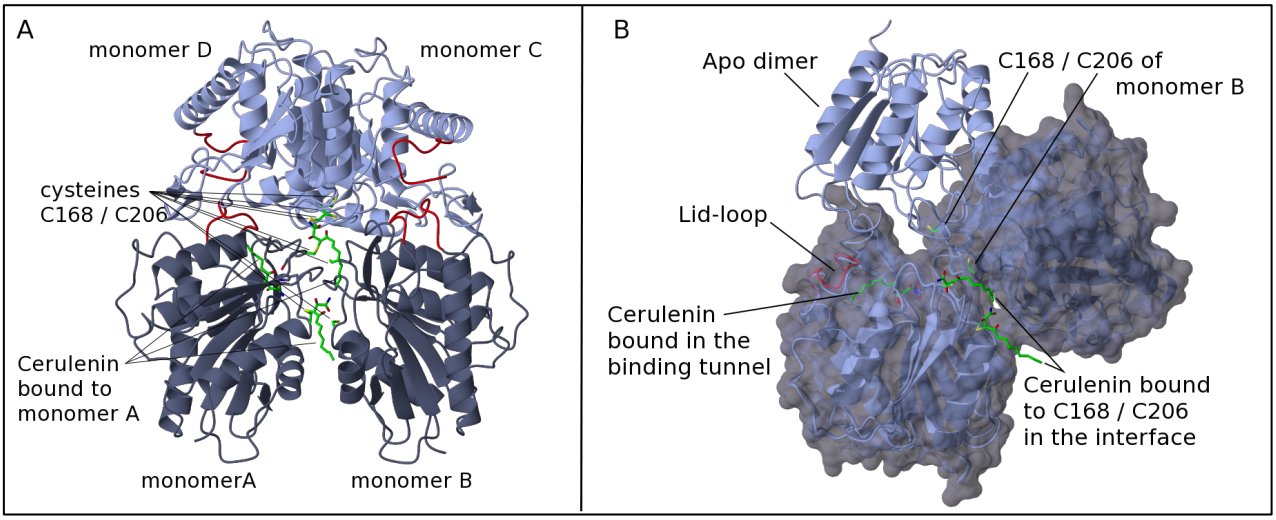

Figure 43: A: Content of the asymmetric unit of the human APT1 – Cerulenin complex. The four monomers do not form a contact comparable to the dimer of human APT1 apo form. B: Interface of the human APT1 – Cerulenin complex (dark blue, surface) compared to the human APT1 apo dimer (light blue, ribbon, from[69]). Two monomers of each structure were superposed highlighting the differing position of the respective second monomer of the structure. Cerulenin is bound to the active site serine with the hydrophobic tail inside the binding tunnel. Both cysteine residues located on the protein surface are covalently modified by Cerulenin as well and contribute to the new interface in the crystal.

Cerulenin binds at the active site with the tail in the binding tunnel. The aliphatic chain is half as long as palmitate, the acyl moiety of the natural substrate, and stretches from the entrance of the binding tunnel between L73 and L171 to the middle of the tunnel marked by W140. A diffuse electron density is observed at the active site serine, indicating a mixture of two covalent binding modes and complicating precise model building. The electron density of the head group is not defined enough to clearly identify a preferred binding mode, but the binding mode via the ether formed at C3 fitted slightly better to the electron density (Figure 45A). Two hydrogen bonds stabilize the head group: the hydroxyl group resulting from the opened epoxide at C2 binds inside the oxyanion hole via H-bond to the backbone amide of L25. The amide head is coordinated via H-bonds to Nε of H203 and the backbone carboxyl of L25 (see Figure 46). The activated epoxide of Cerulenin can be attacked on two chemically nearly identical positions, resulting in irreversible ethers (Figure 44). Both reactions are energetically comparable, and thereby lead to a mixture of both possible adducts and a diffuse electron density, if Cerulenin is not coordinated during the nucleophilic attack.

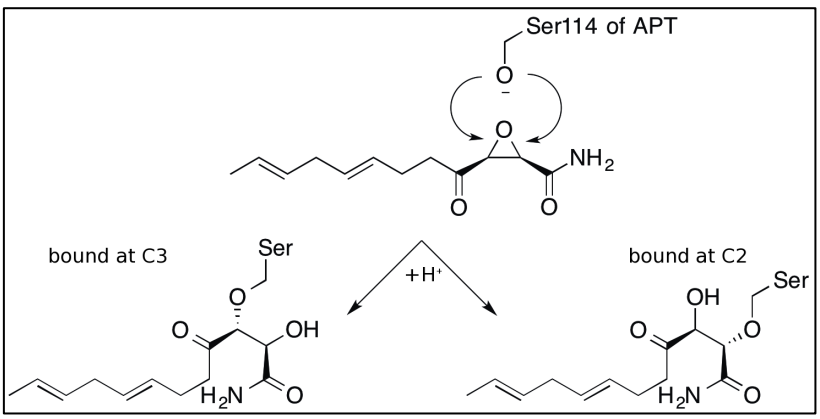

Figure 44: Nucleophiles can attack the epoxide of Cerulenin at both C2 (right) and C3 (left) position, resulting in a mixture of two adducts. Image created using ChemBioDraw13.

The two Cerulenin molecules bound to the surface cysteines are not bound in one defined orientation in the interface between the two proteins, resulting in no or only weak electron density for the aliphatic tail. Cerulenin adducts at both surface exposed cysteines are less well described by electron density than at the active site (Figure 45B & C). The Cerulenin adducts in monomer A are shown in Figure 45 as an example and are compared to the published structure of the covalent FabF-Cerulenin complex (Figure 45D).

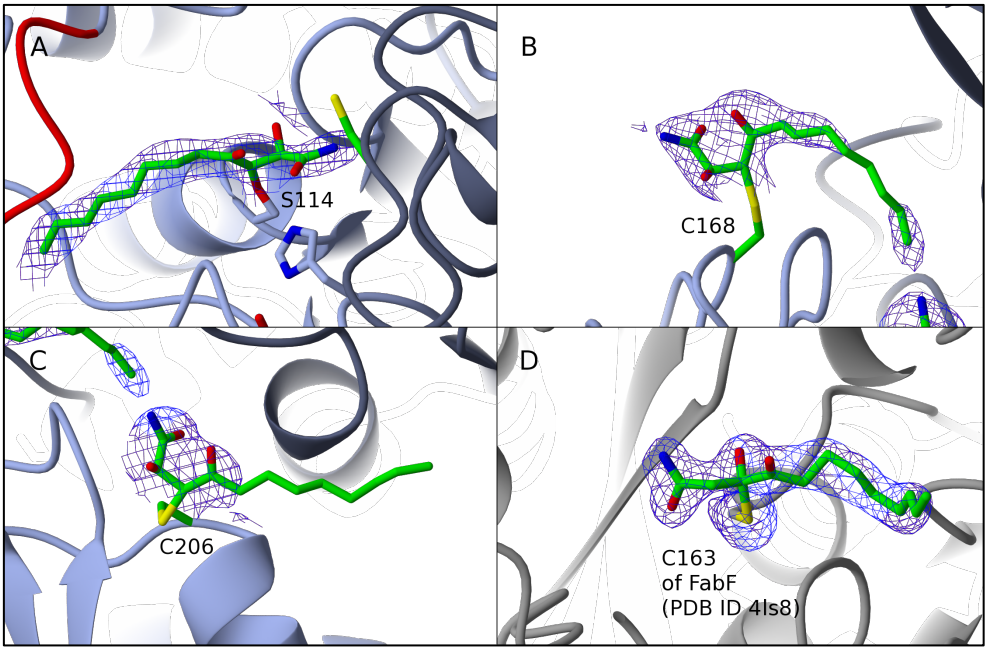

Figure 45: Comparison of the Cerulenin adducts observed in at the active site of human APT1 (A), and at both surface exposed cysteines (B, C) at 2.5 Å resolution. The high-resolution structure of the biological target of Cerulenin, FabF, is shown in the inhibited state with Cerulenin covalently bound to its active site cysteine 163 (D, PDB ID 4ls8, 2.1 Å resolution). The Fo-Fc electron density is shown at 1σ.

The lack of a preference for one binding mode results in a mixture and ambiguous electron density, which complicates building the adduct structure of the complex. Furthermore, the recently published high-resolution structure of Cerulenin covalently inhibiting its biological target FabF (PDB ID 4ls8) opens another question. The structure solved at a resolution of 2.1 Å shows a clear electron density of covalently bound Cerulenin, but the electron desity supports an adduct that is chemically difficult to explain. Cerulenin was attacked by the thiol of cysteine at C3 and is covalently bound. The epoxide oxygen, however, is not located at C2 as it would be expected according from the S_N2 reaction. As stated in[85], the unambiguous electron density only supports the oxygen bound to the C3, resulting in a O,S-hemiketal. The authors suggest a more complex reaction mechanism with its natural target, involving a rearrangement after initial attack[85].

The electron density of the human APT1 – Cerulenin complex is not defined enough to support a complex adduct that underwent this chemically challenging rearrangement. Therefore, the adduct bound at C3 (which fitted best into the electron density) containing the α-hydroxyl group was built in the structure of human APT1 - Cerulenin complex. An analysis of the interactions of Cerulenin bound at the active site is shown in Figure 46.

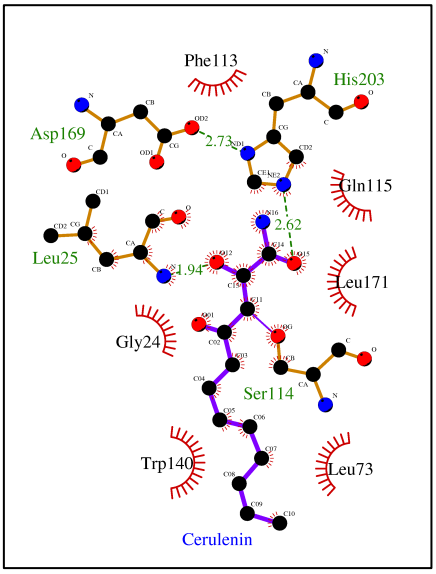

Figure 46: Interactions of human APT1 with the major conformation of Cerulenin covalently bound at its active site. The covalent adduct to the active site serine binds with the hydrophobic tail inside the binding tunnel. The short head group forms two hydrogen bonds, one between the hydroxyl group at C2 and the amide of L25, and another between the amide and Nε of H203. Interactions visualized using LigPlot+[91].

Albeit Cerulenin is less well coordinated (possibly bound as a mixture of both adducts at C2 and C3) than both palmostatins (described in Chapter 5.1.2 and 5.1.3), the complex structure proves the feasibility of using activated epoxides as nucleophilic trap for APT. The reactivity must be significantly reduced to avoid unspecific modification of solvent-accessible thiols if one would want to use Cerulenin as serine hydrolase specific inhibitor.

5.1.5 Crystal structure of human APT1 in complex with 2-Bromopalmitate

2-Bromopalmitate (2BP) is the α-brominated derivative of APTs natural product palmitate. 2BP is widely used as inhibitor of palmitoylation in cell experiments *in vivo* in order to interfere with palmitoylation mediated subcellular localization of proteins. Recently, 2BP was published to be an inhibitor of human APT1 and 2, inhibiting depalmitoylation as well[87]. The mode of inhibition was described as “uncompetitive”, meaning that the inhibitor binds to the pre-formed enzyme-substrate complex. The above presented structures of yeast APT in complex with palmostatin B and palmostatin M, and co-purified tunnel-bound fatty acids in *Xenopus tropicalis* APT1 homolog[69], provided evidence for binding of long-chained aliphatic molecules inside the binding tunnel. Due to the nearly identical structure of 2BP with palmitate, an identical and thus competitive binding mode to palmitate inside the hydrophobic binding tunnel[69] was expected, which would at least partially contradict the idea of an uncompetitive inhibitor[87]. To resolve this contradiction, the complex of human APT1 and 2BP was co-crystallized and represents the first structure of human APT1 in complex with a non-covalent inhibitor. The binding site was verified via Stopped Flow measurements, described in Chapter 5.1.7.

To prepare the 2BP complex, human APT1 was pre-incubated with a 3-fold molar excess of 2BP for 10min at 50˚C, as complex formation is facilitated at increased temperatures (Stefan Baumeister, private communication). The protein-inhibitor mixture was subjected to screening for suitable conditions as described in Material and Methods, covering a total of 768 conditions.

Crystals grew at several conditions, and a strong preference for conditions containing various PEGs of small to medium molecular weight at a pH range between 4.6 and 8.5 was observed. Significantly better electron density for 2BP corresponding to higher occupancy was observed at pH $\geq$ 7.0. Large, single crystals also grew in one PEG-free condition containing 1.0 M $(NH_4)_2SO_4$ and 0.1 M Bicine, pH 9.0 and this crystal was isolated using perfluorated 4500 cryo oil to prevent ice formation upon freezing the crystal. As the monomeric structure of the human APT1 – 2BP complex is nearly identical in different crystals belonging to different space groups obtained under different conditions, only the best diffracting crystal is presented here which grew in screening condition Core1 B2 under a strong but easily removable skin. Diffraction data was collected as described in Material and Methods at X10SA at SLS, Villigen, (CH) using monochromatic x-rays of 0.9242 Å wavelength to provide anomalous data to support the position of the bromine atom.

Table 5: Crystallographic statistics of human APT1 in complex with 2BP. Crystals were grown in JCSG Core1 condition B2. Values for the highest shell are given in parentheses. Values for Ramachandran plot are given for favoured, allowed and outlier.

	human APT1 + 2BP		
Data collection		Refinement	
Space group	$P2_1$	Resolution (Å)	46.37 - 1.6 (1.64 - 1.6)
Cell dimensions		Number of Reflexes	1733591 (128472)
a, b, c (Å)	72.59 62.08 114.67	Rwork	17.6 (28.3)
α, β, γ (°)	90.00 106.13 90	Rfree	21.2 (34.7)
Resolution (Å)	45.87 -1.6 (1.64 - 1.60)	Number of Atoms	
Monomers / au	4	Protein	6866
Wave length (Å)	0.92045	Ligand/Ions	247
CC $^1/_2$	99.9 (75.4)	Water	1276
I / σ(I)	19.93 (1.70)	B-factor (Å2)	
Completeness (%)	98.3 (97.3)	Protein	21.5 ± 8.2
Redundancy	6.94 (6.99)	Ligands	30.0 ± 9.6
		Solvent	35.6 ± 9.1
		RMSD	
		Bond length (Å)	0.0244
		Bond angle (°)	2.23
		Ramachandran (%)	97.14 / 2.86 / 0.0
		Clashscore	7.74
		Rotamer outlier	1.19
		Molprobity score	1.64

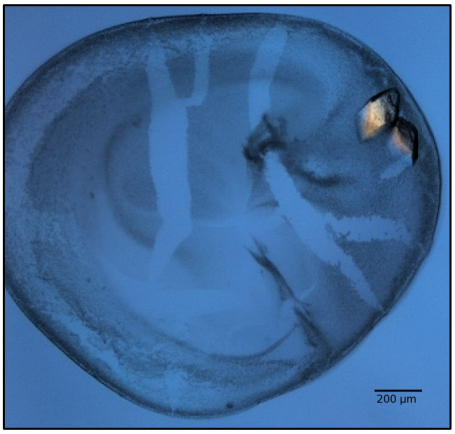

Figure 47: Crystals of human APT1 in complex with 2-bromopalmitate, grown in Core1 B2 containing 0.1 M HEPES at pH 7.5 and 20% PEG 8000. The complex was pre-incubated prior to setting up the crystallization plate. Crystals appear within 12 hours and grow for eight days. Photograph taken using Formulatrix Rock imager.

The best-diffracting crystal of human APT1 in complex with 2BP contains 4 monomers per asymmetric unit, forming two dimers similar to each other (rmsd of 0.43Å over 443 amino acids) and relatively similar to the apo form of human APT1 (Figure 48A, rmsd of 0.55 Å over 219 amino acids). The second monomer of the two dimer of the human APT1 - 2BP complex is rotated by 4.1˚ and 6.9˚ compared to human APT1 apo protein crystallized in P1[69]. The active site and the entrance to the binding tunnel is blocked in the dimer interface in this crystal similar to the apo form of human APT1 (not shown), and 2BP is bound inside the binding tunnel of human APT1, similar to the co-purified palmitic acid in complex with *X. tropicalis* APT1 previously described[69]. The conformation of the lid-loop and side chains forming the tunnel entrance are not changed, minor movements (in the range observed between multiple monomers of one crystal) can be observed for the lid-loop as induced fit by binding of 2BP (Figure 48B).

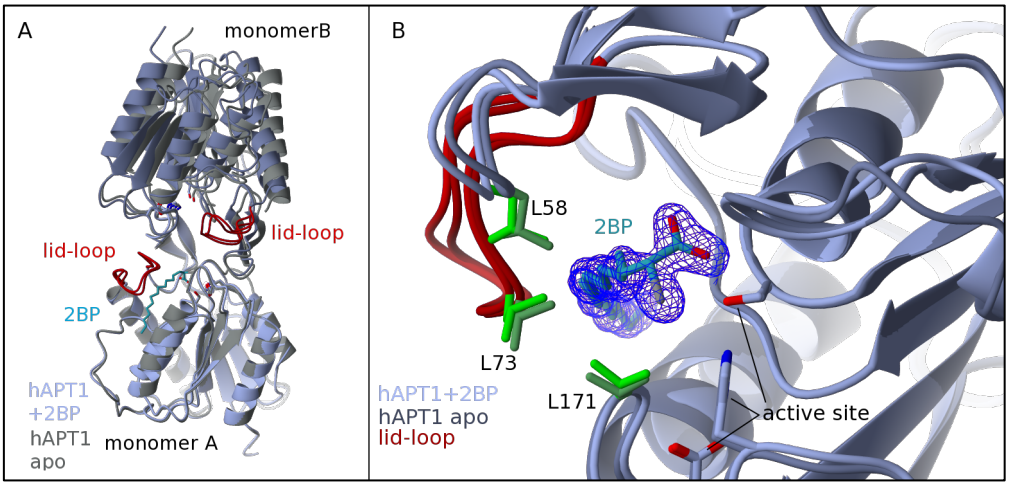

Figure 48: A: Comparison of the dimer formed by human APT1 in complex with 2BP (blue) and the apo form of human APT1 (grey). The active site residues and 2BP are shown as sticks, the lid-loop is highlighted in red. B: Superimposition of human APT1 in complex with 2BP (light blue) and crystallized in the apo form (dark blue) Only minor changes in conformation of the lid-loop (light / dark red respectively) or the side chains forming the tunnel entrance (light / dark green) are observed upon binding 2BP (turquoise) inside the tunnel.

Overall, twelve peaks of the anomalous electron density map were found in the asymmetric unit. Two peaks are located at the head group of 2BP next to the active site of each monomer, and two further peaks are found in both dimer interface. Their intensities given in I/σI are listed in the

following table. The intensity ratio between major and minor conformation shows a preference for 2BP to bind in the major conformation with the carboxyl head coordinated by the oxyanion hole.

Table 6: Intensities of the peaks of the anomalous map for bromide, given in I/σI.

Intensity [I/σI]	Major	Minor	Interface AD / BC
Monomer A	28.5	7.0	21.0
Monomer B	25.8	7.3	14.0
Monomer C	25.2	8.1	15.6
Monomer D	27.8	10.2	10.7

The anomalous signal was calculated from the data set collected at the high-remote edge of bromine (0.92045Å) at X10SA at SLS and was used to verify the presence and the position of the bound 2BP (and to exclude a co-purified fatty acid). Two peaks of the anomalous map were observed in the forked electron density of 2BP close to the active site serine (Figure 49), indicating that 2BP binds in two orientations. Comparing the intensity of the signals, one is about 3- to 4-fold stronger than the other. Consequently, the stronger and weaker signals were assigned to two conformations termed major and minor conformation, respectively. The electron density of both signals is shown in Figure 49.

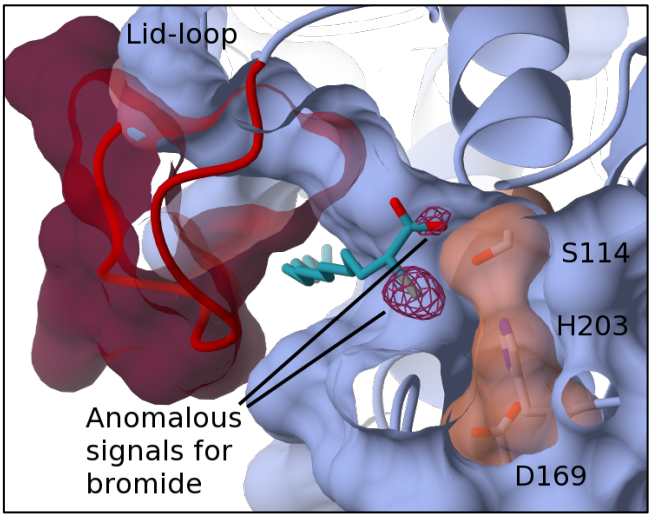

Figure 49: Human APT1 co-crystallized with 2BP. Human APT1 is shown in blue with the catalytic triad highlighted as sticks, and the lid-loop shown in red. 2BP is shown as turquoise sticks. Electron density of the anomalous signals of the α-bromide of 2BP is shown scaled to 5.0 σ. 2BP is shown in the major conformation, fitting the α-bromide into the strongest anomalous electron density, and the carboxylate bound in the oxyanion hole. In the minor conformation, the α-bromide binds inside the oxyanion hole.

The electron density of 2BP is very well defined due to the high resolution (1.6 Å) and occupancy. This allows a differentiation between both enantiomers of 2BP present in the racemic mixture obtained from Sigma Aldrich. The electron density supports fitting of R-2BP in the major conformation, with the carboxyl head group forming hydrogen bonds to the backbone amides of L25 and Q115 of the oxyanion hole, and as the amide head of Q115 and S114 (Figure 50). A water molecule coordinated by H203 and the backbone amide of L25 forms a H-bond to the carboxyl head of 2BP. The bromine of 2BP is located close to the side chain of L171, which forms the lower part of the tunnel entrance. I70, G72, L73 are located in the lid-loop and form with F176, L179,

T180, and W140 the hydrophobic tunnel, in which the aliphatic chain of 2BP is bound (Figure 50). R144 is located at the rear exit of the binding tunnel, and the aliphatic part of its side chain contacts with the tip of 2BP.

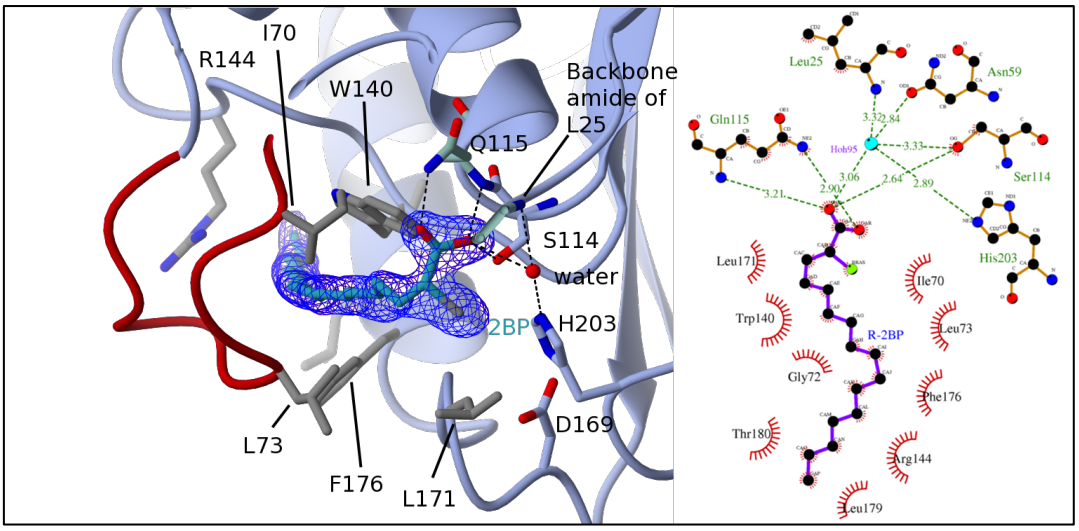

Figure 50: Coordination of R-2BP in major conformation. The carboxyl head group is coordinated via H-bonds to the backbone amides of L25 and Q115, the side chain amide of Q115, the hydroxyl of S114, and a water molecule that itself is coordinated by imidazole side chain of H203 and the backbone amide of L25. The α-bromide is located close to L171 at the tunnel entrance. H-bonds are shown as dashed lines, the amino acids involved in hydrophobic interactions with 2BP are shown with a transparent surface. Image created using CCP4mg[93], LigPlot+[91] and labeled using Gimp[4].

2BP is a chiral molecule, and the R-enantiomer fits well into the electron density in the major conformation described above. To fit 2BP in the minor conformation, satisfying the anomalous signal inside the oxyanion hole, the S-2BP enantiomer was used in order to remain in the same geometry at the Cα of 2BP. A cross-validation using the R-2BP in the minor and S-2BP in the major conformation including switched occupancies resulted in slightly higher R_{free} and a worse fit into the electron density. In all monomers, 2BP is bound with 50% occupancy of R-2BP in the major, and 30% occupancy of S-2BP in the minor conformation. Refining the 2BP molecules with higher occupancies resulted in negative difference electron density (2Fo-Fc) at the head group.

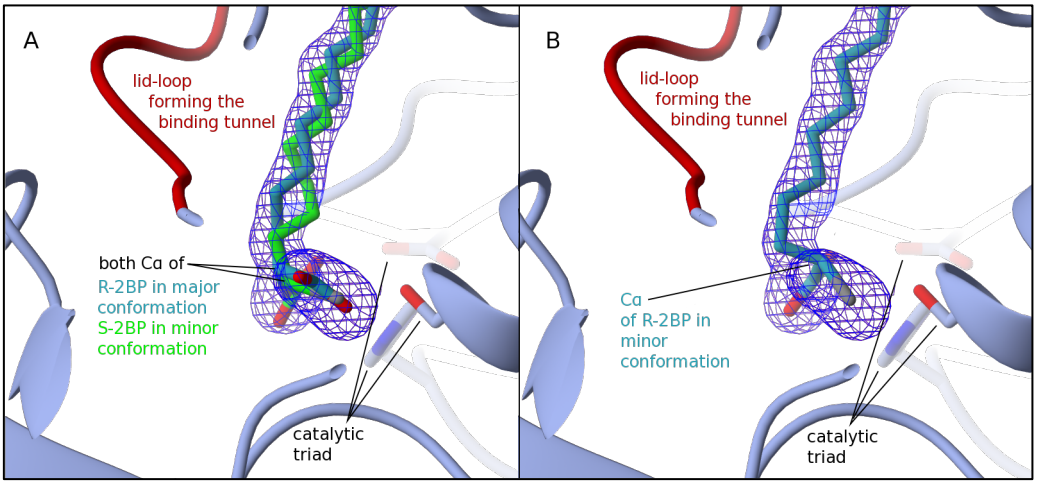

Figure 51: Panel A shows R-2BP bound in the major conformation, and S-2BP bound in the minor conformation. This arrangement fits the electron density well, the Cα atoms of both 2BP are at the same position and cause no clashes. Panel B: R-2BP fitted in the minor reveals a worse fit into the electron density, and furthermore causes some clashes.

In addition to the two peaks of the anomalous map at the active site corresponding to the α-bromide of 2BP in two conformations, two additional anomalous signals of perfectly round shape were detected in the dimer interface. In both similar dimers, these bromides are located next to and coordinated by the side chains of N59 and M64 of both monomers and a water molecule (Figure 52). These signals can be explained by free bromide ions that are probably impurities from the synthesis of the compound, which was bought from Sigma Aldrich (~97% purity). An overview of the anomalous signals observed at the active site and in a dimer interface is given in Figure 52.

The first structure of human APT1 (PDB ID 1fj2) was phased via SAD using sodium bromide added to the cryo protectant[58]. This structure contains 40 bromide ions per asymmetric unit, of which two bromide ions are found close to the active site. The positions of the bromide anions in the respective dimer interfaces differ between the published structure soaked with bromide (1fj2) and the 2BP – complex presented here, probably due to the different dimer interface. However, the oxyanion hole of human APT1 in the structure 1fj2 contains a bromide anion, and the same position is also occupied by the α-bromide of 2BP bound in the minor conformation (Figure 49).

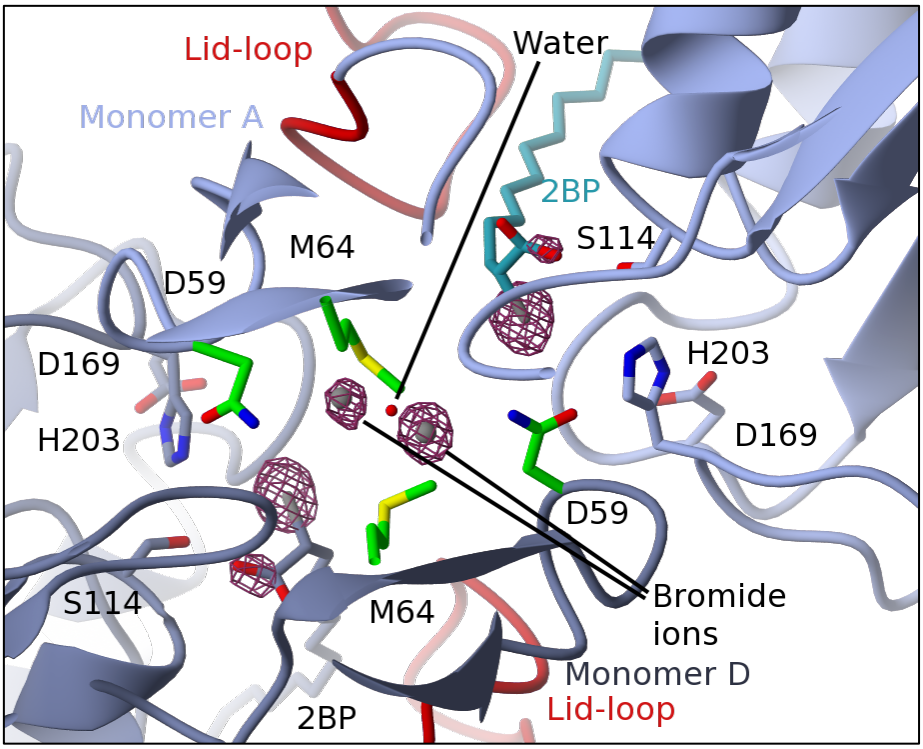

Figure 52: Position of bromide ions in the dimer interface of human APT1 co-crystallized with 2BP. The interacting amino acids N59 and M64 of both chains with the two bromide ions are highlighted as green sticks. 2BP bound in the hydrophobic tunnel is presented in the major conformation.

Summarized, the crystal structure of human APT1 in complex with 2BP revealed binding of 2BP inside the hydrophobic binding tunnel. The electron density of 2BP is well defined due to high resolution and occupancy and supported by the anomalous signal for the bromide. Binding of 2BP inside the tunnel means a competitive mode of inhibition. To exclude this binding mode as a crystallographic artifact, binding of 2BP to human APT1 was monitored via Stopped Flow, described in chapter 5.1.7.

5.1.6 Summary of APT – inhibitor complexes

The structures of palmostatin B and palmostatin M bound to yeast APT provide structural insight into the interactions of both inhibitors on atomic scale. Since the amino acids involved in binding the core and head group are conserved, the binding mode could similar in human APT1 (Figure 40). The complex structure with Cerulenin showed that it is possible to covalently modify the active site serine in a complex of human APT1, and also demonstrated the potential of activated epoxides as nucleophilic trap for APTs. Cerulenin modifies surface-exposed cysteines as well, thus being less selective compared to palmostatin B and M. The complex of human APT1 and 2BP, being the first non-covalent inhibitor complex structure of human APT1, shows that 2BP binds inside the tunnel and acts as a competitive inhibitor of human APT1. The lid-loop of yeast APT and human APT1 appears to be rather rigid in those structures and ligand binding has only minor effects on its conformation (Figure 48B). The pre-formed solvent-accessible hydrophobic binding tunnel is a rare, if not even unique feature of APTs among other α,β-hydrolases. Therefore, further investigations on the role of the lid-loop forming the tunnel and its influence on substrate binding and coordination during catalysis, and product release were conducted using several mutants with altered properties regarding length and flexibility of the lid-loop resulting in different length and shape of the binding tunnel as described in the following.

5.1.7 Binding of 2BP to human APT investigated by Stopped Flow

Binding of 2BP to human APT1 was to be further characterized by Stopped Flow measurements. The crystal structure of human APT1 in complex with 2BP shows 2BP exclusively bound inside the hydrophobic tunnel, as described in Chapter 5.1.5. The shallow groove on the surface of APT (see Figure 10) was found to bind PEG molecules in some crystals structure of human APT solved in our group [unpublished observation]. A closely related esterase has a PEG molecule bound in a similar position (see Figure 6, PDB ID 3cn9, [57]). Thus, the possibility that this position could present a second binding site for 2BP was investigated in Stopped Flow measurements.

Human APT1 contains three tryptophan residues. A ligand binding assay based on the intrinsic fluorescence of tryptophan present in the wild type protein was established by Stefan Baumeister and is described in Chapter 7.6 of Material and Methods. As presented in the introduction in Figure 10, two of the three tryptophan residues are located at positions of interest. The first, W140, forms the inner wall of the hydrophobic binding tunnel. The second tryptophan, W32, is located in the shallow groove next to the active site, which could accommodate a moiety of the natural substrate like e.g. the peptide of palmitoylated H-Ras. W67 is buried inside the protein. Mutants lacking either W32 or W140 were used in Stopped Flow experiments (as described in Material and Methods Chapter 7.6.1) to unravel the rate constants of 2BP binding at the two specified sites.

As shown in Figure 53A, wild type APT (blue curve) containing tryptophan residues both in the tunnel and at the groove (and thus detects both binding events simultaneously) shows a fast initial decline that reaches a base line within 5 seconds with a very slow nearly linear decline over the full course of the measurement. The signal of 2BP binding inside the hydrophobic tunnel and at the

shallow groove can be split using mutants lacking the tryptophan at one binding site each. Human APT1 W32F detects only the signal of W140 in the tunnel (Figure 53, red curve) and shows a fast decline of the signal within 5 seconds, indicating fast binding of 2BP inside the tunnel. In contrast, human APT1 W140F should detect binding at the groove (Figure 53, green curve) and shows a very slow decline, not reaching equilibrium within 60 seconds. Since the fast binding of 2BP inside the tunnel is the stronger signal, the curves of 2BP binding to human APT1 wild type and W32F mutant have a very similar profile. The 2BP effect on W32 in the groove is slower by orders of magnitude compared to the tunnel binding. This signal is not necessarily caused by binding (only), it could also be caused by unspecific binding and/or be indicative of slow denaturation or unfolding of the protein as has been found at higher concentrations of 2BP (Stefan Baumeister, personal communication). This shows that the signal of 2BP binding to human APT1 wild type is dominated by the binding inside the tunnel, and thus the negligible effect of 2BP on W32 binding at the groove on the binding signal of the wild type was ignored in further experiments (see Chapter 5.2.14) for practical purposes.

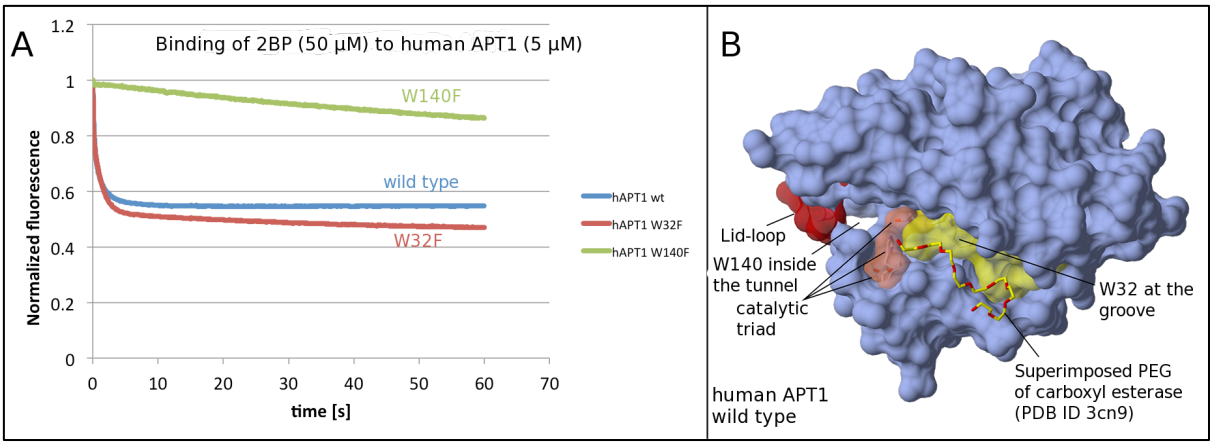

Figure 53: Panel A: The binding of 2BP (50µM) to human APT1 (5 µM) was assessed by Stopped Flow measurements. The wild type is shown in blue. The binding rates of 2BP inside the hydrophobic tunnel (W32F, red) and at the adjacent shallow groove (W140F, green) can be separated using mutants lacking the other tryptophan. As seen in the scaled data, equilibrium for binding inside the tunnel is reached in less than 5 seconds, while binding inside the shallow groove is slower and not finished after 60 seconds. Data scaled and normalized and plotted using Microsoft Excel. Panel B: Overview of both binding sites of 2BP on human APT1 wild type. Labels added using Gimp[4].

Both binding signals of human APT1 wild type (Figure 53, blue) and the W32F mutant (Figure 53, red) contain two fast binding rate constants. A fit with a single exponential shows systematic deviations. In general, multi-exponential fits are dynamic and can be unstable if no parameter is initially known and both rates are within a comparable range. Attempts to deconvolute the binding rate constants failed as the rates determined could be varied by an order of magnitude still resulting in a fit of similar quality. Therefore, the 2BP binding curves were compared qualitatively.

The slow binding at the groove cannot be the cause for the two fast binding rates observed in human APT1 wild type and W32F mutant, since the W32 mutant lacks the tryptophan residue at the groove and thus does not detect 2BP binding there. An induced fit of 2BP inside the tunnel or a rearrangement of the lid-loop upon binding would be the first and most obvious suggestion for the two fast binding rates, but this was contradicted in another experiment where a lid-loop lacking

mutant also showed two fast binding rates (described in Chapter 5.2.14). Another possibility would be binding of 2BP to a monomeric and dimer species of APT since human APT1 forms a (weak) dimer that most likely needs to dissociate to enable 2BP binding inside the hydrophobic tunnel. A third possibility would be that binding of 2BP inside the tunnel could cause minor alterations of the protein structure and thus indirectly affect the fluorescence of W67 inside the protein (an known effect observed in intrinsic tryptophan fluorescence measurements called “tryptophan cross-talk”).
As seen from the Stopped Flow results, the rate constant for binding of 2BP inside the hydrophobic tunnel is much faster than the binding rate at the groove observed in the W140F mutant. This is in agreement with a K_D of ~1 µM for the specific binding site in the tunnel and a high second K_D of about 100 µM for 2BP for rather (unspecific binding) at the second binding site observed in the tryptophan fluorescence binding assay [Stefan Baumeister, unpublished observation].

5.1.7.1 Human APT1 binds 2BP when presented in DOCP vesicles

The biological substrates of human APT1 are attached to cellular membranes via a palmitoyl anchor. Therefore, it was tested if human APT1 is able to bind 2BP when incorporated in multi-lamellar DOPC vesicles (vesicle preparation see Chapter 7.6.3). The measurement is shown in Figure 54 and reveals that the binding rate of 2BP incorporated in DOPC vesicles to human APT1 (blue) is comparable to binding of free 2BP (green). In contrast, a suspension of mixed CHAPS - 2BP micelles prevents binding of 2BP to human APT1 (data not shown), indicating that binding of 2BP to CHAPS micelles is stronger than binding to human APT1 or DOPC vesicles.

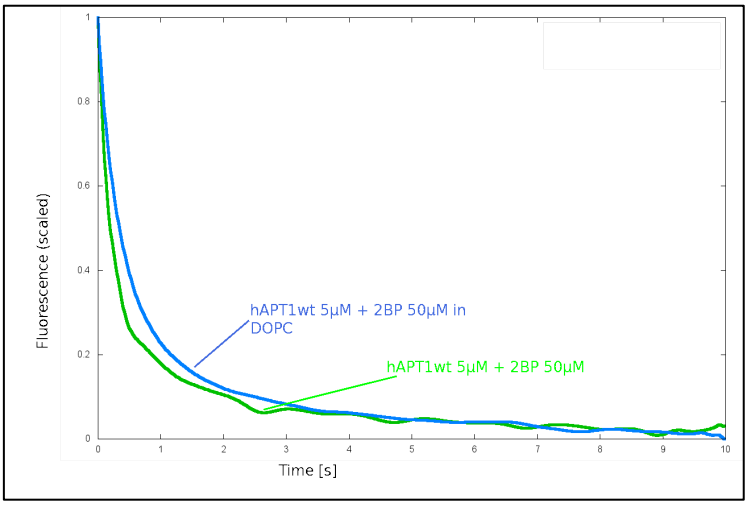

Figure 54: Comparison of the binding rates of human APT1 wild type (5 µM) and free 2BP (50 µM, blue) or 2BP (50 µM) presented in multi-lamellar DOPC vesicles (1 mM). Data plotted by Ingrid Vetter using GnuPlot[94] and annotated using Gimp[4].

The similar binding rates of free 2BP and 2BP in DOPC vesicles is remarkable for the following reason: The association rate constant is dependent on the ligand concentration (unit: M^{-1} s^{-1}). The protein and total 2BP concentration is similar in both measurements. In the presence of DOPC vesicles, 2BP is most likely randomly incorporated within the multiple layers of the DOPC vesicles since it has a high affinity for the lipids (2BP extraction from a complex with human APT1 by DOPC vesicles shown in Figure 55). Thus, the effective 2BP concentration on the accessible surface of the DOPC vesicles, and the fraction of free 2BP (depending on the equilibrium) has to be lower

than in the case of free 2BP. Therefore, the fact that the concentration-dependent binding rates are comparable indicates two possibilities: Either 2BP binding to human APT1 is enhanced when presented in vesicles, or the free 2BP concentration is in the saturation of the maximal binding rate in both cases.

5.1.8 Dissociation of the human APT1 – 2BP complex investigated by Stopped Flow

The dissociation of 2BP from a pre-formed complex with human APT1 wild type or selected mutants was measured via Stopped Flow as described in Chapter 7.6.2. To extract 2BP from its complex with human APT1, equilibrium was changed using high affinity 2BP binders injected via the second syringe. Three different 2BP binders were tested on their suitability to measure release of 2BP from human APT1 wild type complex. L-FABP, a tryptophan-free fatty acid binding protein, has a high affinity for fatty acids in the low nanomolar range (60 nM for palmitate, [95]) and was estimated to have a high affinity for 2BP due to the high similarity. The vesicle-forming lipid DOPC, and CHAPS, a detergent were tested as well. The dissociation rates of human APT1 wild type in complex with 2BP using the three competitors are shown in Figure 55 and are (as expected) depending on the specific competitor used to sequester 2BP. The significantly slowest dissociation of the human APT1 wild type – 2BP complex is observed when adding DOPC vesicles; the system does not reach equilibrium within the here presented time frame of 2 seconds (but does in approximately 10 seconds, data not shown). The initial extraction rates of L-FABP and CHAPS are comparable, but L-FABP exhibits a slower second phase (which will be discussed in the following part) than in the case of CHAPS. CHAPS as a detergent could potentially influence the protein structure itself or the lid-loop in particular to actively facilitate 2BP release apart from changing the equilibrium concentrations. No biological relevant connection between human APT1 and L-FABP is known that would imply an active ligand dissociation-activating mechanism. Therefore, L-FABP was chosen as competitor for further experiments like the comparison of the dissociation rate of selected human APT1 mutants presented in Chapter 5.2.15.

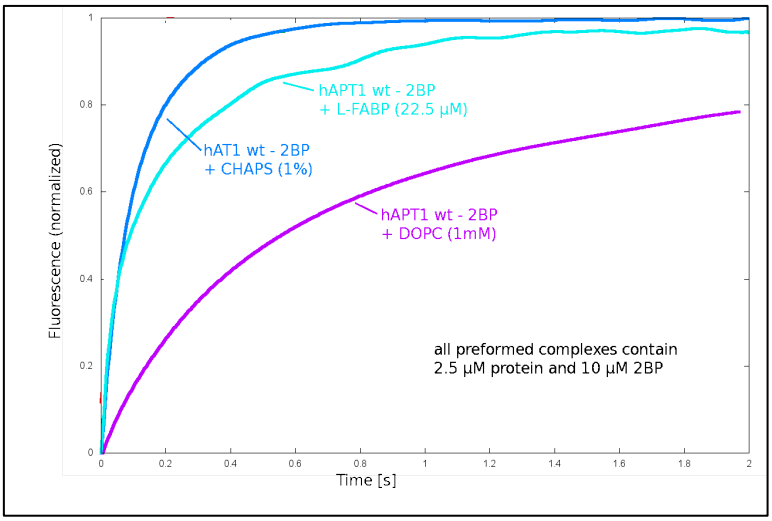

Figure 55: Comparison of the dissociation rates of the human APT1 - 2BP complex using different competitors. The human APT1 – 2BP complex always contained 2.5µM protein and 10 µM 2BP. The release rate could depend on the binding rate and/or the affinity to the competing reagent.DOPC (purple) causes a slower dissociation rate constant of the human APT1 – 2BP complex compared to L-FABP (cyan) or CHAPS (blue) used as competitor. Data averaged, normalized, and plotted by Ingrid Vetter using gnuplot[94]. Labels were added using Gimp[4].

The curve using 1% CHAPS as competitor can be reasonably well fitted using one apparent dissociation rate constant estimated to be in the range of k_{off} = 30- 40 s^{-1} (see Figure 116 in Appendix). However, as both other competitors show two dissociation rates, it is possible that CHAPS affects the structure of the protein and thus actively enhances the dissociation rate and causes it to be monophasic. Using L-FABP, the data can be fitted estimating a first, faster apparent dissociation rate constant of k_{off} = 50-65 s^{-1}, and a second, slower rate constant of k_{off} = 3 - 8 s^{-1} (see Figure 117 in Appendix). The faster dissociation rate is about 2-fold higher than the single dissociation rate constant estimated for the experiment using 1% CHAPS, which is not a significant difference considering the quality of the fit and the resulting range of dissociation rate constants. The two dissociation rates are potentially caused by the two binding sites of human APT1, the faster dissociation rate might then results from 2BP unspecifically bound e.g. near W32 at the groove. The second slightly slower dissociation rate is probably caused by the more stable tunnel-bound 2BP.

The dissociation constant of a complex K_D is defined as $K_D = k_{off} / k_{on}$, [96], and is an expression of the affinity of a complex. Taking the K_D of around 1 µM of 2BP for the binding tunnel (Stefan Baumeister, private communications) and the estimated k_{off} in the range of 8 s^{-1} (diss. rate constant of 2BP from human APT1 when adding L-FABP) solving the above equation would result in a calculated k_{on} of 8 x10^6 mol^{-1} s^{-1}. This is multiple orders of magnitude higher than the association rate constants estimated from binding experiments. The 2BP concentration assumed in the k_{on} measurement is the most likely cause of this discrepancy, as little is known about the effect of micelle formation and aggregation on the concentration of free 2BP. Also, potential adsorption of the hydrophobic 2BP to wall of the reaction vessel or unspecific binding on the protein surface affects the 2BP concentration. This hypothesis is corroborated by another observation: the binding rate constants k_{on} estimated from several experiments of different 2BP concentrations can only be measured with very large errors and do not show concentration dependency (although k_{on} has the unit of s^{-1} M^{-1} and thus is dependent on the ligand concentration). This indicates that the effective 2BP concentration is comparable in these measurements, but significantly lower than the assumed input concentration of 2BP due to the before mentioned uncertain problems of micelle formation or aggregation.

5.2 Analysis of the lid-loop forming the hydrophobic binding tunnel

Lipases usually have a lid-domain covering the active site and the hydrophobic patch around it. Lipases are often interfacially activated by membranes and uncover the active site to enable catalysis. In contrast, esterases have a solvent accessible active site. APTs contain a loop that helps to form a structural motif that, to my knowledge, has not been observed within the family of α,β-hydrolases: a pre-formed solvent-accessible hydrophobic tunnel located next to the catalytic triad. The outer wall of this tunnel is formed by the lid-loop.

This raises the questions if the lid-loop is flexible, and if the flexibility of the lid-loop is linked to protein activity; how the binding tunnel is held in an open, solvent-accessible state; how its shape affects substrate binding; and if the tunnel is essential for substrate turnover. To address these questions, several lid-loop mutants have been subjected to activity assays, “Stopped Flow” measurements, and structural analysis.

5.2.1 Design of different lid-loop mutants

The conformation of the lid-loop is determined by polar contacts as well as hydrophobic van-der-Waals interactions. The side chains of the residues S74, D76, S77, and Q78 (Figure 56) are facing the solvent and do not address the protein core. Side chains of I70 and I71, located at the N-terminal hinge of the lid-loop, are buried in the inside or facing towards the C-terminal hinge, respectively, acting as anchors of the hinge. Of the remaining amino acids, G72 lacks a side chain, and P75 forms the tip of the lid-loop and is located close to F176, thus closing the outer wall of the tunnel. The side chain of L73 is located close to L171 and L58 (green sticks in Figure 56) in about 4 to 4.5Å distance, within the range of van-der-Waals interactions, and probably helps to anchor the lid-loop. The side chains of these three leucines form a hydrophobic entrance of the binding tunnel and are conserved in higher animals. A detailed overview of the lid-loop is shown in Figure 56.

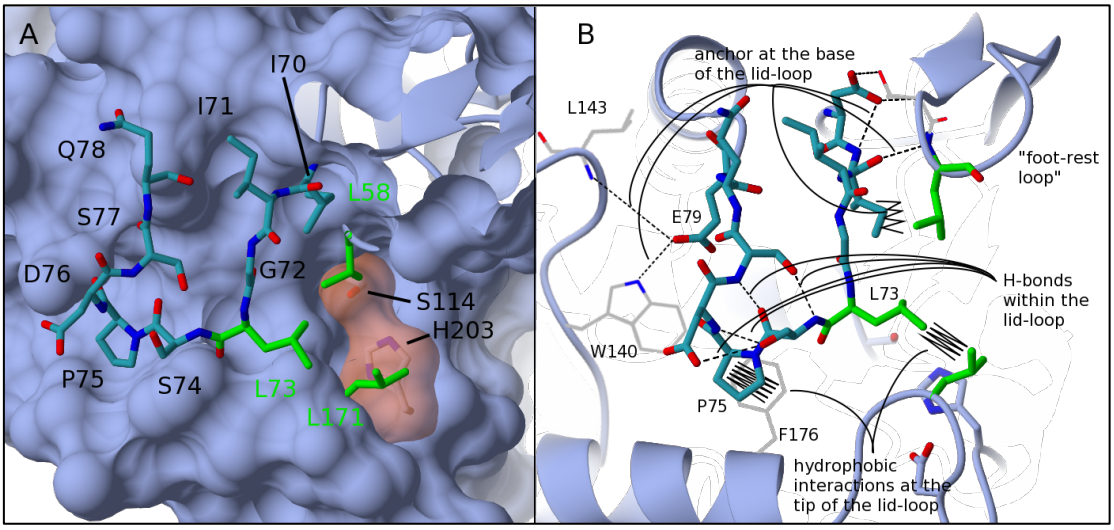

Figure 56: Panel A: Amino acids of the lid-loop shown as sticks. Polar amino acids like S74, D76, S77, and Q78 are facing with their side chains into the solvent. Notably, L73 is located at the tip of the lid-loop forming the tunnel entrance with L171 and L58 (all three highlighted in green) next to the active site. Panel B: Schematic view of the interactions that are suspected to keep the lid-loop in the wild type conformation.

In order to explore the role of the different residues within the lid-loop, three types of mutants were created, addressing different properties of the lid-loop. Firstly, we investigated the effect of mutating the three leucines forming the outer part of the tunnel entrance by alanine and valine mutations (L171A, L171V, L58A, L73A).

As second type of mutation, we explored the effect of an elongated lid-loop inspired by the APT-related protein SOBER1 from *A.thaliana* [69] that has an extended lid-loop and is not able to hydrolyze long-chained substrates, by extending the lid-loop of APT with a Leu-Pro insert in between G72 and L73.

The third group of mutants contains lid-loop truncations of various lengths to investigate the influence of the lid-loop length on activity. Six distinct truncations were generated by deleting either two, four or six residues of the lid-loop (ΔG72L73, ΔL73S74, ΔS74P75, ΔI71-S74, ΔL73-D76, ΔI71-D76).

5.2.2 Crystal structures and biochemical activity of human APT1 L171A and L171V mutants

Human APT1 L171V and L171A mutants were assayed on their activity against the fluorescent substrate PPTS (see Chapter 7.5.1). Figure 57 shows their activity compared to human APT1 wt. Human APT1 L171V shows a slightly increased activity compared to the wild type, with a k_{cat}, of 3.9 ± 0.32 s^{-1} and a K_M of 3.79 ± 1.09 µM. In contrast, human APT1 L171A has a marginally reduced activity of k_{cat} of 2.70 ± 0.20 s^{-1} and a K_M of 2.84 ± 0.77 µM.

These changes, however, are not a significant alteration of the activity profile, as indicated by the errors of k_{cat} and K_M of the averaged data points of duplicate measurements.

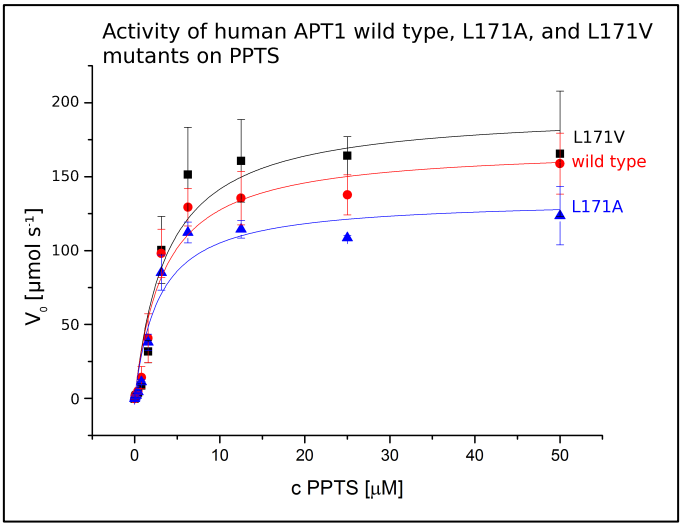

Figure 57: Activity assay of human APT1 wild type, L171A, and L171V using PPTS as substrate. Plotted is k_{cat} versus the substrate concentration. The activity did not significantly change by the mutations compared to the wild type. Data averaging of the duplicate measurements and error calculation was done with Microsoft Excel, the plot was fitted with Origin Pro.

Table 7: Kinetic parameters of human APT1 wild type, L171A and L171V mutants on PPTS used as test substrate.

	V_{max} [µmol s^{-1}]	k_{cat} [s^{-1} x10^4]	K_M [µM]	k_{cat} / K_M [$µM^{-1}$ s^{-1} x10^4]
L171V	195 ± 16	3.90 ± 0.32	3.79 ± 1.09	1.03
wild type	170.5 ± 11	3.41 ± 0.22	3.38 ± 0.77	1.01
L171A	135 ± 10	2.70 ± 0.20	2.84 ± 0.77	0.95

Both mutants were subjected to screening for conditions suitable for crystallization. The crystallization drops and conditions in which the best-diffracting crystals grew are shown in Figure 58. Crystals were isolated directly from screening plates and diffraction data collected at SLS, Villigen, Switzerland, as described in Material and Methods.

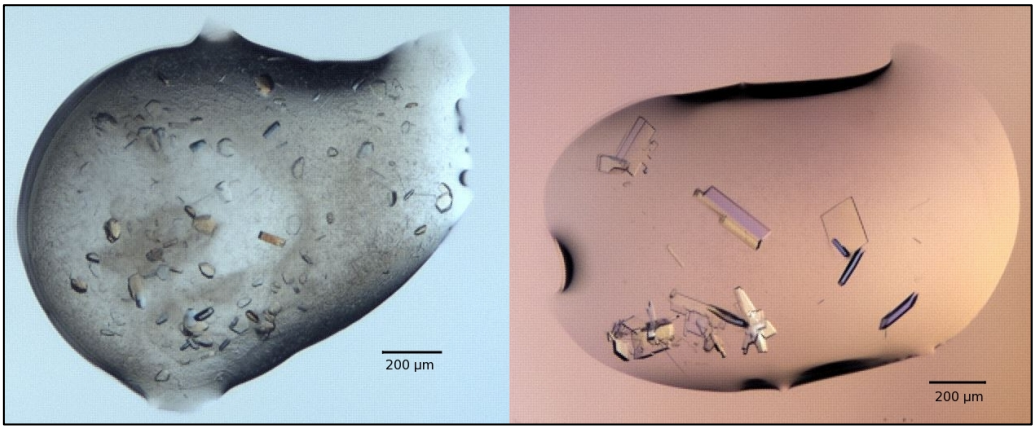

Figure 58: Crystals of human APT1 L171A (left) and L171V (right). Crystals of the L171A mutant grew in condition D12 of PACT screen from Qiagen, containing 0.1 M Tris pH 8.0, 20% PEG 6000, and 0.01 M $ZnCl_2$. Crystals of L171V grew in Core2 E4, containing 0.1 M MES pH 6.0, 1.0 M LiCl, and 10% PEG 6000. Crystals of both mutants grew within 13 days. Photographs taken using Formulatrix Rock Imager and scale bar inserted using Gimp[4].

The structures of both hAPT1 L171A and L171V mutants were solved by molecular replacement using human APT1 wild type as template and belong to space group $P2_1$ with 4 monomers per asymmetric unit and P1 containing 2 monomers per asymmetric unit, respectively. The crystallographic statistics for both L171 mutants are presented in Table 8.

Table 8: Crystallographic table of human APT1 L171A and L171V. Values for the highest shell are given in parentheses. A molecule of MES is bound to human APT1 L171V. Values for Ramachandran plot are given for favoured, allowed and outlier.

	human APT1 L171A	human APT1 L171V		human APT1 L171A	human APT1 L171V
Data collection			Refinement		
Space group	$P2_1$	P1	Resolution (Å)	48.53-2.20 (2.26-2.20)	38.01 -1.28 (1.31-1.28)
Cell dimensions			Number of Reflexes	239761 (16921)	323611 (8311)
a, b, c (Å)	76.88, 55.50, 101.55	38.5, 40.9, 71.9	Rwork	23.15 (30.5)	18.33 (26.2)
α, β, γ (°)	90.0, 112.1, 90.0	102.1, 95.6, 106.2	Rfree	28.03 (32.2)	20.43 (25.5)
Resolution (Å)	48.52-2.20 (2.26-2.20)	38.01-1.28 (1.31-1.28)	Number of Atoms		
Monomers / au	4	2	Protein	6685	3474
Wave length (Å)	0.91639	0.92019	Ligand/Ions	-	12
CC $^1/_2$	99.3 (73.0)	99.8 (68.3)	Water	143	705
I / σ(I)	6.99 (1.94)	9.5 (1.77)	B-factor (Å2)		
Completeness (%)	99 (99.76)	82.3 (32.3)	Protein	44.0 ± 13.6	13.0 ± 6.0
Redundancy	3.05 (2.92)	1.86 (1.67)	Ligand	-	22.6 ± 4.4
			Water	42.0 ± 12.5	28.7 ± 8.9
			RMSD		
			Bond length (Å)	0.013	0.0271
			Bond angle (°)	1.552	2.37
			Ramachandran (%)	97.40, 2.37, 0.23	98.27, 1.73, 0.00
			Clashscore	8.70	7.22
			Rotamer outlier (%)	5.36	2.08
			Molprobity score	2.14	1.64

Both mutations of L171 do not cause any significant changes within the overall structure of human APT1. The 1.94 Å structure of the apo form of human APT1 belonging to space group P1[69] is used as reference. The L171A mutant monomers have an average rmsd of 0.48 Å^2 over 219 Cα compared to the wild type and form a dimer similar to the wild type (rotated by 6.3 to 7.1˚), despite the different crystallization conditions and space group. The conformation of the lid-loop does not differ from the wild type lid-loop in any of the four monomers (see Figure 60 for details). The structure of human APT1 L171V belongs to the same space group (P1) as the apo form of human APT1 wild type with a similar unit cell [69]. The two monomers have an average rmsd of 0.39 Å compared to the wild type. Again, the conformation of the lid-loop is not altered in the mutant. The dimer is nearly identical (rotated by 1˚) compared to the wild type, and only the loop region containing T28/G29/H30 is present in an alternative conformation, which has been observed in various structures of APT, sometimes within different monomers of one crystal.

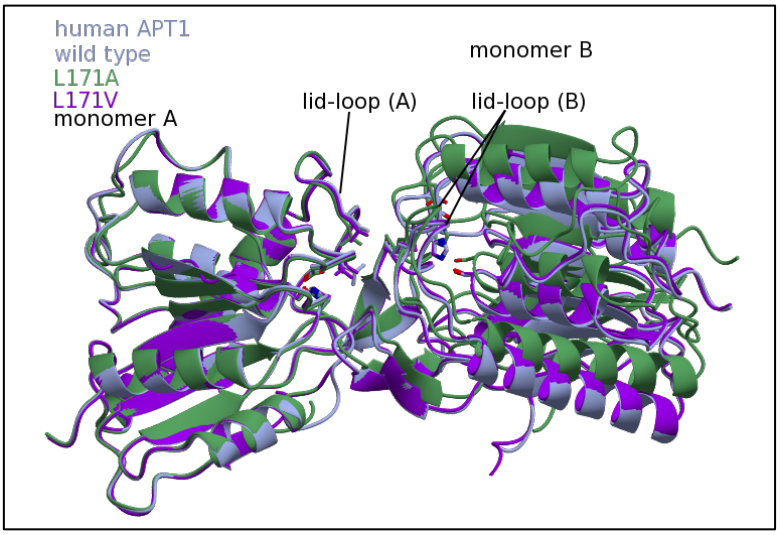

Figure 59: Comparison of human APT L171A (green) and L171V (purple) mutants with the wild type (blue). The typical dimer is formed in the crystals of both mutants, being rotated by 6.3 to 7.1˚ for the L171A mutant, and 1˚ for the L171V mutant.

The relative B-factors can be used as an indicator of flexibility when comparing different parts of a structure. The 1.94 Å resolution structure of human APT1[69] shows average B-factors of 17.6 and 21.4 Å^2 for the Cα atoms of the lid-loops of monomer A and B, respectively, and an overall B-factor of 12.5 Å^2. In the four monomer of human APT1 L171A, the average B-factor of the Cα atoms of the individual lid-loops ranges from 38.8 to 48.3 Å^2, and is not significantly increased compared to the average B-factor of the whole protein (41.2 Å^2). The lid-loops are partially stabilized by neighbor molecules.

The Cαs of the lid-loop in human APT1 L171V have an average B-factor of 13.5 and 17.1 Å^2 in monomer A and B, respectively, which is set in relation to 11.4 Å^2 of the whole protein and comparable to the wild type structure. In the P1 space group, the lid-loop is not obstructed or stabilized by crystal contacts but is exposed to a solvent channel. This means that the lid-loop of the wild type as well as the human APT1 L171V odes not show significant flexibility even if not constrained by a neighboring symmetry related molecule. The lid-loops of both mutants are compared to the wild type in the following Figure 60.

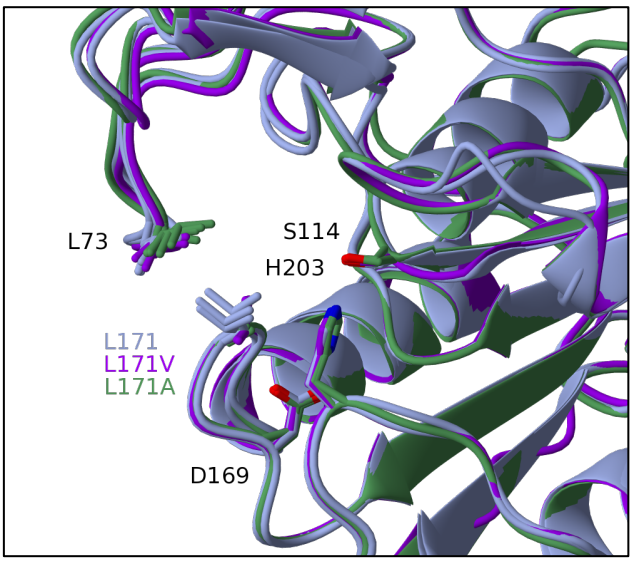

Figure 60: Superimposition of human APT1 wt (blue) with all crystallographically related monomers of the L171A (green) and L171V (purple) mutants. The representation is focused on L171. The conformation of the lid-loop is identical to the wild type, leaving the hydrophobic binding tunnel (perpendicular to the paper plane) unchanged in length and shape.

Taken together, the crystal structures of both mutants show no significant difference in neither the shape of the lid-loop nor tunnel from the wild type, which corresponds to the similar hydrolytic activity for the long-chain PPTS substrate observed in the activity assays. Thus, it looks like there is no significantly stabilizing effect of the L73-L171 hydrophobic interaction on the conformation of the lid-loop.

5.2.3 Crystal structure of human APT1 L58A mutant

L58 is the second leucine located at the protein surface close to L73 of the lid-loop, and is located in the “foot-rest” loop (see Figure 56). An alanine mutant was designed to test for the stabilizing effect of L58 on the lid-loop.

Human APT1 L58A was subjected to screening for crystals as described in Material and Methods. Crystals (Figure 61) were directly isolated from the screening plate, X-ray diffraction data was collected at X10SA at SLS, Switzerland. The crystal belongs to space group C2 and the structure was refined to 2.62 Å resolution as described in Material and Methods. The crystallographic statistics are summarized in Table 9.

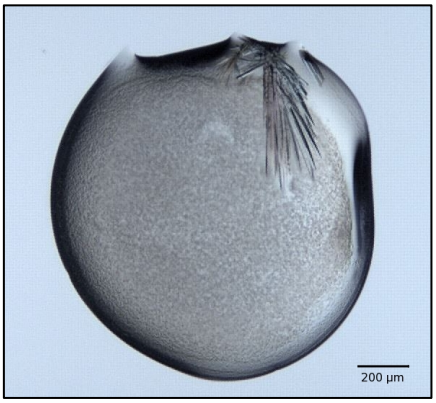

Figure 61: Crystallization drop of human APT1 L58A. Crystals grew within 21 days in condition B11 of Core3 available from Qiagen containing 0.2 M sodium formate and 20% PEG 3350. Photograph taken by Formulatrix Rock Imager.

Table 9: Crystallographic statistics of human APT1 L58A. Values for the highest shell are given in parentheses. Values for Ramachandran plot are given for favoured, allowed and outlier

	human APT1 L58A		
Data collection		Refinement	
Space group	C2	Resolution (Å)	127.58-2.62 (2.69-2.62)
Cell dimensions		Number of Reflexes	364026 (21382)
a, b, c (Å)	181.52, 79.73, 154.94	Rwork	19.8 (50.1)
α, β, γ (°)	90.00, 124.5710, 90.00	Rfree	26.5 (52.4)
Resolution (Å)	50.0-2.62 (2.69-2.62)	Number of Atoms	
Monomers / au	8	Protein	13336
Wave length (Å)	0.99989	Ligand/Ions	37
CC $^1/_2$	99.2 (37.2)	Water	215
I / σ(I)	7.67 (1.24)	B-factor (Å2)	
Completeness (%)	98.1 (83.7)	Protein	67.1 ± 19.0
Redundancy	3.45 (3.22)	Ligands	78.6 ± 7.0
		Solvent	62.6 ± 15.4
		RMSD	
		Bond length (Å)	0.0117
		Bond angle (°)	1.55
		Ramachandran (%)	95.17, 4.60, 0.23
		Clashscore	4.72
		Rotamer outlier (%)	6.63
		Molprobity score	2.20

Similar to the L171 mutants, the L58A mutation does not change of the conformation of the lid-loop or the overall conformation, and the monomers have an rmsd in the range of 0.54 to 0.62 Å^2 over 219 amino acids to human APT1 wild type. The asymmetric unit contains four dimers comparable to the dimer of human APT1 wild type[69]. The second monomer of the dimers is rotated between 5.6 and 7.9° compared to the wild type structure. An analysis of the crystal packing reveals that the lid-loop is stabilized by a neighbor via a salt bridge between the guanidine head of R144 and the carboxylic acid of D76 in monomers B, D, F, and H, while the tip of the lid-loop does not form crystal contacts in monomers A, C, E, and G. Thus, one molecule of each dimer has a lid-loop involved in crystal contacts, and the other has a free lid-loop. This is also reflected in the B-factors of the lid-loops, which are in the range between 48.8 and 71.1 Å^2, but systematically lower for monomer B, D, F, and H (54.2 Å compared to 66.1 Å) which form a salt bridge via D76 of the lid-loop. The overall B-factor is 59.5 Å^2.

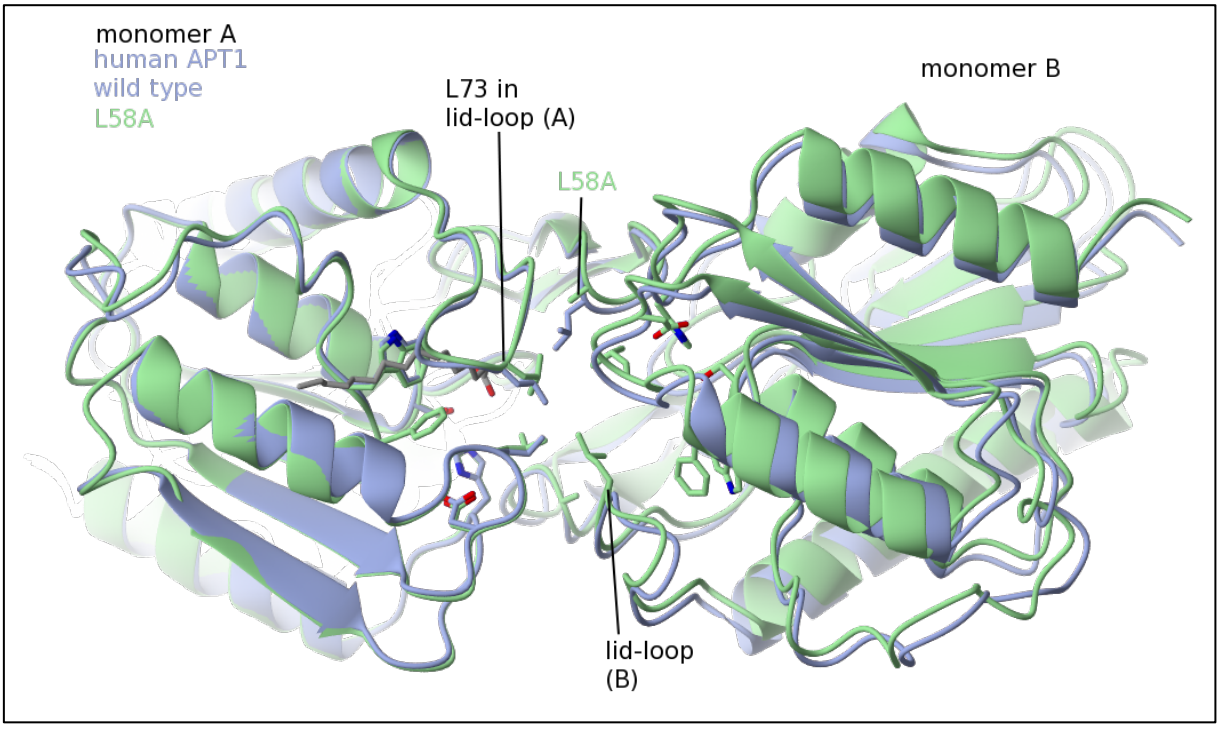

Figure 62: Comparison between human APT1 wild type (blue) and L58A mutant (green), containing eight monomers per asymmetric unit that form four dimers. The monomers are highly similar to the wild type with an rmsd of 0.54 to 0.62 Å over 219 amino acids, and no conformational change of the lid-loop is observed. The dimers are rotated by 5.6 to 7.9° compared to the wild type.

Interestingly, the monomers A, C, E, and G (with the free lid-loop) show a linear electron density inside the tunnel, while the other monomers contain only water molecules. Here, the side chain of F176 is rotated into the tunnel, a conformation only possible in absence of a tunnel-binding ligand. The linear density is not well defined at both ends, but a palmitate molecule fits into the density without causing negative difference electron density to appear. Thus the density could be a co-purified fatty acid. A PEG molecule is unlikely, as despite the presence of PEG is most crystallization conditions of human APT1, no PEG molecule was observed to bind inside the tunnel. Each palmitate-bound monomer forms a dimer with an empty monomer. The lid-loop of the palmitate - containing monomers is slightly opened by about 1 Å to accommodate the ligand inside the tunnel. This has also been observed for the wild type in complex with 2BP (compare Figure 48), and was discussed in Chapter 5.1.5 for the structure of human APT1 in complex with 2BP. However, the L58A mutation allows the small “foot-rest” loop containing L58 to move away from the lid-loop (Figure 63), the Cα of L58A is dislocated by 1.0 to 1.5 Å compared to the wild type. The conformation of this loop also differs in both apo form structures of human APT1 wild type([69], and PDB ID 1fj2), which differ in space group, dimer formation and crystal packing, and it lokks as if this “foot-rest” loop is flexible enough to adapt (in a certain extend) to its environment.

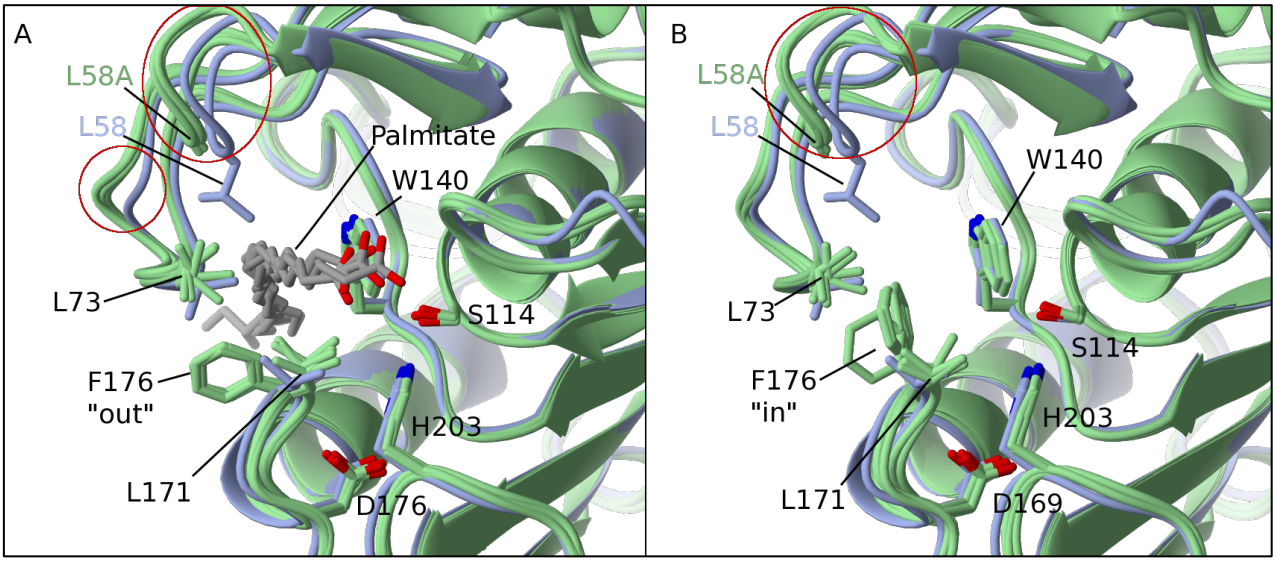

Figure 63: Comparison between the palmitate-bound (A) and empty (B) tunnel of human APT1 L58A (shown in green). In all monomers, the loop containing L58 is moved upwards compared to the wild type (shown in blue). (A): Palmitate bound inside the tunnel corresponds to an opening of the lid-loop by about 1 Å. F176 is shifted out of the lumen of the tunnel. (B): Movement of F176 into the binding tunnel.

Summarized, L58 is not a crucial residue for the conformation of the lid-loop, but instead causes the neighboring “foot-rest’ loop to move away from the lid-loop. Interestingly, the mutant L58A seems to facilitate binding of a ligand inside the tunnel, perhaps allowing an easier opening of the lid-loop due to reduced fixation of the lid-loop by the “foot-rest” loop. Also, crystal packing seems to influence ligand binding, since one monomer of the dimers is empty.

5.2.4 Crystal structure and biochemical activity of human APT1 L73A mutant

The previous chapters showed that mutations of either L58 or L171, the suspected interaction partner of L73, did not alter activity of the biochemical protein or the shape of the binding tunnel. In this chapter, the role of leucine L73, located in the lid-loop and forming the tunnel entrance (Figure 56), is investigated on its biochemical activity using the PPTS activity assay (Chapter 7.5.1), and structurally via x-ray crystallography. In contrast to the L58A and L171A mutants, human APT1 L73A showed a significantly decreased activity compared to the wild type in the PPTS activity assay. V_{max} was decreased to about 30% of the wild type with a k_{cat} of 0.95 ± 0.32 s^{-1}, while K_M is also reduced to 0.94 ± 0.28 µM.

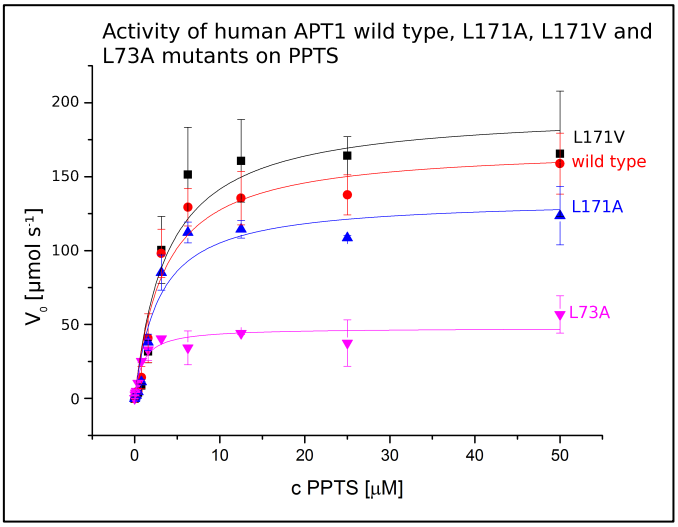

Figure 64: Human APT1 L73A activity on PPTS compared to human APT1 wt, L171A and L171V. The L73A mutation decreases k_{cat} to about 30% compared to human APT1 wild type. The apparent K_M observed in the assay is also decreased, indicating a stronger binding of PPTS to the mutant. Data averaging and error calculation was done using Microsoft Excel, data was plotted and fitted using Origin Pro.

Table 10: Kinetic parameters of human APT1 wild type and L73A mutant on PPTS used as test substrate.

	V_{max} [µmol s^{-1}]	k_{cat} [s^{-1} x10^4]	K_M [µM]	k_{cat} / K_M [μM^{-1} s^{-1} x10^4]
L171V	195 ± 16	3.90 ± 0.32	3.79 ± 1.09	1.03
wild type	170.5 ± 11	3.41 ± 0.22	3.38 ± 0.77	1.01
L171A	135 ± 10	2.70 ± 0.20	2.84 ± 0.77	0.95
L73A	47.5 ± 3	0.95 ± 0.06	0.94 ± 0.28	1.01

Human APT1 L73A was subjected to screening for suitable crystallization conditions as described in Material and Methods. Crystals of satisfying quality (Figure 65) were isolated directly from screening condition and diffraction data was collected at X10SA at SLS, Villigen, (CH). The data was processed and the structure solved via Molecular Replacement using the wild type as template as described in Material and Methods. The crystal belongs to space group $P2_1$ and contains one monomer per asymmetric unit. The final model was refined to a resolution of 1.6 Å with an R_{work} of 19.8% and R_{free} 24.6%. The crystallographic statistics are presented in the following Table 11.

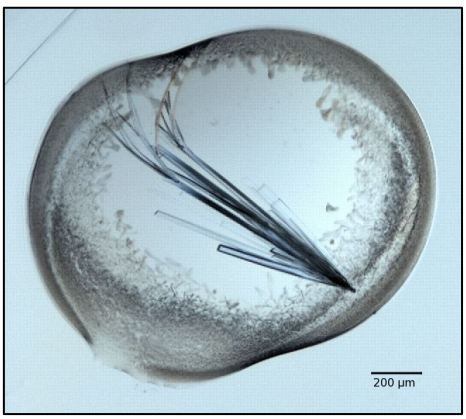

Figure 65: Crystallization drop of human APT1 L73A. Well-diffracting crystals were obtained from screening condition Core1 A2 of Qiagen, containing 0.1 M Bicine, pH 8.5 and 20% PEG 6000. Photograph taken by Formulatrix Rock Imager.

Table 11: Crystallographic statistics of human APT1 L73A. Values for the highest shell are given in parentheses. A molecule of bicine is bound to the protein. Values for Ramachandran plot are given for favoured, allowed and outlier.

	human APT1 L73A		
Data collection		Refinement	
Space group	$P2_1$	Resolution (Å)	47.36 - 1.6 (1.64 - 1.6)
Cell dimensions		Number of Reflexes	166881 (12618)
a, b, c (Å)	35.65 57.41 47.92	Rwork	19.8 (28.5)
α, β, γ (°)	90.00 98.76 90.00	Rfree	24.6 (38.3)
Resolution (Å)	47.36 - 1.60 (1.64 - 1.6)	Number of Atoms	
Monomers / au	1	Protein	1681
Wave length (Å)	0.91639	Ligand/Ions	11
CC $^1/_2$	99.8 (71.7)	Water	212
I / σ(I)	10.77 (1.81)	B-factor (Å2)	
Completeness (%)	99.7 (99.5)	Protein	23.7 ± 7.4
Redundancy	3.37 (3.44)	Ligands	56.7 ± 1.0
		Solvent	38.6 ± 8.4
		RMSD	
		Bond length (Å)	0.0067
		Bond angle (°)	1.32
		Ramachandran (%)	98.22, 1.78, 0.0
		Clashscore	6.74
		Rotamer outlier (%)	2.70
		Molprobity score	1.7

The L73A mutant does not form a dimer under the conditions and belonged to the best-diffracting APT crystals investigated to date. A comparison of the structure of human APT1 wild type and the L73A mutant shows that the overall structure is unchanged with an rmsd of 0.53 $Å^2$ covering 217 Cα. However, the conformation of the lid-loop is significantly changed compared to the wild type and folded into the tunnel (see Figure 67). As the crystal contacts also differ from the wild type (Figure 66A), it raises the question if the packing influences the lid-loop conformation, or the lid-loop conformation is also altered in solution, and thus enables the altered crystal interface. The tip of the lid-loop forms two salt bridges via the backbone amide of S74 and the side chain of D76 to the side chains of Q207 and Q208 of the neighbor molecule (see Figure 66B), thus the lid-loop conformation could be influenced by the neighbor molecule and be a crystalization artifact. Furthermore, a lid-loop in the wild type conformation would not fit in the L73A crystal and would clash with a neighbor molecule. However, keeping in mind that a comparable conformation of the lid-loop has not been observed in a crystal structure of the wild type of human APT1 before, it is more likely that the L73A mutation causes the lid-loop to fold into the tunnel also in solution, and the changed conformation of the lid-loop allows the altered crystal packing via this new interface (Figure 66A). An analysis of this interface using PISA[97] predicts no complex formation of human APT1 L73A via this interface in solution. The electron density of the lid-loop is well defined, while

some side chains of the preceding “foot-rest” loop containing L58 are less well defined. The average B-factor of the Cα atoms of the lid-loop is higher than the average over all Cα atoms, with 31.6 and 23.2 Å^2, respectively. The slightly increased B-factor of the lid-loop shows that it is probably flexible and not locked in the crystal interface.

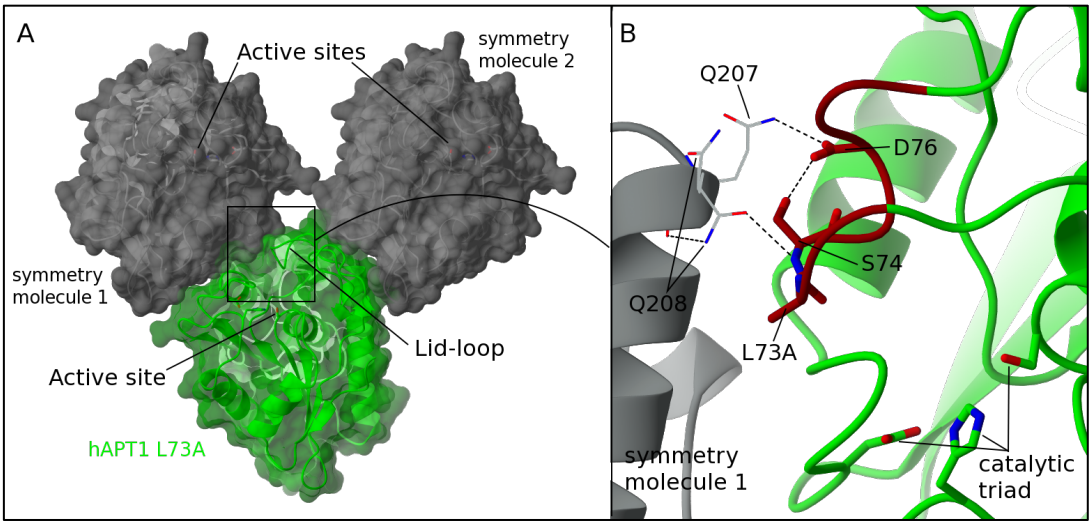

Figure 66: Panel A: Overview of the crystal contacts of human APT1 L73A shown in green. The symmetry mates are presented in grey. The protein dies not form the typical dimer, and the lid-loop is not involved in crystal contacts. Panel B: Detailed view on the two H-bonds formed between the backbone amide of S74 and the carboxyl side chain of D76 of the lid-loop (red) and the side chains of Q207 and Q208 of the crystal neighbor (grey).

The structure shows a significant conformational change of the lid-loop compared to the wild type which has not been observed in any structure of human APT1 so far. P75 of the lid-loop is moved into the hydrophobic tunnel and blocks it, as shown in the superimposition with human APT1 wild type in Figure 67.

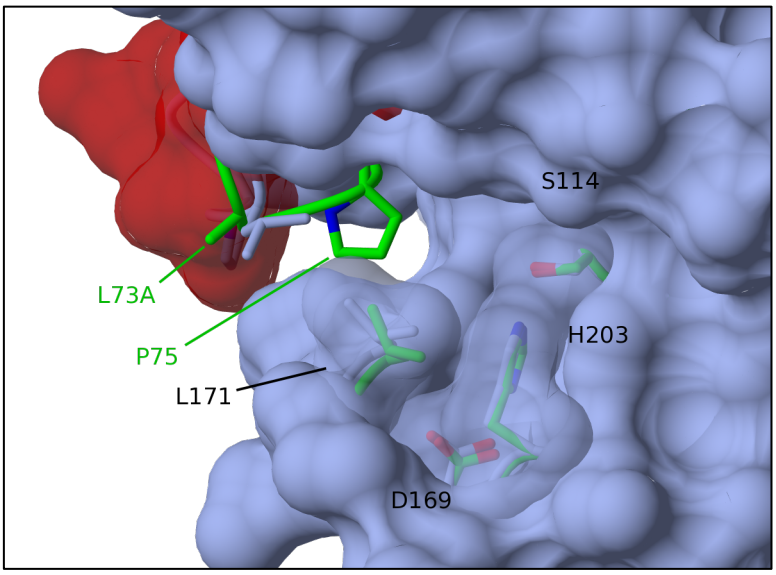

Figure 67: Comparison of human APT1 wt (blue) and human APT1 L73A (lime green). Human APT1 wt is shown as surface representation with the lid-loop colored in red to highlight the wild type shape of the binding tunnel. The mutation causes L73A to rotate and exposes the side chain to the solvent; this enables P75 to move into the tunnel towards the inner wall and obstruct it. The catalytic triad can be seen through the transparent surface.

A comparison of human APT1 wild type and L73A mutant in ribbon representation (Figure 68) highlights the significantly different conformation of the whole lid-loop. The Cα of L73A is moved by 2.5 Å, but the rotation by 45° of the side chain from an inward pointing L73 to outward facing Cβ of

the alanine L73 enables the strong movement of the following amino acids of the lid-loop. The non-polar side chain of P75 is moved in front of W140 inside the hydrophobic tunnel, over a distance of 5.5 Å comparing the Cα of P75 in the L73A mutant and human APT1 wild type. The less well-defined electron density of the turn containing L58, indicating a destabilization of the “foot-rest” lid-loop; it looks like it might have two conformations. This could be caused either by the missing L73 side chain (also the Cα of L58 is less moved than the rest of the “foot-rest” loop), or by the changed conformation of the preceding residues, e.g. the carbonyl of I71 is flipped and thus does not form the H-bond to the backbone amide of L58. The conformation of the “foot-rest” loop differs between L73A mutant and wild type of up to 1 Å distance, observed at the Cα of M60. The amide head group of N61 forms a H-bond to the backbone amide of P6 of the neighbor molecule, due to the crystal packing, and L5 of the symmetry related molecule would come very close to N61, which is rotated away a bit in the structure of the L73A mutant. Thus, the packing of the N-terminus to the “foot-rest” loop would also be a potential reason for the destabilization of this loop, and is likely to be the cause.

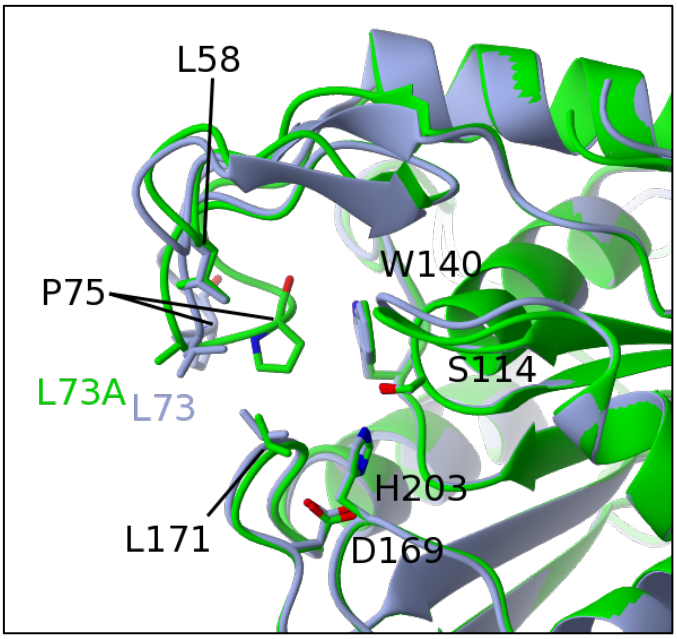

Figure 68: Comparison of human APT1 wild type (blue) and L73A (green). The large movement of P75 in the lid-loop closing the tunnel involves a movement of the whole lid-loop. The Cα of P75 of L73A moves by 5.5 Å compared to the wild type. The L58 containing loop is less well defined, and reliable measurements of the movement are not possible.

Interestingly, one molecule of bicine is bound at the groove close to W32, coordinated by D27, S205, and two water molecules as shown in the following figure, stressing the potential of this groove as a potential secondary binding site, e.g. for the peptide moiety of the natural substrate (palmitoylated proteins).

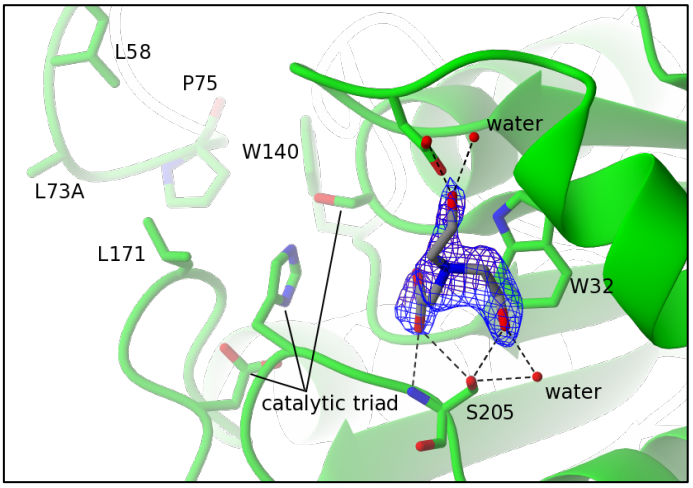

Figure 69: Bicine (grey) from the crystallization buffer binds at the groove on top of W32 next to the active site. Bicine is coordinated by H-bonds to the side chain hydroxyl and backbone amide of S205, the side chain of D27 and two water molecules. Electron density of bicine is contoured to 1 σ.

The collapsed tunnel of human APT1 L73A raised the question if the tunnel can be reformed upon substrate binding or if the tunnel is closed permanently. The reduced but existent biochemical activity (Figure 64) indicates that substrates can bind at least next to the active site, but it was unclear if the tunnel could still accommodate an acyl chain. Therefore, human APT1 L73A was co-crystallized in complex with 2BP and the structure is described in Chapter 5.2.5.

5.2.5 Crystal structure of human APT1 L73A in complex with 2BP

The complex of human APT1 L73A and 2BP was prepared similar to the wild type complex described in Chapter 5.1.5. Briefly, the protein was mixed with a 3-fold molar excess of 2BP and heated to 50 ˚C for 5 to 10 min, and then subjected to co-crystallization and yielded crystals in a few conditions. Interestingly, the best-diffracting crystals grew in a condition that does not contain PEG, unlike most crystallisation conditions of human APT1. Diffraction data was collected at X10SA at SLS at 0.92 Å x-ray wavelength, the adsorption edge of bromide, to obtain an anomalous signal to support fitting of 2BP into the electron density. The structure belongs to space group $P2_12_12_1$ and was solved via Molecular Replacement using human APT1 wild type as template and refined to 1.85 Å as described in Material and Methods. The crystallographic statistics are summarized in Table 12.

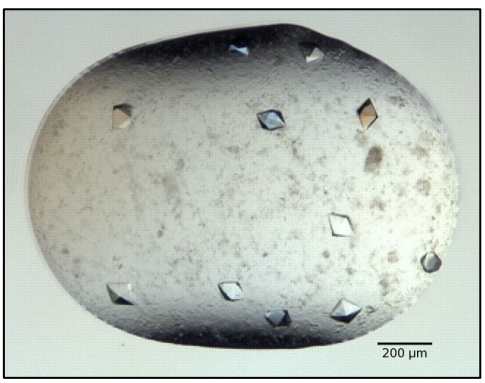

Figure 70: Crystallization condition of human APT1 L73A in complex with 2BP. The best-diffracting crystals grew in condition Core4 G5, containing 0.1 M MES pH 5.0 (final pH 6.0) and 1.6 M $(NH_4)_2SO_4$. withing 2 days. Human APT1 L73A was preincubated with 2BP (5 mM) for 5 to 10 min at 50 ˚C, as described in Chapter 5.1.5. Photograph taken by Formulatrix Rock Imager.

Table 12: Crystallographic statistics of human APT1 L73A in complex with 2BP. Values for the highest shell are given in parentheses. Besides the four molecules of 2BP bound inside the tunnel, two sulfates ions are observed within the asymmetric unit. Values for Ramachandran plot are given for favoured, allowed and outlier.

	human APT1 L73A + 2BP		
Data collection		Refinement	
Space group	$P2_12_12_1$	Resolution (Å)	49.09 – 1.85 (1.90 - 1.85)
Cell dimensions		Number of Reflexes	1011337 (76477)
a, b, c (Å)	73.97, 109.70, 109.79	Rwork	27.45 (37.7)
α, β, γ (°)	90.0, 90.0, 90.0	Rfree	32.65 (44.7)
Resolution (Å)	49.09 – 1.85 (1.90 - 1.85)	Number of Atoms	
Monomers / au	4	Protein	6729
Wave length (Å)	0.92018	Ligand/Ions	86
CC $^1/_2$	99.7 (69.0)	Water	481
I / σ(I)	10.89 (2.20)	B-factor (Å2)	
Completeness (%)	100 (100)	Protein	33.9 ± 10.9
Redundancy	6.86 (6.98)	Ligands	58.1 ± 18.9
		Solvent	36.0 ± 8.4
		RMSD	
		Bond length (Å)	0.0130
		Bond angle (°)	1.66
		Ramachandran (%)	97.20, 2.46, 0.34
		Clashscore	12.39
		Rotamer outlier	4.37
		Molprobity score	2.24

The human APT1 L73A - 2BP complex crystallizes in a different space group and unit cell than the L73A apo protein. The asymmetric unit of the complex contains four monomers that do not form the typical dimer of human APT1 wild type[69], but a dimer rotated by 113°, but similar (1.8° rotated) to the dimer observed in the published structure (PDB ID 1fj2, [58]). The lid-loop is located next to a solvent channel, but is partially stabilized by crystal contacts, forming a H-bond between D76 of the lid-loop, and R40 of symmetry mates (see Figure 71). The average B-factor of the Cα in the four lid-loops is 41.7 Å and in the range of the average B-factor of 34.4 Å^2 of all Cαs atom in the protein. This indicates a stabilization of the lid-loop both by 2BP and/or crystal contacts.

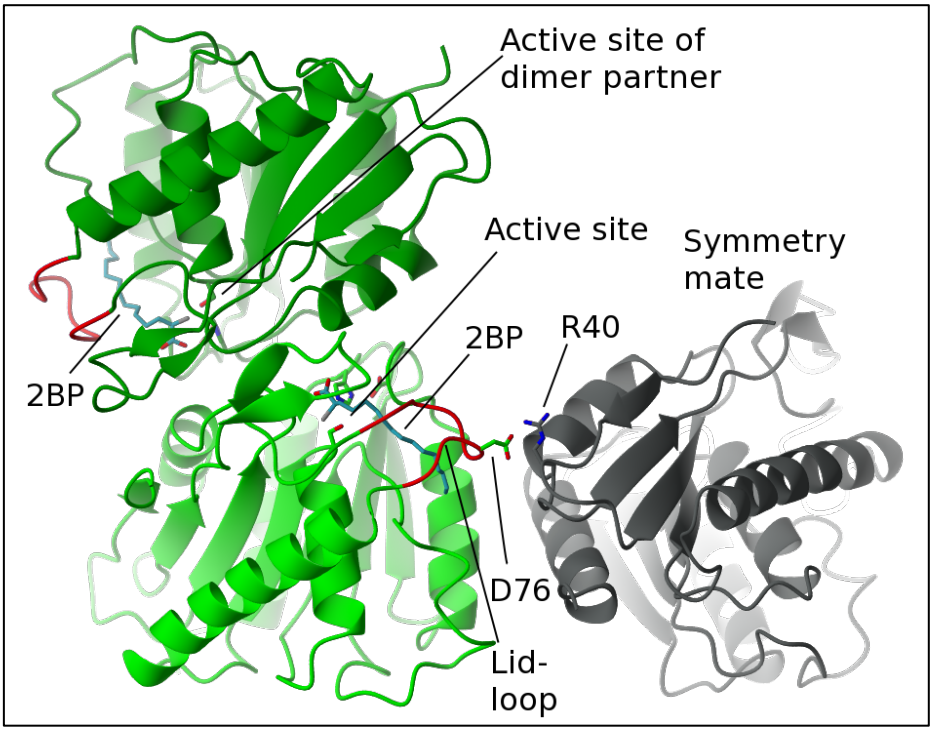

Figure 71: Crystal contacts of human APT1 L73A in complex with 2BP.The dimer molecules (as observed in PDB ID 1fj2, [58]) are presented in green. The lid-loop (red) is not part of the dimer interface, but stabilized via a salt bridge formed by D76 to R40 of a symmetry mate (grey). 2BP (cyan) bound inside the hydrophobic tunnel.

The electron density shows an well-defined elongated electron density inside the binding tunnel. However, it lacks the typical bifurcated head group of 2BP next to the active site. Electron density continues into the tunnel in varying intensity in all four monomers. The linear density could fit to long-chained PEG, but PEG has not been observed bound inside the tunnel in any structure of human APT1 so far, nor is it present in the screening condition, assuming no contamination. More liekly is a co-purified fatty acid, as observed in *X. tropicalis* APT1 [69].

In order to support positioning of 2BP in the structure, an anomalous map corresponding to . However, no significant anomalous signal of bromide could be detected in the whole asymmetric unit, either indicating a disordered binding of 2BP in human APT1 L73A, or the presence of a co-purified molecule, e.g. a fatty acid. The elongated density in the tunnel could also indicate a sliding motion of 2BP with the head group not exclusively bound directly next to the active site. This would also explain the absence of an anomalous signal for bromide. Interestingly, the complex was crystallized at pH 5.0; the pH being lower than for complexes of human APT1 wild type with 2BP, which was observed to crystallize in complex with 2BP at pH 6.5 to 8.5 (see Chapter 5.1.5). For comparison, 2BP was fitted in a orientation related to the major conformation of wild type complex (see Figure 49).

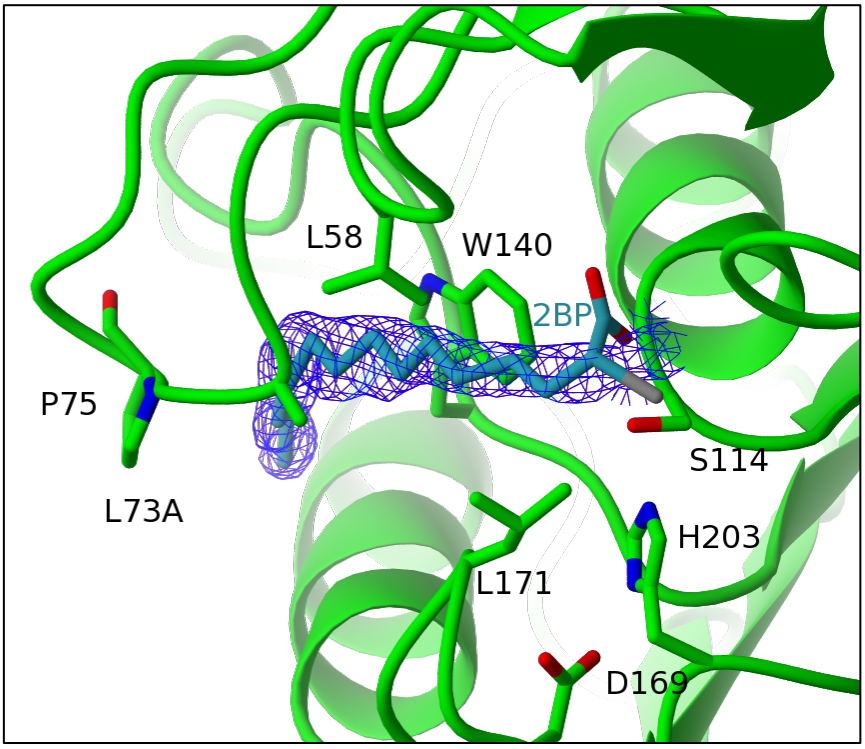

Figure 72: Electron density of the unknown ligand in the hydrophobic binding tunnel. The 2Fo-Fc density is long and linear, but lacks a clear furcation at the head group of 2BP. Moreover, no anomalous signal of bromide could be detected. 2BP (cyan) was fitted for refinement, but the head group does not fit into the density. This might be caused by undefined binding with multiple conformations, e.g. sliding motions of 2BP within the tunnel.

A comparison of hte human APT1 L73A + 2BP complex with the published apo form structure of human APT1 (PDB ID 1fj2, [58]), that both form similar dimers, again shows a different conformation of the “foot-rest” loop shifted towards L73A, and indicates that this is potentially caused by the shortened side chain. A comparison of the 2BP complexes of human APT1 L73A mutant and the wild type is shown in Figure 73, and reveals no significant difference of the backbone of the lid-loop. In the 2BP complex of L73A mutant, the “foot-rest” loop containing L58 is again moved by ~1 Å compared to the apo form of human APT1 wild type[69]. However, movements in this range are also observed for human APT1 wild type apo form and the 2BP complex, and argues against (as mentioned above) that L73A as main cause for the movement of the “foot-rest” loop. The movement of the “foot-rest” loop is more likely due to crystal contacts, but the shortened L73A side chain could facilitate this movement due to a reduced stabilization.

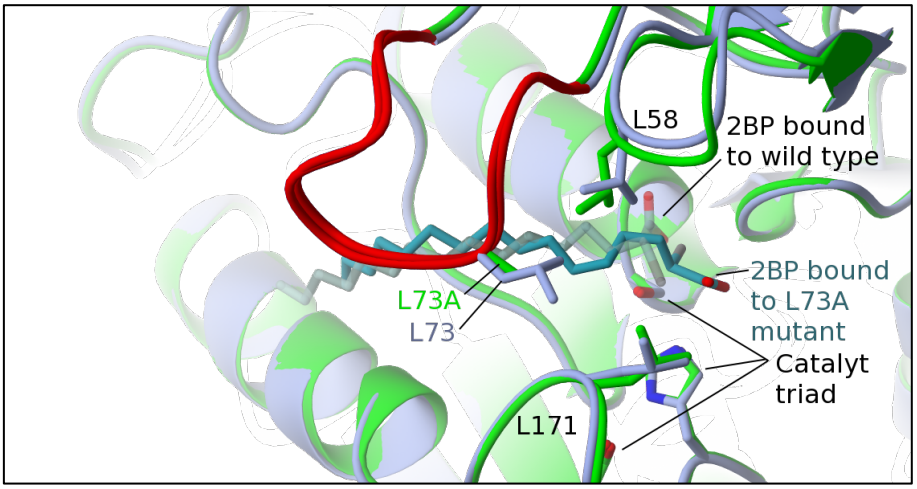

Figure 73: Comparison of the complexes of 2BP with human APT1 L73A and human APT1 wild type (Chapter 5.1.5, Table 5). The conformation of the lid-loop is identical, but the L58 containing loop is moved by 1 Å towards L73A; the shortened side chain enables this movement. In human APT1 wild type, 2BP (cyan, transparent) is bound with the head at the active site. In the L73A mutant, 2BP (cyan, solid) most likely can slide within the binding tunnel leaving the head group without defined electron density.

The altered side chain in the L73A mutant leaves a small gap between L171 and L58, as highlighted in the surface representation in Figure 74. This gap supports the movement of L58 mentioned before, and is partially filled by its side chain. Comparing the position of 2BP in the human APT1 wild type and L73A complex reveals differences. Bound 2BP could either be pushed out of the active site by the movement of L58, but could also slide its head into the gap. The binding in multiple orientations can result in a less defined electron density and also explain the lack of a strong anomalous signal for bromine.

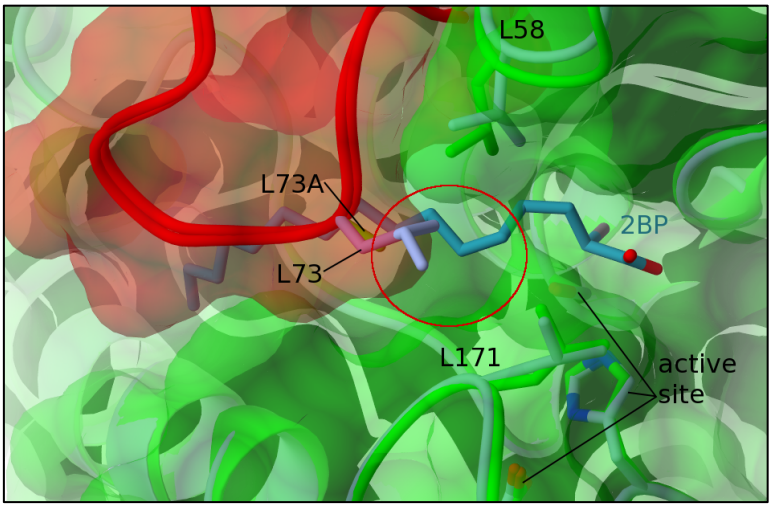

Figure 74: Human APT1 L73A mutation (surface representation) causes a small gap (encircled in red) between L171 and L58. This gap is partially filled by the movement of L58 towards the lid-loop. The head group of 2BP could be moved away from the active site by the movement of L58, but could also remain in the gap between L58 and L171, thus explaining the ambiguous electron density.

Taken together, L73, located in the lid-loop with its side chain between L58 and L171, is an amino acid relevant for the formation of the tunnel. The lid-loop of the apo form of the L73A mutant folds back into the tunnel and thus collapses the hydrophobic tunnel in absence of ligands, indicating the importance of the L73 side chain as structural anchor of the lid-loop. The biochemical activity of human APT1 L73A is reduced to 30%. However, the structure of the complex with 2BP proves the lid-loops ability to bind substrates inside a re-formed binding tunnel.

5.2.6 Crystal structure and biochemical activity of human APT1 LP insertion mutant

The homolog of APT in *A. thaliana* (characterized by Marco Bürger in his thesis [69]) has an extended lid-loop containing a leucin-prolin (LP) insertion between G72 and the above discussed L73, as seen from the sequence alignment shown in Figure 75.

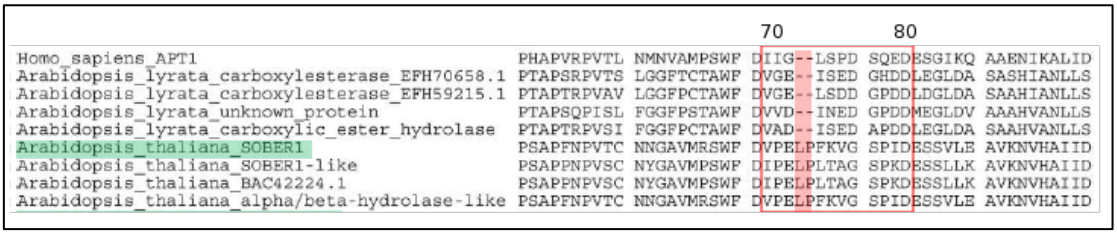

Figure 75: Sequence alignment of human APT1 and the APT1 homolog in *A. thaliana* SOBER1 (name highlighted in green). The lid-loop is within the red square, the LP insert present in SOBER1 is highlighted in red. Taken from [69] (Table 4.15, p.121) and modified using Gimp [4].

The binding tunnel of the APT homolog in *A. thaliana* SOBER1 is closed by the side chains of the leucine of the insertion and a phenylalanine present in the lid-loop, and only very little biochemical activity on PNP-ester substrates longer than propionate was observed[69]. A human APT1 LP insertion mutant was assayed against PPTS as test substrate for hydrolytic activity on long-chained substrates in a detergent-free system. Strikingly, the extended lid-loop mutant show for PPTS as test substrate a k_{kat} reduced to 20% of hAPT wild type, a level roughly comparable to the L73A mutant (see Chapter 5.2.4). Surprisingly, the apparent K_M derived from the activity assay is reduced to 1.72 ± 0.35 µM, approximately 50% of the wild type.

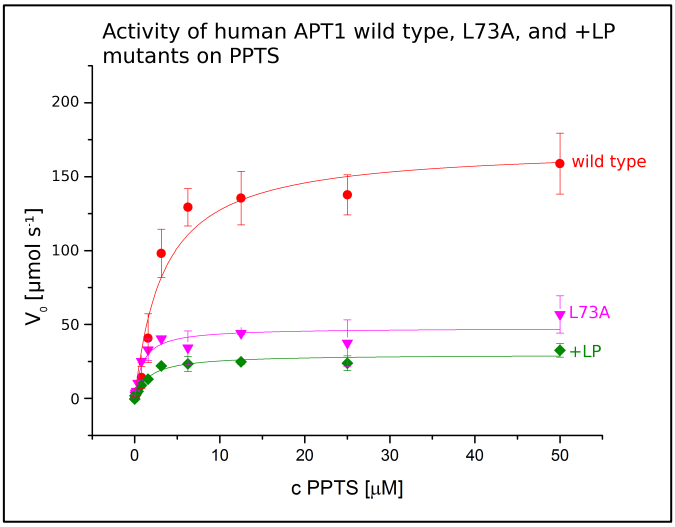

Figure 76: Activity of human APT1 +LP mutant on PPTS. As shown in the graph, its V_{max} is reduced compared to human APT1 wild type and in the range of human APT1 L73A. K_M is not slightly lower than the wild type. Data averaging and error calculation was done with Microsoft Excel, the plot was fitted with Origin.

Table 13: Kinetic parameters of human APT1 wild type, L73A and +LP mutants on PPTS used as test substrate.

	V_{max} [µmol s^{-1}]	k_{cat} [s^{-1} x10^4]	K_M [µM]	k_{cat} / K_M [$µM^{-1}$ s^{-1} x10^4]
wild type	170.5 ± 11	3.41 ± 0.22	3.38 ± 0.77	1.01
L73A	47.5 ± 3	0.95 ± 0.06	0.94 ± 0.28	1.01
+LP	29.5 ± 1.5	0.59 ± 0.03	1.72 ± 0.35	0.34

Screening for crystallization conditions for the human APT1 +LP mutant was performed as described in Material and Methods (Chapter 7.3.2). Crystals were isolated directly from the screening plate. Diffraction data was collected at X10SA at SLS, and processed as described in Material and Methods. The crystal (Figure 77) belongs to space group $P2_1$ with one molecule per asymmetric unit and diffracted to a resolution of 2.0 Å. The structure was solved via Molecular Replacement using human APT1 wild type as template. The crystallographic statistics is presented in Table 14.

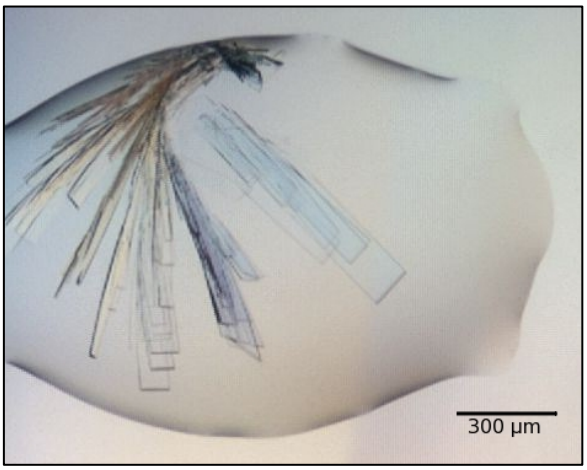

Figure 77: Crystallization drop of human APT1 +LP mutant. Crystals grew within 21 days in condition Core1 C10 containing 0.1M HEPES, pH 6.5 (final pH 7.0) and 20% PEG 6000. Photograph taken using Formulatrix Rock Imager.

Table 14: Crystallographic statistics of human APT1 +LP. Values for the highest shell are given in parentheses. Values for Ramachandran plot are given for favoured, allowed and outlier.

	human APT1 +LP		
Data collection		Refinement	
Space group	$P2_1$	Resolution (Å)	37.71-2.00 (2.05-2.00)
Cell dimensions		Number of Reflexes	46843 (3390)
a, b, c (Å)	36.37 59.44 49.55	Rwork	18.1 (27.6)
α, β, γ (°)	90.0 100.03 90.0	Rfree	21.1 (31.6)
Resolution (Å)	37.7 - 2.0 (2.05 - 2.00)	Number of Atoms	
Monomers / au	1	Protein	1685
Wave length (Å)	0.97962	Ligand/Ions	0
CC $^1/_2$	99.9 (78.8)	Water	78
I / σ(I)	18.91 (1.97)	B-factor (Å2)	
Completeness (%)	99.5 (99.2)	Protein	45.1 ± 13.1
Redundancy	3.3 (3.3)	Ligands	-
		Solvent	54.5 ± 11.4
		RMSD	
		Bond length (Å)	0.0071
		Bond angle (°)	1.23
		Ramachandran (%)	98.20, 1.80, 0.0
		Clashscore	4.71
		Rotamer outlier (%)	1.09
		Molprobity score	1.27

Interestingly, the +LP mutation crystallizes in the same space group and roughly comparable crystal packing as the L73A mutation (see Figure 78). The protein does not form the human APT1 wild type dimer, and wild type of human APT1 cannot form this crystal interface, as the lid-loop would clash with its neighbor. Residues P74 to D77 of the extended lid-loop of human APT1 +LP are at the interface to the symmetry molecule, the backbone amide of D78 (D76 in wild type) forms an H bond to the side chain of Q210 (Q208 in wild type) of the neighbor, and P77 (P75 in wild type) is largely buried in the interface. This raises the question if the crystal contact forces the lid-loop into the observed conformation and thus the observed lid-loop conformation is a crystallization artifact, or if the lid-loop pre-forms this conformation in solution and thus enables the altered crystal interfaces. An analysis of this interface using PISA[97] predicts no quaternary complex formation of human APT1 +LP in solution (see Chapter 5.4). The increased average B-factor of the Cα atoms of the lid-loop (67.9 Å^2, compared to the average overall Cα atom B-factor of 43.7 Å^2) indicates that the lid-loop is not fixed in the interface. Thus, it can be assumed that the lid-loop forms this conformation in solution.

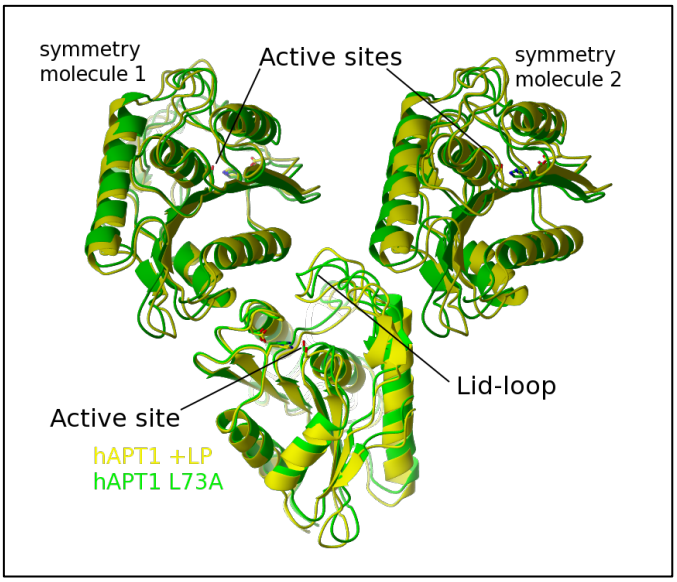

Figure 78: Comparison of the interfaces of human APT1 +LP (yellow) and L73A (green). Both mutants belong to the same space group and have comparable packing, probably as the lid-loop of both mutants is folded into the tunnel. Human APT1 +LP mutant crystallized with a different unit cell (approx. 2 Å difference on all axes, compare Table 11 and Table 14).

In Figure 79, the structure of the human APT1 +LP mutant is compared to human APT1 wild type. The comparison revealed that the binding tunnel is blocked by the inserted L73 and L75 (L73 in wild type, see sequence alignment in Figure 75) in this crystal structure of the mutant. The wild type tunnel entrance is closed by with the side chain of L73, and L75 is located in front of W140, which marks the middle of the human APT1 wild type tunnel. Similar to the human APT1 L73A mutant, the human APT1 +LP mutant does not pre-form an accessible hydrophobic tunnel, and binding of long-chain substrates would require a rearrangement of the lid-loop. However, the remaining biochemical activity (at the level of only 20% of the wild type) observed in the PPTS activity assay indicates that a reformation of the tunnel is possible, similar to human APT1 L73A mutant (see Chapter 5.2.4 and 5.2.5). Thus, the LP insertion alone is not sufficient to abolish biochemical

activity and the further differences in the sequence of the lid-loop of SOBER1 (see Figure 75) might be responsible for the abolished biochemical activity of SOBER1 on long chain substrates.

The side chain of L58 is rotated compared to the apo form of human APT1 wild type, as its wild type conformation would clash with the G72 of the extended lid-loop. The overall conformation of the “foot-rest” loop is not affected.

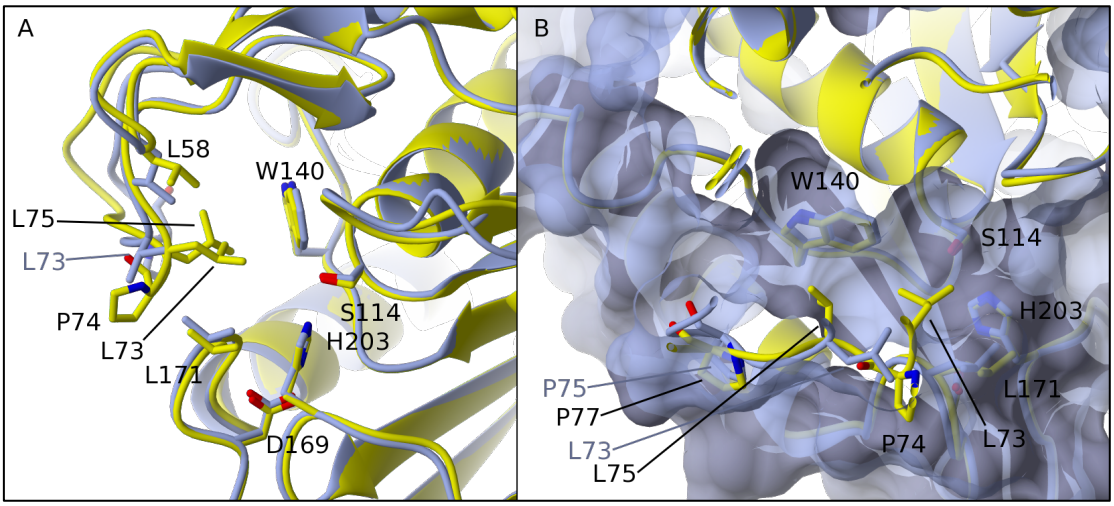

Figure 79: Superimposition of human APT1 wild type (blue) and human APT1 +LP mutant (yellow). A: The view through the binding tunnel reveals its blockage by L73 and L75 of the extended lid-loop. L75 is located close to W140 in the middle of the tunnel, while the inserted L73 blocks the tunnel entrance directly at the active site serine. B: View rotated by 90° and cut through the surface, L73 and L75 are visible blocking the entrance next to S114 and middle part at W140 of the tunnel, respectively. Amino acids not forming the lid-loop are numbered according to the wild type; the wild type lid-loop is labeled in blue.

Albeit the mutations are of different nature, the lid-loop is folded into the tunnel in both human APT1 +LP and L73A mutants. This is probably caused by the missing stabilizing effect of the side chain of L73: in the extended lid-loop of the +LP mutant, the side chain is dislocated from its wild type position, while the side chain is lacking in the L73A mutant. In Figure 80, both structures are compared. While in the human APT1 +LP mutant, the side chains of the inserted L73 and L75 block the complete tunnel beginning from the entrance, the tunnel of the human APT1 L73A mutant is blocked by P75 in front of W140, which marks the middle of the wild type tunnel.

The different shape of the entrance to the blocked tunnel also influences the side chain of L58, which is rotated in the +LP mutant due to the extended lid-loop as the conformation of L73A would clash.

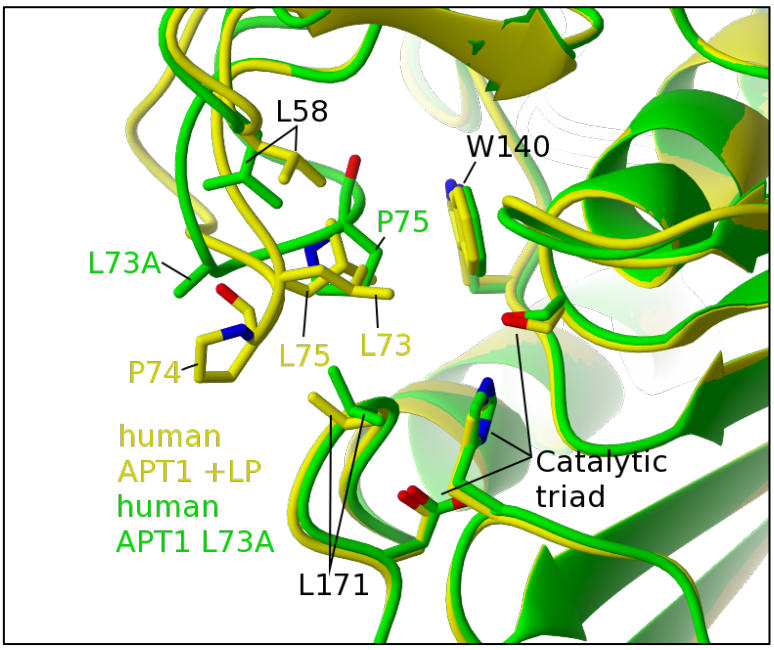

Figure 80: Comparison of the lid-loop of human APT1 +LP (yellow) and L73A (green). Both mutations remove the stabilizing effect via the side chain of L73, and thus the lid-loop is folded into the tunnel. In human APT1 +LP, the tunnel is blocked by the side chains of the inserted L73 at the entrance and L75 in the middle of the wild type tunnel, marked by W140. In human APT1 L73A, the stump of L73A is rotated outwards, thus enabling P75 to move into the middle of the tunnel.

Attempts to co-crystallize the +LP mutant with 2BP resulted in a few conditions with small crystals, but no diffraction data of reasonable quality could be collected from these crystals, therefore no complex structure of this mutant with 2BP is available.

In conclusion, the fact that both the human APT1 L73A and the +LP mutants show the lid-loop collapsed into the tunnel suggest that removal or shifting the L73 side chain eliminates the interactions that are most important for stabilization of the open tunnel.

5.2.7 Biochemical activity of lid-loop truncation mutants ΔL73S74 and ΔS74P75 of human APT1

The investigation of the influence of the length of the lid-loop on tunnel shape and activity of APT included deletion mutants of the lid-loop. Three versions of lid-loop mutants lacking two amino acids each were prepared, and two of these mutants with a shortened lid-loop, human APT1 ΔL73+S74 or ΔS74+P75, could be crystallized (see the following Chapter 5.2.8 and 5.2.10) and subsequently were tested on their biochemical activity on PPTS. Both mutants behave similarly in the biochemical assay and have a reduced k_{cat} on PPTS to about 20 to 25% compared to the wild type, which is in the range of the previously described human APT1 L73A and human APT1 +LP (see Chapter 5.2.6). The apparent K_M of both mutants is again reduced compared to the wild type.

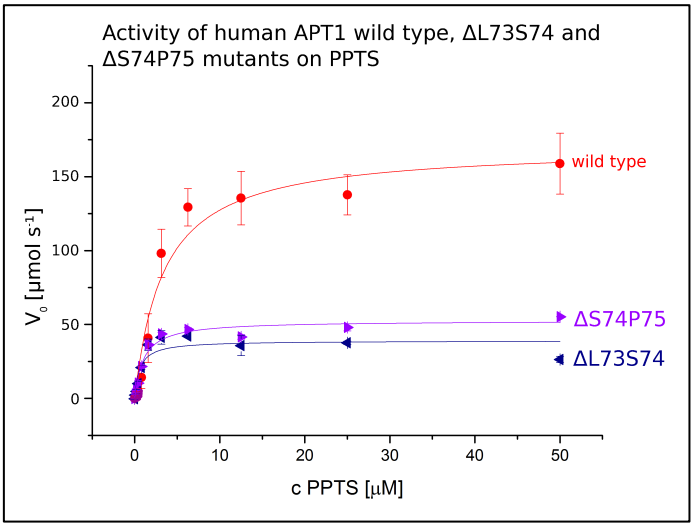

Figure 81: Lid-loop deletion mutants compared to human APT1 wild type activity on PPTS. Both human APT1 ΔL73S74 and ΔS74P75 mutants show a k_{cat} reduced to about 25% of the wild type. Data averaging and error calculation was done with Microsoft Excel, the plot was fitted with Origin.

Table 15: Kinetic parameters of human APT1 wild type, ΔL73S74 and ΔS74P75 mutants on PPTS used as test substrate.

	V_{max} [µmol s^{-1}]	k_{cat} [s^{-1} x10^{4}]	K_M [µM]	k_{cat} / K_M [μM^{-1} s^{-1} x10^{4}]
wild type	170.5 ± 11	3.41 ± 0.22	3.38 ± 0.77	1.01
ΔL73S74	39 ± 3.5	0.78 ± 0.07	0.59 ± 0.25	1.32
ΔS74P75	52.5 ± 2.5	1.05 ± 0.05	1.03 ± 0.20	1.02

5.2.8 Crystal structure of human APT1 ΔL73S74

Human APT1 ΔL73S74 was subjected to screening for crystallization conditions, and optimized conditions yielded crystals of high quality belonging to space group C2 (Figure 82). Diffraction data was collected at X10SA at SLS to a resolution of 2.55 Å. The structure was solved by Molecular Replacement using human APT1 wild type as template. The asymmetric unit contains eight monomers. The crystallographic statistics is summarized in Table 16.

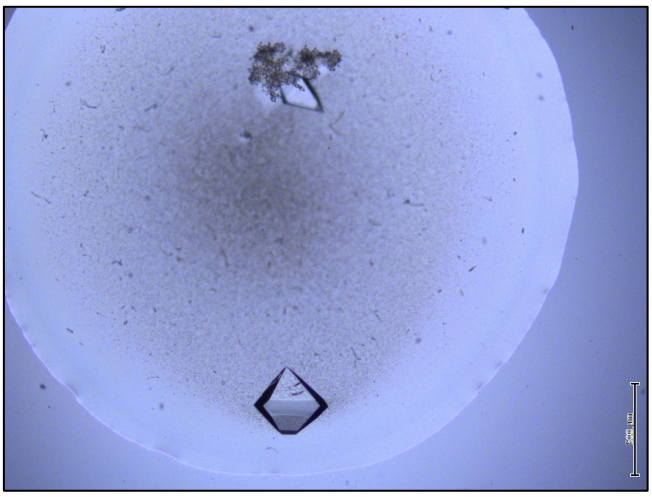

Figure 82: Crystallization drop of human APT1 ΔL73S74. The protein crystallized within 3 days in condition Core1 B12 of Qiagen. Larger and better diffracting crystals were obtained from optimization in a 24-well grid screen in a condition containing 0.1 M KF and 21% PEG 3350. Photograph taken using an Olympus DP21 camera attached to an Olympus CX-60 microscope with a polarization filter.

Table 16: Crystallographic statistics of human APT1 ΔL73S74. Values for the highest shell are given in parentheses. Values for Ramachandran plot are given for favoured, allowed and outlier.

	human APT1 ΔL73S74		
Data collection		Refinement	
Space group	C2	Resolution (Å)	49.09 - 2.55 (2.62 - 2.55)
Cell dimensions		Number of Reflexes	174535 (13357)
a, b, c (Å)	106.57, 105.23, 143.74	Rwork	25.3 (32.7)
α, β, γ (°)	90.0, 92.88, 90.0	Rfree	32.1 (38.3)
Resolution (Å)	49.09 - 2.55 (2.62 - 2.55)	Number of Atoms	
Monomers / au	8	Protein	13360
Wave length (Å)	0.97886	Ligand/Ions	0
CC $^1/_2$	98.2 (41.6)	Waters	79
I / σ(I)	5.96 (2.00)	B-factor (Å2)	
Completeness (%)	96.0 (97.5)	Protein	51.1 ± 20.3
Redundancy	1.79 (1.81)	Ligand	-
		Waters	33.9 ± 8.4
		RMSD	
		Bond length (Å)	0.0125
		Bond angle (°)	1.54
		Ramachandran (%)	95.29 / 3.63 / 1.08
		Clashscore	8.18
		Rotamer outlier (%)	3.15
		Molprobity score	2.19

The asymmetric unit contains eight monomers that are arranged in four dimers, which are rotated about 9˚ - 11˚ compared to the typical human APT1 wild type dimer[69]. Despite the shortened lid-loop, the mutation does not significantly alter the dimer type formed under this crystallization condition. The overall structure of human APT1 ΔL73S74 mutant is similar to the wild type, as indicated by the average rmsd of 0.65 Å over 217 Cα. The crystal structure reveals that the shortened lid-loop still pre-forms an accessible hydrophobic tunnel in all eight monomers (see Figure 83). This could be influenced by the dimer, which is predicted (using PISA[97]) to be stable in solution. The shape of the tunnel entrance at the active site is changed due to the shortened lid-loop that leaves a gap between L58 and L171 due to the deletion of L73. A comparison of the surfaces of human APT1 wild type and ΔL73S74 is given in Figure 83.

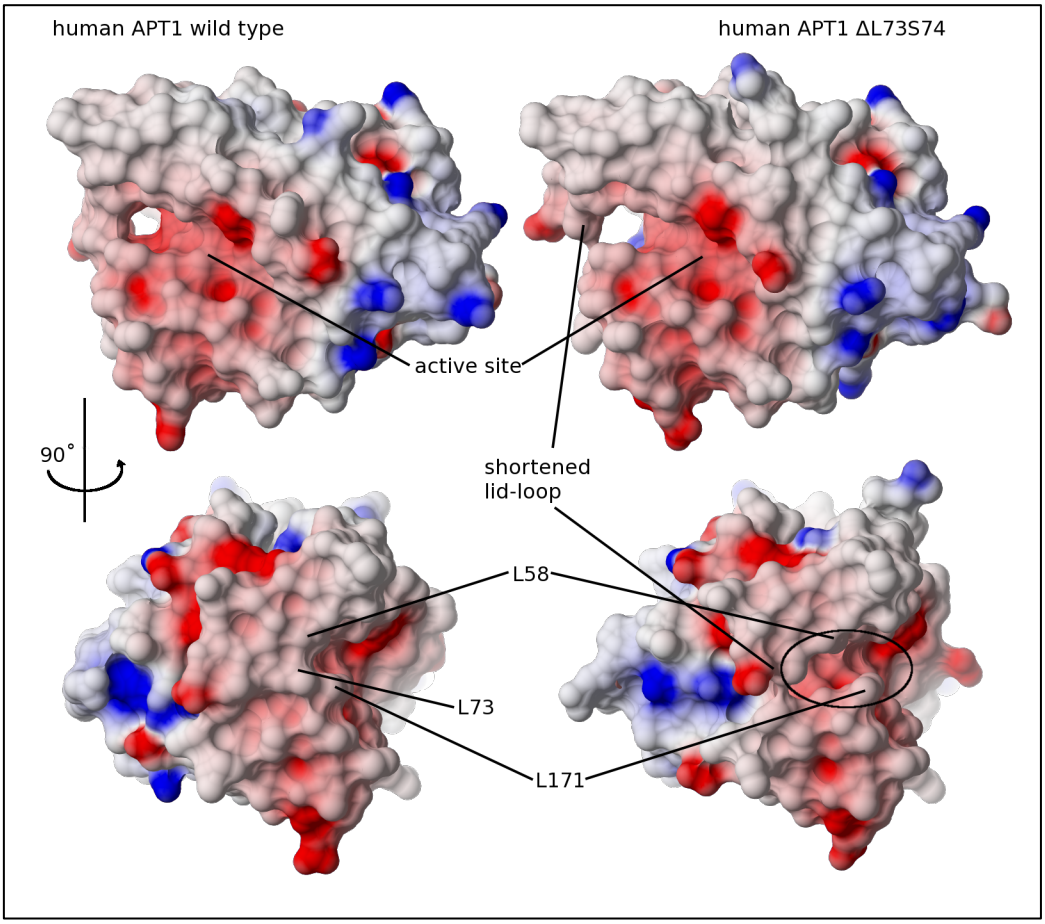

Figure 83: Comparison of human APT1 wild type with human APT1 ΔL73S74. Both proteins form a comparable dimer in the crystal, despite the shortened lid-loop. The shortened lid-loop changes the tunnel entrance and length, leaving a gap (encircled) between L171 and L58.

The shortened lid-loop pre-forms a binding shorter tunnel of a diameter comparable to the wild type. The high number of eight molecules in the asymmetric unit further allows a statistical analysis on the conformation of the lid-loop. Structure refinement omitting NCS restraints resulted in a better structure model as indicated by the lower R_{free}, indicating that the conformation of the lid-loop slightly varies between the eight monomers. The differences within the monomers of human APT1 ΔL73S74 could be due to varying contacts to neighboring molecules. The superimposition of all eight monomers of human APT1 ΔL73S74 (salmon) with the apo-form of human APT1 wild type (blue) is shown in Figure 84. The lid-loop is stabilized by crystal contacts, partially by van-der-Waals interactions within the dimer (I71-M200, P73-P168) and by neighbor molecules via a salt bridge formed between D74 and either K45 of the neighbor, or by an H-bond network with the backbone of different amino acids of the N-terminus. However, the B-factors of the lid-loops varies strongly, with monomer A having a B-factor of 39.0 $Å^2$ lower than the average B-factor of 48.5 $Å^2$ of all Cα in the eight monomers, while monomer B, C, and D have B-factors of 50.0, 47.3, 45.8 $Å^2$ that are in the range of the overall average B-factor. The lid-loops of the remaining four monomers have an increased B-factor of 62.2 to 72.1 $Å^2$. No correlation between an increased B-factor and the interaction of the lid-loop by the described salt bridge or H-bonds to the N-terminus of neighbor molecules is observed.

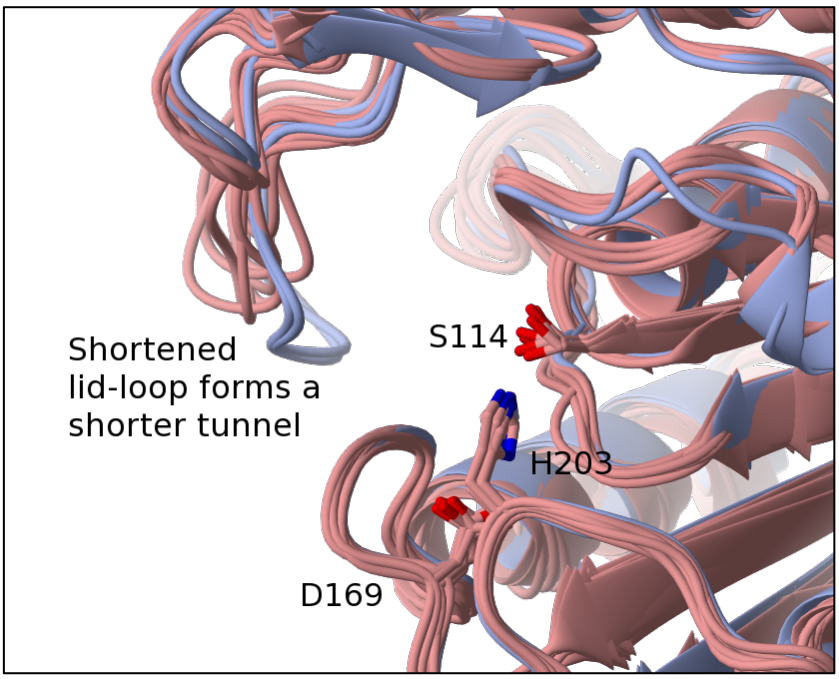

Figure 84: Comparison of the lid-loop conformation of human APT1ΔL73S74 (salmon) and wild type (blue). The shortened lid-loop pre-forms a hydrophobic tunnel in all eight monomer.

The structure of the lid-loop in the shortened mutant differs significantly from the wild type. In the wild type of human APT1, the side chain of L73 forms the tunnel entrance, and S74 and P75 the tip of the lid-loop. In the shortened lid-loop of the ΔL73S74 mutant, the deletion of L73 and S74 results in a shift of the Cα of P73 by 5.0 to 7.5 Å (varying between the individual monomers) towards the position of L73 in the apo-form of human APT1 wild type (see Figure 85). Thus, in the ΔL73S74 mutant, P73 forms the tunnel entrance.

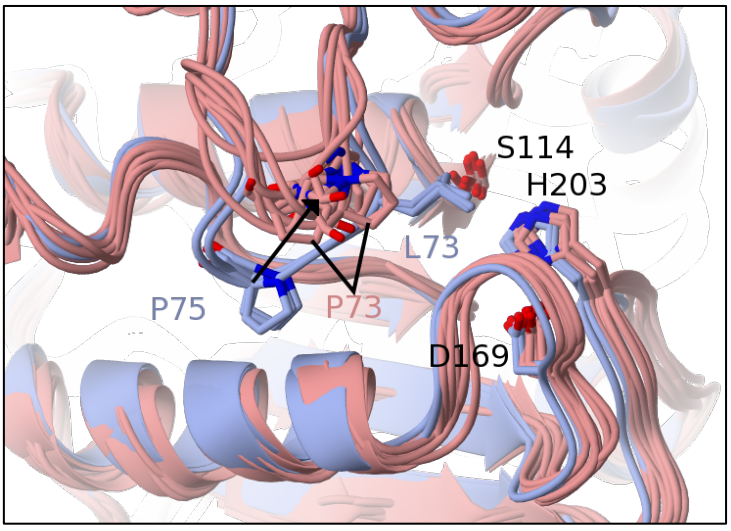

Figure 85: Side view of the binding tunnel in human APT1 ΔL73S74 (salmon) with human APT1 wild type (blue) as reference. P73 moves to the position of L73 of human APT1 wild type. The detailed structure of the lid-loop varies between the different monomers of the ΔL73S74 mutant.

The eight molecules in the asymmetric unit are sufficient for a statistical analysis of side chain conformation. R144 and F176 are located at the end of the binding tunnel. To enable binding of long-chained ligands reaching to the exit of the tunnel, both side chains have to be rotated outside of the tunnel, as it is the case in e.g. the complex of human APT1 wild type with 2BP (Figure 86B) or human APT1 L58A (Figure 63). In the absence of any ligand bound inside the tunnel, both amino

acids can move into the binding tunnel, but as observed in this crystal, not necessarily do so. Figure 86A illustrates the four possible combinations of either both side chains inside the tunnel, or one side chain inside and the other side chain rotated out of the tunnel, or both side chains rotated out of the binding tunnel and leaving it solvent occupied. The observation of these multiple conformations within one crystal shows that these conformations are energetically equivalent or determined by minor details of the crystal packing environment.

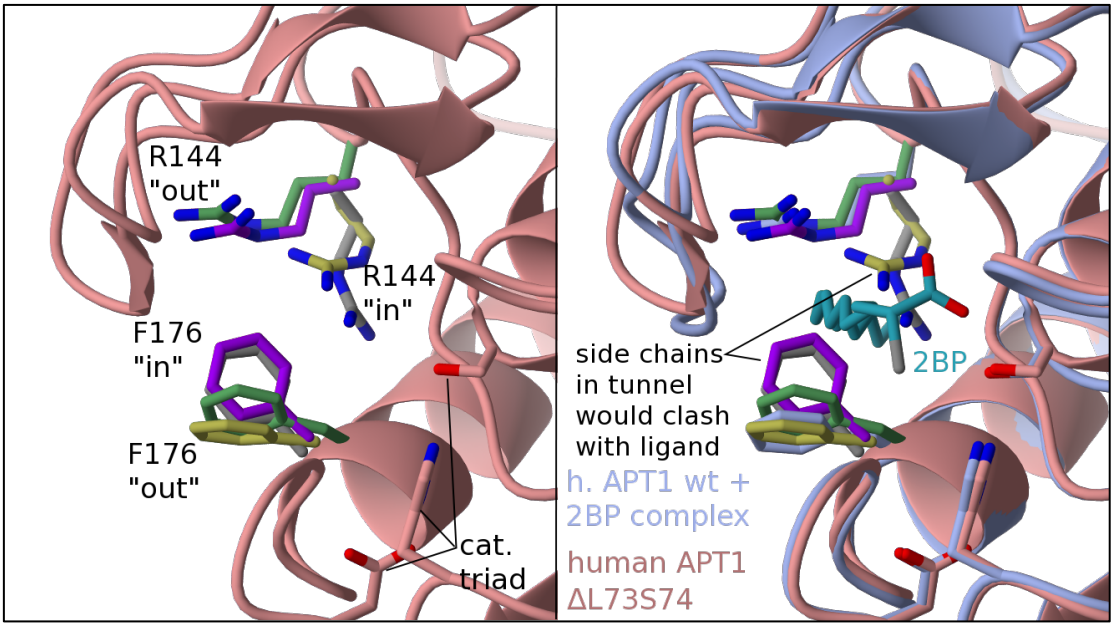

Figure 86: Panel A: View on human APT1 ΔL73S74 with focus on R144 and F176, located at the end of the hydrophobic binding tunnel. A superimposition of the eight monomers present in the asymmetric unit reveals that all four possible combinations of side chain conformations are present within one crystal: both R142 and F174 together (grey, monomer H) are located inside the tunnel, either R144 (yellow, monomer B) or F176 (purple, monomer D) are separately rotated into the tunnel, or the tunnel is free (green, monomer A). Panel B: Comparison with human APT1 wild type in complex with 2BP (cyan), which illustrates the clash of 2BP with side chains rotated into the tunnel.

The apo structure of human APT1 ΔL73S74 shows that the shortened lid-loop still pre-forms a hydrophobic tunnel. The tunnel entrance is significantly changed, which could be the reason for the reduced biochemical activity. Interestingly, the dimer formation in the crystal is not significantly affected as the dimer is rotated by about 10˚ compared to the apo form of human APT1 wild type. The effect of the shortened lid-loop on ligand binding was investigated by co-crystallization of a complex with 2BP described in Chapter 5.2.9.

5.2.9 Crystal structure of human APT1 ΔL73S74 in complex with 2BP

The complex of human APT1 ΔL73S74 and 2BP was prepared similar to the human APT1 wild type 2BP complex described in Chapter 5.1.5 and subjected to screening for crystallization conditions as described in Material and Methods. In the case of the human APT1 ΔL73S74 2BP complex, a mixture containing 1.5 mM of protein and 5 mM of 2BP was incubated for 10 min at 45˚C before crystal setup. Crystals of satisfying size and quality (Figure 87) were isolated directly from the screening plate. Diffraction data was collected at X10SA at SLS using monochromatic x-rays of 0.9188 Å wavelength to obtain an anomalous data for bromine present in the inhibitor 2BP. The crystal belonged to space group C2 and diffracted to 1.62 Å. Diffraction data was processed as

described in Material and Methods. The structure was solved via Molecular Replacement using the apo form of human APT1 ΔL73S74 as search model. The crystallographic statistics are presented in Table 17.

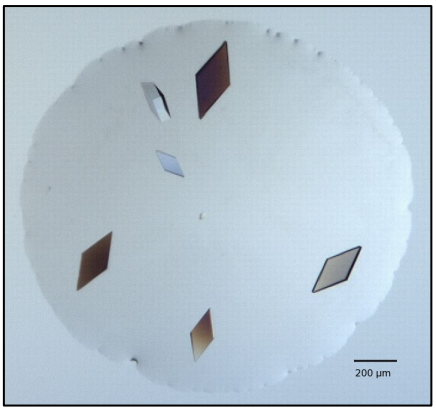

Figure 87: Crystals of human APT1 ΔL73S74 in complex with 2BP grew in condition Classics F2 containing 1.6 M $MgSO_4$, and 0.1 M MES pH 6.5 within 8 days. Photograph taken by Formulatrix Rock Imager and scale bar inserted using Gimp[4].

Table 17: Crystallographic statistics of human APT1 ΔL73S74 in complex with 2BP. Values for the highest shell are given in parentheses. Values for Ramachandran plot are given for favoured, allowed and outlier.

	human APT1 ΔL73S74 + 2BP		
Data collection		Refinement	
Space group	C2	Resolution (Å)	
Cell dimensions		Number of Reflexes	428980 (56755)
a, b, c (Å)	139.37, 57.71, 64.33	Rwork	22.22 (35.5)
α, β, γ (°)	90.0, 92.71, 90.0	Rfree	25.74 (40.2)
Resolution (Å)	69.61-1.62 (1.66-1.62)	Number of Atoms	
Monomers / au	2	Protein	3393
Wave length (Å)	0.91882	Ligand/Ions	74
CC $^1/_2$	99.2 (61.4)	Water	472
I / σ(I)	6.97 (1.61)	B-factor (Å2)	
Completeness (%)	97.5 (86.4)	Protein	19.5 ± 7.4
Redundancy	3.4 (3.2)	Ligand	35.1 ± 11.0
		Water	30.9 + 10.5
		RMSD	
		Bond length (Å)	0.0116
		Bond angle (°)	1.63
		Ramachandran (%)	97.33, 2.45, 0.22
		Clashscore	10.69
		Rotamer outlier (%)	3.23
		Molprobity score	2.06

The complex crystallizes in a different condition and space group than the apo form of the human APT1 ΔL73S74 mutant described in the previous chapter. Under this condition, the protein forms a dimer via the same interface as the typical dimer found in the apo form human APT1 wild type crystallized in P1[69]. The dimer of human APT1 ΔL73S74 in complex with 2BP is rotated by 5.4° compared to the dimers of the apo form of human APT1 ΔL73S74 (see 5.2.8) and rotated by 12.3°

compared to the apo form of human APT1 wild type. The two monomers of the human APT1 ΔL73S74 – 2BP complex have different environments (see Figure 88). The lid-loop of monomer A is buried in the dimer interface and a symmetry molecule of itself that stabilizes the lid-loop by a salt bridge of 3.7 to 4.0 Å distance between D74 and R142 (R144 in the wild type) that is located at the exit of the binding tunnel. The lid-loop of monomer B does not form this interaction, as the crystal interface differs and the symmetry-related molecule is located farther away, leaving the tunnel exit exposed to a solvent channel. The B-factors of the Cα of the lid-loop are increased to 35.7 and 30.5 Å^2 in monomer A and B, respectively, compared to the average overall B-factor of 20.0 Å^2, and the electron density of the lid-loop of monomer A is weaker than in monomer B, despite the crystal contact in monomer A. Strong electron density for 2BP can be seen inside the shortened tunnel. However, the shortened lid-loop is not significantly stabilized upon binding of 2BP, as indicated by the B-factor, which is also 1.7-fold increased compared to the protein overall B-factor. The following Figure 88 provides an overview of the lid-loop's surface contacts.

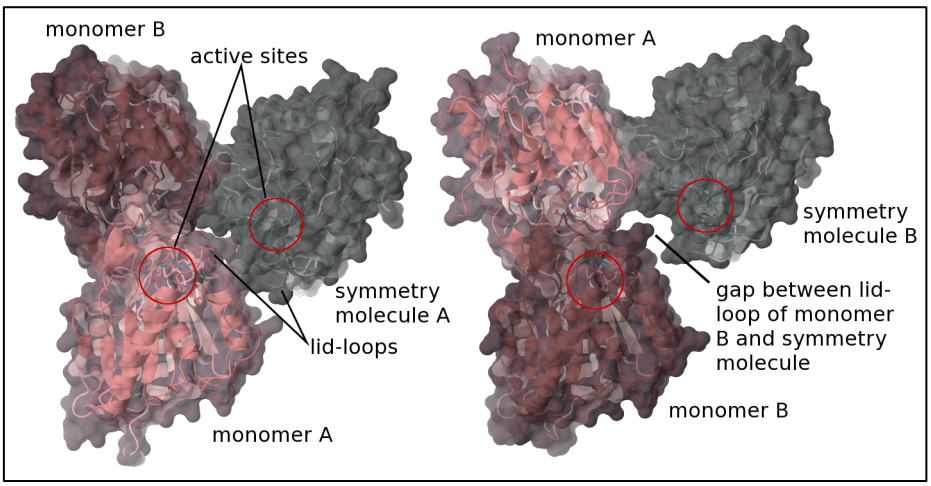

Figure 88: Comparison of the crystal contacts of monomer A (salmon) and monomer B (dark pink). The left side presents the close contact next to the lid-loop between monomer A and its symmetry mate (grey). On the right side, shown in the same orientation, a gap is found between monomer B and its symmetry mate (grey). The active sites are encircled in red.

The conformation of the lid-loop of the complex of human APT1 ΔL73S74 with 2BP differs slightly from the apo form. The inhibitor bound inside the tunnel prevents the inward movement of P73 and the lid-loop into the binding tunnel, thus the Cα of P73 is located about 2 Å further out in the 2BP complex compared to the apo form of human APT1 ΔL73S74. The shortened lid-loop is unable to form the proper entrance of the hydrophobic tunnel, leaving a gap between the side chains of L58 and L171 and forming the tunnel entrance in front of the side chain of W140, which marks the middle of the wild type tunnel. In addition, the shortened lid-loop leaves a wider exit of the tunnel. The anomalous signal of the α-bromide was used to verify the presence of 2BP and its binding mode, similar to the complex of human APT1 wild type - 2BP complex described in chapter 5.1.5. Interestingly, the binding mode of 2BP differs between the two monomers, in contrast to the complex of hAPT1 wild type with 2BP that contains an identical binding mode in all four monomers (see chapter 5.1.5). In monomer A of the human APT1 ΔL73S74 - 2BP complex, two peaks of the anomalous map are observed, one at the active site and a second inside the binding tunnel,

corresponding to the α-bromine of 2BP bound in two positions. The first is identical to the major conformation of 2BP in the human APT1 wild type complex, where the carboxylate of 2BP is bound in the oxyanion hole next to the active site serine (Figure 89, anomalous signal 1). No binding mode similar to the minor conformation of 2BP in the human APT1 wild type complex is observed.

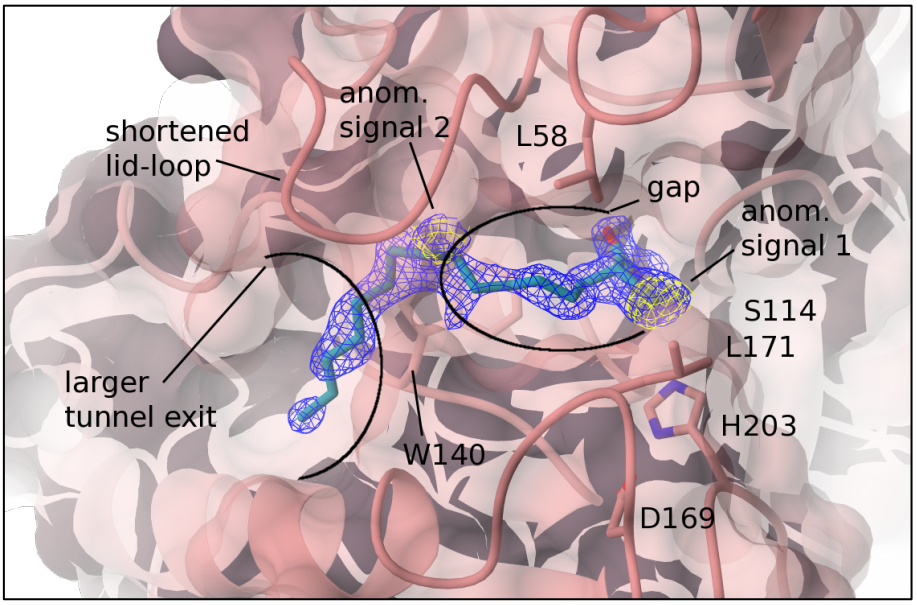

Figure 89: Detailed view on human APT1 ΔL73S74 in complex with 2BP(cyan). 2BP is presented in the binding mode supported by the stronger anomalous signal (yellow, right) for the α-bromide atom. Due to the shortened lid-loop, the lacking L73 leaves a gap between L58 and L171. The tunnel entrance of the ΔL73S74 mutant is formed in front of W140, next to the second anomalous signal (yellow, left).

The conformation of 2BP bound to human APT1 ΔL73S74 shown in Figure 89 is comparable to 2BP bound to human APT1 wild type (Figure 90). In both complexes of the human APT1 wild type and ΔL73S74 mutant, the carboxylic head group of 2BP is coordinated by the oxyanion hole formed by the backbone amides of L25 and Q115 next to the active site serine. The aliphatic tail is bound inside the hydrophobic tunnel formed by the lid-loop. The high flexibility of 2BP allows induced fit to the altered shape of the binding tunnel in the ΔL73S74 mutant, and thus differs in its conformation from 2BP bound to the wild type (Figure 90).

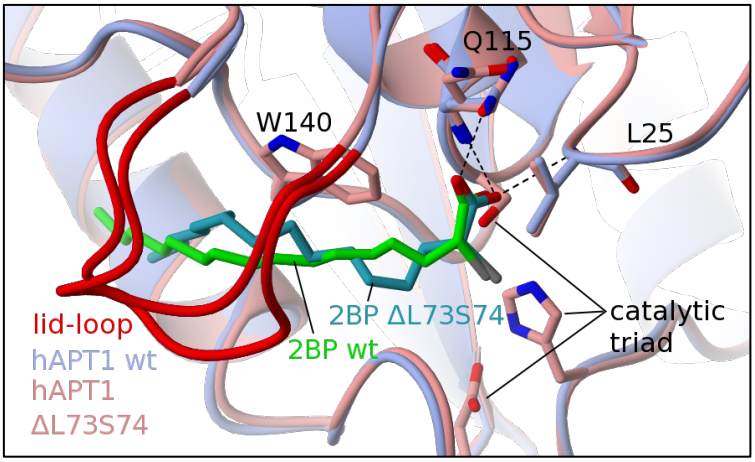

Figure 90: Comparison of the conformation of 2BP bound to human APT1 ΔL73S74 (pink) and human APT1 wild type (blue). The head group of both 2BP molecules is coordinated via H-bonds to the oxyanion hole formed by L25 and Q115. The aliphatic chain is bound inside the tunnel formed by the lid-loop (red), and is adapted to its shape and thus differs between 2BP bound to the wild type (green) and 2Bp bound to human APT1 ΔL73S74 (cyan).

The second peak of the anomalous density map in monomer A of the human APT1 ΔL73S74 - 2BP complex corresponds to the α-bromide of 2BP bound in an alternative conformation with the head group at the altered tunnel entrance of human APT1 ΔL73S74 (Figure 91). This supports the hypothesis that 2BP can slide into the binding tunnel until the charged head group of 2BP is next to the new tunnel entrance. 2BP is not completely covered by the shortened lid-loop. The electron density of the tip of 2BP protruding from the tunnel exit is weaker than for the part bound inside the tunnel. An adjustment of the occupancy of both molecules of 2BP resulted in a 60:40 distribution of 2BP in favor for the binding mode with the carboxylic head group located at the oxyanion hole next to the active site. The conformation of 2BP bound with the head group at the new tunnel entrance inside the tunnel found in monomer A is shown superimposed with the human APT1 wild type (2BP complex, 2BP not shown) in Figure 91. The side chain of L73 is part of the wild type tunnel entrance, and the comparison shows that the head group is located at the middle of the wild type tunnel.

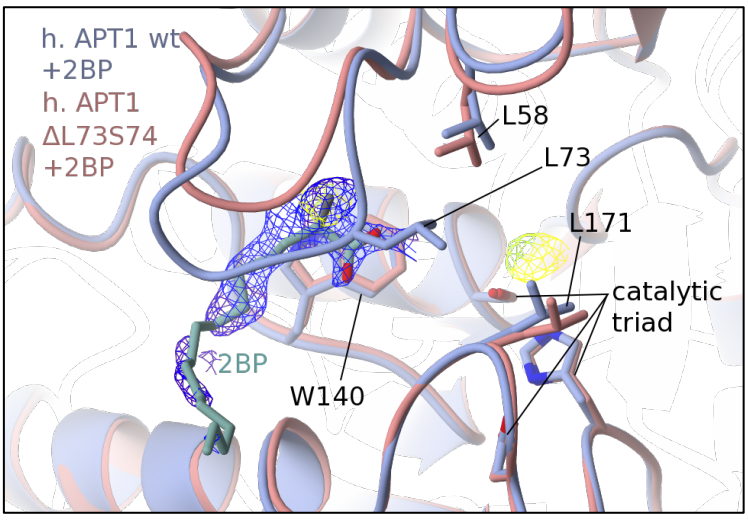

Figure 91: Comparison of the 2BP complexes of human APT1 ΔL73S74 (pink, 2BP in cyan) and wild type (blue, 2BP not shown). The shortened lid-loop of human APT1 ΔL73S74 monomer A (pink) enables the binding mode of 2BP (cyan) with its head group located at the new tunnel entrance formed next to W140, which marks the middle of the wild type tunnel. The 2Fo-Fc electron density of 2BP is shown in blue and contoured to 1 I/σI, while the anomalous density is presented at a level of 3.5 I/σI in yellow.

The protruding part of 2BP bound in the second conformation in monomer A is located in the interface between monomer A and its symmetry molecule (see Figure 88). This artificial cavity is lined with the hydrophobic side chains of M174, F176 and L179 from monomer A, and P173 and P73 of the symmetry mate of monomer A, which all form hydrophobic contacts to the tail of 2BP bound in the tunnel of monomer A, and *vice versa*.

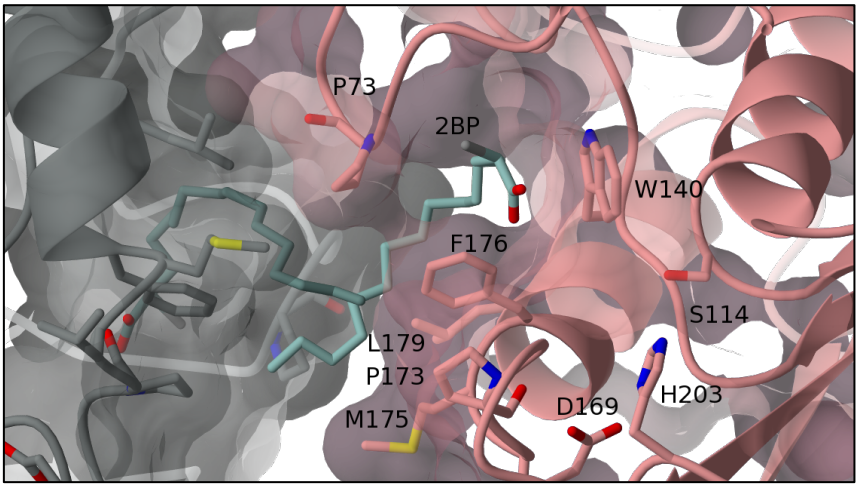

Figure 92: Hydrophobic space between monomer A (salmon) and its symmetry mate (grey). The molecule 2BP (cyan) bound with the head at the new tunnel entrance of monomer A has the tunnel exit protruding tip located in the interface between monomer A and its symmetry mate. The side chains of amino acids in the distance of van-der-Waals interactions with 2BP are shown as sticks. Side chains outside the lid-loop are numbered according to the wild type.

Monomer B contains one strong anomalous peak for bromide plus two weak ones and the elongated electron density of 2BP resides inside the binding tunnel. Interestingly, the forked density of the head group of 2BP is found at the rear exit of the tunnel. The electron density of the reverse conformation is well defined and the carboxylic head group has a charged interaction with the guanidine moiety of the R144 side chain at the tunnel exit. A strong peak in the anomalous density map supports this conformation. There are two further weak peaks of the anomalous map at two 'bulks' next to the linear density of 2BP, one close to the active site, potentially indicating weak binding of 2BP in the conformation observed in the human APT1 wild type complex, and one towards the dimer interface, between N59 and M64 of both monomers. However, these signals are very weak and nearly on the level of background noise (independent of the resolution cut-off of the anomalous map), and as one molecule of 2BP fitted according to the strongest anomalous density peak explains the electron density well, alternative conformations were not included in the model building process. The reverse binding mode found in monomer B is presented in Figure 93.

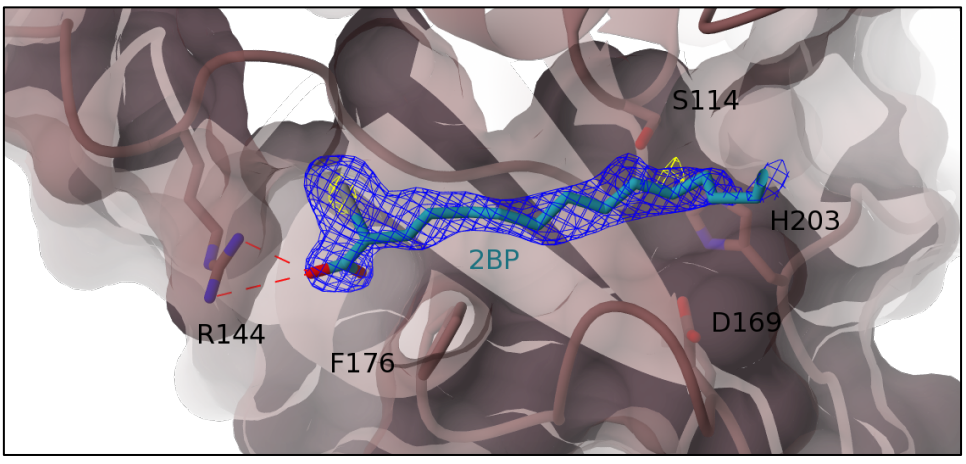

Figure 93: Orientation of 2BP in the human APT1 ΔL73S74 complex bound to monomer B. The well-defined forked electron density (blue, contoured to 1 I/σI) and the anomalous signal of bromine (yellow) support the presented binding mode with the carboxylic acid forming a charged interaction with the guanidine moiety of the R144 side chain. The weaker anomalous signal closer to the active site lacks density for the forked head group, but could correspond to weakly bound 2BP in the major conformation as observed in monomer A and the wild type.

Summarized, the two monomers of the asymmetric unit contain 2BP bound in three conformations, of which two were not observed in the human APT1 wild type complex. Both new orientations of 2BP bind with the carboxylic head group distant from the active site; either slid deeper into the tunnel due to the different shape of the tunnel entrance of the human APT1 ΔL73S74 mutant, or at its wider exit. A substrate bound in a similar manner would have the cleavable ester located outside of the active site, thus being bound in an unproductive binding mode. The relevance of this binding mode is further analyzed in chapter 5.2.13.

5.2.10 Crystal structure of human APT1 ΔS74P75

The second successfully crystallized mutant of human APT1 containing a shortened lid-loop lacked amino acids S74 and P75, shifting the double deletion by one amino acid further compared to the mutant described in the Chapter 5.2.8. Human APT1 ΔS74P75 was screened for crystallization conditions and suitable crystals (shown in Figure 94) were isolated directly from the screening plates. The selected crystal belonged to space group $P2_1$ and diffraction data to a resolution of 1.85 Å was collected at X10SA at SLS, Villigen, as described in Material and Methods. The structure was solved by Molecular Replacement using the structure of human APT1 apo as template.

Table 18: Crystallographic statistics of human APT1 ΔS74P75. Values for the highest shell are given in parentheses. A molecule of HEPES is bound to the protein. Values for Ramachandran plot are given for favoured, allowed and outlier.

	human APT1 ΔS74P75		
Data collection		Refinement	
Space group	$P2_1$	Resolution (Å)	48.72-1.85 (1.90-1.85)
Cell dimensions		Number of Reflexes	113133 (8495)
a, b, c (Å)	36.47, 58.46, 49.63	R_{work}	21.45 (40.9)
α, β, γ (°)	90.0, 100.96, 90.0	R_{free}	25.33 (40.0)
Resolution (Å)	48.72-1.85 (1.90-1.85)	Number of Atoms	
Monomers / au	1	Protein	1646
Wave length (Å)	0.91639	Ligand/Ions	15
CC $^1/_2$	99.8 (85.5)	Water	102
I / σ(I)	10.33 (1.93)	B-factor (Å^2)	
Completeness (%)	99.7 (100)	Protein	37.3 ± 13.1
Redundancy	3.30 (3.35)	Ligand	95.8 ± 8.5
		Water	43.8 ± 8.9
		RMSD	
		Bond length (Å)	0.0112
		Bond angle (°)	1.55
		Ramachandran (%)	94.47, 3.61, 0.92
		Clashscore	10.48
		Rotamer outlier (%)	1.14
		Molprobity score	1.96

Figure 94: Crystallization drop of human ΔS74P75. Crystals grew within 13 days in screening condition Core1 B5 containing 0.1M HEPES pH7.5, 20% PEG 4000 and 10% 2-Propanol. Photograph taken using Formulatrix Rock Imager.

The structure of human APT1 ΔS74P75 contains one monomer per asymmetric unit, which does not form a crystal contact via the typical dimer interface observed for the apo form of human APT1 wild type[69]. Compared to the apo form of human APT1 wild type, the structure has an overall rmsd of 0.52 over 214 aa. The shortened lid-loop forms a tunnel and is not affected by salt bridges or H-bonds, but the side chain of L73 is part of the interface to the neighbor. The protein is not predicted (using PISA[97]) to form stable assemblies via interfaces to the neighbors shown in Figure 95A. The average B-factor of all Cα atoms of the whole protein is 35.7 Å^2, and the B-factor of the lid-loops Cα atoms is slightly increased with a value of 49.4 Å^2. This is in a range comparable to the wild type structure that also has a 1.5-fold increased B-factor of the lid-loop compared to the overall B-factor. The crystal contacts of human APT1 ΔS74P75 are compared to the dimer of the apo form of human APT1 wild type in Figure 95A.

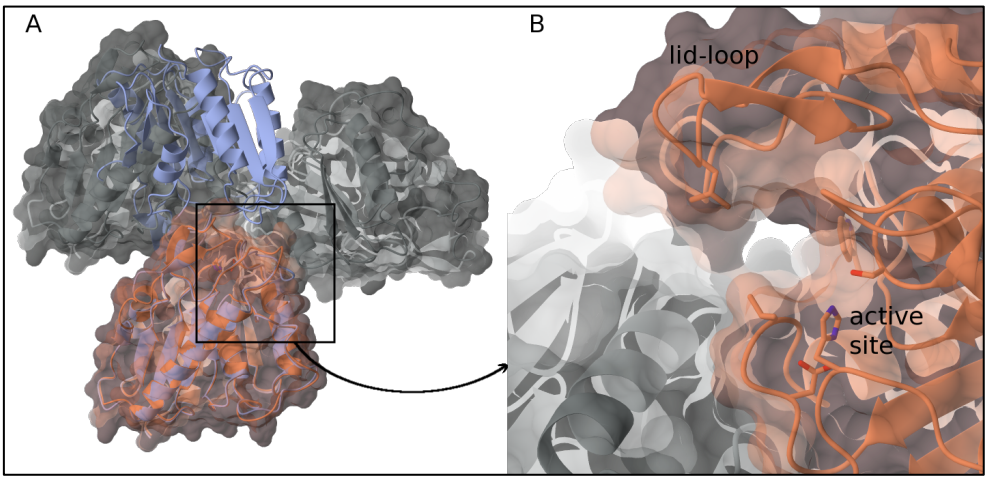

Figure 95: Panel A: Crystal contacts of human APT1 ΔS74P75 (orange) and the symmetry molecules (grey) compared to the dimer formed by human APT1 wild type (blue ribbon). Panel B: Close-up on the symmetry mate next to the lid-loop. No salt bridges or H-bonds between the lid-loop and the symmetry mate (grey) could be detected.

The lid-loop of human APT1 ΔS74P7 pre-forms a short tunnel with a wider tunnel entrance and exit. Despite the high resolution, the electron density of the lid-loop is weak at the tip of the lid-loop formed by L73 and D74 (D76 in the wild type). In human ΔS74P75, the side chain of L73 forms the tip of the lid-loop instead of forming the tunnel entrance, and the Cα of L73 is dislocated by 5.4 Å

compared to the apo form of human APT1 wild type. This results in a gap between L58 and L171 as illustrated in Figure 96, similar to the gap observed in human APT1 ΔL73S74 (see Figure 83). Since the asymmetric unit contains only one monomer, a comparison between several monomers of the asymmetric unit, as in the previous case of human APT1 ΔL73S74, is not possible.

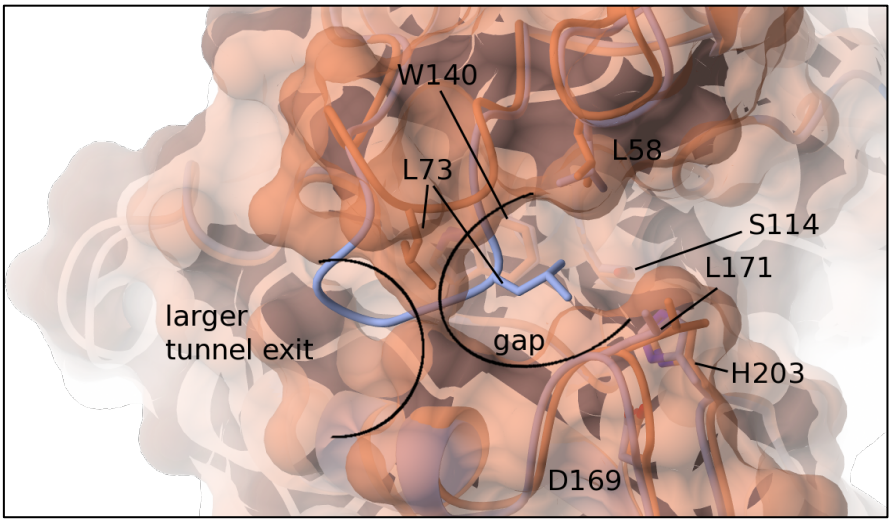

Figure 96: Side view of human APT1 ΔS74P75 (orange) compared to the apo form of human APT1 wild type (blue) The shortened lid-loop significantly alters the tunnel shape, L73 is dislocated by 5.4 Å (measured at the Cα) and forms the tip of the lid with its side chain. The resulting gap between L58 and L171 creates the tunnel entrance in front of W140, comparable to human APT1 ΔL73S74. The tunnel exit is also wider than in the apo form of human APT1 wild type.

The superimposition of the lid-loop of human APT1 ΔL73S74 and ΔS74P75 mutants (Figure 97) shows some differences. In human APT1 ΔS74P75, the new tunnel entrance formed by the side chain of L73 is slightly larger and shifted further compared to the ΔL73S74 mutant (see also Figure 99). As the lid-loop of the ΔS74P75 mutant lacks the rigid P75, it is more flexible and forms a larger tunnel exit.

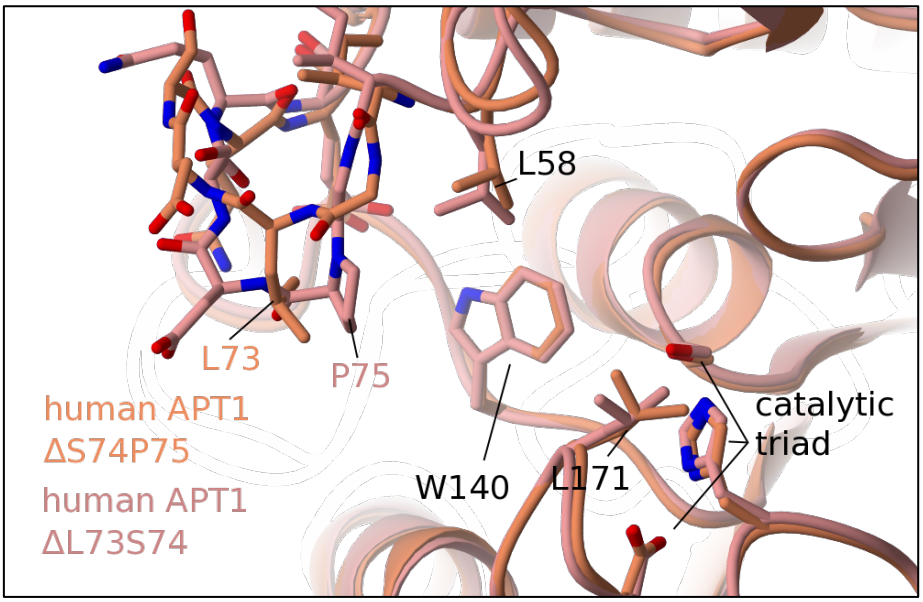

Figure 97: Superimposition of the lid-loops of human APT1 ΔL73S74 (pink) and ΔS74P75 (orange). In human APT1 ΔS74P75, the tunnel entrance is formed by the side chain of L73 and is slightly larger compared to the tunnel entrance of human APT1 ΔL73S74 formed by P75 (wild type numbering).

Taken together, the crystal structure of human APT1 ΔS74D75 shows a similar effect on the tunnel formed by the lid-loop as observed for the human APT1 ΔL73S74 mutant. The shortened lid-loop

pre-forms a tunnel, but leaves a gap between L58 and L171, resulting in a tunnel entrance formed in front of W140, which marks the middle of the tunnel of human APT1 wild type. The tunnel exit is also wider than in human APT1 wild type. The biochemical activity is reduced to ~20% of the wild type, comparable to the activity of human APT1 ΔL73S74 (Figure 81). A structure of a complex with 2BP could not be obtained so far due to insufficient diffraction quality of the crystals.

5.2.11 Human APT1 ΔI71-D76 lid-truncation mutant shows lowest activity

Human APT1 ΔI71-D76 contains a complete truncation of the lid-loop by deleting six amino acids from I71 to D76 and shows the lowest biochemical activity of all mutants of this study. Figure 98 shows the Michaelis-Menten kinetics using PPTS as substrate. The fitted curve is defined by few data points at low concentrations before reaching V_{max}. While still being significantly active compared to the auto-hydrolysis control of PPTS, the mutant shows a k_{cat} rate of 0.079 x10^4 s^{-1}, that is 3% activity compared to the wild type of human APT1, indicating that the lid-loop is essential for catalysis. Another reason for the nearly abolished activity could be a not properly folded protein. From this residual activity, a very low apparent $K_{M,app}$ of 0.43 ± 0.16 was calculated from the fit, being 40-fold lower than the K_M of human APT1 wild type. However, this value should be treated with caution.

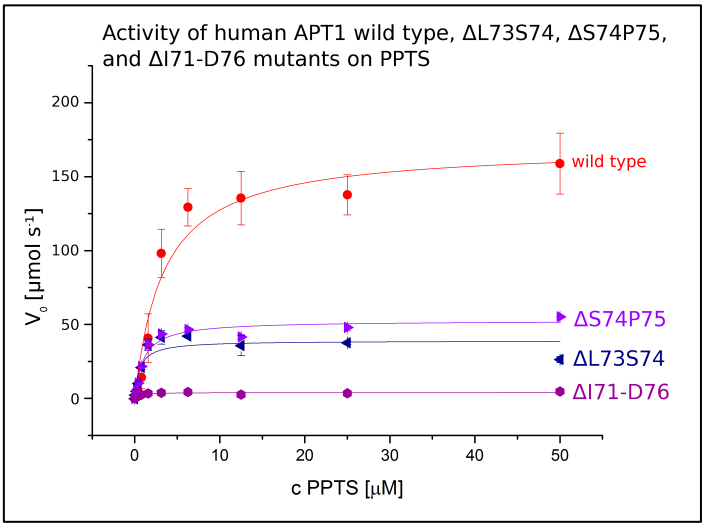

Figure 98: Comparison of the biochemical activity of human APT1 Δ71-76 to human APT1 wild type and the lid-loop shortened ΔL73S74 and ΔS74P75 mutants of human APT1. While the shortened lid-loop reduced the activity to ~20%, the complete removal of the lid-loop nearly abolishes biochemical activity, reducing it to 3% compared to the wild type. Data averaging and error calculation was done with Microsoft Excel, the plot was fitted with Origin.

Table 19: Kinetic parameters of human APT1 wild type, ΔL73S74, ΔS74P75 and ΔI71-D76 mutants on PPTS used as test substrate.

	V_{max} [µmol s^{-1} x10^4]	k_{cat} [s^{-1} x10^4]	K_M [µM]	k_{cat} / K_M [$µM^{-1}$ s^{-1} x10^4]
wild type	170.5 ± 11	3.41 ± 0.22	3.38 ± 0.77	1.01
ΔL73S74	39 ± 3.5	0.78 ± 0.07	0.59 ± 0.25	1.32
ΔS74P75	52.5 ± 2.5	1.05 ± 0.05	1.03 ± 0.20	1.02
ΔI71-D76	3.95 ± 0.3	0.079 ± 0.006	0.43 ± 0.16	0.18

5.2.12 Crystallization of human APT1 ΔI71-D76

So far, no structural data of the lid-less ΔI71-D76 mutant of human APT1 is available. Screening for crystallization conditions for human APT1 ΔI71-D76 failed to result in crystals of promising quality and size. Optimization of conditions resulting in initial hits in 24well plate format grid screens either failed to reproduce the crystals or could not improve the unsatisfactory x-ray diffraction quality of the initial hits. Two further deletion mutants, human APT1 ΔI71-S74 and ΔL73-D76, did not yield promising crystal hits either. The pure protein of human APT1 ΔI71-D76 cannot be concentrated as high as human APT1 wild type or the other mutants (maximum of 11 mg/ml of human APT1 ΔI71-D76 compared to 30-40 mg/ml for human APT1 wild type), as the protein precipitates upon further concentration. As the activity assay data shows a low yet significant activity that also follows Michaelis-Menten kinetics, it is unlikely that the protein is completely denatured.

5.2.13 Hypothetical non-productive binding mode of PPTS enabled by the non-wild type tunnel entrance

Some lid-loop mutants of human APT1 investigated in this thesis show a reduced efficiency in the hydrolysis of the test substrate PPTS compared to the human APT1 wild type, and all except human APT1 +LP, where it is unknown, have an altered shape of the tunnel entrance. The hypothesis is that the linear palmitate moiety of the substrate slides into the hydrophobic tunnel until the larger (thio-)ester is stopped at the entrance. Thus, a different shape of the tunnel entrance caused by mutations of the lid-loop can result in unproductive binding of the substrate, with the ester dislocated from the active site serine and the oxyanion hole (see Figure 91). A comparison of the structures of human APT1 ΔL73S74 and ΔS74P75 mutants reveals a comparable change of the shape of the tunnel entrance. The shortened lid-loop causes a gap between L58 and L171 (Figure 99, compare also Figure 83), and thus the tunnel entrance is formed further away from the active site. In the wild type of human APT1, this gap is filled by the side chain of L73, which forms a part of the tunnel entrance.

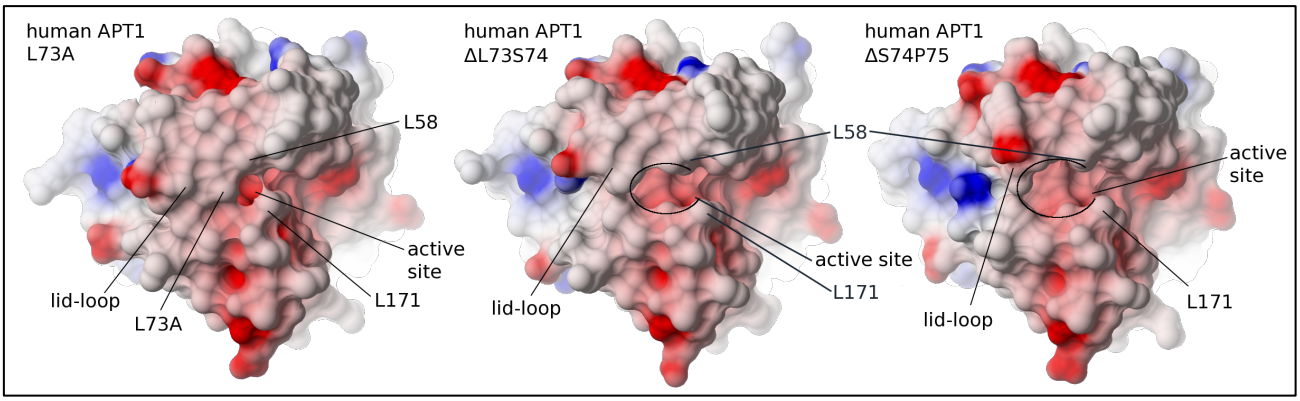

Figure 99: Comparison of the surface of the human APT1 lid-loop mutants ΔL73S74 and ΔS74P75. Both mutations cause a gap between L58 and L171, thus the tunnel entrance is not formed next to the active site but farther away. Electrostatic surface potential is presented in a gradient of blue over white to red (from positive to negative). Electrostatic surface potential calculated and image created using CCP4mg[93].

The gap between L58 and L171 is also present in the structure of human APT1 L73A (when co-crystallized with 2BP binding inside the tunnel), although to a lesser extent (Chapter 5.2.5, see

Figure 74). It can be assumed that the changed tunnel entrance of the L73A mutant of human APT1 also enables unproductive binding of PPTS in a conformation comparable to the hypothesized binding of PPTS described in Figure 100.

The extended lid-loop of the apo form of human APT1 +LP insertion mutant folds into the tunnel and blocks it (Figure 79). This mutant is active, so rearrangement of the lid-loop is necessary for ligand binding in a re-formed tunnel that is expected to enable efficient substrate turnover. The lack of structural data of a complex and thus the shape of the tunnel entrance of this mutant prevents description of a potential binding mode of the substrate.

No structural data is available for the four (ΔI71-S74 and ΔL73-D76) and six (ΔI71-D76) amino acid lid-loop truncation mutants. The very short (respectively missing) lid-loop cannot form a tunnel, so these mutants are expected to be strongly impaired in substrate coordination, which is corroborated by the nearly abolished biochemical activity of the human APT1 ΔI71-D76 mutant.

It can be assumed that the unproductive binding mode of 2BP observed in the complex with human APT1 ΔL73S74 could potentially also occur in the other mutants of human APT1 that show a comparably reduced biochemical activity (20 to 30% of the wild type) and shape of the tunnel entrance. The 2BP complex of human APT1 ΔL73S74 has a high resolution and well-defined electron density for the 2BP molecules bound in multiple conformations, resulting in an unproductive binding mode of 2BP (with the carboxylic head group at the mutant tunnel entrance, see Figure 91). Modeling was used to check if the substrate PPTS used for the biochemical assay could fit in this non-productive binding mode with the palmitate ester position as the carboxylic head group of 2BP. The model of the PPTS fluorophore head group (HPTS) was added next to the carboxylic acid head of 2BP, mimicking the proposed hypothetical non-productive binding mode of a PPTS molecule (illustrated in Figure 100). In this position, the hypothetical palmitate ester of PPTS is 7.2 Å away from the active site serine. By interesting coincidence, one sulfonate group of PPTS would bind inside the oxyanion hole close to the active site serine, and the aromatic pyranine ring system is located between the hydrophobic side chains of L58 and L171. Both interactions are likely to stabilize this hypothetical binding mode.

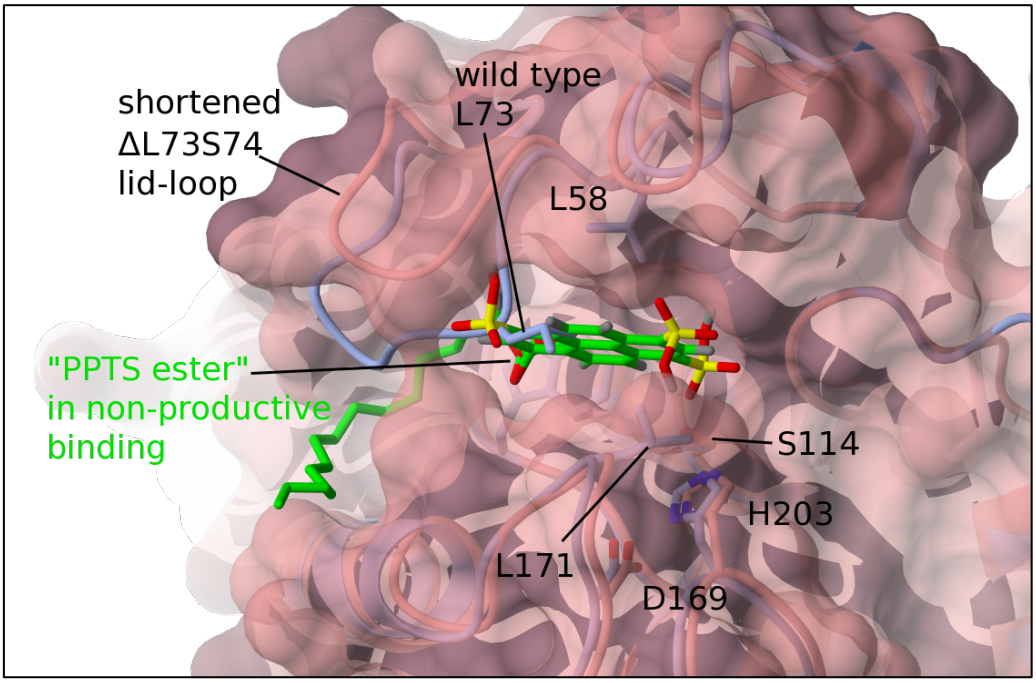

Figure 100: Hypothetical binding mode of PPTS, created by fitting HPTS next to 2BP in the unproductive binding mode observed in the human APT1 ΔL73S74 + 2BP complex. The hypothesis is that the gap between L58 and L171 (resulting from the shortened lid-loop) enables PPTS to slide deeper into the tunnel until reaching the new entrance, thus binding with the ester dislocated from the active site. This proposed unproductive binding mode would prevent hydrolysis, and stresses the important function of a correctly formed tunnel entrance in coordinating the substrate.

Summarized, this hypothetical binding mode could explain the reduced activity of the lid-loop mutants of human APT1. The structure of human APT1 ΔL73S74 in complex with 2BP reveals the important function of the tunnel entrance formed by the lid-loop in positioning the substrate's ester. The entrance of the binding tunnel limits the penetration depth of palmitate into the tunnel similar to a funnel. In the wild type it positions the ester close to the active site serine and the oxyanion hole, which is essential for efficient ester hydrolysis catalyzed by human APT1. Binding with the ester dislocated from the active site cannot result in APT-catalyzed hydrolysis, thus being a "non-productive binding mode", which can be observed in the 2BP complex of the human APT1 ΔL73S74 mutant. The PPTS test substrate is bound with its aliphatic chain inside the tunnel and the aromatic pyranine ring system in the gap between the hydrophobic side chains of L58 and L171, and with one sulfonate group in the oxyanion hole. This unproductive binding mode could potentially be stronger than binding next to the catalytic serine and cause substrate inhibition, but no evidence for substrate inhibition (a peak of V_{max} and a decline at further increasing substrate concentration) was observed in the biochemical data.

5.2.14 Binding of 2BP is dependent on the lid-loop of human APT1

Binding of 2BP to human APT1 wild type or the ΔI71-D76 lid-loop lacking mutant was measured via Stopped Flow as described in Material and Methods (Chapter 7.6.1) and in Chapter 5.1.7. A comparison of the association rate of 2BP to human APT1 wild type (Figure 101, green) and the human APT1 ΔI71-D76 mutant lacking the complete lid-loop (Figure 101, red) shows that the binding rate of the mutant is – unexpectedly – significantly decreased compared to the wild type. The data of human APT1 wild type and mutant both show more than one binding rate constant, and

thus require a multi-exponential fit. As mentioned in Chapter 5.1.7 describing 2BP binding to human APT1 wild type, multi-exponential functions can be unstable if the rate constants are too similar as in the case here, and thus the binding data is compared qualitatively.

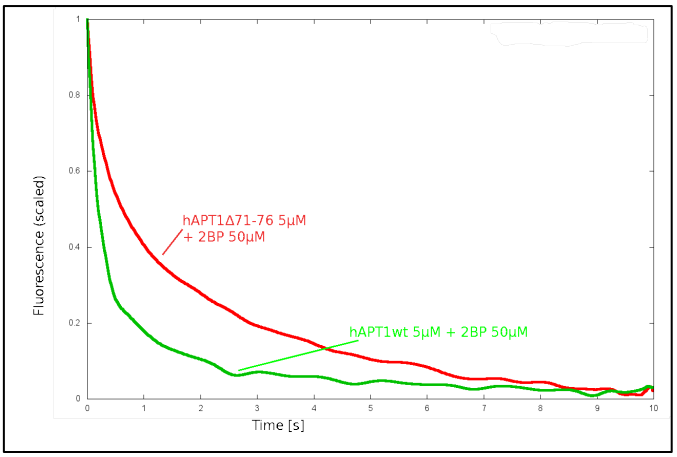

Figure 101: Stopped Flow measurements of binding of 2BP to human APT1 wild type (green) and the lid-lacking mutant Δ71-76 (red). 5 µM of human APT1 (wild type or mutant) were mixed with 50 µM of 2BP. The lid-loop lacking mutant shows a reduced binding rate compared to the wild type. Data averaged, normalized, and plotted by Ingrid Vetter using gnuplot[94]. Labels were added using Gimp[4].

The facts that also the human APT1 ΔI71-D76 mutant contains more than one binding rate (like the wild type) corroborates that rearrangements of the lid-loop are not the only reason for the multiple binding rate constants. The significantly reduced binding rate of human APT1 ΔI71-D76 is an indicator that although W140 (forming the inner wall of the tunnel in the wild type) is quenched by 2BP binding it might not be readily accessible from the solvent in the mutant. Hypothetically, the deletion mutant of human APT1 could form (unspecific) aggregates via the exposed inner wall of the hydrophobic tunnel (due to the lacking lid-loop) and thus reduce the accessibility of the remaining inner wall of the tunnel (and slow down the binding rate of 2BP, see Figure 101). Blocking of the active site by this mechanism cold also explain the strongly reduced biochemical activity of the mutant (see Figure 98). However, aggregation is contradicted by the observed high dissociation rate of 2BP from the human APT1 ΔI71-D76 2BP complex (see Figure 102, red curve). Therefore, unspecific binding, similar to the slow binding observed for 2BP at the groove (see Figure 53, green curve), could be an explanation for the reduced binding rate despite the direct accessibility (as the lid-loop und thus the tunnel is lacking). 2BP would then bind unspecifically at the new hydrophobic patch of the mutant without influencing the fluorescence signal of W140, and over time arranges itself next to the W140 side chain, i.e. 2BP could be sequestered at the additional binding sites, reducing the concentration of free 2BP. Thus, the complete ensemble would show an apparent slower binding rate of 2BP.

5.2.15 Dissociation of human APT1 lid-loop – 2BP complexes

Three lid-loop mutants of human APT1 were selected to compare the dissociation rate of their respective 2BP complex with human APT1 wild type. Human APT1 L73A contains only a point mutation, which probably increases the flexibility of the lid-loop (see Chapter 5.2.4); human APT1 ΔS74P75 contains a shortened lid-loop forming a shorter tunnel with wider entrance and exit (see

Chapter 5.2.10); and human APT1 ΔI71-D76, whose biochemical activity is reduced to 3% compared to the wild type and probably cannot form a tunnel at all since the lid-loop is too short (see Chapter 5.2.11). The qualitative comparison of the dissociation rates of the respective 2BP complex measured via Stopped Flow (using L-FABP as competitor) is shown in Figure 102. The 2BP complexes of human APT1 wild type (blue) and the L73A (green) and ΔS74P75 (magenta) mutants show two fast dissociation rates, while the human APT1 ΔI71-D76 mutant (red) can be described reasonably well using a single dissociation rate constant. The dissociation rate of the human APT1 ΔI71-D76 mutant is the fastest of the tested mutants, and corresponds to a dissociation of 2BP independent of the lid-loop (which is lacking in the ΔI71-D76 mutant). A comparably fast dissociation rate is also present in the 2BP complexes of the wild type and the L73A and ΔS74P75 mutants (Figure 102). Since this rate is present in 2BP complexes of the human APT1 wild type and lid-loop mutants, it is probably lid-loop independent and corresponds to 2BP unspecifically bound at the groove close to W32. After the first fast dissociation rate, the 2BP complexes of both human APT1 L73A and ΔS74P75 mutants show a comparable second fast dissociation rate that is significantly increased compared to the second fast dissociation rate of the 2BP complex of human APT1 wild type. Concluding from this, the second and slower rate (not present in the ΔI71-D76 mutant) could correspond to the influence of the lid-loop on the dissociation of 2BP bound inside the tunnel, which is faster in the mutant complexes due to the less stabilized 2BP by the (shorter) tunnel formed by the mutant lid-loop (see Chapters 5.2.5 and 5.2.9) compared to the wild type of human APT1. A potential third rate could be explained by the dissociation of dimers formed of the complex, which is likely to influence the release of 2BP from the tunnel, but dimerization plays probably a minor role at this protein concentration (protein concentration of 5 µM, dimer K_D of 2.8 µM[69]).

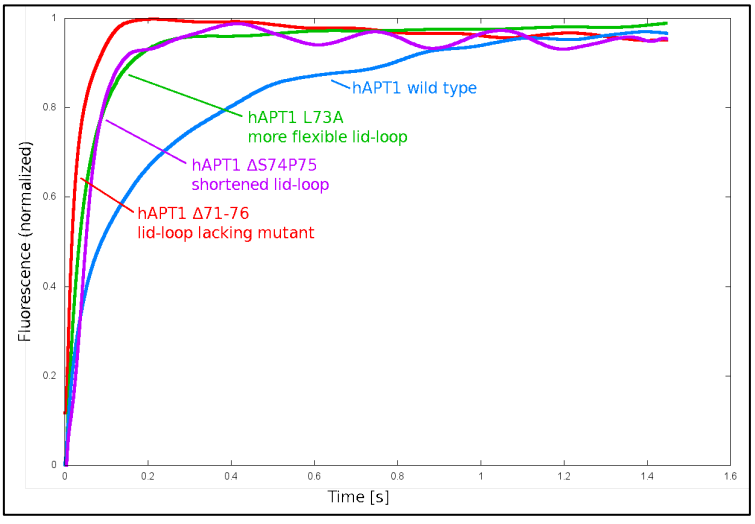

Figure 102: Comparison of the dissociation of 2BP (20 µM) complexes of human APT1 wild type and selected human APT1 lid-loop mutants (all APTs 5 µM). L-FABP (45 µM) is used as competitor to bind 2BP. The first fast dissociation rate of 2BP is roughly comparable for the four measurements and probably corresponds to unspecifically/weakly bound 2BP close to W32 at the groove. This rate is expected to be independent of the lid-loop and the lid-loop lacking mutant ΔI71-D76 (red) can indeed be described using only this rate. The second dissociation rate is slower in the wild type (blue) than in the L73A (green) and ΔS74P75 (magenta) mutants, and would be expected to be sensitive to the influence of the lid-loop (which is less stable in the mutants) on the dissociation. The influence of dimer dissociation on the release of 2BP from the complex is unknown and could add a further rate constant to the equation. Data averaged, normalized, and plotted by Ingrid Vetter using gnuplot[94]. Labels added using Gimp[4].

As described in Chapter 5.1.8, the dissociation constant K_D (a measurement for affinity) is defined as $K_D = k_{off}/k_{on}$ and could be determined from the binding rate constant and dissociation rate constant. However, since no reliable rate constants can be determined from complex formation and dissociation, the affinity of 2BP towards the human APT1 wild type and ΔI71-D76 mutant was compared qualitatively. The faster complex formation (k_{on}) and a slower dissociation (k_{off}) results in a lower K_D of human APT1 wild type for 2BP (and thus a higher affinity) compared to the human APT1 ΔI71-D76 lid-loop lacking mutant. This appears to be a contradiction to the previously (in the activity assay) determined apparent K_M (see Chapter 5.2.11), which is significantly lower for the human APT1 ΔI71-D76 mutant than for the wild type (see Figure 98). However, only under conditions where the turnover number k_{cat} is insignificantly small compared to k_{off}, K_M is a reasonable approximation of K_D. As these conditions are not fulfilled, K_M cannot be compared to K_D. Taken together, human APT1 wild type containing the properly folded lid-loop is faster in the formation of the complex with 2BP and slower in its dissociation, compared to the lid-loop lacking mutant ΔI71-D76. This corresponds to an (expected) higher affinity of human APT1 wild type for 2BP compared to the lid-loop lacking mutant. The single fast dissociation rate of 2BP form the lid-loop lacking mutant ΔI71-D76 probably corresponds to dissociation of unspecifically bound 2BP. A second fast dissociation rate is only present in lid-loop containing and therefore tunnel forming mutants, and thus are likely to be lid-loop dependent. It is observed that this dissociation rate is faster in the L73A and ΔS74P75 mutant than in the human APT1 wild type, which indicates that 2BP is probably less tightly bound due to the more flexible lid-loop and wider tunnel entrance that is found in the corresponding crystal structures (see Chapter 5.2.5 and 5.2.9).

5.2.16 Summary of the lid-loop mutants of human APT1

Summarized, the study of various mutants addressing the flexibility and shape of the lid-loop revealed that a properly formed tunnel entrance is essential for efficient biochemical activity. Table 20 provides an overview of the results of the human APT1 lid-loop mutants.

Human APT1 L58A and L171A mutants show that both residues are not crucial for the stabilization of the lid-loop and formation of the wild type shaped tunnel. However, shortening the L73 side chain to alanine significantly decreases the stabilization of the lid-loop and thus increases the flexibility of the lid-loop significantly to enable the lid-loop to fold into the tunnel (see x-ray structure of human APT1 L73A, Figure 67). In addition, the shorter side chain of the L73A mutant alters the shape of the tunnel entrance, which then becomes less efficient in coordinating a ligand bound inside the tunnel (see Chapter 5.2.5), thus reducing the biochemical activity to about 30%. The crystal structure of human APT1 +LP insertion mutant showed that two leucine side chains of the extended lid-loop are located inside the tunnel and thus block it (see Figure 79). Here, rearrangement of the lid-loop would be necessary to allow ligand binding inside the tunnel. Due to the lack of a structure of a complex, no information on the shape of the tunnel and its entrance with a ligand bound inside is available, but it can be speculated that the altered lid-loop, even when “opened” to allow substrate binding, is unable to position the substrate in an optimal way. It is not a purely competitive

effect of the blocked tunnel since the K_M value is not significantly altered (reduced to 50%). Biochemical activity of the human APT1 +LP mutant is reduced to about 30% of the wild type, the same level as human APT1 L73A.

Shortening the lid-loop results in a reduction of the biochemical activity to about 20% compared to human APT1 wild type: both structures of human APT1 ΔL73S74 and ΔS74P75 have a shorter tunnel that is pre-formed in the absence of a ligand, has a wider exit and the entrance forms at the middle of the wild type tunnel (see Figure 83 and Figure 99). This relocated entrance enables binding of the substrate in an unproductive orientation, as concluded from the complex structure of human APT1 ΔL73S74 and 2BP (see Figure 91 and Figure 100). The complete truncation of the lid-loop nearly abolished biochemical activity, most likely due to the inefficient substrate positioning during catalysis caused by the lacking tunnel.

Dimer formation (see Table 20 and Figure 115) is influenced by the shape of the hydrophobic patch and tunnel entrance but is not exclusively dependent on it, as the wild type dimer is also observed for the apo form of human APT1 ΔL73S74.

Table 20: Overview of the lid-loop mutants described in this thesis. The biochemical activity is given in percent compared to human APT1 wild type. Except the human APT1 ΔI71-D76 lid-loop truncation mutant, mutants without structural data were not characterized biochemically.

Mutant of human APT1	Crystal structure	wild type tunnel	Dimer formation in crystal (° rotated compared to wt)	Biochemical activity (% of wild type)
L171A	yes	yes	yes (6.3-7.1°)	100%
L171V	yes	yes	yes (1°)	100%
L58A	yes	yes	yes (5.6-7.9°)	-
L73A	yes (apo and +2BP)	loop in tunnel	no dimer	30%
L73A+L171A	no	-	-	-
+LP	yes	loop in tunnel	no dimer	30%
ΔG72L73	no	-	-	-
ΔL73S74	yes (apo and +2BP)	wider entrance + exit	yes (9-11°)	20%
ΔS74P75	yes	wider entrance + exit	no dimer	20%
ΔI71-S74	no	-	-	-
ΔL73-D76	no	-	-	-
ΔI71-D76	no	-	-	3%

5.3 Shallow groove as potential secondary binding site

The exact binding mode of a palmitoylated protein to APT is unknown since no crystal structure of a complex is available so far, but the hydrophobic tunnel has been identified as the primary binding site of the palmitoyl moiety (see co-purified fatty acids[69] and product-mimicking 2BP, Chapter 5.1.5) and seems to be required to position the cleavable ester at the active site (see Chapter 5.2).

This shallow groove leads to the active site and binding tunnel, as shown in Figure 103 and could be a secondary binding site for e.g. the peptide chain of a palmitoylated protein or a second lipid

anchor. The surface of this groove is conserved to large extent in shape and surface charge in APTs of different organisms and other α,β-hydrolases, as for instance in the carboxyl esterase of *P. aeruginosa* (PDB ID 3cn9, [57]), which crystallized with a PEG bound into this groove (see Figure 6). Other molecules besides PEG have been observed to weakly bind at this groove, for instance the hydrophobic 2BP (communication by Stefan Baumeister, also shown via Stopped Flow, Figure 53), or the polar buffer bicine in the crystal structure of human APT1 L73A (Figure 69), revealing the ambiguous binding potential of the groove. Therefore, this groove is investigated by biochemical and structural methods using 2BP and a hexadecylated peptide mimicking the palmitoylated N-terminus of human APT1 (see Chapter 3.4.1) as test ligand for human APT1 as described in the following.

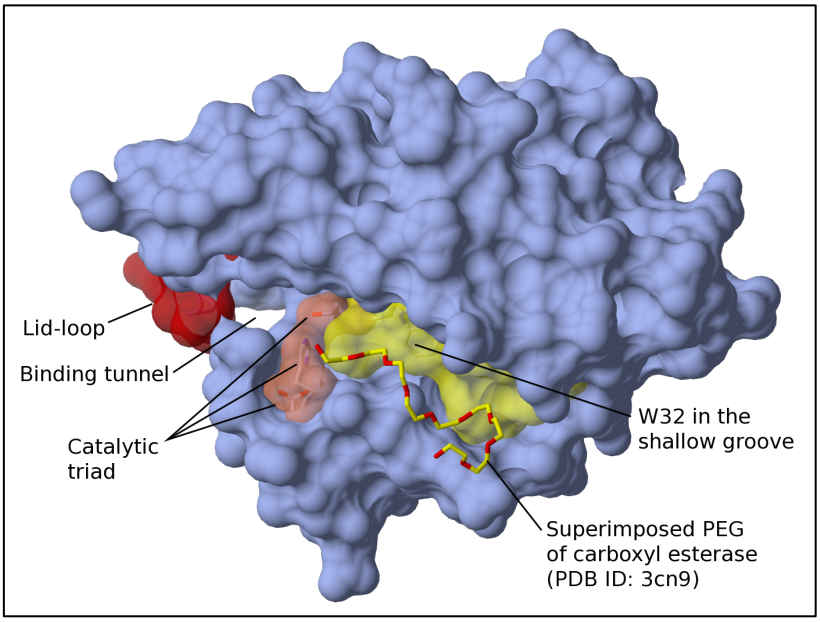

Figure 103: Overview of the surface topology of human APT1. The lid-loop is shown in red, the catalytic triad in orange, and the shallow groove in yellow. A PEG molecule of the superimposed structure of a bacterial carboxyl esterase (PDB ID 3cn9, [57]) reveals the surface groove as potential secondary binding site.

5.3.1 Obstacles for crystallographic investigation of the shallow groove as secondary binding site

Binding assays based on the intrinsic tryptophan fluorescence of W32 (see Figure 103) have shown that 2BP binds with a weak affinity in the range of 100 µM in the groove next to the active site [communications by Stefan Baumeister]. This binding mode has not been observed unambiguously so far in any crystal structure of human APT1 with 2BP, although the groove often shows weak density that could be correspond to a partially disordered 2BP molecule (Stefan Baumeister, private communications). To further address the question whether the groove might bind palmitoylated peptide of substrate proteins with higher affinity than 2BP, human APT1 wild type was subjected to co-crystallization with a hexadecylated peptide corresponding to the N-terminus of human APT1 (residues 1-10, see Figure 113). It was shown that APT1 is palmitoylated N-terminally and able to de-palmitoylate itself[98,99], thus, an un-cleavable hexadecylated thioether was attached to the N-terminal cysteine in position 2 of the peptide. However, no peptide was visible in the crystal. One possible reason for the failure to obtain a complex with a peptide could be

the fact that the wild type of human APT1 forms a dimer with a K_D of 2.8 µM as described [69]. In the most common form of the dimer, the side chain of M60 (located in the loop next to the lid-loop) blocks the groove of the dimer partner as shown in Figure 104 and competes with the binding of ligands at this site.

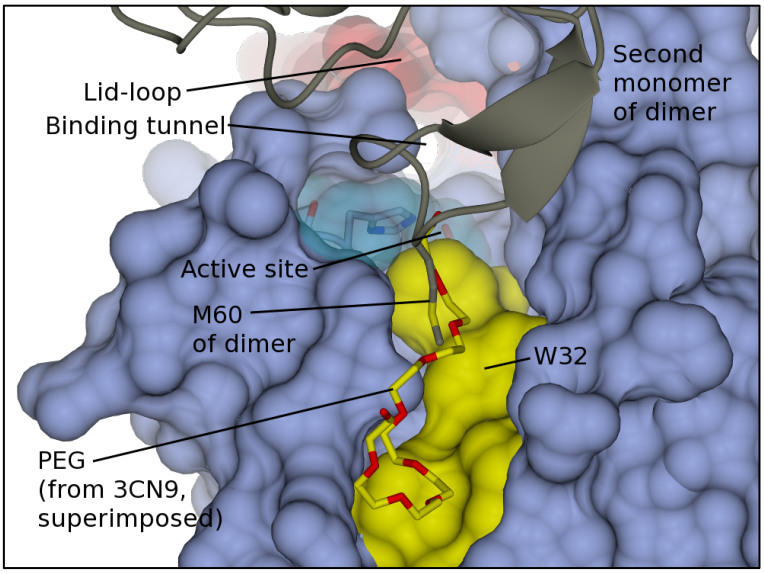

Figure 104: The side chain of M60 of the dimer partner blocks the shallow groove (yellow), which potentially hosts the substrate protein. The groove is located next to the active site (cyan), and the entrance of the binding tunnel formed by the lid-loop (red). The structure of the *P. aeruginosa* carboxyl esterase (PDB ID 3cn9, [57]) contains a molecule of PEG bound at the groove, which is superposed here (yellow sticks) to highlight the potential binding site.

To enable ligand binding, the groove needs to be made accessible by either removing the side chain of M60 and/or rearranging the dimer. The effect of a shortened side chain or removal of M60 was investigated by X-ray crystallography using M60S and ΔM60 mutants of human APT1, respectively. M60 is not part of the lid-loop or tunnel, or involved in an expected binding motif on the monomeric protein, therefore a mutation or deletion of M60 was not expected to alter the proteins binding characteristics. The structures presented in the following part were obtained and refined by B. Darius Bothe during his master thesis[100] under my supervision.

5.3.2 Crystal structure of human APT1 M60S apo and in complex with 2BP

Human APT1 M60S, both as apo form and in complex with 2BP, was subjected to screening for suitable crystallization conditions. Co-crystallization with 2BP was carried out as described before in Chapter 5.1.5. Briefly, 1.3 mM protein was mixed with 5 mM 2BP and heated to 50 ˚C for 5 to 10 min while being mixed gently with the fingers. Crystals were isolated directly from the screening plate (Figure 105) as described in Material and Methods. The apo form and the 2BP complex of human APT1 M60S diffracted to 1.95 Å and 1.85 Å, respectively, at X10SA at SLS. The diffraction data was processed and the structure solved via Molecular Replacement using human APT1 wild type as template as described in Material and Methods. The crystals of the apo form and the 2BP complex belonged to space group $P2_12_12_1$ and $P2_1$, respectively[100]. The crystallographic statistics are summarized in Table 21. Both data sets were collected at the bromine edge to potentially allow precise localization supported by the anomalous signal of 2BP in the complex form.

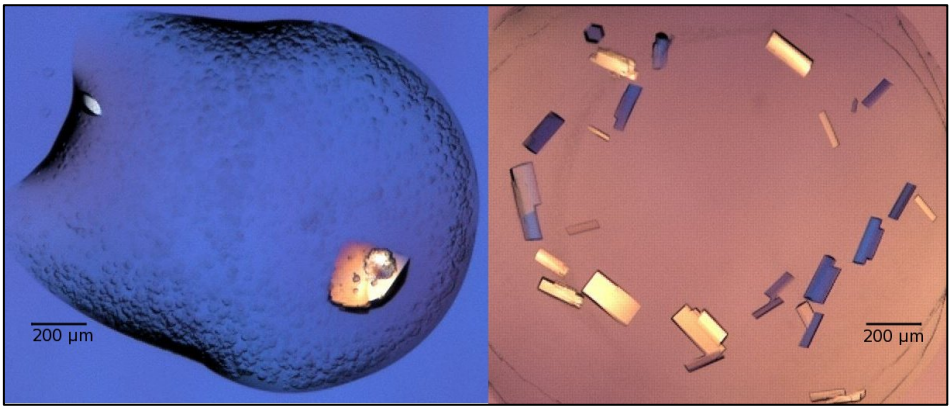

Figure 105: Left: Crystallization condition for the apo form of human APT1 M60S: Condition PEG screen, C7 containing 0.1 M MES at pH 6.5, and 25% PEG 3000 resulted in crystals within 5 days. Right: Crystals of the human APT1 M60S – 2BP complex appeared within 12 hours and were grown for five days in condition PEG screen, C11 containing 0.1 M MES at pH 6.5 and 20% PEG 10,000. Photographs taken using Formulatrix Rock Imager.

Table 21: Crystallographic statistics of the structures of human APT1 M60S as apo form and in complex with 2BP. Values for the highest shell are given in parentheses. Values for Ramachandran plot are given for favoured, allowed and outlier.

	human APT1 M60S apo	human APT1 M60S +2BP		human APT1 M60S apo	human APT1 M60S +2BP
Data collection			Refinement		
Space group	$P2_12_12_1$	$P2_1$	Resolution (Å)	42.32 - 1.95 (2.00 - 1.95)	46.43 - 1.85 (1.90 - 1.85)
Cell dimensions			Number of Reflexes		561706 (42019)
a, b, c (Å)	70.850 77.830 143.550	72.17, 61.63, 114.08	R_{work}	18.40 (24.0)	16.27 (21.4)
α, β, γ (°)	90.0, 90.0, 90.0	90.0, 101.98, 90.0	R_{free}	23.57 (27.7)	20.72 (27.7)
Resolution (Å)	42.32 - 1.95 (2.00 - 1.95)	46.43 - 1.85 (1.90 - 1.85)	Number of Atoms		
Monomers / au	4	4	Protein	6748	6892
Wave length (Å)	0.91939	0.91939	Ligand/Ions	0	158
CC $^1/_2$	99.9 (73.5)	99.8 (77.6)	Water	342	943
I / σ(I)	13.25 (2.19)	11.50 (2.21)	B-factor (Å^2)		
Completeness (%)	100 (100)	99.6 (99.7)	Protein	36.0 ± 8.9	28.8 ± 8.2
Redundancy	6.93 (6.86)	13.37 (13.45)	Ligand	-	57.3 ± 19.4
			Water	41.4 ± 8.8	43.2 ± 11.4
			RMSD		
			Bond length (Å)	0.0163	0.0199
			Bond angle (°)	1.31	1.93
			Ramachan-dran (%)	96.89 / 3.11 / 0.0	97.26 / 2.52 / 0.22
			Clashscore	16.61	16.73
			Rotamer outlier (%)	3.12	2.11
			Molprobity score	2.28	2.11

Both the apo form of human APT1 M60S mutant and the complex with 2BP crystallized well in conditions containing different polyethylene glycols (PEG). The overall structure of the protein is similar to the wild type of human APT1, having an average rmsd of 0.52 Å and 0.55 Å for the apo form and the 2BP complex of human APT1 M60S, respectively. The formation of the typical dimer[69] is observed in both crystal structures. In the apo form of human APT1 M60S, the second monomers of the two dimers of the asymmetric unit are rotated by 2.3˚ and 3.2˚, respectively compared to the apo form of human APT1 wild type. The 2BP complex of human APT1 M60S forms a similar dimer, on average rotated by 5.4˚ (4.9˚ and 5.8˚) compared to the apo form of human APT1 wild type. Comparing the apo form and the 2BP complex of human APT1 M60S to each other, both structures contain two dimers per asymmetric unit, but these dimers are not arranged similarly as the space group and unit cell differs between both crystals. Between the apo form and the 2BP complex of human APT1 M60S, the second monomer of the dimers are rotated by 3.9˚, and no significant overall change of the protein structure is caused by binding of 2BP, as both structures have an average rmsd of 0.47 Å over 221 amino acids.

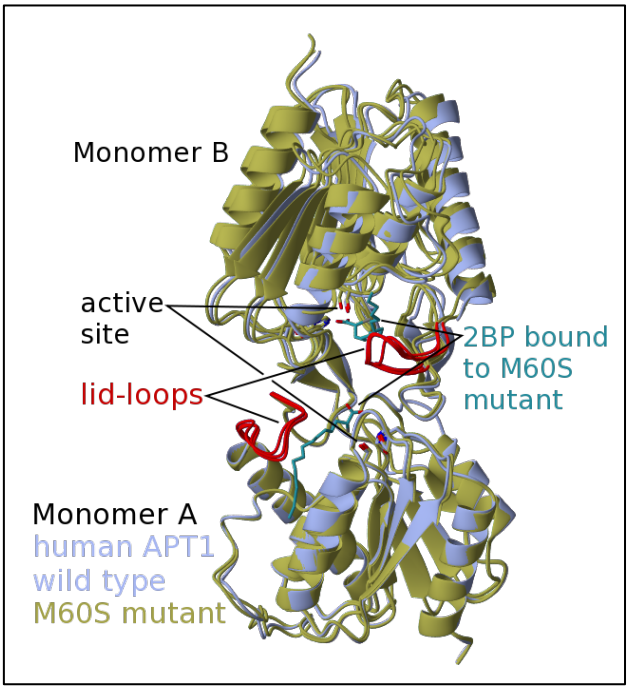

Figure 106: Comparison of the human APT1 wild type (blue) dimer with the dimers formed by the human APT1 M60S mutant as apo form and 2BP complex (yellow).

As the wild type dimer is still formed, the groove is still not completely accessible as it is blocked by the side chain of M60S, although to a lesser extent due to the shorter side chain (Figure 107). In the structure of human APT1 M60S in complex with 2BP, 2BP binding can be observed in the hydrophobic tunnel identical to the wild type structure (see 5.1.5). At the partially blocked groove, a short linear density can be observed. This density could correspond to a molecule of 2BP that was co-crystallized, or a molecule of PEG of the crystallization condition. This density lacks a forked head group, and no peak corresponding to the bromide atom was found in the anomalous map, thus a short PEG molecule that originates from the crystallization condition is most likely and was

fitted into the density. Interestingly, the structure of human APT1 M60S in the apo form did not contain a density in the groove, indicating that a (partially disordered) 2BP molecule is still a possibility. On the other hand, the observed difference could be due to the different size of PEG in the condition, as the apo form and complex crystallized in PEG 3000 and PEG 10,000, respectively.

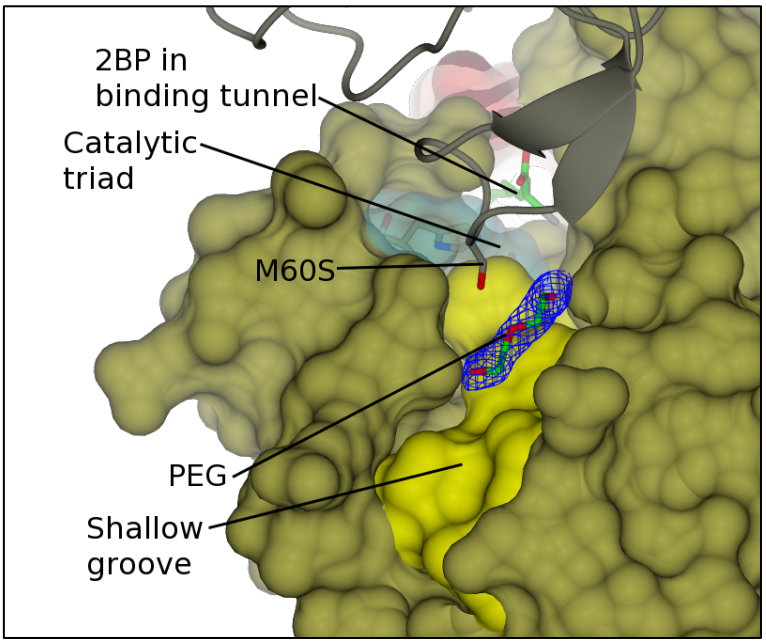

Figure 107: Human APT1 M60S (gold) in complex with 2BP(green, bound inside the tunnel) still forms the wild type dimer (dimer partner shown in grey) and contains a (partially) blocked groove (highlighted in yellow) next to the active site (cyan). The electron density ($2F_o$-F_c, blue, scaled to 1σ) of a short linear ligand is observed at the groove, and was fitted to a PEG molecule (green), but it could also correspond to a partially disordered 2BP molecule since no density was observed in the apo form.

Taken together, the M60S mutation in human APT1 does not change the dimer formed, and thus still partially blocks the groove with the – albeit shortened – serine side chain. A short, linear electron density was observed at the groove, lacking a forked head group and peak at the anomalous map, and was thus fitted to a molecule of PEG. As a further attempt to disrupt the dimer, a deletion of M60 was structurally investigated as described in the next chapter.

5.3.3 Crystal structure of human APT1 ΔM60 apo form and in complex with 2BP

The 2BP complex of human APT1 ΔM60 was prepared similarly to the wild type 2BP complex and the procedure is described there (see 5.1.5). Briefly, 1.3 mM protein was mixed with 5 mM 2BP and heated to 50 ˚C for 5 to 10 min, mixing the solution by gently tapping the tube with the finger. Screening for crystallization conditions for human APT1 ΔM60 as apo form and in complex with 2BP resulted in crystals under conditions containing short-chained PEGs shown in Figure 108. Crystals of the apo form also grow in the condition of the 2BP complex (and vice versa). Diffraction data was collected from crystals grown in the conditions shown in Figure 108 at X10SA at SLS, Villigen, and the apo form and complex diffracted to a resolution of 1.34 Å and 1.56 Å, respectively. Both crystals belonged to the space group P1 with a similar unit cell. The structures were solved via Molecular Replacement using human APT1 wild type as template. The structure of human APT1 ΔM60 apo form was refined to an R_{free} and R_{work} of 18.22% and 15.56%, respectively, and the 2BP

complex was refined to an R_{free} and R_{work} of 19.98% and 16.72%, respectively. The crystallographic statistics are shown in Table 22.

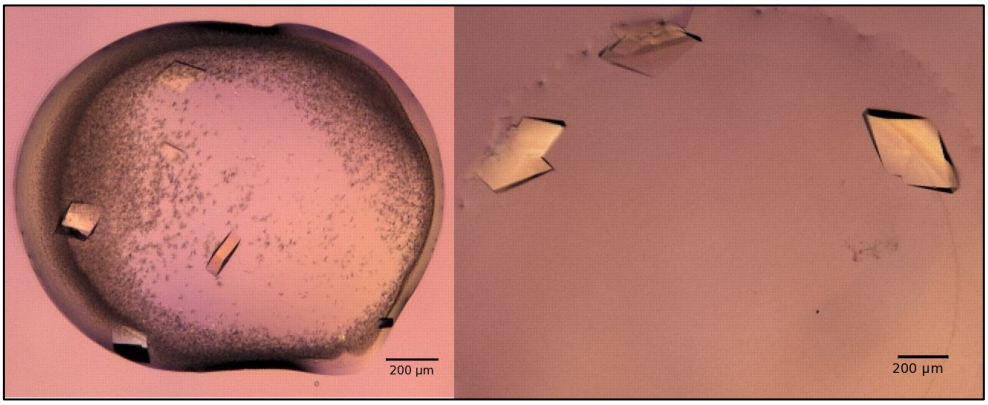

Figure 108: Crystallization condition of human APT1 ΔM60 containing 0.1 M Tris at pH 8.5, and 30% PEG 400 (PEG B9, apo, left) or 30% PEG 300 (PEG B8, 2BP complex, right), respectively. The complex was prepared as described in Chapter 5.1.5. No additional cryo protectant was added as the conditions are cryogenic. Photograph taken using Formulatrix Rock Imager.

Table 22: Crystallographic statistics of human APT1 ΔM60 in absence and presence of 2BP. Values for the highest shell are given in parentheses. Values for Ramachandran plot are given for favoured, allowed and outlier.

	human APT1 ΔM60 apo	human APT1 ΔM60 +2 BP		human APT1 ΔM60 apo	human APT1 ΔM60 +2 BP
Data collection			Refinement		
Space group	P1	P1	Resolution (Å)	35.63 - 1.34	35.71 - 1.56
Cell dimensions			Number of Reflexes	157075	97589
a, b, c (Å)	39.66, 39.67, 69.70	39.71, 39.76, 69.87	R_{work}	16.99 (18.6)	17.12 (16.8)
α, β, γ (°)	86.95, 88.91, 63.95	89.07, 87.10, 63.92	R_{free}	19.68 (23.1)	20.46 (21.5)
Resolution (Å)	50 - 1.34	50 - 1.43	Number of Atoms		
Monomers / au	2	2	Protein	3293	3413
Wave length (Å)	0.91939	0.91939	Ligand/Ions	0	67
CC $^1/_2$	99.7 (93.0)	99.7 (97.7)	Water	577	293
I / σ(I)	12.18 (4.03)	15.88 (6.5)	B-factor (Å^2)		
Completeness (%)	91.7 (86.5)	78.8 (36.0)	Protein	13.6 ± 4.8	14.1 ± 5.0
Redundancy	2.48 (1.84)	1.79 (1.68)	Ligand	-	29.4 ± 10.4
			Water	30.5 ± 10.7	23.6 ± 6.7
			RMSD		
			Bond length (Å)	0.0216	0.0204
			Bond angle (°)	1.88	1.70
			Ramachan-dran (%)	98.21 / 1.79 / 0.0	97.14 / 2.86 / 0.0
			Clashscore	12.36	11.85
			Rotamer outlier (%)	0.86	2.15
			Molprobity score	1.60	2.00

Both the apo form and the complex of human APT1 ΔM60 contain two monomers per asymmetric unit, and in contrast to human APT1 M60S, the dimer arrangement differs from the human APT1 wild type dimer[69] by a rotation of 136˚ of the second monomer. Since the crystallization conditions do not differ significantly in pH, salt or precipitant from other conditions that contain the wild type dimer, the rotation of the second monomer is likely to be caused by the ΔM60 mutation, In the wild type, the M60 side chain is located at the groove of the neighbor molecule in the “standard” dimer. The comparison to the human APT1 wild type dimer and the new interface is shown in Figure 109.

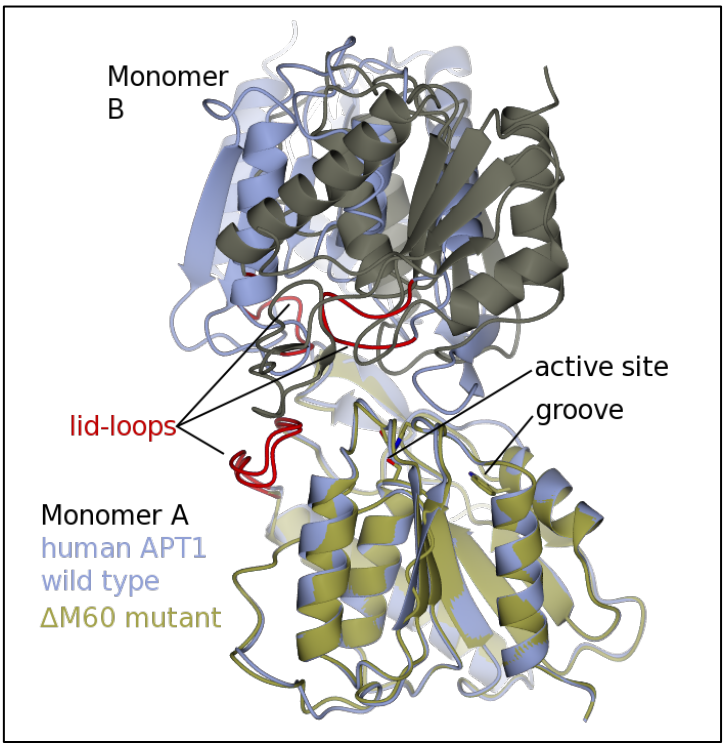

Figure 109: Comparison of the human APT1 wild type (blue) dimer with the largest non-crystallographic interface in the crystal of human APT1 ΔM60 mutant (yellow). Monomer B of the ΔM60 mutant is rotated by 136˚ compared to the wild type dimer.

The rotation of the second monomer of human APT1 ΔM60 moves the (in the wild type) M60 containing “foot-rest” loop away from the shallow groove, which is now occupied the side chain of M202. In the new dimer, M202 does not block the groove to the same extent as M60 of the wild type as it binds closer to the active site, still, it reduces the space available at the groove and the passage to the active site and binding tunnel is not free, as shown in Figure 110. The dimer is symmetric, so both binding sites are buried equally. Both in the apo form and the 2BP complex, a linear density can be observed close to the indole side chain of W32, comparable to the M60S mutant (compare Figure 107). A bifurcated density or an anomalous signal of bromide could not be detected at the binding groove. As this electron density is present in both the apo form and the 2BP complex, it probably corresponds to a molecule of PEG from the crystallization condition.

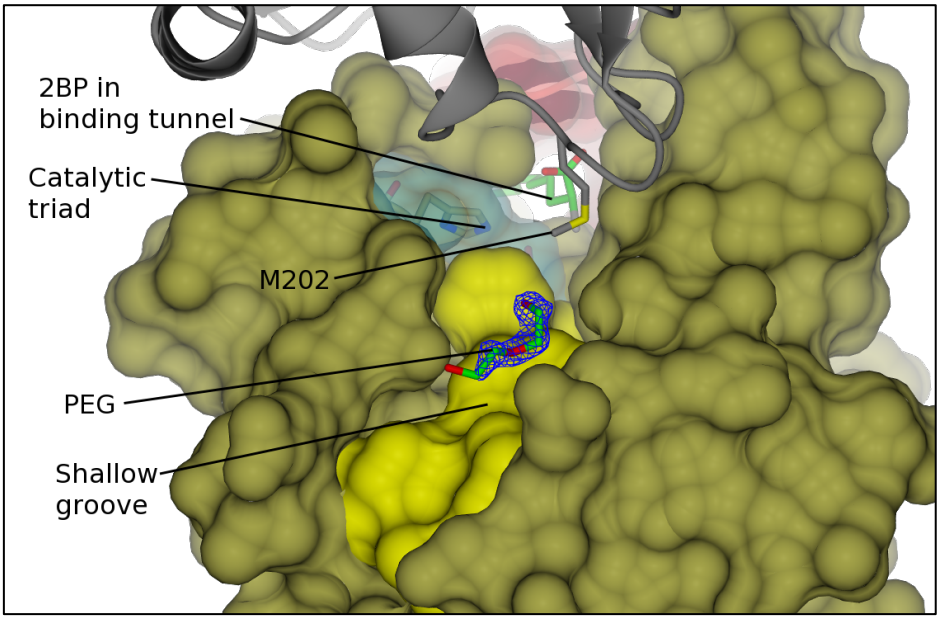

Figure 110: Human APT1 ΔM60 (gold) crystallized in complex with 2BP. Due to the new dimer orientation, M202 of the dimer partner (grey) is located at the groove (yellow), narrowing the connection between the groove and active site (cyan). 2BP (green) binds inside the binding tunnel, but the electron density at the groove (2Fo-Fc scaled to 1σ shown) is present in both the apo form and the 2BP complex, and thus was fitted with a short PEG molecule.

Darius Bothe also tried soaking and co-crystallization with various alkylated peptides that he synthetized during his thesis, but no peptide complex structure of any human APT1, neither wild type nor ΔM60S mutant, could be obtained [100].

A human APT1 ΔM60 structure co-crystallized with a peptide and solved from a crystal grown in a PEG-free condition containing 0.1 M imidazole at pH 6.5 and 1.0 M sodium acetate as precipitant (Qiagen screen Core3 E10) showed the presence of water molecules in the groove, but no electron density of a peptide (data not shown). This supports the conclusion that in the structures obtained from PEG-containing crystallization conditions presented here, PEG and not 2BP is binding at the groove, most likely not due to a higher affinity but rather due to the higher concentration.

Since M202, which is blocking the groove of the human APT1 ΔM60 mutant, is located next to H203 of the catalytic triad, a M202 deletion mutant seemed to be likely to alter the proteins structure and function too much, therefore, the less drastic M202A mutation was chosen. The human APT1 ΔM60 + M202A double mutation was cloned, purified and screened for crystallization conditions as described in Chapter 5.3.4.

5.3.4 Crystal structure of human APT1 ΔM60+M202A

The double mutant was subjected to screening for conditions suitable for crystallization as apo form and in complex with a hexadecylated N-terminal APT1 peptide (see Figure 113). Two well diffracting crystals of human APT1 ΔM60+M202A grew in Core2 G8 containing 0.16 M $(NH_4)_2SO_4$, 0.08 M NaAc pH 4.6, 20% PEG 4000, and 20% glycerol (Crystal form 1) and Core3 D1 containing 1 M K Na tartrate, 0.2 M NaCl, and 0.1 M imidazole at pH 8.0 (Crystal form 2). Crystal form 1 was isolated in a thin liquid film of reservoir without an additional cryo protectant. Crystal form 2 was cryo-protected using perfluorated polyether of 2900 Da average molecular weight as cryo oil.

Diffraction data of both crystals was collected on a Nonius microstar rotating copper anode and detected on a mar345 dtb image plate detector in-house at MPI Dortmund. Data processing was carried out as described in Material and Methods; the structures were solved via Molecular Replacement using human APT1 wild type as template, and roughly refined to a resolution of 2.2 Å. The preliminary crystallographic statistics are shown in the following Table 23.

Table 23: Crystallographic statistics of both human APT1 ΔM60+M202A. Values for the highest shell are given in parentheses. Values for Ramachandran plot are given for favoured, allowed and outlier.

	human APT1 ΔM60+M202A (Crystal 1)	human APT1 ΔM60+M202A (Crystal 2)		human APT1 ΔM60+M202A (Crystal 1)	human APT1 ΔM60+M202A (Crystal 2)
Data collection			Refinement		
Space group	P1	C2	Resolution (Å)	36.44 - 2.22 (2.28 - 2.22)	35.86 – 2.22 (2.35 - 2.22)
Cell dimensions			Number of Reflexes	33429 (5033)	9627 (1403)
a, b, c (Å)	41.64, 68.18, 76.23	68.00, 41.46, 71.96	R_{work}	22.91 (26.1)	33.87 (40.8)
α, β, γ (°)	112.15 104.31 89.91	90.00, 94.68, 90.00	R_{free}	31.05 (38.9)	37.74 (42.5)
Resolution (Å)	36.44 - 2.22 (2.36 - 2.22)	35.86 - 2.22 (2.28 - 2.22)	Number of Atoms		
Monomers / au	4	1	Protein	6761	1632
Wave length (Å)	1.5418	1.5418	Ligand/Ions	76	0
CC ½	99.7 (97.1)	99.0 (88.0)	Water	203	0
I / σ(I)	11.45 (6.05)	7.25 (3.21)	B-factor ($Å^2$)		
Completeness (%)	90.4 (84.6)	95.5 (87.7)	Protein	18.9 ± 8.7	33.6 ± 13.6
Redundancy	2.14 (2.05)	4.23 (3.78)	Ligand	43.0 ± 11.5	-
			Water	25.1 ± 11.6	-
			RMSD		
			Bond length (Å)	0.013	0.011
			Bond angle (°)	1.670	1.518
			Ramachan-dran (%)	94.98 / 4.24 / 0.78	92.66 / 5.05 / 2.29
			Clashscore	21.27	16.48
			Rotamer outlier (%)	8.13	5.29
			Molprobity score	2.86	2.73

The crystal structure of human APT1 ΔM60+M202A crystallized in P1 (crystal form 1) contains four monomers per asymmetric unit. The largest interface formed in this crystal is rotated and tilted by 138° compared to the wild type of human APT1 (Figure 111A). A comparison of the interface of human APT1 ΔM60 (see Chapter 5.3.3) and human APT1 ΔM60+M202A shows that these interfaces are not identical, but the second monomer is rotated further by about 10° (see Figure 111C). The overall structure of human APT1 ΔM60+M202A mutant is not altered from the wild type, having an rmsd of 0.56 Å over 218 amino acids.

In crystal form 2, which belongs to space group C2, the monomer of the asymmetric unit forms a dimer with a crystallographic symmetry mate, and is again rotated by 138˚ compared to the wild type of human APT1. Despite the different space group, the interfaces formed in both crystal forms of the ΔM60+M202A mutant are identical and differ only by 1.4˚ rotation, which is in the range observed for multiple dimers within the asymmetric unit of one crystal.

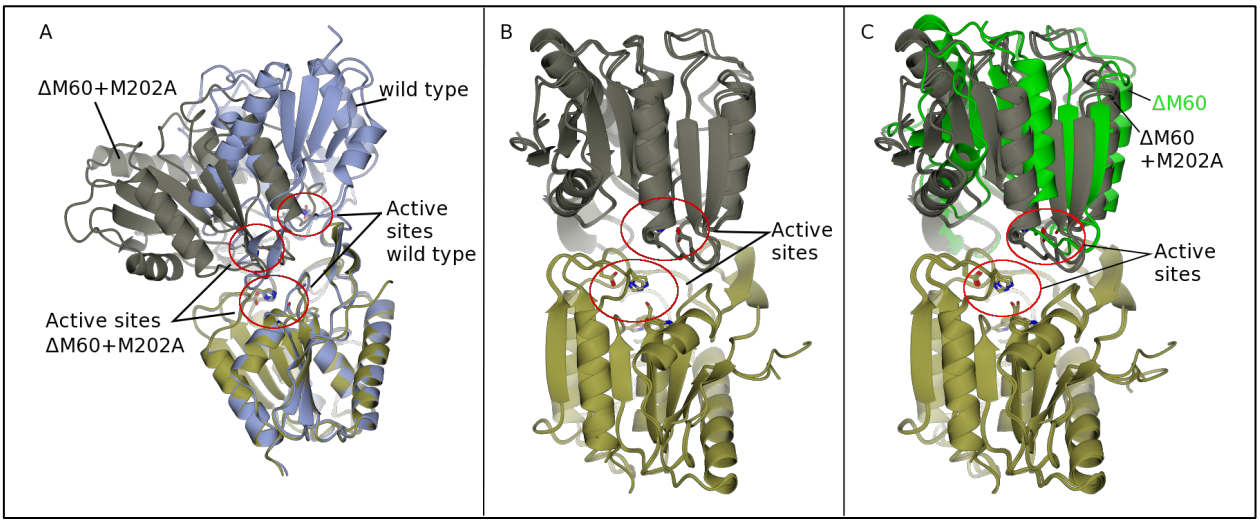

Figure 111: Panel A: Comparison of the human APT1 wild type dimer (blue) and human APT1 ΔM60+M202A (yellow/grey). The second molecule of the dimer is tilted by 138˚ compared to the wild type. Panel B: Comparison of the dimer of both crystal structures obtained for human APT1 ΔM60+M202A. The second monomer of the dimer is rotated by 1.4˚ between both structures. Panel C: Comparison between human APT1 ΔM60+M202A and ΔM60 (second monomer shown in green), the second monomer is rotated by 10˚ between the different mutants. The active sites are encircled in red.

The connection between the groove and the active site is not completely blocked due to the shorter side chain of the M202A mutation, but in the crystal, it forms a restricted entrance with a diameter of less than 5 Å. In addition, P170 of the dimer partner narrows the gap between the two molecules deeper buried in the interface and closer to the active site. In crystal form 1, a weak elongated electron density is observed at the binding tunnel, but not at the groove. The density inside the tunnel could fit the hexadecyl chain or palmitate, but electron density for the rest of the peptide is lacking. PEG has not been observed to bind inside the tunnel, and the condition of crystal form 2 is PEG-free. It is possible that the density could be caused by a co-purified fatty acid as it has been found in *X. tropicalis* APT1 and some human APT1 crystal forms (private communications Marco Bürger).

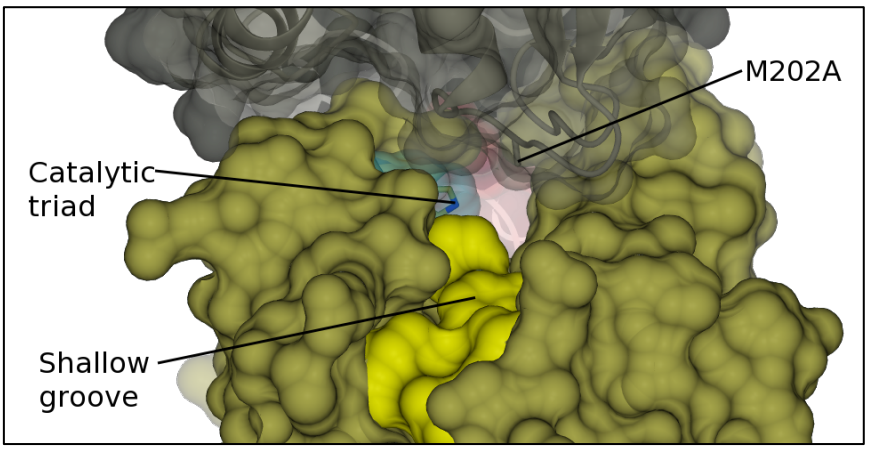

Figure 112: View on the tunnel entrance of human APT1 ΔM60+M202A (gold) that is restricted in size by the second monomer as observed in two crystal structures. The space between the groove (yellow) and the catalytic triad (cyan) is narrowed but not completely blocked by M202A of the dimer partner (shown in grey).

Summarized, although some conditions of the protein - peptide mixture resulted in crystals, no structures contained clear evidence that the peptide was bound.

Even the double mutant ΔM60+M202A cannot provide enough space to accommodate a hexadecylated peptide in the binding groove (with the aliphatic tail inside the hydrophobic binding tunnel). The amino acids of the second molecule of the dimer narrowing the connection between groove and active site are M202A and P170. Both amino acids are flanking positions of the catalytic triad (S114, H203 and D169), so a deletion mutation is not feasible due to the high probability of causing serious effects on the protein's structure. Since the hexadecylated cysteine of the peptide is not at the very terminus of the peptide, even more space would be required in the crystals to accommodate residues. The crystallization project was stopped at this point due to the limited chances of success. Therefore, binding of a hexadecylated peptide was investigated via the fluorescence based activity assay as described below.

5.3.5 Inhibition of human APT1 by a hexadecylated peptide

A hexadecylated decapeptide with the N-terminal sequence of human APT1 (M_{palm}CGNNMSTPL, shown in Figure 113) was synthesized by Philipp Cromm as described in Material and Methods (see Chapter 7.6.4). For reasons of stability, a hexadecyl thioether was chosen instead of the natural palmitoyl thioester at the side chain of Cys2. In vivo, the human APT1 N-terminus can be palmitoylated and is probably hydrolysable by the protein, thus it cannot be used for crystallization. The first 10 N-terminal amino acids of human APT1 were chosen since it was proposed that human APT1 can de-palmitoylate itself and human APT2[98,99]. Darius Bothe worked in parallel on the co-crystallization with different Ras-peptides in his master thesis[100].

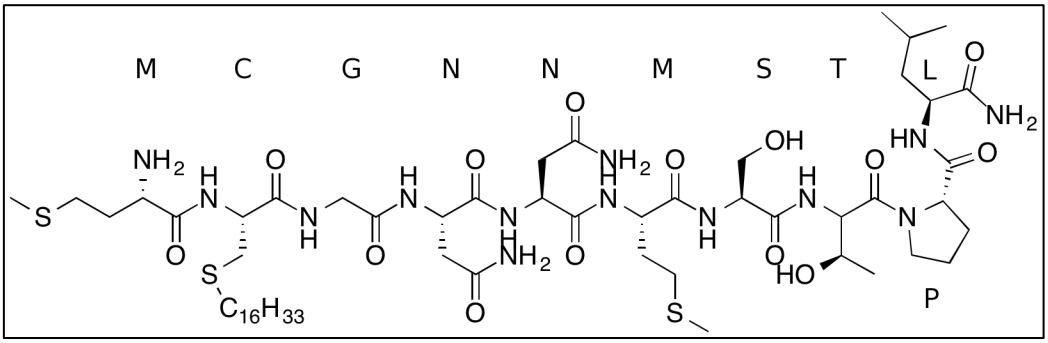

Figure 113: Structure of the hexadecylated N-terminal human APT1 peptide, which covers the first 10 amino acids. The C-terminus is amidated to increase solubility in aqueous buffer. For stability reasons, Cys2 was modified as a hexadecyl thioether instead of the natural palmitoyl thioester. Figure created using ChemBioDraw 13.

The peptide was tested on its inhibitory potency on human APT1 ΔM60 using OPTS (commercially available from Sigma Aldrich) as a substrate. The activity assays was performed as described in Material and Method (Chapter 7.5.2). The ΔM60 mutation of human APT1 was chosen for this assay due to the expected reduced stability of the protein dimer (see Chapter 5.3.3) and thus increased accessibility of the groove. The ΔM60+M202A mutant was not available at the time the assay was performed. The result of the measurement is shown in Figure 114. Biochemical activity of human APT1 is inhibited by the hexadecylated peptide in a concentration-dependent mechanism. The IC_{50} of the peptide to human APT1 ΔM60 can be estimated from the three replicates of the measurements to be in the range between 20 to 80 nM. These results are preliminary and the assay should be optimized and repeated to validate and further refine the IC_{50} value. The very strong inhibitory effect of the hexadecylated peptide indicates a binding mode blocking the active site. The aliphatic tail is expected to bind inside the tunnel, and if the high affinity proves to be true, the peptide moiety confers additional

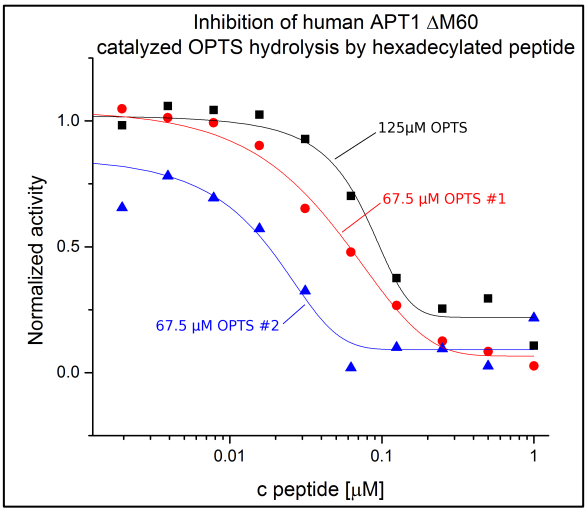

Figure 114: Inhibition of human APT1 ΔM60 catalyzed OPTS hydrolysis by the hexadecylated peptide. The three independent measurements give differing high-affinity IC_{50} values in the range between 20 to 80 nM and confirm the inhibitory effect of the hexadecylated peptide. Data evaluated using Microsoft Excel and plotted using Origin Pro.

In the future, peptide binding at the groove could be verified via intrinsic tryptophan fluorescence measurements using the human APT1 W140F mutant (see Chapter 5.1.7). An unmodified peptide could be used as control.

Summarized, all attempts to co-crystallize or soak a peptide into human APT1, either wild type or a mutant have failed to obtain a crystal structure with unambiguous electron density proving the complex formation so far. One reason might be that the binding sites in the crystal are obstructed by dimer formation. High-affinity binding of a hexadecylated peptide near the active site could be shown via its concentration dependent inhibition of human APT1 ΔM60.

5.4 Analysis of the dimer interface of lid-loop mutants and point mutations

In crystals of human APT1 wild type, the active site is buried in the interface of a dimer (see Figure 11) formed in all structures solved to date including the published structure of human APT1 wild type ([58], PDB ID: 1fj2). The relative position of the second molecule of the dimer mostly differs by a few degrees in various crystals obtained under different, mostly PEG containing conditions, but the analysis of structures containing multiple dimers in the asymmetric unit shows that these usually also vary by a few degree (see human APT1 L58A, Chapter 5.2.3). In contrast, the wild type structure of human APT1 published in 2000 (PDB ID 1fj2, [58]) shows a rotation of 112° compared to the "standard" dimer found in this work as well as in earlier work [69]; the N-terminal cloning artifact of the construct of the published structure was proposed to cause this rotation.

To further investigate the properties of this dimer interface, the binding energy of the interfaces of human APT1 wild type and mutants were calculated using PISA[97] of the CCP4i program package[101]. The ΔG value given by PISA for each interaction surface is a prediction of the free energy generated upon complex formation via this interface. The ΔG value depends on the size of the hydrophobic interaction surface, but the stabilizing effect of hydrogen bonds and salt bridges (though both are reported) are not considered in the prediction. The free solvation energy ΔG can be used as rough estimate of the binding strength. Based on this calculation, PISA offers a prediction if the quaternary complex could potentially be stable in solution.

All lid-loop mutations described in Chapter 5.2 were investigated with respect to the interfaces formed in the crystal (Table 24). The rotations compared to the typical dimer of human APT1 wild type are listed in the last column. The interfaces of the wild type structures of human APT1 and APT2 solved by Marco Bürger[69] are used as reference.

In human APT1, mutations L58A, L171A, and L171V have no strong effect on the conformation and flexibility of the lid-loop or the overall structure of the protein, and do not significantly change the dimer formed in crystals. In contrast, the human APT1 L73A mutant crystallizes as a monomer in the asymmetric unit. The side chain of L73 is crucial for stabilization of the lid-loop in the wild type conformation, and apparently the lid-loop is essential for the formation of the canonical dimer as its disturbance destroys the dimer (see Figure 66). The human APT1 L73A - 2BP complex shows that the hydrophobic tunnel can be reformed upon ligand binding and contains a larger crystal contact, but this interface is rotated by 113° compared to the typical dimer of the wild type apo form of human APT1, and is similar orientation as PDB ID 1fj2 [58]. The same effect on the crystal interfaces has been observed for the LP insertion mutant that crystallizes as monomer in the same space

group with similar interfaces as human APT1 L73A apo form (see Figure 78), although the conformation of the lid-loop differs between both mutants. Interestingly, human APT1 ΔL73S74 that contains the shortened lid-loop still forms the "standard" dimer comparable to the wild type (see Chapter 5.2.8), while the ΔS74P75 mutation that has a similarly shortened lid-loop crystallizes via different crystal interfaces (see Chapter 5.2.10).

The results show that the human APT1 wild type dimer and similar dimer formed by various mutants are comparably stable, as derived from the calculated ΔG of about -16 kcal/mol. The mutants forming other crystal contacts close to the hydrophobic patch show that these crystal contacts are smaller and thus less strong than the wild type dimer. This is also illustrated in Figure 115.

Table 24: Calculated free solvation energy of the dimer interface of the human APT1 wild type forming the canonical dimer and lid-loop mutants as well as mutations designed to alter dimer formation. The proteins written in *italics* do not form a single large interface similar to the wild type, but two smaller interfaces. If the asymmetric unit contains more than one dimer, the range of the interface size and free solvation energy is given. Values calculated using PISA[97] of the CCP4I suite[101].

dimer interface	Area [Å^2]	ΔG [kcal/mol]	H-bonds	Salt bridges	Rotation [°]
hAPT1 wt (crystal form P1, standard dimer, [69])	810	-16.2	2	0	-
hAPT1L171V	777	-15.4	2	0	1
hAPT1 L171A	809	-15.3	2	0	6.3 – 7.1
hAPT1 L58A	810 - 844	-16.7 / -18.1	2	0	5.6 – 7.9
hAPT1 ΔL73S74	790 - 856	-16.2 / -17.6	4 / 6	0	9 – 11
hAPT1 M60S	737	-13.2	5 / 3	0 / 0	2.7 – 5.3
rotated dimer interface					
1fj2	1170	-27.6	4	0	136
hAPT1 L73A + 2BP	996 - 1056	-23.4 / -25.3	2 / 4	0	138 (as 1fj2)
hAPT1 ΔM60	601	-10.1	2	0	136
hAPT1 ΔM60+M202A	754	-12.0	5	0	138
human APT2 wt	1045	-27.2	2	0	167
Monomers	Crystallographic interfaces area [Å^2]				
hAPT1 L73A	478 - 540	-4.4 / -8.0	3 / 4	1 / 2	-
hAPT1 +LP	417 - 578	-4.3 / -9.4	3 / 4	0 / 1	-
hAPT1 ΔS74P75	410 - 470	-4.8 / -8.3	1 / 3	0 / 2	

As described in Chapter 5.3, the groove of human APT1 wild type is blocked by the second monomer of the dimer. To enable crystallographic investigations of the groove as potential binding site for peptides, mutants of human APT1 were designed to interrupt the dimers and increase the space to enable peptide binding. The truncation of M60 side chain to serine did not change the dimer, but reduces the buried interface area and thus the calculated free solvation energy of this interface (see Table 24). The deletion of M60 further weakens the interaction and causes the protein to crystallize with a different dimer interface that is rotated by 136°, as shown in Chapter

5.3.3. In this new dimer, the groove now hosts the side chain of M202 instead of M60. Shortening the side chain of M202 to alanine in addition to ΔM60 causes the new dimer to slightly rotate further by 10˚ compared to the human APT1 ΔM60 mutant, but the groove is still partially blocked. The free solvation energy is increased due to the larger interface (which in addition also contains more salt bridges, see Table 24). The dimer with the smallest buried interface is formed by human APT1 M60S with a ΔG of 13.2 kcal/mol, indicating that the side chain of M60 has a strong contribution to the formation of the wild type dimer (ΔG of -16.2). Deletion of M60 also shortens the loop next to the lid-loop, and reduces the buried area of the dimer interface. The additional truncation of the M202 side chain to alanine in the ΔM60+M202A mutant increases the size of the buried interface slightly and stabilizes the rotated dimer.

The structure of human APT2 was solved by Marco Bürger in his thesis[69]. The crystallographic dimer interface of human APT2 is larger, and a higher ΔG of -27.2 kcal/mol has been predicted by PISA. PISA predicts the dimer of human APT2 to be stable in solution. However, AUC experiments determined human APT2 as monomeric in solution[69], revealing the limitation of the quaternary complex prediction by PISA.

A superimposition of the dimers comparable to the wild type of human APT1 (blue) is presented in Figure 115A, and contains human APT1 L58A, L171A, L171V, ΔL73S74, and M60S mutants. The alternative dimer-like contacts are shown in Figure 115B, superimposed with the wild type are human APT1 ΔM60, L73A+2BP and human APT2. Their individual rotation compared to the wild type is given in Table 24.

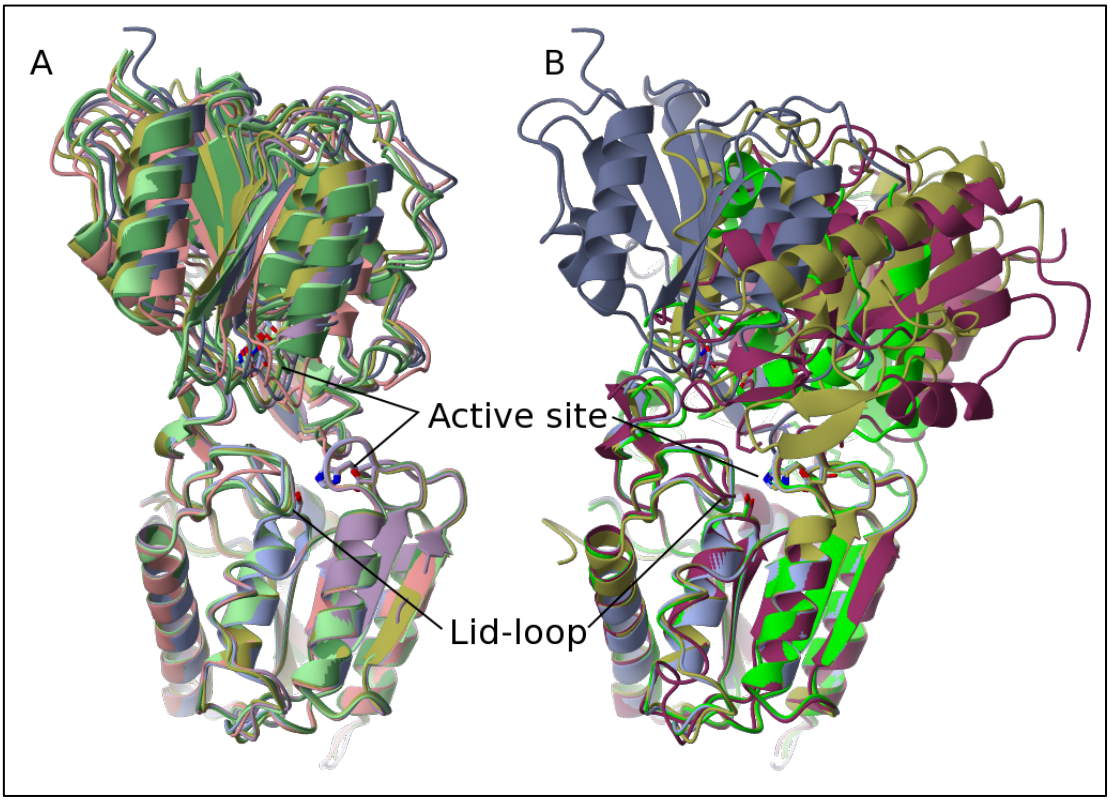

Figure 115: Superimposition of the typical human APT1 wild type dimer and mutants. Panel A shows the human APT1 wild type dimer (blue, from [69]), superimposed with L58A(light green), L171A(green), L171V(purple), ΔL73S74(salmon), and M60S(gold) mutants. Panel B shows the wild type dimer in blue, superposed with ΔM60 (gold), and L73A+2BP (neon green) mutants and human APT2 (maroon). Human APT1 L73A + 2BP forms the same dimer as the published structure of human APT1 (PDB ID 1fj2, not shown).

5.4.1 Analysis of the interface formed between the lid-loop and the core of APT in human APT1 wild type and lid-loop mutants

PISA[97] was used to analyze the influence of the mutations on the binding strength of the lid-loop of human APT1. The calculations were performed using modified structure files, as described in detail in Material and Methods Chapter 7.7. Briefly, the lid-loop was given a different Chain ID to be treated as a different molecule not covalently attached to the core protein (by deleting D69 and D80 of the hinge regions). For comparison and to account for conformational changes of the lid-loop caused by the leucine to alanine mutations, the respective mutations were also done *in silico* by side chain truncation without further energy optimization on the apo structure of human APT1 wild type structure and used as theoretical value.

The data shown in Table 25 contains two parts of the lid-loop analysis. The first part investigates the importance of the three leucines L58, L73 and L171 on the interaction strength between the lid-loop and protein. The second part describes the more drastic mutations affecting the length of the lid-loop. In general, the interaction between the lid-loop and the core protein is reduced if one of the three leucines 58, 73 or 171 is mutated. The mutation of L58 and L171 to alanine only slightly decreases interaction area. The free solvation energy calculated from the actual crystal structure is always lower than the theoretical value, calculated from *in silico* mutations of human APT1 wild type. This is most likely caused by slight movements of the loops caused by the mutations.

In the second group, the lid-loop shows larger conformational changes. The side chain of L73 is located in the middle of the three leucines and stabilizes the lid-loop in the wild type conformation. Shortening the side chain of L73 results in the lid-loop folding into the hydrophobic tunnel as shown in Chapter 5.2.4, thus stabilizes the interaction with the protein due to the increased contact surface, which is confirmed by the significantly decreased ΔG value. Interestingly, in the structure of human APT1 L73A in complex with 2BP, the lid-loop is in a conformation comparable to the wild type (Figure 72), enabling a comparison of the lid-loops binding energy with other structures.

The ΔG of the L73A mutant (in complex with 2BP, to keep the lid-loop in the tunnel-forming conformation, see Chapter 5.2.5) has the weakest interaction (-3.8 kcal/mol vs. 6.9 kcal/mol of the wild type), although the confirmation of the lid-loops of human APT1 wild type and L73A mutant in complex with 2BP are in a comparable conformation (see Figure 73). This significant difference is not seen in the theoretical value obtained from the *in silico* L73A mutant.

The extended lid-loop of the +LP mutation occupies the hydrophobic tunnel with the side chain of the inserted L73 and L75 (wild type L73), thus increasing the interaction surface with the protein core. This stabilization of the lid-loop is also reflected in the decreased ΔG, which is the lowest of all mutants (-9.4 kcal/mol).

Shortening the lid-loop reduces the interaction surface and thereby also the binding strength. No significant difference in the ΔG is observed between both ΔL73S74 and ΔS74P75 lid-loop mutants, both are similarly increased compared to the wild type.

While the lid-loops of human APT1 wild type and all mutants except the shortened ΔL73S74 and ΔS74P75 are predicted to form stable complexes with the core protein in solution, the interaction of

the L73A mutant and the shortened lid-loops are weaker and a theoretical complex formation is not predicted. This suggests an increased flexibility as the result of the smaller interaction surface and less optimal substrate binding and catalysis, as shown in Chapter 5.2.13.

Table 25: Free energy of the lid-loop of human APT1 wild type and lid-loop mutants. The lid-loop was treated as separate molecule by changing the Chain ID and removing D69 and D80 of the hinge regions. The binding energy between the lid-loop and protein was calculated using PISA[97] available in the CCP4I program suite[101]. The influence of the three leucines L58, L73 and L171 on the binding energy of the lid-loop was additionally calculated from *in silico* mutants of the human APT1 wild type structure as theoretical values.

Group 1: wild type tunnel	Interface Area [Å^2]	Stable complex predicted?	ΔG [kcal/mol]	Theoretical ΔG [kcal/mol]	Number of H-bonds	Number of Salt bridges
hAPT1 wt	448	yes	-6.9	-6.9	3	1
hAPT1 L58A	452	yes	-4.5	-5.9	7	0
hAPT1 L171A	517	yes	-5.8	-6.6	5	1
hAPT1 L171A + *in silico* L58A	484	yes	-4.8	-5.5	5	1
hAPT1 L58A + *in silico* L171A	444	yes	-4.3	-5.5	7	0
hAPT1 L73A +2BP (2BP bound inside wild type-like tunnel)	452	yes	-3.8	-5.9	5	0
Group 2: lid-loop significantly changed						
hAPT1 L73A apo (lid-loop folded into the tunnel)	501	yes	-6.1	/	5	2
hAPT1 +LP	545	yes	-9.4	/	5	0
hAPT1 ΔL73S74	378	uncertain	-4.5	/	4	0
hAPT1 ΔS74P75	315	uncertain	-4.4	/	4	0

5.4.2 Comparing the lid-loop of human APT and lipases

Lipases contain large lids that cover the complete hydrophobic patch around the active site and exclude it from the solvent in their inactive state. Contact to (bio-) membranes triggers the opening of the lid and its attachment or insertion into the membrane to enable catalytic activity. It is tempting to assume that the lid-loop if APTs might have a similar role as the lid in lipases as regulatory element by e.g. inserting into the membrane or even opening up upon membrane association. Indeed the opm database (orientation of protein in membranes, [102]) predicts a partial insertion of APT into membranes. Therefore, in the following the properties of the lids of lipases and APT are compared. The $\Delta G_{transfer}$ values upon membrane insertion predicted from crystal structures available in the PDB database is taken from the opm database, and compared to the predicted dissociation energy of the lid-loop of APT and lipases using PISA as described in Chapter 7.7 of Material and Methods. In addition to APT, Table 26 shows the values of *Bacillus* and *C. rugosa* lipase in open and closed form, of cutinase, and of the (to human APT1) most similar esterase of *P. aeruginosa*. The *Bacillus* lipase is the structurally most similar mono-acylglycerol lipase to human APT1 (PDB structure similarity search), having an rmsd of 2.14 Å over 162 amino acids and 15.4%

sequence identity. The lipase of *C. rugosa* was chosen because of the availability of both open and closed state, and the reasonable similarity, having an rmsd of 2.5 Å over 172 amino acids and 11% sequence identity. The cutinase of *A. oryzae* was chosen due to the high similarity to APT and high resolution of the structure. The carboxyl esterase of *P. aeruginosa* is the protein with the most similar structure (rmsd of 1.31 over 206 amino acids and 34% sequence identity) found in the literature to human APT1, besides human APT2 and APTs of other organisms.

Table 26: Comparison of the free solvation energy ΔG of human APT1 dimer, the estimated free solvation energy of the lid-loop and the lid-loops of related lipases shown together with their theoretical membrane insertion energies as calculated for the opm database[102].

	Buried dimer area [Å^2]	Dimer ΔG [kcal/mol]	Buried lid-loop area [Å^2]	Lid-loop ΔG [kcal/mol]	ΔG [kcal/mol] opm database	Depth [Å] opm database
hAPT1 [69]	810	-16.2	448	-6.9	-4.7	9.6 ± 2.0 Å
Bacillus sp. monoglycerid lipase (PDB ID 4lhe, [56])	952	-12.5	952	-12.5	n.d.	n.d.
C. rugosa open (PDB ID 1lpp, [103])	monomer	monomer	lid opened	lid opened	-28.0	10.0 ± 0.4
C. rugosa closed (PDB ID 1trh, [104])	monomer	monomer	1132	-21.3	-7.4	4.0 ± 1.3
A. oryzae cutinase (PDB ID 3gbs, [105])	monomer	monomer	no lid	no lid	-12.6	11.2 ± 0.5
P. aeruginosa esterase (PDB ID 3cn9, [57])	monomer	monomer	no lid	no lid	-4.1	3.5 ± 2.1

The lid of the *Candida rugosa* lipase 1 (PDB ID 1trh, [104]) releases a ΔG of -21.3 kcal/mol upon binding to the core protein. The opm database[102] predicts a $\Delta G_{transfer}$ of -28.0 kcal/mol for the open form of *C. rugosa* lipase 1 (PDB ID 1lpp, [103]) upon binding to a biomembrane, while the closed form of the lipase (PDB ID 1trh, [104]) gains a $\Delta G_{transfer}$ of -7.4 kcal/mol. The opened lid and three other loops are predicted to be partially inserted up to 10 Å into the outer membrane, allowing the active site being placed directly at the membrane, while the penetration depth of the closed lid structure is significantly reduced and the active site residues moved away and shielded from the membrane. This emphasizes the energetic preference of the lid of lipases to open up upon membrane insertion and enables substrates to access the active site.

A comparison revealed that the interface between the large lid and the core protein of lipases, e.g. *Bacillus* sp. monoglycerol lipase (PDB ID 4lhe, [56]) is roughly comparable in size and free solvation energy to the dimer of human APT1 (ΔG of -12.5 kcal/mol and -16.2 kcal/mol, respectively). The *Aspergillus oryzae* cutinase 1 (PDB ID 3gbs, [105]) is used as example for an α,β-hydrolase active on long chained fatty acid esters, but lacking a lid that shields the active side from the solvent in the inactive state. Similar to APTs, this cutinase is predicted to be inserted into the membrane by 11.2 Å with the active site serine located at the membrane surface resulting in a $\Delta G_{transfer}$

of -12.6 kcal/mol. Other cutinases (PDB ID 1oxm, 3dcn, 4oyy and 5ajh) are also predicted to be partially inserted into membranes in a comparable depth with a comparable $\Delta G_{transfer}$. Inspections of wild type structures of cutinase published in the PDB database revealed that they contain one monomer per asymmetric unit. A detailed investigation [Jelsch1998] revealed that under certain conditions cutinases can form a head-to-head dimer with crystallographic neighbors, e.g. triggered by mutations or ligand binding[106]. However, the apo form of the wild type crystallizes as monomer, thus indicates a monomeric state and membrane association instead of a soluble dimer with a shielded active site (as a contrast to human APT1, which weak dimer has a K_D of 2.8 µM[69]).
Carboxyl esterase of *P. aeruginosa* (PDB ID 3cn9, [57]) (see Chapter 3.4) also lacks a lid and contains an open, solvent-accessible active site. The predicted $\Delta G_{transfer}$ of -4.1 kcal/mol upon membrane "insertion" of 3.5 Å could indicate a weak membrane attachment rather than a real insertion, but as esterases are inactive on long-chained fatty acid esters it is unlikely that this predicted interaction has a biological relevance at all.

The role of the lid-loop of human APT differs from the lid of lipases. In human APT, the lid-loop pre-forms a stable hydrophobic tunnel that coordinates the substrate close to the active site serine (see Chapter 5.2). The opm database predicts a $\Delta G_{transfer}$ of -4.7 kcal/mol upon 9.6 Å deep membrane insertion of human APT1. However, the prediction does not account for the potential flexibility of the lid-loop, which hypothetically could open up when inserted in a membrane (triggered by an unknown mechanism) comparable to lipases, and also resulting in a stronger interaction with the membrane, (see $\Delta G_{transfer}$ of *C. rugosa* lipase in open and closed form, Table 26). The $\Delta G_{transfer}$ upon membrane insertion of one protein can differ significantly depending on the state of the lid as seen from the *C. rugosa* lipase 1 ($\Delta G_{transfer}$ = -28.0 and -7.4 kcal/mol of open and closed lid, respectively). This potentially is also the case for APTs, as lid-loop opening was observed in one crystal structure of *Oryza punctata* APT[69], and could be a hypothetical secondary function of the lid in substrate extraction from membranes. This is pure speculation as no structure of human APT1 with an opened lid-loop is available in the literature and it is not possible to calculate the $\Delta G_{transfer}$ of own structures (e.g. *O. punctata* APT containing the opened lid-loop[69]). Furthermore, human APT has been reported to be palmitoylated at the N-terminus[98,99], which would increase the membrane affinity significantly.

6 Discussion

6.1 *S. cerevisiae* APT serves a model for structural investigation of inhibitor complexes

In this thesis, the putative Ras-regulator acyl protein thioesterases (APT) were investigated structurally and biochemically and co-crystallized with various inhibitors. APTs feature a pre-formed solvent-accessible hydrophobic binding tunnel that is a rare (and possibly unique) structural motif only found in APTs of different organisms. The tunnel is located next to the active site and was shown to be essential for the catalysis of long-chained fatty acid substrates, as the APT homolog of *A. thaliana*, SOBER1, which has a blocked tunnel is limited in its activity to shorter substrates[69]. Thus, it is assumed that the aliphatic moiety is bound inside the tunnel during catalytic hydrolysis. However, to my knowledge only one complex structure was known, the structure of *X. tropicalis* APT1 in complex with a co-purified palmitic acid / stearic acid mixture showing that the aliphatic product of the de-palmitoylation reaction indeed binds inside the hydrophobic tunnel[69].

Attempts to co-crystallize or soak covalent and non-covalent ligands or inhibitors into human APT1 or APT2 were not successful prior to this thesis as the active site is usually occluded in a dimer interface (see Figure 11). APTs of other organisms were structurally investigated before[69], and APT of *Saccharomyces cerevisiae* was found to crystallize in four different space groups, all with an accessible active site. The high sequence identity of 36% between yeast APT and human APT1 and the conservation around the active site (see Figure 23) justifies the use of yeast APT as a model for structural investigation of inhibitor binding.

Inhibitors of the palmostatin class were designed on basis of orlistat (see Figure 13) to covalently address human APT1 and APT2 without isoform specificity using a β-lactone core as nucleophilic trap for the active site serine and an aliphatic tail as substrate mimic. The complex of yeast APT with palmostatin B solved in this thesis provided evidence that the aliphatic tail of the covalent inhibitor is indeed located inside the hydrophobic tunnel (see Figure 30). As designed, the ester is formed upon opening the β-lactone core by the nucleophilic serine and can be regarded as a mimic of the covalent reaction intermediate, the palmitoylated serine (see Figure 7). Palmostatin B contains a bulky aromatic head group that structurally differs from the suspected natural substrates, a palmitoylated peptide or lysophosphocholine. Indeed, the aromatic head of palmostatin B has limited contribution to the binding affinity due to its rigidity and limitation in forming H-bonds (see Figure 30, Chapter 3.4.3). The high-resolution structure of the covalent yeast APT – palmostatin B complex provides an explanation why the enzyme regenerating hydrolysis reaction is drastically slower (half life of minutes, private communications with Christian Hedberg) than the turnover of a substrate (in the range of ~20 µsec, or 3.41 x 10^4 s^{-1}, see Table 7). As seen from the reaction mechanism schematically presented in Figure 7, the covalent reaction intermediate of APT is regenerated by a nucleophilic attack on the palmitoyl ester by a water molecule that is activated by

the histidine side chain of the catalytic triad. The position of this water molecule is occupied by the hydroxyl group of the β-lactone (see Figure 32), and thus probably slows down the off-rate of inhibitors of the palmostatin class that have the same chirality as palmostatin B. The β-lactone core and aliphatic tail is identical between palmostatin B and palmostatin M, which is reflected in a similar binding mode of this part of both inhibitors (compare Figure 33 and Figure 36) and a similar slow off-rate (communication with Stefan Baumeister). The head group of palmostatin was designed to mimic the charge and H-bond network expected to be formed by lysophosphocholine or a peptide backbone and is connected via a longer and more flexible linker than the head group of palmostatin B (see Figure 13). The interaction of the palmostatin M head group is influenced by crystal contacts in two of four monomers (see Figure 37), but confirms an interaction with the backbone amide of L23 of *S. cerevisiae* APT (see Figure 36) in the "free" monomer. The amino acids involved in the interaction with palmostatin M in the "free" monomer are conserved from yeast to human APT1 (Figure 23). Thus, the interaction with L23 of yeast APT is also possible in human APT1. The tunnel entrance is not conserved between human APT1 and yeast APT (see Figure 20), therefore the orientation of the tertiary amide head next to the aromatic W77, probably caused when the space in front of L23 is blocked by crystal contacts, has to be different in human APT.

Judging from the yeast crystal structure, inhibitors containing an extended head group that targets the conserved residues of the groove close to the active site might result in more potent inhibitors. The monomers of the palmostatin M complex are rearranged compared to the apo structure of yeast APT and orientated in such way that the active site is completely accessible through a large solvent channel (Figure 35).

The complex structures of yeast APT with palmostatin B and palmostatin M provide detailed insight on the inhibitor's binding mode on atomic level. Optimized inhibitors derived from the structures presented in this thesis should include a specific and strong-binding head group in a pre-formed active conformation that could be iteratively optimized via structure based rational design. The reduction of rotational freedom of the very flexible head group of palmostatin M either by introducing a macro-cycle could further increase the affinity below the current low nanomolar range[77]. However, the general problem of the inhibitor's inactivation after binding and release due to the hydrolysis of the opened β-lactone needs to be circumvented by introducing a reversibly binding and hydrolytically stable trap for the nucleophilic serine to extend the half-life of the inhibitor and thus its effect inside the body.

6.1.1 Cerulenin binding to human APT1 provides insight into epoxides as nucleophilic trap

Cerulenin is a commercially available natural product functioning as specific inhibitor of fatty acid synthases (see Chapter 3.4.4) and potent bacterial antibiotic, that has been investigated for its potential in treatment of cancer[107] and obesity[108]. The epoxide function of Cerulenin could act as a nucleophilic trap, similar to the β-lactone of palmostatin inhibitors, and its binding to human APT1 was verified via ESI-MS (see Figure 41). Since APT is not the biological target of Cerulenin, the

inhibitor is not adapted to the active site of APT.The crystal structure confirmed a covalent adduct at the active site, but also two unspecific adducts at surface exposed cysteine side chains (see Figure 45). Despite the reasonable resolution of 2.5 Å, the electron density of the Cerulenin adducts is not sufficiently clear to unambiguously define the binding mode of Cerulenin. Most likely a mixture of adducts at C2 and C3 carbon (see Figure 44) formed at the active site serine are observed in the crystal. Thus, the structure of the most probable complex was build according to slightly diffuse electron density and chemical knowledge, both supporting an opening of the epoxide by forming the ether bond to the active site serine at C3, leaving the hydroxyl group on C2 (compare Figure 45). This structure is different from a recently published covalent complex of Cerulenin with FabF published by Trajtenberg[85]. This FabF-Cerulenin complex is well described by the strong electron density and the high resolution (2.1 Å), and describes the covalent complex to form a hemiketal (PDB ID 4ls8, [85]). A hemiketal is expected to be unstable and its formation requires some intermediate rearrangements. Hemiketals are the result of an alcohol reacting with a ketone, not with an epoxide. The publication by Trajtenberg[85] lacks, as stated therein, a satisfying explanation for the formation of the O,S-hemiketal observed in the covalent FabF – Cerulenin complex, but it is suggested by the authors that Cerulenin might undergo some further rearrangements after initial binding, catalyzed by the FabF. The unambiguous electron density of the complex (PDB ID 4ls8) does not tolerate a different binding mode, but it is unlikely that APT can catalyze a similar rearrangement of unspecifically bound Cerulenin.

Despite the unspecific attack of the catalytic serine of APT on the epoxide of Cerulenin, the complex structure shows the potential of an epoxide as trap for the active site serine. In addition, Cerulenin is also bound by surface exposed cysteines. The reactivity of the epoxide of Cerulenin is increased by the flanking electron-drawing carboxyl and amide, and could potentially be modulated to create a more specific and less reactive inhibitor of APT by removing one of the carboxyl groups. On the other hand, high reactivity and a stable covalent adduct have a high potential to be cytotoxic, and thus limits a clinical application.

6.1.2 2-Bromopalmitate serves as a product mimic to investigate the binding to APT

Crystallographic investigations of the binding mode of the natural product palmitate to human APT1 were not available prior to this thesis. Surprisingly, a fatty acid was observed in a crystal structure only once in form of a co-purified in *X. tropicalis* APT1[69] where it was co-purified from *E. coli*. Mass spectrometry revealed that it was a 50:50 mixture of palmitic / stearic acid. Neither co-crystallization nor soaking approaches could obtain a complex of human APT with a fatty acid bound inside the pre-formed tunnel. At least one of the reasons probably is that long-chain fatty acids exhibit a low solubility in aqueous solutions. 2BP is a product mimic with high similarity to palmitate and increased aqueous solubility compared to unmodified fatty acids, despite the fact that its structure only differs by the additional bromine in α-position to the carboxylic acid. Indeed, mixing of 2BP with human APT1 wild type and mutants resulted in non-covalent complexes with near-complete occupancy of the ligand. 2BP is bound to APT1 with the aliphatic chain inside the tunnel while the

polar head is located at the active site at the entrance of the tunnel. The carboxylic acid forms H-bonds with the oxyanion hole (see Figure 50). The positioning of the inhibitor inside APT leads to a model where the entrance acts as a funnel for substrates and inhibitors and sterically restricts the fatty acid moiety to slide deeper into the tunnel. This hypothesis was investigated in detail in Chapter 5.2 and is discussed in Chapter 6.2 below.

A further advantage of 2BP in crystallographic studies is the anomalous signal of the α-bromide. This anomalous signal enabled us to discover two distinct binding modes of 2BP in the human APT1 wild type protein (see Figure 49) with either the carboxylic acid or alternatively the α-bromide coordinated by the oxyanion hole (which obviously cannot be observed for palmitate as it lacks a substituent at the α-position to the carboxylic acid). This structure confirms binding of the carboxylic head group inside the oxyanion hole, which usually stabilizes the tetrahedral intermediate of the opened ester during hydrolysis (see Figure 7). Heating the protein - 2BP mixture up to 50 ˚C before crystallization resulted in crystals of better quality and higher 2BP occupancy. The higher temperature increases the solubility of 2BP and the exchange dynamics of 2BP micelles potentially formed in aqueous suspensions. This interesting finding also raised the question if opening of the lid-loop can be thermodynamically triggered to facilitate binding of ligands inside the tunnel, inspiring the mutations targeting the flexibility of the lid-loop.

6.2 Analysis of the lid-loop

A lid-loop that pre-forms a solvent-accessible hydrophobic binding tunnel is a very rare (if not even unique) structural motif found only in acyl protein thioesterases. The exact function of the lid-loop and the substrate-binding tunnel has not been thoroughly investigated to date. So far, the lid-loop pre-formed the wall of the hydrophobic tunnel in all structures of APTs. Interestingly, in the crystal structure of an APT from *O. punctata* two of four monomers of the symmetric unit are found in a conformation with an opened lid-loop. This could be due to unusual crystal packing and/or the harsh crystallization condition at pH of 10.5 [69], or it might indicate a potential flexibility of the lid-loop that might even have a physiological relevance, e.g. an opening of the lid-loop upon membrane binding. It is unknown if the lid-loop is interfacially activated and facilitates substrate extraction from a hydrophobic environment like a cellular membrane in case of APTs natural substrates, or from a vesicle or micelle in a biochemical assay. In the first structural characterization of an APT (PDB ID 1fj2, [58]), the lid-loop is suggested to play a role in the dimerization of the protein. However, the dimer formed in crystals is changed when the cloning artifact is shortened[69], so the lid-loop is not the only factor that determines the dimer.,An accessible binding tunnel has been proven to be essential for catalysis by long-chained fatty acid substrates[69], the closing or shortening of the tunnel shifted the protein's specificity towards short-chained substrates, but its potential function in substrate coordination has not been investigated so far. Another role of the lid-loop could be the ejection of palmitate from the tunnel at the active site to

prevent product inhibition. This is in accordance with the fact that only one fatty acid complex structure of an APT (*X. tropicalis* in complex with co-purified palmitic acid / stearic acid) is known[69]. These potential functional properties of the lid-loop were investigated by introducing mutations into the lid-loop designed to affect its flexibility and length, thereby changing the shape of the binding tunnel formed by the lid-loop. The mutations on the lid-loop can be grouped according their type as described in Chapter 5.2: The first group contains single point mutations of one of the three leucines 58, 73 and 171 to test for their role in stabilizing the lid-loop of human APT1 in its wild type conformation. The second group contains mutants with extended or shortened lid-loop that cause a decrease of biochemical activity, by either blocking the tunnel with side chains or relocating the tunnel entrance. A complete truncation of the lid-loop in the third group leads to a drastically decreased biochemical activity of the protein and failed to crystallize so far. The three groups are described in more detail in the following.

6.2.1 The side chain of L73 is essential for a pre-formed tunnel

Human APT1 L58A or L171A mutants have no significant effect on the conformation of the lid-loop and the tunnel formed by the lid-loop (see Figure 63 and Figure 60, respectively). Biochemical activity is not significantly affected by shortening the L171 side chain, as the k_{cat} is 2.70 ± 0.20 s^{-1} x10^4 for the L171A mutant compared to 3.41 ± 0.22 s^{-1} x10^4 of the wild type in the PPTS assay (see Figure 57). However, the mutation of L73 located at the tip of the lid-loop enabled a previously not observed conformation of the lid-loop: in the crystal, the lid-loop of the L73A mutant has the Cβ of L73A pointing towards the solvent and P75 relocated into the tunnel (see Figure 67). This conformation change is enabled by the decreased stabilitzation of the lid-loop caused by the shortened L73 side chain, showing its crucial role in the formation of the wild type tunnel shape. The electron density for the lid-loop in the L73A crystal is well defined, and although the lid-loop is involved in two H-bonds with the crystal neighbor, it is unlikely that this conformation is a crystallization artifact. Human APT1 L73A forms different crystal contacts than the typical wild type dimer (see Figure 66), and an analysis of the crystal interfaces using PISA[97] predicts no complex formation via this interface in solution. The crystallization conditions are comparable to other conditions which resulted in well-diffracting crystals of human APT, containing short to mid-sized PEGs, low salt concentration and a pH between 6.0-8.5, so the changed crystal packing is not the result of a harsh crystallization condition, as potentially in the case of *O. punctata* APT[69]. This corroborates that the different shape of the lid-loop is caused by the lack of the L73 side chain. Apparently, the aliphatic side chain of L73 keeps the tip of the lid-loop in its position and rigid enough to prevent folding into the tunnel. L73 interacts with both L58 and L171, but a deletion of one of the latter is not sufficient to destabilize the lid-loop enough to bind inside the tunnel (see Figure 60 and Figure 63). A double mutation of L58A+L171A which might be in a similar conformation of the lid-loop of L73A would argue in favor of this hypothesis (not tested). The side chain of L73 also forms a part of the tunnel entrance (see Figure 56A). The shortened side chain of the L73A mutation results in a gap between L58 and L171 (see Figure 74). This gap widens the

entrance of the tunnel and enables the substrate to slide deeper into the tunnel, moving the thioester away from the active site into a most likely unproductive binding mode. Thus, the position of the ligand's head group differs between both complexes (Figure 73). The complex of human APT1 L73A with 2BP also has a weaker electron density than the 2BP complex of human APT1 wild type and lacks a strong anomalous signal, indicating a less defined binding of the ligand compared to the wild type complex. The importance of the defined conformation of the lid-loop is reflected by the lower biochemical activity. The activity of the L73A mutant is decreased to about 30% in case of the L73A mutant to a k_{cat} of 0.95 ± 0.06 s^{-1} x10^4 compared to a k_{cat} of 3.41 ± 0.22 s^{-1} x10^4 for the wild type in the PPTS assay (see Table 10). The biochemical data shows a reduced K_M of 0.94± 0.28 µM compared to 3.37 ± 0.77 µM of the wild type. K_M is defined as $K_M = (k_{off} + k_{cat}) / k_{on}$. Thus, the 4-fold reduced K_M is most likely the result of the significantly reduced activity (V_{max} 25% of the wild type) in combination with an only slightly increased dissociation rate (not quantified, see Figure 102).

6.2.2 The extended lid-loop blocks the binding tunnel

The extended lid-loop containing a +LP insertion between G72 and L73 was designed in analogy to the APT1 homolog of *A. thaliana*, SOBER1, that is impaired in catalysis of long-chained substrates due to its obstructed tunnel[69]. The crystal structure of the human APT1 +LP mutant showed that this insertion leads to a steric blocking of the tunnel by the side chains of L73 and L75 (Figure 79), comparable to *A. thaliana* SOBER1[69]. The opening and formation of the hydrophobic tunnel by rearranging the whole lid to enable binding of a long-chained fatty acid substrate poses an energetic barrier. However, while *A. thaliana* APT1 is fully inactive on substrates containing an ester longer than propionate [69], the extension of the lid-loop in human APT did not abolish activity on the long-chained substrate PPTS, but reduced it to ~25% of the wild type (see Figure 76). This residual activity indicates that the extended lid-loop is most likely still able to form a tunnel upon binding of a long, aliphatic substrate. A structure of the 2BP complex of the extended lid-loop mutant could not be solved so far, thus the binding mode of 2BP (or the test substrate PPTS) to the +LP insertion mutant remains unclear. Like the other mutants that have a reduced biochemical activity (L73A, ΔL73S74 and ΔS74P75), the extended lid-loop mutant of human APT1 shows a lower apparent K_M (see Table 13).

The reduced biochemical activity seen in reduced V_{max} (and k_{cat}, see Table 13) is most likely caused by the lower efficiency in productive binding of substrate molecules and stabilization of the transition state compared to the wild type. The 2-fold reduced apparent K_M (compared to the wild type) could result from the lower activity (V_{max}, see Figure 76), while the binding and dissociation rates are not significantly altered (not tested).

6.2.3 Shortened lid-loops still pre-form a short hydrophobic tunnel but fail to efficiently coordinate the substrate

The crystal structures of human APT1 ΔL73S74 and ΔS74P75 mutations were solved in the course of this thesis (see Chapter 5.2.8 and 5.2.10). In contrast, no suitable crystallizing condition could be identified for human APT1 ΔP75D76. Possible reasons for this are discussed further below in this chapter. Both available structures show that the shortened lid-loop pre-forms a tunnel in the absence of a ligand. The tunnel has a wider entrance and exit, as the shortened lid leaves a large gap between L58 and L171. This gap reduces the efficiency to coordinate the substrate next to the active site, shown by the structure of human APT1 ΔS74P75 in complex with 2BP, where 2BP is bound in multiple orientations (Chapter 5.2.8). The complex structure contains two monomers per asymmetric unit revealing three binding modes for 2BP (see Figure 89, Figure 91 and Figure 93). In monomer A, 2BP is bound in two partially occupied orientations that are occupied with a ratio of 60 to 40. The favored orientation is identical to the major conformation observed in human APT1 wild type with the carboxylic acid group of 2BP located in the oxyanion hole (see Figure 90). The second binding mode observed with the lower occupancy binds deeper inside the binding tunnel, with the head group located at the new entrance formed by the shortened lid-loop in front of W140 (Figure 91), the bromide of 2BP inside the hydrophobic tunnel, and the carboxylic acid of 2BP facing the solvent. Both binding modes show a strong electron density and anomalous signals for bromide at both positions. Monomer B contains electron density for one binding mode of 2BP, where the head group of 2BP is located at the enlarged tunnel **exit** instead of at the entrance close to the active site (see Figure 93). In this inverse binding mode, the carboxylate of 2BP is coordinated by the guanidine group of the R144 side chain located at the tunnel exit. The peak of the anomalous map for bromine is weaker in monomer B, which indicates that this binding mode is less occupied and might be in equilibrium with further less defined binding modes, most likely including a conformation of 2BP similar to the wild type complex. The fact that the shortened lid-loop enables multiple binding modes of 2BP that have the carboxylate dislocated from the active site strongly supports the hypothesis that the wild type tunnel shape formed by the lid-loop is essential for efficient substrate coordination.

The structure of human APT1 ΔL73S74 in complex with 2BP also shows that the new tunnel entrance allows 2BP to slide deeper into the tunnel. The human APT1 ΔS74P75 mutant is similar shape of the tunnel entrance despite the different deleted residues of the lid-loop (see Figure 97 and Figure 99). Thus, it is likely that the binding mode of ligands is similar in both mutants. A binding mode comparable to the one observed for 2BP is also plausible for the substrate PPTS. It is possible to place a hypothetical pyrene ring system on top of the deeper bound 2BP to simulate the ‘PPTS’ ester bound in an unproductive binding mode with the ester dislocated from the active site and thus unavailable for enzyme-catalyzed hydrolysis (Figure 100). In this hypothetical orientation, the aromatic pyrene ring system fits nicely into the gap between the aliphatic side chains of L58 and L171, and by interesting coincidence, one oxygen atom of a sulfonate group precisely fits inside the oxyanion hole next to the active site. This binding mode might be stabilized

by interactions between the aromatic pyrene ring and the hydrophobic side chains of L58 and L171. A second unproductive binding mode with the aliphatic chain sticking reversely in the binding tunnel with the pyrene rings of the substrate located at the exit of the tunnel is also thinkable, but less clear where the pyrene rings would be coordinated.

Both ΔL73S74 and ΔS74P75 mutants show a reduced V_{max} (and k_{cat}) in the activity assay (see Table 15) that can be explained by the reduced efficiency to coordinate a ligand or substrate molecule, as shown by the complex structure (see Figure 91). The ΔL73S74 and ΔS74P75 mutants show a 3- and 5-fold reduced apparent K_M, respectively (see Table 15). K_M is correlated to the affinity (K_D) under certain conditions (k_{off} >>k_{cat}), but these are not fulfilled (see Chapter 5.1.8). The reduced K_M could result from the strong reduction of activity (V_{max} or k_{cat}), while the dissociation (k_{off}) rate is less affected by the mutation (not quantified, compare Figure 102), since the PPTS substrate is stabilized in the gap between L58 and L171 (see Figure 100).

Extensive shortening or complete truncation of the lid-loop of human APT1, as tested with the ΔI71-S74, ΔL73-D76, and ΔI71-D76 lid-loop truncation mutants, results a reduced solubility, and these mutants could not be concentrated as high as the wild type or the shorter lid-loop mutants of human APT1. This indicates some tendency to aggregate during concentration of the protein, potentially due to formation of an even larger solvent-exposed hydrophobic patch due to the removed lid-loop that needs to be covered by intermolecular contacts. Moreover, no crystal structure could be obtained for any of the proteins, which argues for an unstable protein and/or unspecific aggregation. Without a lid-loop, the formation of a proper hydrophobic tunnel is impossible, probably leading to unspecific and unproductive binding of the substrate on the remaining surface the forms the inner wall of the wild type binding tunnel. This hypothesized unspecific interaction with the substrate is reflected in a strong decrease of v_{max}. The human APT1 Δ71-76 truncation mutant shows a residual activity of only 3% compared to the wild type using PPTS as test substrate (see Table 19). Protein aggregation via the hydrophobic surface could block the active site and further reduce the activity.

6.2.4 The wild type lid-loop stabilizes ligand binding

Stopped Flow measurements using the intrinsic tryptophan fluorescence of human APT1 reveal a slower binding rate (k_{on}) of 2BP by human APT1 Δ71-76 mutant than for the wild type (see Figure 101). The 2BP binding rate of the lid-loop lacking mutant is faster by orders of magnitudes than binding detected at the groove using the human APT1 W140F mutant (compare Figure 54 and Figure 101), thus the signal corresponds to the new and open hydrophobic patch. This is counter-intuitive, as the open hydrophobic patch of the lid-loop lacking ΔI71-D76 mutant is expected to be more accessible than the narrow tunnel, and thus show a faster binding rate. However, the new hydrophobic patch most likely enables unspecific binding distant to W140, thus causing no decrease of the fluorescence signal. Over time, the unspecifically bound ligand rearranges itself closer to the side chain of W140, and thus the ensemble causes a slow binding signal. The reduction of the binding rate could be also caused by aggregation of the Δ71-76 mutant via the new

hydrophobic patch, thus being dependent on the dissociation of these aggregates. This could be investigated by analytical ultracentrifugation.

The tested lid-loop mutants also exhibit a faster dissociation of 2BP from the complex than the wild type of human APT1 (see Figure 102). All proteins, including the lid-loop lacking human APT1 ΔI71-D76 mutant contain a first, similar fast dissociation rate. This rate most likely corresponds to the dissociation of 2BP from the groove, which is weakly (and potentially unspecifically) bound (K_D of ~100 µM, communications with Stefan Baumeister). The signal of the ΔI71-D76 mutant can be fitted using a single rate, thus, 2BP bound at the new hydrophobic patch has a comparable dissociation rate as 2BP bound at the groove. The wild type of human APT1 and the mutants containing a lid-loop show a second fast binding rate, which is faster for the L73A and ΔL73S74 mutant than for the wild type of human APT1. It is most likely that this dissociation rate corresponds to 2BP bound inside the tunnel, since it is missing in the ΔI71-D76 mutant that lacks the lid-loop. The less stable lid-loop of the mutants enables the faster dissociation rate compared to the wild type (see Figure 102 and Chapter 5.2.15).

The faster lid-loop dependent dissociation rate (k_{off}) of the mutants corroborates the expected reduced affinity (K_D) towards 2BP. Since the binding rate (k_{on}) was not measured, K_D cannot be determined and it is not clear if the affinity is truly lower, but the weaker electron density of 2BP observed in the complexes with human APT1 L73A and ΔL73S74 (see Chapters 5.2.5 and 5.2.9, respectively) indicates a less stable binding of 2BP.

6.2.5 Calculation of the binding strength of the lid-loop to the core protein

PISA[97] as used to test if the observed effect on the stability of the lid-loop in the mutants is also corroborated by the theoretical calculation (see Table 25). First, the single point mutants used to investigate the effect of the leucine side chains of residue 58, 73 and 171 were analyzed. The calculated binding strength of the lid-loop of human APT1 wild type and the L58A and L171A mutants is comparable and not significantly reduced by the mutation (see Table 25). However, the binding strength of the lid-loop to the core protein of human APT1 L73A in complex with 2BP (to prevent folding of the lid-loop into the tunnel, see Chapter 5.2.4 and 5.2.5, 2BP is not considered in the calculation) is significantly reduced to -3.8 kcal/mol (compared to -6.9 kcal/mol of the wild type). This indicates that the L73A mutation causes further minor structural changes that eventually lead to the significant destabilization of the lid-loop. This was also tested using theoretical *in silico* mutants based on the apo structure of human APT1 wild type. The lid-loop binding strength of the *in silico* L58A, L73A and L171A mutants is within the same range as the wild type and does not corroborate the increased flexibility in case of the L73A mutant observed the crystal structure, most likely due to the lack of minor conformational change that are present in the real crystal structures.

The extended lid-loop of human APT1 +LP is present in such a conformation that two leucine side chains (one is part of the Pro-Leu insertion) are bound inside the tunnel, and thereby increases the interaction surface (545Å^2 vs. 448Å^2 for the wild type) and strength significantly (-9.4 kcal/mol vs. -6.9 kcal/mol for the wild type). The shortened lid-loops have a smaller interaction surface with

the core protein and thus a reduced binding strength. but surprisingly, the free dissociation energy is lower than of the human APT1 L73A + 2BP complex predicting a stronger binding to the core protein.

Except the shortened ΔL73S74 and ΔS74P75 lid-loop mutants, all lid-loop – core protein "complexes" are predicted to be stable in solution (see Table 25). The predictions of the stability in solution for the shortened lid-loops are within an area of uncertainty of the prediction. However, these predictions have to be treated with caution, as e.g. the dimer of human APT2 is predicted to be stable, but AUC experiments could not detect any dimerization[69].

6.2.6 Peptide binding to human APT1

APT-catalyzed de-palmitoylation of palmitoylated proteins has been proven by biochemical assays[109] and *in vivo* studies[98,99], but structural data of a complex of APT with a modified peptide is missing to date. The shallow groove (see Figure 10) next to the active site could potentially be a binding site for either a second lipid modification (found e.g. in N-Ras[33]) or the protein chain next to the palmitoylated cysteine(s). A PEG molecule from the crystallization condition was found to bind at this groove in a related esterase structure (PDB ID 3cn9, [57]), and weak binding of 2BP at this groove was observed by Stefan Baumeister (private communications). Indications for a second binding site for 2BP could be verified in Stopped Flow measurements (see Figure 53). However, more detailed structural information could not be gathered, as the 2BP complex of human APT1 wild type contains no anomalous signal at the groove (see Chapter 5.1.5).

All trials to obtain a complex by soaking or co-crystallization of a peptide modified with an acyl chain failed so far since in all available crystal forms of human APT1, the passage between the putative binding site and the active site is blocked by the side chain of M60 of the second molecule of the crystallographic dimer (see Figure 104). In an effort to circumvent this obstacle, M60 was shortened to serine or deleted from human APT1. The dimer interface changes indeed, but, unfortunately, its position is then replaced in the new interface by M202 (see Figure 110), the neighbor position of H203 of the catalytic triad so that the available space is still too small for a larger ligand. A human APT1 ΔM60+M202A double mutant contains a slightly larger cavity (see Figure 112) between the groove and active site, but yet co-crystallization with hexadecylated peptides (see Chapter 5.3 and [100]) still failed to reveal the binding mode of the peptide to date, indicating that the cavity is still too small.

Activity of human APT1 ΔM60 on OPTS could be inhibited using a hexadecylated peptide (see Figure 114), corresponding to the N-terminal sequence of human APT1 with the cysteine stably modified via a hexadecyl thioether that is resistant to hydrolysis by APT (see Figure 113). The ΔM60 mutant of human APT1 was used due to the expected reduced dimer K_D compared to the wild type (2.8 µM). The inhibition of APT activity confirmed the binding of the hexadecylated peptide in a mode that blocks the active site, but cannot answer the question if the peptide is bound at the groove as well. Initial IC_{50} values of 20 to 80 nM estimated from the activity assay indicate a high affinity, but these results need to be verified.

In the future, groove binding by peptides could be verified via Stopped Flow using the tryptophan mutants (see Figure 53). Such an experiment should show fast binding of a hexadecylated peptide at the groove (using human APT1 W140F mutant) driven by the fast binding of the aliphatic tail inside the tunnel. An unmodified peptide of the same sequence could be used as a control and is expected to show slow binding (similar to 2BP binding at the groove, see Figure 53) and to dissect the contribution of the hexadecyl chain on peptide binding.

6.3 Comparison of lipases, esterases and APT

APT, along with lipases, esterases, the human depalmitoylases PPT1 and PPT2, and cutinases belong to the class of α,β-hydrolases, a family that has developed different mechanisms during evolution to cover the hydrophobic patch at the active site. (see Chapter 3.4) Lipases contain a large lid that folds back onto the patch, shielding the whole hydrophobic surface and the active site from the solvent. Lid opening of lipases is often (not always) interfacially activated upon membrane binding, and thus enables access to the active site when the parts of the lipase are inserted into the membrane (compare PDB IDs 1lpp and 1trh,[102,104]). Cutinases and esterases have a solvent-accessible active site and completely lack a lid to cover the hydrophobic patch[110] since their substrates are often hydrophilic. PPT1 and PPT2 are responsible for lysosomal protein de-palmitoylation[72,111], but lack the structural motif of a pre-formed binding tunnel. Cutinases are secreted enzymes produced in phytotoxic bacteria that degrade the protective cuticle (consisting of polyester of fatty acids) of plants[106,110,112]. Human APT1 could be structurally considered in between these classes of lipases that contain a lid and cutinases/PPT1/PPT2 without a lid, that are all able to hydrolyze long-chain substrates. It possesses a shorter lid-loop that creates a pre-formed solvent-accessible hydrophobic tunnel next to the active site. Human APT1 and APT2 have been shown to be palmitoylated themself[98,99], indicating their (temporal) membrane association. Therefore, a mechanism of association of APT to the membrane and lid-loop opening (comparable to lipases), potentially to facilitate substrate extraction from the membrane, could be hypothesized.

Comparison of the size of the interface of the lid of lipases and the lid-loop of APT to the core protein, and the dimerization interface of APT shows that both the lipase lids and the dimer of APT are in a comparable range of free solvation energy around ΔG of about -20kcal/mol (see Table 26). Stability predictions calculated by PISA have to be treated with caution, as e.g. the crystallographic dimer interface of human APT2 is larger than human APT1, but in contradiction to this, AUC experiments indicate no dimer formation of human APT2, whereas human APT1 forms a moderately stable dimer with a K_D of 2.8 μM[69]. The calculated $\Delta G_{transfer}$ of the membrane insertion of proteins deposited at the opm database[102] lists a value of -4.7 kcal/mol for human APT1 (PDB ID 1fj2, [58], see Table 26). The $\Delta G_{transfer}$ gained from the membrane insertion of human APT1 is lower than its homo dimerization (-16.2 kcal/mol) or even the binding strength of the lid-loop of human APT1 (-6.9 kcal/mol). The closed form of *C. rugosa* lipase (PDB ID 1trh, [104]) has a $\Delta G_{transfer}$

in the same range of human APT1, which however is four-fold increased if the lid-loop is present in its open conformation (PDB ID 1llp, [103]).

The insertion depth of the open form of *C. rugosa* lipase and human APT1 wild type is comparable (see Table 25). It could be hypothesized that the lid-loop of APT could also open upon membrane insertion of the protein, potentially triggered by membrane attachment mediated by N-terminal palmitoylation of APT [98,99], and thus the membrane insertion is strengthened (similar to *C rugosa* lipase open and closed form, see Table 25). The opened lid-loop could be involved in extraction of the substrates membrane anchors, as besides the propyl isomerase FKBP12 [113] no other co-factor has been identified so far (see Chapter 3.3.1). The Stopped Flow measurements (see Figure 53) show that human APT1 wild type binds 2BP at comparable rates from a solution of free 2BP and 2BP incorporated in multi-lamellar DOPC vesicles (resulting in a reduced 2BP concentration on the surface of the vesicles, see 5.1.7.1), indicating a possible surface activation of human APT.

7 Material and Methods

7.1 Chemicals

Chemicals were purchased from Amersham-Pharmacia (Freiburg), Fluka (Neu-Ulm), GE (Freiburg), Merck (Darmstadt), Qiagen (Hilden), Roche (Mannheim), Roth (Karlsruhe), Serva (Heidelberg) and Sigma-Aldrich (Deisenhofen) at the highest purity grades available. Crystallization screens were obtained from Qiagen (Hilden) as 15 ml tubes and aliquoted by Georg Holtermann using a Lissy liquid handling robot (Zinsser Analytics, Frankfurt).

Palmostatin B and palmostatin M were a kind gift from Christian Hedberg, former group leader at the Department of Chemical Biology at MPI Dortmund, now Professor at Univesity of Umeå, Sweden.

Cerulenin (CAS Number 17397-89-6, ≥98% purity) was purchased from Sigma-Aldrich (Deisenhofen).

2-Bromopalmitic acid (CAS Number 18263-25-7, ≥97% purity) was purchased from Sigma-Aldrich (Deisenhofen) as a racemic mixture.

7.1.1 Kits

QIAprep Spin Miniprep Kit	Qiagen (Hilden)
QIAquick Gel Extraction Kit	Qiagen (Hilden)
QIAquick PCR Purification Kit	Qiagen (Hilden)
Dye-Deoxy-Terminator mix	Perkin Elmer (Überlingen)

7.1.2 Enzymes

Alkaline phosphatase	Calbiochem (Merck, Darmstadt)
BSA	Sigma (Deisenhofen)
Dnase I	Roche (Mannheim)
PreScission protease	GE Healthcare
Restriction enzymes	New England Biolabs (Schwalbach)
T4 DNA ligase	New England Biolabs (Schwalbach)

7.1.3 Protein and nucleic acid standards

Wide Range, SDS7 protein marker	Sigma (Deisenhofen)
Lambda phage DNA	Invitrogen (Karlsruhe)

7.1.4 Buffers

6x DNA loading buffer	30% (v/v) Glycerin
	0.25% (w/v) bromphenol blue
	0.25% (w/v) xylencyanole

	solved in TAE buffer
TAE buffer	40 mM Tris, pH 8.0
	40 mM acetic acid
	1 mM EDTA
SDS buffer	25 mM Tris
	192 mM Glycine
	2% (v/v) SDS

7.1.5 Bacterial strains

DH5α F- ϕ80dlacZΔM15 Δ(lacZYA-argF) U169 recA1 endA1 λ- hsdR12(rK-, mK+) supE44, thi-1 gyrA, relA1

BL21 (DE3) codon+ RIL *E. coli* B F– dcm ompT hsdS(rB– mB–) gal λ(DE3)

7.1.6 Media and antibiotics

Luria Bertani (LB)	10 g/L Bacto tryptone
	10 g/L NaCl
	5 g/L Yeast extract
SOC medium	2% (w/v) Bacto tryptone
	0.5% (w/v) Yeast extract
	10 mM NaCl
	2.5 mM KCl
	10 mM $MgCl_2$
	20 mM Glucose

Antibiotics were used from GERBU (Gaiberg) and added to the media after sterilization in following final concentrations:
Ampicillin 100 mg/L
Kanamycin 50 mg/L
Chloramphenicol 25 mg/L

7.1.7 Machines

FPLC (Gradifrac systems)	Pharmacia (Stockholm, SE)
pH meter	Knick (Berlin)
Centrifuges	Beckman (München)
Tabletop centrifuges	Eppendorf (Hamburg)
Sonifier 450	Branson (Dietzenbach)
Balances	Satorius (Göttingen)
Magnetic stirrer RCT basic	Eppendorf (Hamburg)
VortexGenie	Scientific Industries (Bohemia, NY, USA)

Pipettes	Eppendorf (Hamburg)
BioPhotometer	Eppendorf (Hamburg)
PAGE chambers	BioRad (München)
DNA electrophoresis chambers	BioRad (München)
Microplate photometer Infinite M200	Tecan Group (Männedorf, CH)
Microplate shaker	Variomag (USA)
Liquidator96	Steinbrenner (Wiesenbach)
Mosquito crystal	TTPLabtech (Melbourn, UK)
Rock Imager 1000	Formulatrix (Bedford, MA, USA)
MAR345 Image Plate Detector	X-Ray Research (Norderstedt)
MicroMax-007HF Rotating anode	Rigaku (Ettlingen)
MicroStar Rotating Anode	Bruker (Billerica, MA, USA)
Stopped Flow	Applied Photophysics (Leatherhead, UK)

7.2 Cloning, Protein Expression and Purification

I gratefully acknowledge Patricia Stege for molecular engineering and cloning of all plasmid constructs, heterologous expression using *E.coli*, and purification of all protein constructs I worked with in the course of this PhD thesis.

Molecular biology protocols for cloning and mutation as well as the protocols for protein expression and purification are well established by Patricia Stege and were carried out by her as described before[62,69].

7.2.1 Preparation of chemically competent *E. coli*

Preparation of chemically competent *E. coli* followed a standard protocol[114]. *E. coli* cells without antibiotic resistance were cultured on an agar plate at 37 °C overnight. 10 large colonies were used to inoculate 250 ml SOC medium and grown at 19°C, vigorously shaking to OD_{600} = 0.5. The cells were chilled on ice for 10 min and pelleted by spinning at 4000 rpm for 10 min at 4°C. For washing, cells were gently resuspended in 80 ml ice-cold TB buffer and stored on ice for 10 min. After spinning again at 4000 rpm (10 min, 4°C), cell pellets were gently resuspended in 20 ml ice-cold TB buffer and 1.4 ml DMSO. The homogeneous suspension of chemically competent cell was then aliquoted to 100 µl, flash-frozen in a dry ice-ethanol bath, and stored at -80°C.

7.2.2 Transformation of chemically competent *E. coli*

Chemically competent cells were transformed using the heat shock protocol. After thawing on ice, cells were incubated on ice with plasmid DNA for 30 to 60 min, followed by a heat shock at 42 ˚C for 30 s. Cells were shortly chilled on ice. 800 µl of SOC medium (without antibiotics) was added to the cells, which were incubated for 60 min at 37 ˚C on a shaker to allow expression of the antibiotic resistance genes. Cells were plated on LB agar plates containing the respective antibiotic.

7.2.3 Isolation of plasmid DNA

Cell lysis, isolation and purification of plasmid DNA, and DNA extraction from agaraose gels were carried out as described in and using the QIAquick PCR Purification Kit, the QIAprep Spin Miniprep Kit and the QIAquick Gel Extraction Kit.

7.2.4 Separation of DNA using agarose gel electrophoresis

DNA fragments are separated in agarose gels according to their electrophoretic mobility, which is reciprocally proportional to their number of base pairs[115]. Agarose gel electrophoresis was carried out in horizontal chambers according to a standard procedure using agarose concentrations of 0.8-2% (w/v) for the separation of DNA fragments. Gels were prepared by boiling agarose in TBE buffer, which also serves as running buffer. DNA samples were mixed with 6x loading buffer and separated by a constant voltage of 90-160 V. Gels were stained with 1% ethidium bromide or SYBR red (1:10,000 dilution) and excited with UV-light on a standard transluminator. BstEII-digested lambda DNA was used as DNA standard.

7.2.5 Polymerase chain reaction

The polymerase chain reaction (PCR) is the biotechnological method for specific amplification of DNA sequences. Performing a conventional PCR, a DNA template sequence, a pair of specific primers, which hybridizes with the flanking sites, all four deoxyribonucleotide triphosphates (dNTPs), and a thermostable DNA polymerase are necessary[116,117]. For subcloning into the pGEX expression vectors the gene fragments of interest were amplified by a standard PCR protocol as follows: Initial dsDNA denaturation at 98 °C for 1 min, then 35 cycles consisting of denaturation at 98 °C for 1 min, primer annealing at 57 °C for 30 s, elongation at 72 °C. Finally a last elongation step at 72 °C for 10 min was carried out.

7.2.6 DNA sequencing

DNA sequencing was carried out according to a standard protocol. The plasmid DNA was first amplified by PCR as follows: A 20 µl sample containing 4 µl of terminator reaction mixture, 100-300 ng of plasmid template DNA, and 5 pmol of sequencing primer was subjected to the following PCR: 96°C for 10s, 50°C for 5s, 60°C for 2 min. These steps were repeated 30 times and at the end the reaction was cooled down to 4°C. The PCR product was then precipitated using 2 µl of 3 M Sodium acetate and 50 µl of 100% ethanol. After vortexing the sample and incubating it for 15 min at room temperature, it was centrifuged for 10 min at 10,000 g at 4°C. The supernatant was then discarded; the pellet washed using 400 µl of 70% ethanol, centrifuged again for 10 min at 10,000 g at 4°C. The supernatant was discarded again and the pellet dried. Analysis of the DNA fragments was carried out in in-house facilities.

7.2.7 Molecular cloning of genes and gene fragments

The DNA template was used as a template for PCR amplification. The resulting PCR product was gateway cloned into a pGEX 4T1 expression vector (GE Healthcare), the primer was modified to

encode a PreScission protease cleavage site immediately upstream to the start codon, that leaves after protease cleavage of the purified protein a cloning artifact of the amino acids GP at the N-terminus.

7.2.8 Expression and purification of proteins

E. coli BL21 Codon +RIL cells were transformed using the appropriate cloned construct. Cells were grown at 25 °C in 800 ml cultures in Erlenmeyer flasks to an OD_{600}=0.8, or in a LEX reactor up to an OD_{600}=2.0, and protein expression was induced overnight at 20 °C using 0.1 mM IPTG. Cells were harvested, lysed using a high pressure cell disruptor, cell debris was removed by centrifugation at 100,000 g, and the supernatant was loaded on a GSH affinity column. The column was washed with 20 column volumes of buffer. PreScission protease (GE Healthcare) was then loaded on the column and slowly circulated over the column overnight. Afterwards, all cleaved protein was washed from the column. The entire GSH affinity chromatography[118] was carried out under the following buffer conditions for acyl protein thioesterases and related proteins: 20 mM Tris-HCl pH 8.5, 150 mM NaCl, 5% Glycerol, 5 mM DTE. The protein was subjected to subsequent gel filtration, using the following buffer: 20 mM Tris-HCl pH 8.0, 30 mM NaCl, 1 mM TCEP-HCl. Finally, the protein was concentrated using appropriate kDa MWCO spin filters, and flash-frozen.

7.2.9 SDS PAGE

Protein samples were analyzed using the denaturing SDS polyacrylamide electrophoresis method (SDS-PAGE), either following the Laemmli[119] or the Schägger/Jagow[120] protocol. SDS is an anionic detergent that denatures the proteins and shields their charges, making their mobility in the gel (driven by the electric field) dependent on their mass only. Protein samples were mixed with 4x loading buffer containing 10% SDS, 500 mM Tris/HCl, pH 6.8, 59% glycerol, 10 mM β-mercaptoethanol, 0.01% bromphenol blue, and 0.01% xylencyanol. To aid denaturation, this mixture was heated to 95˚C for 10 min. Gels used in this study consisted of two gels. The upper collection gel consists of 5% (w/v) acrylamide/bisacrylamide solution in 125 mM Tris/HCl, pH 6.8 buffer, polymerized by adding 0.1% (w/v) APS (ammonium perooxodisulfate) and 0.04% (w/v) TEMED (N,N,N,N-tetramethylethylendiamine). The lower sample separation gel consists of 8-18% (w/v) acrylamide/bisacrylamide solution and 125 mM Tris/HCl, pH 8.8, and was polymerized again by adding 0.1% (w/v) APS and 0.04% (w/v) TEMED. Electrophoresis was run at constant amperage of 50 mA per gel.

7.2.10 Coomassie staining of protein gels

Following SDS-PAGE, gels were stained in hot coomassie brilliant blue solution (40% (v/v) ethanol, 10% (v/v) acetic acid, 0.2% (w/v) coomassie brilliant blue G250) for 10 min. To reduce the background staining, gels were destained in boiling water.

7.2.11 Size exclusion chromatography

Size exclusion chromatography allows separation of proteins according to their hydrodynamic radius. Proteins with a smaller hydrodynamic radius have more interaction with the porous stationary phase (the column material) and thus to a longer retention time[3,121]. To achieve optimal protein separation the correct pore size of the stationary phase is required. For analytical purposes, a Superdex200 or Superdex75 10/30 column was used at a flow of 0.5 ml/min, for purification, a Superdex200 or Superdex75 16/60 or 26/60 column was used at a flow of 1.5-3 ml/min. The columns were run on a Gradifrac system (Pharmacia).

7.2.12 Determination of protein concentrations

Protein concentrations were measured by absorption at 280 nm caused by their amino acids tryptophan and tyrosine. The protein concentration is hereby derived from the absorption using the Lambert-Beer law[122] as described before[123,124]. A Nanodrop 1000 Photometer (PeqLab) was used to determine the absorbance.

7.2.13 Mass spectrometry

The precise mass of pure proteins, a mixture of few proteins, or covalent protein-inhibitor adducts can be detected via Electron-Spray Ionization mass spectrometry coupled to liquid chromatography (LC-MS). The sample was diluted in pure water to a concentration of 80 µM, and 10 µl of the dilution were added to 10 µl of pure acetonitrile and 2.2 µl of 1% TFA (0.1% final concentration). The sample was mixed and centrifuged at 16,000 rpm for 5 min. The clear supernatant was transferred to a HPLC vial. The protocol for the LC-MS using a LCQ (ThermoFisher) was as following: 10 µl containing 400 pmol protein were injected into a standard C4 column that was run with an linear acetonitrile gradient from 0% to 80% within 5 min, coupled to ESI-MS. Alternatively, 10 µl sample (400 pmol) can be directly injected into the ESI-MS system without sample separation via LC.

7.3 Protein Crystallogenesis

7.3.1 Summarized theory of crystallogenesis

Crystal growth is based on pushing the concentration of a molecule, proteins in this case, beyond the solubility level to form a solid, crystalline precipitant[125]. The transition is required to be slow enough to allow the proteins to arrange in a three-dimensional order to form crystals; if the solution is supersaturated too fast, the proteins precipitate in an amorphous state. Controlled concentration of the protein solution is achieved in a sealed environment, containing a hydroscopic reservoir that draws water the protein containing solution, thus slowly concentrating the protein. The protein solution is mixed with the reservoir to slow down the concentration process and prevent the drop containing the protein to completely dry out. Hydroscopic molecules like polyethylene glycols (PEGs), volatile alcohols, and high concentration of salts are used as precipitants. Additionally,

buffers controlling the pH and salts regulating the ionic strength are added to the solution that can be further modified using organic or biological compounds, termed additives, to improve crystal quality. The composition of the solution resulting in crystals is not predictable, thus the empirical methods requires a high parallel number of trial and error experiments to screen for conditions suitable to grow crystals. These conditions can be further refined, if necessary, by fine-tuning the concentration of both protein or precipitant, the temperature or volume of the crystallization drop to regulate the velocity of supersaturating the protein [125].

7.3.2 Crystallization screening

Screening for crystallization conditions were performed at 293 K in Corning 3553 / 3550, Greiner Low Profile CrystalQuick or TTP IQintelli 96-well plates. A Steinbrenner Liquidator96 was used to transfer the mother liquor from the master block to the screening plate. The crystallization drops consisted of 100 nl protein and mother liquor solution each, the reservoir had a volume of 70 µl. In general, proteins were kept on ice until being transferred to a Greiner V-shape 96-well plate used for setup of crystallization plate by TTP labtech Mosquito robot. The 2BP complexes were prepared as following: 47.5 µl of 1.3 to 1.5 µM protein stock solution was mixed with 2.5 µl of 2BP stock solution (100 mM in DMSO) to a final concentration of 5 mM and heated up to 50 ˚C for 5-10 minutes and mixed gently several times during incubation by flicking the tube with the finger.

7.3.3 Crystallization refinement in hanging drops

Crystallization conditions were refined in hanging drop experiments using 24-well tissue culture plates from Linbro or Crychem and glass cover slides. Plates that are not pre-greased were sealed using Baysilon silicon oil that was applied to the edge of the well using a syringe with an attached 200 µl tip. 1 µl of protein solution was mixed with the reservoir on glass slides in a ratio of 1:1 to a total volume of 2 µl, and the glass cover slip was turned upside down to seal the well. Crystals of *S. cerevisiae* APT in complex with palmostatin B and palmostatin M were obtained by drying 0.5 µl of 100 mM DMSO stock of the respective inhibitor on glass slides over night to minimize the DMSO concentration in the crystallization drop while maintaining high amounts of inhibitor. 1 µl of protein solution was added onto the dried inhibitor, and mixed with 1 µl of reservoir solution.

7.3.4 Crystal preparation for x-ray diffraction experiments

Crystals were isolated using pre-mounted CryoLoops (Hampton). Isolated crystals were soaked for a few seconds in cryogenic solutions which composition is based on the reservoir solution. Different cryo-protectants like glycerol, small PEGs or sugars were used. If the usage of cryo-protectants resulted in visible damage of the crystal, or low-quality diffraction with either low resolution or smeared or streaky spots, crystals were isolated without cryo-protectant directly from the crystallization drop and tested at room temperature for diffraction of the crystal. In case of cryogenic crystallization conditions, crystals were directly isolated from the crystallization drop in a thin liquid film without additional cryo-protectant and flash frozen in liquid nitrogen.

7.4 X-ray crystallography

7.4.1 Summarized theoretical background

According to the Law of Ernst Abbe (Eq. 1)[126], the maximum resolution is determined by the wavelength of the light used for the observation. The resolution is the smallest distance in which two details or objects are still resolved as two individuals[127].

$$d = \frac{\lambda}{2\,NA} \qquad \text{(Eq. 1)}$$

d: resolution

λ: wavelength used for the observation

NA: Numerical Aperture

Visible light in the range of 400 to 800 nm, as used in optical microscopes, is suitable for direct observation by eye. The Numerical Aperture of modern optical microscopes using immersion oils is increased to ~1.5[128], and thus restricts the resolution limit to 200 nm. This is suitable to study (sub-)cellular processes, but insufficient to describe molecules. The average distance of carbon bonds in organic compounds as proteins are in the range of 150 pm or 1.5 Å[129]. To observe the position of single atoms, x-rays of a wavelength of around 1 Å are required[127]. X-rays are not directly observable by the naked human eyes[130], and their interaction with the atom electron shell is rather weak[125,127]. Multiple simultaneous measurements are performed within a crystal to enhance the signal strength, which is then measured on a detector[125,127]. This leads to systematic additions of the signal, when the criteria of Bragg's law (Eq. 2) is fulfilled:

$$n\,\lambda = 2\,d\,sin\theta \qquad \text{(Eq. 2)}$$

n: natural number

λ: wavelength

d: distance between lattice planes

θ: angle between the incident x-ray beam and lattice plane

The resulting distinctive diffraction pattern needs to be converted to an interpretable map. The intensities of the reflections are indexed and integrated, reducing the diffraction data from a set of images to one list of intensities[127]. The Structure Factor (correlating to the measured intensity) of each recorded reflection can be described in polar form as shown in (Eq. 3)[125] below:

$$F_{hkl} = |F_{hkl}| \exp i\alpha_{hkl} \qquad \text{(Eq. 3)}$$

F_{hkl} : amplitudes of the diffracted x-ray

α_{hkl}: phases of the diffracted x-ray

The transformation to an electron density function given in a cartesian coordinate system is calculated via Fourier-transformation as shown in (Eq. 4)[127].

$$\rho(xyz) = \frac{1}{V} \cdot \sum_{hkl} |F_{hkl}| \cdot \exp[-2\pi i(hx + ky + lz) + i\alpha_{hkl}] \quad \text{(Eq.4)}$$

This Fourier transformation requires both amplitude and phase of each observed x-ray. The amplitude is proportional to the intensity measured by the detector, but the phase information cannot be measured and is lost during the experiment. This is the so-called 'phase-problem' of x-ray crystallography.

Phasing via Molecular Replacement requires the known structure of a homologues protein. Amplitudes and phases can be back-calculated from the known structure, and these phases can serve as starting phases to solve the structure[125,127]. The template structure is likely to be differently oriented in a crystal of different space group and unit cell, and must be aligned to the new, unknown structure. This is achieved by a six-dimensional search, in which the template is rotated and translated in three dimensions each. The Patterson functions of the amplitudes calculated from the known template structure and the amplitudes of the measured crystal correlate once the template model is successfully position. The phases calculated from the template in this orientation serve to calculate the initial electron density using the observed amplitudes of the new, unknown structure[125,127]. The model of the template structure is adapted to the sequence and electron density of the new, unknown protein, which in turn can be used to re-calculate phases. These improved phases are used to generate an optimized electron density map, to which the structure is further refined. This iterative cycle is performed until no further optimization is achieved. The quality of the structure is assessed via the R-factor[127], calculated as shown in Eq. 5:

$$R = \frac{\Sigma||F_{obs}|-|F_{calc}||}{\Sigma\,|F_{calc}|} \qquad \text{(Eq. 5)}$$

F_{obs}: measured amplitudes of the structure

F_{calc}: calculated amplitudes of the structure model

The R_{free} factor is used for quality control, which is calculated using a subset (typically 5%) of the measured reflection that is not used for structure refinement to prevent over-fitting[131]. The R-factor is usually in the range of 0.2 for protein structures, depending on the resolution of the diffraction data[127].

7.4.2 X-ray diffraction data collection

Crystals were tested in-house for diffraction quality using a Bruker Microstar or Rigaku Micromax HF-007 rotating anode (operated at 45kV / 50mA and 40kV / 30mA, respectively) as x-ray source. Standard setup included cryo-cooling of the crystals to 100 K using an Oxford cryostat. Diffraction data was collected on mardtb image plate detectors. Test images and data sets were recorded with 1˚ rotation and 3 to 10 min exposure time per image. Diffraction data of the crystal structures presented in this thesis was collected at X10SA beam line at the Swiss Light Source (SLS) at the Paul-Scherrer-Institute in Villigen, Switzerland on a Pilatus 6M detector (Dectris) (unless stated otherwise). Standard data collection settings not requiring anomalous signal for phasing was 0.25˚ rotation at 0.1s exposure time per image with a beam attenuated to 50% intensity and using the 30µm aperture, resulting in a flux of $4x10^{11}$ ph/s at an wavelength of 1.0 Å (12.7keV). Customized strategies like fine slicing (0.1˚ rotation per image) or low-intensity high-redundancy data collection to obtain anomalous signal for heavy atoms in ligands have been applied if required. Indexing and strategy determination was carried out using iMosflm[132] and the automated processing pipeline[133] provided at the X10SA beam line utilizing mosflm[132], parts of XDS[134], cad (available through CCP4I[101]), Pointless[135], phenix.xtriage[136] and gnuplot[94].

7.4.3 Data reduction, phasing and structure building

Diffraction data was indexed, integrated, and scaled using XDS and XSCALE, following to the conversion to mtz file format using XDSCONV, all part of the XDS program package[134]. The structures were solved via maximum likelihood Molecular Replacement using PhaserMR[137] from the Collaborative Computational Project No.4 program suite with interface (CCP4i)[135]. Structure refinement was carried out in iterative cycles of restrained refinement using refmac5[138] and coot[139] until no further convergence (reduction of the R_{free} factor[131]) was observed.

7.4.4 Structure validation

Model validation was carried out using plugins implemented in coot[139] in parallel to the refinement, e.g. to check for Ramachandran outlier[140]. For further validation the program Molprobity[141] was used. The B-factors of the refined structure were extracted from the pdb-file using a script. Crystallographic statistics are summarized in the respective tables for each structure. Dimer analysis was carried out using the Secondary Structure Match (SSM) function implemented in coot[139]. Superimposing of the second monomer of two dimers, the kappa angle of the performed rotation (given in polar coordinates) describes the rotation of the dimer arrangement.

7.4.5 Generation of ligand model restraints

Models and corresponding chemical restraints of small molecule ligands, e.g. buffer components, are readily available at the HIC-UP data base[142] (http://xray.bmc.uu.se/hicup/). Models and restraints of novel ligands were created using ChemBioDraw[143] and eLBOW [144] of the Phenix suite (https://www.phenix-online.org/) [145].

7.4.6 Illustration of crystal structures and annotating images

All images of crystal structures were created using CCP4mg [93] and annotated using Gimp [4], if not stated otherwise.

7.5 Biochemical Activity Assay

Stefan Baumeister established a detergent-free activity assay system using esters of 8-Hydroxypyrene-1,3,6-trisulfonic acid (HPTS) as substrate. 8-Octanoyloxypyrene-1,3,6-trisulfonic acid tri-sodium salt (OPTS) is the commercially available octanoyl ester that can be hydrolyzed by APT. The assay buffer contained 150 mM NaCl and 100mM K_2HPO_4, pH 7.4 without detergent and is suitable for concentrations of OPTS up to 500 mM at room temperature. 8-Palmitoyloxypyrene-1,3,6-trisulfonic acid tri-sodium salt (PPTS) was a kind gift from Stefan Baumeister. Commercially available 8-Hydroxypyrene-1,3,6-trisulfonic acid tri-sodium salt (HPTS) was esterified with palmitic acid to create 8-Palmitoyloxypyrene-1,3,6-trisulfonic acid (PPTS). Reaction and product purification was performed by Stefan Baumeister. PPTS require a carrier to prevent (probably) tight micelle formation that inhibits hydrolysis by human APT1 at concentration higher than 20 µM. Fatty acid binding protein (FABP2, added in 10% molar ratio) was found to suite best without influencing activity of human APT1.

7.5.1 PPTS enzyme kinetics

PPTS hydrolysis kinetics were measured from serial dilutions with a starting concentration of 50.51 µM PPTS and 5.05 µM FABP2. Serial dilution of 99 µl PPTS-FABP2 solution in 99 µl assay buffer (see Chapter 7.5) were carried out directly in the 96 well assay plate, keeping the 10:1 molar ratio of PPTS to FABP2 constant in all conditions. The plate was briefly mixed using a microplate shaker before being transferred to an Infinite M200 microplate reader (Tecan). Fluorophore excitation was set to a wavelength of 415 nm and emission was detected at 520 nm. An initial fluorescence measurement was performed to check for a stable base line. Following the addition of 1 µl of 500 nM protein (5 nM final protein concentration) and brief mixing of the microplate, fluorescence was measured in 45 s intervals for one hour at 27 ˚C. The fluorescence was corrected for auto-hydrolysis.

7.5.2 Inhibitor IC_{50} determined in enzymatic activity assay using OPTS as substrate

OPTS was used in the assay buffer (100 mM K_2HPO_4, pH 7.4 and 150 mM NaCl) as test substrate similarly to PPTS. OPTS has a better aqueous solubility and does not require an additional carrier. The assay can be used to test the potency of inhibitors and determine their IC_{50} towards human APT1, and analogously, the hexadecylated peptide was tested on its inhibitory effect using this protocol. First, the inhibitor in question was dissolved in assay buffer to a concentration of 1 mM, and 100 µl of this solution were added to the first column. The remaining columns were filled with 50 µl of assay buffer. A serial dilution of the inhibitor was prepared by transferring 50 µl of the previous well using an automatic pipette, each step contained automatic mixing by pipetting a volume of 70 µl up and down three times. One column was left as control containing no inhibitor, and another contained no inhibitor or protein to measure autohydrolysis of the substrate. The DMSO stock solution of OPTS (100 mM) was diluted in assay buffer to a concentration of 255 µM, and 49 µl were added to each well. The protein was diluted to 500 nM in assay buffer, and 1 µl was added to each well, resulting in a final concentration of 5nM. The plate was briefly mixed using a microplate shaker and directly transferred to an Infinite M200 microplate reader (Tecan). Excitation wavelength and emission detection were set to 415 nm and 520 nm, respectively, and were measured in 45s intervals for 1 h.

7.5.3 Analysis of the activity assay data

Fluorescence was converted to concentration via a calibration curve covering the concentration range of HPTS formed upon complete substrate turnover. The slope of the linear range of the first 180 s was calculated using Microsoft Excel and plotted against the concentration of PPTS and used to determine the Michaelis-Menten kinetics. Data was plotted and fitted using Origin Pro 9.0G.

7.6 Stopped Flow

The utilization of the tryptophan fluorescence as sensor for ligand binding to APT was investigated and established by Stefan Baumeister [unpublished results]. The intrinsic fluorescence of tryptophan is affected upon binding of ligands in close proximity. Human APT1 contains three

tryptophan residues. W32 is located on the surface at the shallow groove next to the active site; W67 is buried inside the protein core; and W140 forms the inner wall of the hydrophobic tunnel (compare Figure 10) The fluorescence of W32 and W140 change upon ligand binding next to the side chain at the groove and hydrophobic tunnel, respectively. Binding at either the tunnel or groove can be differentiated using the mutants containing the respective tryptophan while lacking the other. The change of fluorescence is the measured signal from which the binding rate constant k_{on} can be determined.

Standard procedure to determine the dissociation rate constant k_{off} is a competition measurement, using a pre-formed complex of protein and fluorescent ligand that is competed off with a non-labeled inhibitor used at higher concentration. As the binding sites of the protein contained the fluorescent label (tryptophan), equilibrium of the 2BP-protein complex was shifted using two different approaches. The first exploits the high affinity of 2BP towards CHAPS-micelles: by mixing a pre-formed hAPT1-2BP complex with a solution containing CHAPS-micelles, dissociated 2BP is rendered unavailable to APT by incorporation into the micelles, thereby shifting the equilibrium away from the complex to free APT at the rate of k_{off}. However, k_{off} from human APT1 could be affected by the interaction of APT with CHAPS micelles. In analogy to CHAPS micelles, both multi-lamellar and uni-lamellar DOPC vesicles were used to bind free 2BP and shift the equilibrium from the 2BP-complex towards the free protein. The second approach is based on the competition for 2BP with a non-fluorescent fatty acid binding protein. Trp-free human L-FABP was used in 14-fold excess to trap 2BP released from hAPT1 wt, shifting the equilibrium and measure the k_{off} rate of the human APT1 - 2BP complex.

7.6.1 Stopped Flow binding rate constant

Binding rate constant k_{on} of 2BP to human APT1 was determined at 298 K by measuring the change of the intrinsic tryptophan fluorescence of a 5 µM protein solution upon mixing with 50 µM 2BP (respective final concentrations) using a Stopped Flow (Applied Photophysics). Standard gel filtration buffer containing 20 mM Tris-HCl pH 8.0, 30 mM NaCl, and 1 mM TCEP-HCl was used. DMSO concentration of protein and inhibitor solution was adjusted to 1% to prevent buffer mixing effects. The excitation wavelength was set to 280 nm and a 320 nm cut-off filter was used for detection. Photomultiplier voltage was adjusted individually for each experiment. Fluorescence was measured for 2 - 60 s.

7.6.2 Stopped Flow dissociation rate constant

A pre-formed complex of human APT1 (2.5 µM) and 2BP (10 µM), and non-fluorescent tryptophan-free L-FABP (22.5 µM) were loaded into the respective syringes of the Stopped Flow. The dissociation of the human APT1 - 2BP complex upon mixing with L-FABP and consecutive L-FABP-2BP complex formation was measured via the change of tryptophan fluorescence of human APT1. Alternatively, 1% v/v CHAPS or 1 mM DOPC vesicles were used as competitor. The excitation wavelength was set to 280 nm and a 320 nm cut-off filter was used for detection. Standard gel filtration buffer was used as for the measurement of the binding rate constant (see Chapter 7.6.1).

The DMSO content was adjusted to the same concentration in both syringes to prevent buffer mixing effects.

7.6.3 DOPC Vesicles

DOPC vesicles were created by freeze-thaw cycles as described before[146]. 157 µl of a DOPC stock solution (10 mg/ml in Trichloromethane) were dried in an Eppendorf tube in a Nitrogen steam and lyophilized over night. The dried DOPC was resuspended in 990 µl APT assay buffer containing 150 mM NaCl, 100 mM K_2HPO_4 at pH 7.4, resulting in a final concentration of 2 mM DOPC. The suspension was placed in an ultrasonic bath for 15 min, then flash-frozen in liquid nitrogen and thawed for 15 min five times before being sonicated for 5 min as the last step to create large multi-lamelar vesicles.

7.6.4 Peptide Synthesis and Modification

Peptides were synthesized by Philipp Cromm using standard Fmoc-strategy using a Rink Amide resin using a peptide synthesizer at the Department of Chemical Biology at the MPI Dortmund as described before[147]. The peptide mimics the first ten amino acids of the human APT1 N-terminus, which are palmitoylated at C2, (M_{C16}CGNNMSTPL, 1290.71 Da, see Figure 113). A self-synthesized building block of the hexadecylated cysteine was used. While the C-terminus is amidated, the N-terminus of the peptide is unmodified to significantly increase solubility. Following synthesis, the peptide was cleaved from the resin using a mixture of 95% TFA, 2.5% TIPSI and 2.5% H_2O as cleaving solution. The peptide was precipitated at -20 ˚C in acetone and the supernatant removed. The washed pellet was taken up in cleaving solution, which was transferred to a round bottom flask and lyophilized. Dried powder was taken up in DMF and purified via HPLC. The pure product was taken up in water and diluted to a concentration of 25 mM.

7.7 Calculation of the free solvation energy using PISA

PISA[97] (part of CCP4I suite[101]) is a program that calculates the theoretical entropy gained (free solvation energy, ΔG) upon complex formation of interfaces of macromolecular assemblies found in crystal structures, and provides a prediction of the stability in solution, and thus of the biological relevance of the respective interface. The free solvation energy is affected by multiple factors; some of these are the size of the interface area, surface charge and hydrophobicity, distance, and complementary of the surface shape[97].

The standard setting of PISA is suitable to predict dimerization/oligomerization of APT via different crystal interfaces. For the calculation of the interaction strength of the lid-loop of different mutants of human APT1, the lid-loop needs to be treaded by PISA as a second molecule. Thus, the lid-loop was separated *in silico* from the core protein by deletion of amino acids D69 and D80 of the hinge region of human APT1 wild type and changing the chain ID.

8 References

[1] C. Sawyers, *Nature* **2004**, *432*, 294–297.
[2] J. M. Berg, J. L. Tymoczko, L. Stryer, *Biochemistry (6th Edn)*, W. H. Freeman, **2006**.
[3] A. Wittinghofer, I. R. Vetter, *Annu. Rev. Biochem.* **2011**, *80*, 943–971.
[4] The GIMP team, GNU Image Manipulation Programm, 1997-2016.
[5] M. V. Milburn, L. Tong, A. M. deVos, A. Brünger, Z. Yamaizumi, S. Nishimura, S. H. Kim, *Science* **1990**, *247*, 939–945.
[6] I. R. Vetter, A. Wittinghofer, *Science's Compass* **2001**, *9*, 1299–1304.
[7] M. Trahey, F. McCormick, *Science* **1987**, *238*, 542–545.
[8] A. Bernards, J. Settleman, *Trends Cell Biol.* **2004**, *14*, 377–385.
[9] M. Trahey, R. J. Milley, G. E. Cole, M. Innis, H. Paterson, C. J. Marshall, A. Hall, F. McCormick, *Molecular and Cellular Biology* **1987**, *7*, 541–544.
[10] A. Schmidt, A. Hall, *Journal of Biological Chemistry* **2002**, *277*, 14581–14588.
[11] A. Schmidt, A. Hall, *Genes Dev.* **2002**, *16*, 1587–1609.
[12] D. D. Leipe, Y. I. Wolf, E. V. Koonin, L. Aravind, *Journal of Molecular Biology* **2002**, *317*, 41–72.
[13] M. Barbacid, *Annu. Rev. Biochem.* **1987**, *56*, 779–827.
[14] J. L. Bos, *Cancer Research* **1989**.
[15] K. Wennerberg, *Journal of Cell Science* **2005**, *118*, 843–846.
[16] J. Colicelli, *Science Signaling* **2004**, re13.
[17] A. Malliri, J. G. Collard, *Curr. Opin. Cell Biol.* **2003**, *15*, 583–589.
[18] B. Quimby, *Curr. Opin. Cell Biol.* **2003**, *15*, 338–344.
[19] V. L. Ha, R. Luo, Z. Nie, P. A. Randazzo, *Advances in cancer research* **2008**, *101*, 1–28.
[20] J. J. Harvey, *Nature* **1964**, *204*, 1104–1105.
[21] W. H. Kirsten, V. Schauf, J. McCoy, *Bibl Haematol* **1970**, 246–249.
[22] K. Shimizu, M. Goldfarb, M. Perucho, M. Wigler, *PNAS* **1983**, *80*, 383–387.
[23] A. Hall, C. J. Marshall, N. K. Spurr, R. A. Weiss, *Nature* **1983**, *303*, 396–400.
[24] A. Parmeggiani, G. W. Swart, K. K. Mortensen, M. Jensen, B. F. Clark, L. Dente, R. Cortese, *PNAS* **1987**, *84*, 3141–3145.
[25] Y. Cenatiempo, F. Deville, J. Dondon, M. Grunberg-Manago, C. Sacerdot, J. W. Hershey, H. F. Hansen, H. U. Petersen, B. F. Clark, M. Kjeldgaard, *Biochemistry* **1987**, *26*, 5070–5076.
[26] K. Scheffzek, M. R. Ahmadian, W. Kabsch, L. Wiesmüller, A. Lautwein, F. Schmitz, A. Wittinghofer, *Science* **1997**, *277*, 333–338.
[27] K. Rittinger, P. A. Walker, J. F. Eccleston, S. J. Smerdon, S. J. Gamblin, *Nature* **1997**, *389*, 758–762.
[28] M. J. Seewald, C. Körner, A. Wittinghofer, I. R. Vetter, *Nature* **2002**, *415*, 662–666.
[29] H. Umanoff, W. Edelmann, A. Pellicer, R. Kucherlapati, *PNAS* **1995**, *92*, 1709–1713.
[30] L. M. Esteban, C. Vicario-Abejon, P. Fernandez-Salguero, A. Fernandez-Medarde, N. Swaminathan, K. Yienger, E. Lopez, M. Malumbres, R. McKay, J. M. Ward, et al., *Molecular and Cellular Biology* **2001**, *21*, 1444–1452.
[31] L. Johnson, D. Greenbaum, K. Cichowski, K. Mercer, E. Murphy, E. Schmitt, R. T. Bronson, H. Umanoff, W. Edelmann, R. Kucherlapati, et al., *Genes Dev.* **1997**, *11*, 2468–2481.
[32] L. Chin, A. Tam, J. Pomerantz, M. Wong, J. Holash, N. Bardeesy, Q. Shen, R. O'Hagan, J. Pantginis, H. Zhou, et al., *Nature* **1999**, *400*, 468–472.
[33] J. F. Hancock, A. I. Magee, J. E. Childs, C. J. Marshall, *Cell* **1989**, *57*, 1167–1177.
[34] J. F. Hancock, H. Paterson, C. J. Marshall, *Cell* **1990**, *63*, 133–139.
[35] A. I. Magee, L. Gutierrez, I. A. McKay, C. J. Marshall, A. Hall, *Dynamic Fatty Acylation of p21N-Ras*, Embo J, **1987**.
[36] L. Brunsveld, H. Waldmann, D. Huster, *BBA - Biomembranes* **2009**, *1788*, 273–288.
[37] M. D. Schaber, M. B. O'Hara, V. M. Garsky, S. C. Mosser, *Journal of Biological Chemistry* **1990**, *265*, 14701–14704.
[38] T. Putilina, P. Wong, S. Gentleman, *Mol. Cell. Biochem.* **1999**, *195*, 219–226.

[39] J. T. Swarthout, S. Lobo, L. Farh, M. R. Croke, W. K. Greentree, R. J. Deschenes, M. E. Linder, *J. Biol. Chem.* **2005**, *280*, 31141–31148.
[40] O. Rocks, M. Gerauer, N. Vartak, S. Koch, Z.-P. Huang, M. Pechlivanis, J. Kuhlmann, L. Brunsveld, A. Chandra, B. Ellinger, et al., *Cell* **2010**, *141*, 458–471.
[41] O. Rocks, A. Peyker, M. Kahms, P. J. Verveer, C. Körner, M. Lumbierres, J. Kuhlmann, H. Waldmann, A. Wittinghofer, P. I. H. Bastiaens, *Science* **2005**, *307*, 1746–1752.
[42] J. A. Duncan, A. G. Gilman, *Journal of Biological Chemistry* **1998**, *273*, 15830–15837.
[43] J. S. Goodwin, K. R. Drake, C. Rogers, L. Wright, J. Lippincott-Schwartz, M. R. Philips, A. K. Kenworthy, *The Journal of Cell Biology* **2005**, *170*, 261–272.
[44] F. J. Dekker, O. Rocks, N. Vartak, S. Menninger, C. Hedberg, R. Balamurugan, S. Wetzel, S. Renner, M. Gerauer, B. Schölermann, et al., *Nature Chemical Biology* **2010**, *6*, 449–456.
[45] M. Rusch, T. J. Zimmermann, M. Bürger, F. J. Dekker, K. Görmer, G. Triola, A. Brockmeyer, P. Janning, T. Böttcher, S. A. Sieber, et al., *Angewandte Chemie International Edition* **2011**, *50*, 9838–9842.
[46] T. J. Zimmermann, M. Bürger, E. Tashiro, Y. Kondoh, N. E. Martinez, K. Görmer, S. Rosin-Steiner, T. Shimizu, S. Ozaki, K. Mikoshiba, et al., *ChemBioChem* **2012**, *14*, 115–122.
[47] D. B. Whyte, P. Kirschmeier, T. N. Hockenberry, I. Nunez-Oliva, L. James, J. J. Catino, W. R. Bishop, J. K. Pai, *Journal of Biological Chemistry* **1997**, *272*, 14459–14464.
[48] F. Ghomashchi, X. Zhang, L. Liu, M. H. Gelb, *Biochemistry* **1995**.
[49] H. Schroeder, R. Leventis, S. Rex, M. Schelhaas, E. Nägele, H. Waldmann, J. R. Silvius, *Biochemistry* **1997**, *36*, 13102–13109.
[50] A. G. Murzin, S. E. Brenner, T. Hubbard, C. Chothia, "SCOP: Fold: alpha/beta-Hydrolases," can be found under http://scop.mrc-lmb.cam.ac.uk/scop/data/scop.b.d.baa.A.html, **n.d.**
[51] A. G. Murzin, S. E. Brenner, T. Hubbard, C. Chothia, *Journal of Molecular Biology* **1995**, *247*, 536–540.
[52] A. Andreeva, D. Howorth, S. E. Brenner, T. J. P. Hubbard, C. Chothia, A. G. Murzin, *Nucleic Acids Res.* **2004**, *32*, D226–9.
[53] M. Nardini, B. W. Dijkstra, *Curr. Opin. Struct. Biol.* **1999**, *9*, 732–737.
[54] H. Chahinian, L. Sarda, *Protein Pept. Lett.* **2009**, *16*, 1149–1161.
[55] J. Pleiss, M. Fischer, R. D. Schmid, *Chemistry and Physics of Lipids* **1998**, *93*, 67–80.
[56] T. Tsurumura, H. Tsuge, *J Struct Funct Genomics* **2014**, *15*, 83–89.
[57] A. Pesaresi, D. Lamba, *Biochimie* **2010**, *92*, 1787–1792.
[58] Y. Devedjiev, Z. Dauter, S. R. Kuznetsov, T. Jones, *Structure* **2000**, *8*, 1137–1146.
[59] H. Sugimoto, S. Odani, S. Yamashita, *Journal of Biological Chemistry* **1998**, *273*, 12536–12542.
[60] T. Toyoda, H. Sugimoto, S. Yamashita, *Biochim. Biophys. Acta* **1999**, *1437*, 182–193.
[61] C. M. Lindgren, I. M. Heid, J. C. Randall, C. Lamina, V. Steinthorsdottir, L. Qi, E. K. Speliotes, G. Thorleifsson, C. J. Willer, B. M. Herrera, et al., *PLoS Genet* **2009**, *5*, e1000508.
[62] M. Burger, T. J. Zimmermann, Y. Kondoh, P. Stege, N. Watanabe, H. Osada, H. Waldmann, I. R. Vetter, *The Journal of Lipid Research* **2011**, *53*, 43–50.
[63] D. C. Yeh, J. A. Duncan, S. Yamashita, T. Michel, *Journal of Biological Chemistry* **1999**, *274*, 33148–33154.
[64] R. Flaumenhaft, N. Rozenvayn, D. Feng, A. M. Dvorak, *Blood* **2007**, *110*, 1492–1501.
[65] V. M. Tomatis, A. Trenchi, G. A. Gomez, J. L. Daniotti, *PLoS ONE* **2010**, *5*, e15045.
[66] Y. Shanado, M. Kometani, H. Uchiyama, S. Koizumi, N. Teno, *Biochemical and Biophysical Research Communications* **2004**, *325*, 1487–1494.
[67] M. Satou, Y. Nishi, J. Yoh, Y. Hattori, H. Sugimoto, *Endocrinology* **2010**, *151*, 4765–4775.
[68] A. Adibekian, B. R. Martin, J. W. Chang, K.-L. Hsu, K. Tsuboi, D. A. Bachovchin, A. E. Speers, S. J. Brown, T. Spicer, V. Fernandez-Vega, et al., *J. Am. Chem. Soc.* **2012**, *134*, 10345–10348.
[69] M. Bürger, Development of a Gfp-Based Assay for the Structural Elucidation of Nuclear Pore Proteins and Biochemical and Structural Investigations of Acyl Protein Thioesterases, Universität Osnabrück, **2012**.
[70] L. A. Verkruyse, S. L. Hofmann, *J. Biol. Chem.* **1996**, *271*, 15831–15836.

[71] D. A. Bachovchin, B. F. Cravatt, *Nat Rev Drug Discov* **2012**, *11*, 52–68.
[72] J. J. Bellizzi, J. Widom, C. Kemp, J. Y. Lu, A. Das, S. L. Hofmann, J. Clardy, in *Pnas*, **2000**, pp. 4573–4578.
[73] R. Smoum, A. Rubinstein, V. M. Dembitsky, M. Srebnik, *Chem. Rev.* **2012**, *112*, 4156–4220.
[74] A. T. Porfetye, Structural and Biochemical Analysis of Acyl Protein Thioesterase-Inhibitor Complexes, Technische Universität Dortmund, **2011**.
[75] E. K. Weibel, P. Hadváry, E. Hochuli, E. Kupfer, H. Lengsfeld, *J. Antibiot.* **1987**, *40*, 1081–1085.
[76] P. Hadváry, H. Lengsfeld, H. Wolfer, *Biochem. J.* **1988**, *256*, 357–361.
[77] C. Hedberg, F. J. Dekker, M. Rusch, S. Renner, S. Wetzel, N. Vartak, C. Gerding-Reimers, R. S. Bon, P. I. H. Bastiaens, H. Waldmann, *Angewandte Chemie International Edition* **2011**, *50*, 9832–9837.
[78] H. Sunaga, H. Sugimoto, Y. Nagamachi, S. Yamashita, *Biochem. J.* **1995**, *308 (Pt 2)*, 551–557.
[79] A. Kawaguchi, H. Tomoda, S. Nozoe, S. Omura, S. Okuda, *J. Biochem.* **1982**, *92*, 7–12.
[80] J. A. Menendez, L. Vellon, I. Mehmi, B. P. Oza, S. Ropero, R. Colomer, R. Lupu, in *Pnas*, **2004**, pp. 10715–10720.
[81] J. A. Menendez, R. Lupu, *Nat Rev Cancer* **2007**, *7*, 763–777.
[82] S. G. Straub, H. Yajima, M. Komatsu, T. Aizawa, G. W. G. Sharp, *Diabetes* **2002**, *51 Suppl 1*, S91–S95.
[83] M. Moche, G. Schneider, P. Edwards, K. Dehesh, Y. Lindqvist, *J. Biol. Chem.* **1999**, *274*, 6031–6034.
[84] A. C. Price, K. H. Choi, R. J. Heath, Z. Li, S. W. White, C. O. Rock, *J. Biol. Chem.* **2001**, *276*, 6551–6559.
[85] F. Trajtenberg, S. Altabe, N. Larrieux, F. Ficarra, D. de Mendoza, A. Buschiazzo, G. E. Schujman, *FEBS J* **2014**, *281*, 2324–2338.
[86] B. C. Jennings, M. J. Nadolski, Y. Ling, M. B. Baker, M. L. Harrison, R. J. Deschenes, M. E. Linder, *The Journal of Lipid Research* **2008**, *50*, 233–242.
[87] M. P. Pedro, A. A. Vilcaes, V. M. Tomatis, R. G. Oliveira, G. A. Gomez, J. L. Daniotti, *PLoS ONE* **2013**, *8*, e75232.
[88] D. Davda, B. R. Martin, *Med. Chem. Commun.* **2014**, *5*, 268–276.
[89] E. F. Pettersen, T. D. Goddard, C. C. Huang, G. S. Couch, D. M. Greenblatt, E. C. Meng, T. E. Ferrin, *J. Comput. Chem.* **2004**, *25*, 1605–1612.
[90] F. J. Dekker, C. Hedberg, *Bioorg. Med. Chem.* **2011**, *19*, 1376–1380.
[91] R. A. Laskowski, M. B. Swindells, *J. Chem. Inf. Model.* **2011**, *51*, 2778–2786.
[92] Z. Zhang, A. G. Marshall, *J. Am. Soc. Mass Spectrom.* **1998**, *9*, 225–233.
[93] S. McNicholas, E. Potterton, K. S. Wilson, M. E. M. Noble, *Acta Cryst Section D* **2011**, *67*, 368–394.
[94] T. Williams, C. Kelley, R. Lang, D. Kotz, J. Campbell, G. Elber, A. Woo, **n.d.**
[95] G. V. Richieri, R. T. Ogata, A. W. Zimmerman, J. H. Veerkamp, A. M. Kleinfeld, *Biochemistry* **2000**, *39*, 7197–7204.
[96] H. Bisswanger, *Enzyme Kinetics. Principles and Methods*, Wiley-VCH Verlag, **2008**.
[97] E. Krissinel, K. Henrick, *Journal of Molecular Biology* **2007**, *372*, 774–797.
[98] E. Kong, S. Peng, G. Chandra, C. Sarkar, Z. Zhang, M. B. Bagh, A. B. Mukherjee, *J. Biol. Chem.* **2013**, *288*, 9112–9125.
[99] N. Vartak, B. Papke, H. E. Grecco, L. Rossmannek, H. Waldmann, C. Hedberg, P. I. H. Bastiaens, *Biophysj* **2014**, *106*, 93–105.
[100] B. D. Bothe, Charakterisierung Der Struktur, Regulation Und Biochemie Von Acyl-Protein-Thioesterasen, Ruhr-Universität Bochum, **2014**.
[101] M. D. Winn, C. C. Ballard, K. D. Cowtan, E. J. Dodson, P. Emsley, P. R. Evans, R. M. Keegan, E. B. Krissinel, A. G. W. Leslie, A. McCoy, et al., *Acta Cryst Section D* **2011**, *67*, 235–242.
[102] M. A. Lomize, A. L. Lomize, I. D. Pogozheva, H. I. Mosberg, *Bioinformatics* **2006**, *22*, 623–625.
[103] P. Grochulski, F. Bouthillier, R. J. Kazlauskas, A. N. Serreqi, J. D. Schrag, E. Ziomek, M. Cygler, *Biochemistry* **1994**, *33*, 3494–3500.
[104] P. Grochulski, Y. Li, J. D. Schrag, M. Cygler, *Protein Sci.* **1994**, *3*, 82–91.

[105] Z. Liu, Y. Gosser, P. J. Baker, Y. Ravee, Z. Lu, G. Alemu, H. Li, G. L. Butterfoss, X.-P. Kong, R. Gross, et al., *J. Am. Chem. Soc.* **2009**, *131*, 15711–15716.
[106] S. Longhi, A. Nicolas, L. Creveld, M. Egmond, C. T. Verrips, J. de Vlieg, C. Martinez, C. Cambillau, *Proteins* **1996**, *26*, 442–458.
[107] T. Mashima, H. Seimiya, T. Tsuruo, *Br. J. Cancer* **2009**, *100*, 1369–1372.
[108] M. Wu, S. B. Singh, J. Wang, C. C. Chung, G. Salituro, B. V. Karanam, S. H. Lee, M. Powles, K. P. Ellsworth, M. E. Lassman, et al., *PNAS* **2011**, *108*, 5378–5383.
[109] K. Görmer, M. Bürger, J. A. W. Kruijtzer, I. Vetter, N. Vartak, L. Brunsveld, P. I. H. Bastiaens, R. M. J. Liskamp, G. Triola, H. Waldmann, *ChemBioChem* **2012**, *13*, 1017–1023.
[110] C. Martinez, P. De Geus, M. Lauwereys, G. Matthyssens, C. Cambillau, *Nature* **1992**, *356*, 615–618.
[111] G. Calero, P. Gupta, M. C. Nonato, S. Tandel, E. R. Biehl, S. L. Hofmann, J. Clardy, *J. Biol. Chem.* **2003**, *278*, 37957–37964.
[112] R. E. Purdy, P. E. Kolattukudy, *Biochemistry* **1975**, *14*, 2832–2840.
[113] I. M. Ahearn, F. D. Tsai, H. Court, M. Zhou, B. C. Jennings, M. Ahmed, N. Fehrenbacher, M. E. Linder, M. R. Philips, *Molecular Cell* **2011**, *41*, 173–185.
[114] H. Inoue, H. Nojima, H. Okayama, *Gene* **1990**, *96*, 23–28.
[115] M. R. Green, J. Sambrook, *Molecular Cloning: a Laboratory Manual*, New York, **2012**.
[116] R. K. Saiki, D. H. Gelfand, S. Stoffel, S. J. Scharf, R. Higuchi, G. T. Horn, K. B. Mullis, H. A. Erlich, *Science* **1988**, *239*, 487–491.
[117] K. Kleppe, E. Ohtsuka, R. Kleppe, I. Molineux, H. G. Khorana, *Journal of Molecular Biology* **1971**, *56*, 341–361.
[118] D. B. Smith, K. S. Johnson, *Gene* **1988**, *67*, 31–40.
[119] U. K. Laemmli, *Nature* **1970**, *227*, 680–685.
[120] H. Schägger, G. von Jagow, *Anal. Biochem.* **1987**, *166*, 368–379.
[121] J. W. Engels, *Bioanalytik*, Springer Spektrum, **2016**.
[122] D. J. Ingle, S. R. Crouch, *Spectrochemical Analysis*, Prentice Hall College Book Division, Old Tappan, NJ, USA, **1988**.
[123] H. Edelhoch, *Biochemistry* **1967**, *6*, 1948–1954.
[124] S. C. Gill, P. H. von Hippel, *Anal. Biochem.* **1989**, *182*, 319–326.
[125] B. Rupp, *Biomolecular Crystallography*, Garland Science, **2010**.
[126] H. L. F. Helmholtz, H. Fripp, *The Monthly Microscopical Journal* **1876**.
[127] G. Rhodes, *Crystallography Made Crystal Clear: a Guide for Users of Macromolecular Models*, Academic Press, **2010**.
[128] M. Abramowitz, M. W. Davidson, "Immersion Media," can be found under http://www.olympusmicro.com/primer/anatomy/immersion.html, **n.d.**
[129] J. Clayden, N. Greeves, S. Warren, P. Wothers, *Organic Chemistry*, Oxford University Press: Oxford, **2001**.
[130] W. C. Röntgen, *Stahel'sche K. Hof- und Universitätsbuch- und Kunsthandlung, Würzburg* **1895**.
[131] A. T. Brünger, *Nature* **1992**, *355*, 472–475.
[132] T. G. G. Battye, L. Kontogiannis, O. Johnson, H. R. Powell, A. G. W. Leslie, *Acta Cryst Section D* **2011**, *67*, 271–281.
[133] "go.com: automated data processing at X10SA at SLS," can be found under https://www.psi.ch/sls/pxii/data-processing-and-analysis, **n.d.**
[134] W. Kabsch, *Acta Cryst Section D* **2010**, *66*, 125–132.
[135] P. R. Evans, *Acta Cryst Section D* **2011**, *67*, 282–292.
[136] P. H. Zwart, R. W. Grosse-Kunstleve, P. D. Adams, *CCP4 Newsletter* **2005**, *43*.
[137] A. J. McCoy, R. W. Grosse-Kunstleve, P. D. Adams, M. D. Winn, L. C. Storoni, R. J. Read, *J. Appl. Cryst.* **2007**, *40*, 658–674.
[138] G. N. Murshudov, P. Skubak, A. A. Lebedev, N. S. Pannu, R. A. Steiner, R. A. Nicholls, M. D. Winn, F. Long, A. A. Vagin, *Acta Cryst (2011). D67, 355-367 [doi:10.1107/S0907444911001314]* **2011**, 1–13.
[139] P. Emsley, B. Lohkamp, W. G. Scott, K. Cowtan, *Acta Cryst Section D* **2010**, *66*, 486–501.
[140] G. N. Ramachandran, C. Ramakrishnan, V. Sasisekharan, *Journal of Molecular Biology* **1963**, *7*, 95–99.

[141] V. B. Chen, W. B. Arendall, J. J. Headd, D. A. Keedy, R. M. Immormino, G. J. Kapral, L. W. Murray, J. S. Richardson, D. C. Richardson, *Acta Cryst Section D* **2009**, 1–10.
[142] G. J. Kleywegt, *Acta Crystallogr D Biol Crystallogr* **2006**, *63*, 94–100.
[143] PerkinElmer Inc., **n.d.**
[144] N. W. Moriarty, R. W. Grosse-Kunstleve, P. D. Adams, *Acta Crystallogr D Biol Crystallogr* **2009**, *65*, 1074–1080.
[145] P. D. Adams, P. V. Afonine, G. Bunkóczi, V. B. Chen, I. W. Davis, N. Echols, J. J. Headd, L. W. Hung, G. J. Kapral, R. W. Grosse-Kunstleve, et al., *Acta Cryst Section D* **2010**, *66*, 213–221.
[146] M. J. Hope, M. B. Bally, L. D. Mayer, A. S. Janoff, P. R. Cullis, *Chemistry and Physics of Lipids* **1986**, *40*, 89–107.
[147] J. Spiegel, P. M. Cromm, A. Itzen, R. S. Goody, T. N. Grossmann, H. Waldmann, *Angewandte Chemie International Edition* **2014**, *53*, 2498–2503.
[148] H. Berman, K. Henrick, H. Nakamura, *Nature Structural & Molecular Biology* **2003**.

9 Acknowledgements

First and foremost, I want to express my sincere gratitude to Dr. Ingrid Vetter for the opportunity to work on this project, the inspirational discussions, her enthusiasm, and the patient and constructive support I received throughout the years as a PhD student. The time in her lab has strongly influenced my scientific development. I would like to thank Prof Dr. Andrea Musacchio for discussions and comments on the progress of my project, and for his time to be the second reviewer of my thesis. I am thankful to Prof. Dr. Daniel Rauh for his encouraging comments and taking his time to serve as the first reviewer of my thesis. I appreciate the constructive comments on my research project I received from Prof. Dr. Roger Goody and Dr. Sven Hennig as members of my internal thesis advisory committee.

Very special thanks go to Patricia Stege for cloning, expression and purification of all proteins worked with during this thesis, and without her, this work would not have been carried out to this extend. I thank Dr. Marco Bürger, former member of the group, for introducing me into the project and providing practical support in the first year, and Stefan Baumeister and Kathrin Estel for their collaborative working attitude.

I thank the crystallographic community in Dortmund and Bochum for mutual support in data collection, and for the trust set in me to collect diffraction data of a wide variety of crystallographic projects. Special thanks go to Mihai Gazdag, a friend and mentor, for the things he taught me and the jolly good times we had at the synchrotron beam line. I thank Georg Holtermann for the maintenance of the equipment in the crystallogenesis and crystallography facilities. I acknowledge the support provided by the beam line staff of X10SA at SLS during our data collection shifts.
I thank the whole IMPRS-CMB team, and especially Christa Hornemann, for the organization of the numerous seminars and retreats that facilitate interdisciplinary scientific and social exchange within the institute.
Appreciation goes to the whole Department 1 for the open and constructive working environment. I am grateful to Claudia Breit, Anika Altenfeld, and Kerstin Klare for general discussions beyond the scientific level during lunch times that significantly contributed to the quality of life during harder times of our concurrent theses. I acknowledge the proof-readers for their necessary and constructive comments, without which my thesis would not have reach this quality.

Finally, I am deeply grateful for the support I experienced from my whole family throughout my studies and PhD. I am grateful to Sandy for bearing me during writing up this thesis.

10 Other publications of this author

L. E. Kemp, M. Rusch, A. Adibekian, H. E. Bullen, A. Graindorge, C. Freymond, M. Rottmann, C. Braun-Breton, S. Baumeister, **A. T. Porfetye**, I. R. Vetter, C. Hedberg, and D. Soldati-Favre, *J. Biol. Chem.* **2013**, *288*, 27002–27018.

P. Meekrathok, M. Burger, **A. T. Porfetye**, I. R. Vetter, and W. Suginta, *Acta Cryst Section F* **2015**, *71*, 1–7.

A. Ursu, D. J. Illich, Y. Takemoto, **A. T. Porfetye**, M. Zhang, A. Brockmeyer, P. Janning, N. Watanabe, H. Osada, I. R. Vetter, S. Ziegler, H. R. Schöler, and H. Waldmann, *Cell Chem Biol* **2016**, *23*, 494–507.

11 Eidesstattliche Versicherung (Affidavit)

Name, Vorname
(Surname, first name)

Matrikel-Nr.
(Enrolment number)

Belehrung:

Wer vorsätzlich gegen eine die Täuschung über Prüfungsleistungen betreffende Regelung einer Hochschulprüfungsordnung verstößt, handelt ordnungswidrig. Die Ordnungswidrigkeit kann mit einer Geldbuße von bis zu 50.000,00 € geahndet werden. Zuständige Verwaltungsbehörde für die Verfolgung und Ahndung von Ordnungswidrigkeiten ist der Kanzler/die Kanzlerin der Technischen Universität Dortmund. Im Falle eines mehrfachen oder sonstigen schwerwiegenden Täuschungsversuches kann der Prüfling zudem exmatrikuliert werden, § 63 Abs. 5 Hochschulgesetz NRW.

Die Abgabe einer falschen Versicherung an Eides statt ist strafbar.

Wer vorsätzlich eine falsche Versicherung an Eides statt abgibt, kann mit einer Freiheitsstrafe bis zu drei Jahren oder mit Geldstrafe bestraft werden, § 156 StGB. Die fahrlässige Abgabe einer falschen Versicherung an Eides statt kann mit einer Freiheitsstrafe bis zu einem Jahr oder Geldstrafe bestraft werden, § 161 StGB.

Die oben stehende Belehrung habe ich zur Kenntnis genommen:

Official notification:

Any person who intentionally breaches any regulation of university examination regulations relating to deception in examination performance is acting improperly. This offence can be punished with a fine of up to EUR 50,000.00. The competent administrative authority for the pursuit and prosecution of offences of this type is the chancellor of the TU Dortmund University. In the case of multiple or other serious attempts at deception, the candidate can also be unenrolled, Section 63, paragraph 5 of the Universities Act of North Rhine-Westphalia.

The submission of a false affidavit is punishable.

Any person who intentionally submits a false affidavit can be punished with a prison sentence of up to three years or a fine, Section 156 of the Criminal Code. The negligent submission of a false affidavit can be punished with a prison sentence of up to one year or a fine, Section 161 of the Criminal Code.

I have taken note of the above official notification.

Ort, Datum
(Place, date)

Unterschrift
(Signature)

Titel der Dissertation:
(Title of the thesis):

Ich versichere hiermit an Eides statt, dass ich die vorliegende Dissertation mit dem Titel selbstständig und ohne unzulässige fremde Hilfe angefertigt habe. Ich habe keine anderen als die angegebenen Quellen und Hilfsmittel benutzt sowie wörtliche und sinngemäße Zitate kenntlich gemacht.
Die Arbeit hat in gegenwärtiger oder in einer anderen Fassung weder der TU Dortmund noch einer anderen Hochschule im Zusammenhang mit einer staatlichen oder akademischen Prüfung vorgelegen.

I hereby swear that I have completed the present dissertation independently and without inadmissible external support. I have not used any sources or tools other than those indicated and have identified literal and analogous quotations.

The thesis in its current version or another version has not been presented to the TU Dortmund University or another university in connection with a state or academic examination.*

*Please be aware that solely the German version of the affidavit ("Eidesstattliche Versicherung") for the PhD thesis is the official and legally binding version.

Ort, Datum
(Place, date)

Unterschrift
(Signature)

12 Appendix

Table 27: Tabular overview of the structures presented in this thesis. The structures of human APT1 M60S and human APT1 ΔM60 (both as apo form and 2BP complex) were solved and refined by Darius Bothe in his master thesis[100] under my supervision.

Protein	Space group	Unit cell (a, b, c, [Å])	Unit cell (α, β, γ, [Å])	Monomers per asymmetric unit	Resolution [Å]
Yeast APT apo	$P2_12_12_1$	44.70, 45.94, 91.22	90, 90, 90	1	1.44
Yeast APT + Palmostatin B	$P2_12_12_1$	44.34 45.26 90.21	90, 90, 90	1	1.70
Yeast APT + Palmostatin M	$P4_22_12$	145.6, 145.6, 96.8	90, 90, 90	4	2.40
Human APT1 + Cerulenin	$P4_22_12$	91.15 91.15 255.53	90, 90, 90	4	2.50
Human APT1 + 2-Bromopalmitate	$P2_1$	72.59 62.08 114.67	90, 106.13, 90	4	1.60
Human APT1 L171A	$P2_1$	76.88, 55.50, 101.55	90, 112.05, 90	4	2.20
Human APT1 L171V	P1	38.5, 40.9, 71.9	102.1,95.6, 106.2	2	1.28
Human APT1 L58A	C2	181.52, 79.73, 154.94	90.00, 124.57, 90.00	8	2.62
Human APT1 L73A	$P2_1$	35.65 57.41 47.92	90.00, 98.76 90.00	1	1.60
Human APT1 L73A + 2BP	$P2_12_12_1$	73.97, 109.70, 109.79	90, 90, 90	4	1.85
Human APT1 +LP	$P2_1$	36.37 59.44 49.55	90.0 100.03 90.0	1	2.00
Human APT1 ΔL73S74	C2	106.57, 105.23, 143.74	90.0, 92.88, 90.0	8	2.55
Human APT1 ΔL73S74 + 2BP	C2	139.37, 57.71, 64.33	90.0, 92.71, 90.0	2	1.62
Human APT1 ΔS74P75	$P2_1$	36.47, 58.46, 49.63	90.0, 100.96, 90.0	1	1.85
Human APT1 M60S apo	$P2_12_12_1$	70.85, 77.83, 143.55	90.0, 90.0, 90.0	4	1.95
Human APT1 M60S + 2BP	$P2_1$	72.17, 61.63, 114.08	90.0, 101.98, 90.0	4	1.85
Human APT1 ΔM60 apo	P1	39.66, 39.67, 69.70	86.95, 88.91, 63.95	2	1.34
Human APT1 ΔM60 + 2BP	P1	39.71, 39.76, 69.87	89.07, 87.10, 63.92	2	1.56
Human APT1 ΔM60+M202A (crystal1)	P1	41.64, 68.18, 76.23	112.15 104.31 89.91	4	2.22
Human APT1 ΔM60+M202A (crystal2)	C2	68.00, 41.46, 71.96	90.00, 94.68, 90.00	1	2.22

Table 28: List of programs used in this thesis

Program	Source	Application
iMosflm	http://www.mrc-lmb.cam.ac.uk/harry/imosflm/ver721/introduction.html [132]	Data collection strategy
XDS Package	http://xds.mpimf-heidelberg.mpg.de/ [134]	Diffraction data indexing, integration and reduction
CCP4I package	http://www.ccp4.ac.uk/ccp4i_main.php [101]	Program suite for protein crystallography
PhaserMR	http://www.ccp4.ac.uk/ccp4i_main.php [137]	Phasing X-ray data
Refmac5	http://www.ccp4.ac.uk/ccp4i_main.php [138]	Structure model refinement
PISA	http://www.ebi.ac.uk/pdbe/pisa/ [97]	Interface analysis
Coot	http://www2.mrc-lmb.cam.ac.uk/personal/pemsley/coot/ [139]	Structure refinement and validation
Phenix package	http://www.phenix-online.org/ [145]	Program suite for protein crystallography
Xtriage	http://www.phenix-online.org/ [136]	Diffraction data quality analysis
eLBOW	http://www.phenix-online.org/ [144]	Generating geometry restraints for ligands
ChemBioDraw	PerkinElmer, Inc [143]	Chemical drawing
MolProbity	http://molprobity.biochem.duke.edu/ [141]	Structure validation
CCP4mg	http://www.ccp4.ac.uk/MG/ [93]	Structure representation
Gimp	http://www.gimp.org/ [4]	Image manipulation and annotation
MagTran	[92]	Mass Spectrometry

Table 29: List of webservers and data banks used in this thesis.

Server / data bank name	Web address	
PISA	http://www.ebi.ac.uk/pdbe/pisa/ [97]	Analysis of protein interface in crystals
Orientations of Proteins in Membranes (opm)	http://opm.phar.umich.edu/ [102]	Prediction of protein insertion into biomembranes
Protein Data Bank (PDB)	http://www.wwpdb.org/ [148]	Data bank for three-dimensional protein structures
Hetero-compound Information Centre – Uppsala (HIC-Up)	http://xray.bmc.uu.se/hicup/ [142]	Structures of hetero compounds used in structural biology

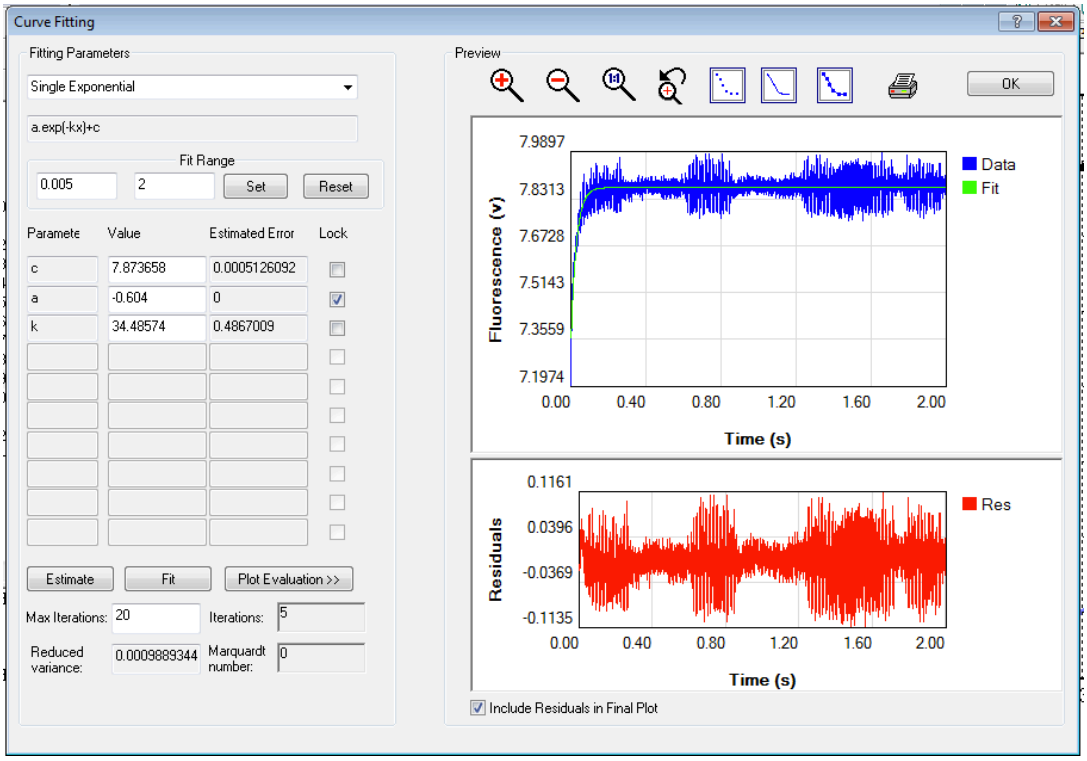

Figure 116: Exemplary measurement of the dissociation rate of human APT1 wild type (5 µM) and 2BP (20 µM) using CHAPS (1%) as competitor. The data can be fitted using a single rate constant in the range of 34 s^{-1}. The noise has a frequency of 50 Hz, unfortunately, the electrical consumer causing this interference is unknown. Screenshot of Pro-Data software (Applied Photophysics) used for data fitting of Stopped Flow measurements.

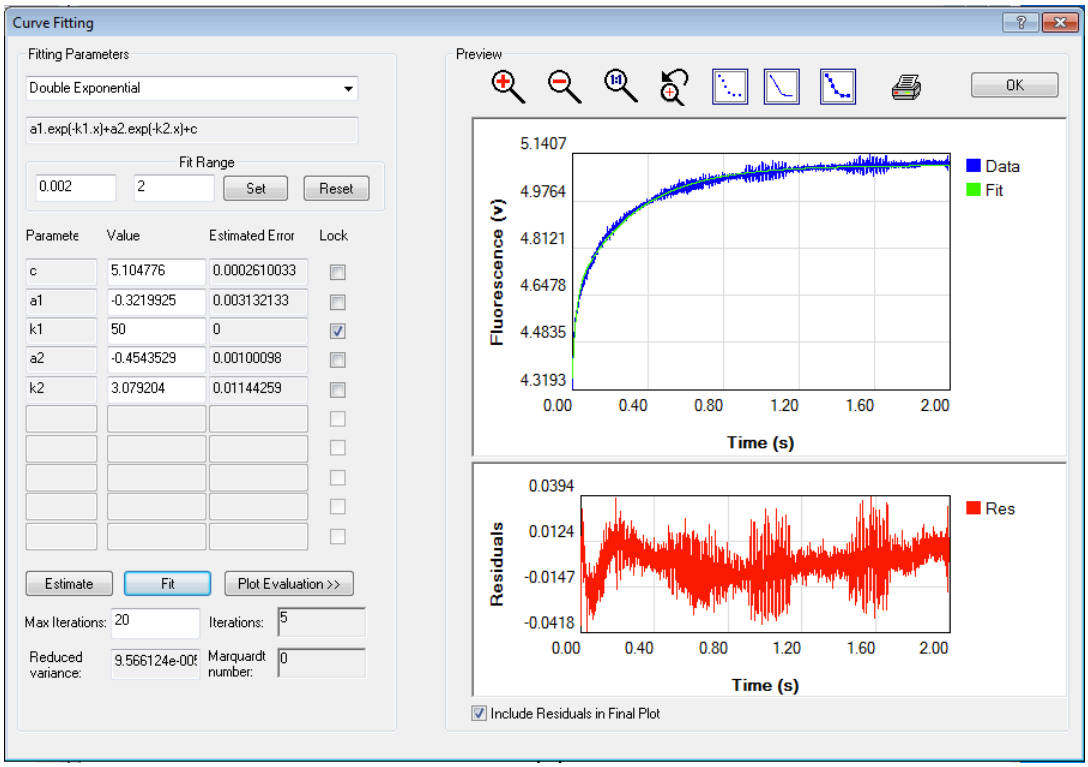

Figure 117: Exemplary measurement of the dissociation rate of human APT1 wild type (5 µM) and 2BP (20 µM) using L-FABP (45 µM) as competitor. The higher dissociation rate constant was estimated in the range of k_{off} = 50 s^{-1} (probably corresponding to 2BP unspecifically bound next to W32 at the groove) compared to k_{off} = 3 s^{-1} (2BP bound inside the tunnel), but has a smaller contribution to the overall signal (-0.32 *versus* -0.45, respectively). The noise has a frequency of 50 Hz, unfortunately, the electrical consumer causing this interference is unknown. Screenshot of Pro-Data software (Applied Photophysics) used for data fitting of Stopped Flow measurements.